RE-ORDER NO. 64-357

CONTRACT NO. 950564
Under NAS7-100

DOCUMENT NO 64SD4329

RF TRANSPARENT, ENERGY ABSORBING, STRUCTURAL ELEMENTS

PHASE II
FINAL REPORT

prepared for

CALIFORNIA INSTITUTE OF TECHNOLOGY
(JET PROPULSION LABORATORY)
4800 OAK GROVE DRIVE
PASADENA, CALIFORNIA

AUGUST 17, 1964

REVISED PAGES SEPT. 2, 1964
REVISED PAGES - FEB. 15, 1965

GENERAL ELECTRIC
MISSILE AND SPACE DIVISION

CONTRACT NO. 950564 DOCUMENT NO 64SD4329

RF TRANSPARENT, ENERGY ABSORBING, STRUCTURAL ELEMENTS

PHASE II FINAL REPORT

prepared for

CALIFORNIA INSTITUTE OF TECHNOLOGY
(JET PROPULSION LABORATORY)
4800 OAK GROVE DRIVE
PASADENA, CALIFORNIA

AUGUST 17, 1964

Wm M Meyers
W. M. Meyers, Spacecraft Design Engineer

H G Lorsch
H. G. Lorsch, Manager, Mechanical Components

GENERAL ELECTRIC
MISSILE AND SPACE DIVISION
Valley Forge Space Technology Center
P.O. Box 8555 • Philadelphia 1, Penna.

TABLE OF CONTENTS

TABLE OF CONTENTS (Continued)

LIST OF ILLUSTRATIONS

LIST OF TABLES

1. FOREWORD

This is the final report on Phase II of the research work performed by the Spacecraft Department of the General Electric Company with assistance from the Space Sciences Laboratory and sponsored by the Jet Propulsion Laboratory of the California Institute of Technology, Pasadena, California, under Contract No. 950564 (subcontract under NASA Contract NAS 7-100). Mr. Russell McFarland, Jr. was the project engineer.

The objective of the contract was to develop and test structural elements which have high specific mechanical impact energy absorption and low electric attenuation in the (S-band) radio frequency range.

The first phase of the contract was initiated on June 5, 1963, and concluded on March 16, 1964. Work covering that phase was reported in "RF Transparent, Energy Absorbing Structural Elements, Phase I, Final Report," Document No. 64SD565, dated March 16, 1964. The second phase was initiated on March 17, 1963, and concluded on August 17, 1964. Work accomplished during this phase is described in this report.

2. ABSTRACT

This is the final report of Phase II of a project for the development and testing of energy absorbing, structural elements having high specific energy absorption and low dielectric constant and loss tangent. The design objective was to improve the mechanical properties of the material developed in Phase I, to determine the effect of angular impact on the material, and to establish the manufacturing limitations in forming the developed material to singly and doubly curved contours. Details of the design, fabrication, testing, and performance of the system are included.

3 INTRODUCTION

The probability of effecting soft landings on the surface of the moon or the planets has spurred the development of more efficient impact energy absorbing materials. Since weight is an overriding consideration for most space missions, the efficiency of such a material is usually defined in terms of the specific energy absorption, which is the mechanical impact energy absorbed, divided by the gross weight of the impact absorbing structural element.

However, if the primary purpose of the energy absorbing structural component is considered, which is to reduce the peak deceleration experienced by the vehicle payload, it becomes obvious that this definition of efficiency by itself is insufficient. In order to minimize payload decelerations, the load deformation curve of the energy absorber should be as flat as possible. Moreover, its elastically recoverable (rebound) energy should be at a minimum. If this requirement is combined with that of high specific energy absorption, it becomes mandatory to absorb energy through as large a thickness of material as possible. This introduces the concept of thickness efficiency, defined as the change in material thickness before and after crushing, divided by the original thickness.

The majority of the presently available, efficient absorbers of mechanical energy are metallic in nature and thus are not transparent to radio frequency (RF) transmission. A notable exception is balsa wood which, however, suffers from non-uniformity and the fact that its physical parameters can neither be closely controlled nor arbitrarily varied. If property variation and control are desired, the use of materials which are generated by natural growth is virtually ruled out.

As a rule, uniaxial tensile or compressive loading is assumed as a matter of course when considering the absorption of mechanical impact energy. However, it is obvious that such a loading condition would hardly ever exist during the case of planetary impact. The direction of the velocity vector of the landing vehicle with respect to the ground may change during impact, or this direction may be unknown prior to impact as, for example, during vertical impact on an inclined surface. It therefore seems prudent during the development phase of impact energy absorbing elements to consider the applicability of such elements to other than uni-directional impact.

A primary requisite for the development of mechanical impact energy absorbing elements, which are transparent to RF transmission, is that this is not simply a materials development problem; the application of the material to structural elements and components is paramount. If a highly efficient material were developed which turned out to be extremely difficult to manufacture or which could only be manufactured in certain shapes, the value of such a development would be highly questionable. Ease of manufacture is, therefore, a consideration which should not be ignored during the development phase.

4. SUMMARY

A design, manufacturing, and test program was carried out for the continued development of glass cloth reinforced, plastic honeycomb material for use as radio frequency (RF) transparent, impact energy absorbing, structural elements suitable for use in lunar or planetary landing vehicles.

At the present stage of development the material is a more efficient impact energy absorber than balsa wood, transparent to RF transmission, readily and cheaply available, and has properties which can be custom tailored to each specific application. In view of the success of the development undertaken thus far, additional work should be pursued on

a. determining the behavior at high and low temperatures likely to be encountered during lunar or planetary landings.

b. improving the adhesive bond strength.

c. fabricating singly and doubly curved honeycomb panels by a new process recently developed outside the scope of this contract.

d. evaluating the strengthened interlaminary bond and the new honeycomb by performing angular impact test,

e. evaluating the effect of the mechanical properties of the landing surfaces on the behavior of this material, particularly under angular impact.

Testing of various glass cloth reinforced, plastic honeycomb designs during Phase I of this contract established the following facts concerning this material.

a. No effect of impact velocity on energy absorption was observed.

b. The primary contributor to energy absorption is the resin and not the glass.

c. The honeycomb elements developed have very low RF attenuation rates.

d. Increases of specific energy with increasing density were observed throughout the range tested.

The three investigations carried out during the present Phase II of the program were the determination of (1) optimum densities for honeycombs of three different size cells, (2) the effect of angular impact on energy absorption properties, and (3) the manufacturing limitations in forming the material into singly and doubly curved surfaces.

In the study of optimum densities, it was found that a 3/16 inch cell glass reinforced phenolic resin honeycomb having a density of 11 lb/cu-ft is optimum and yields an energy absorption value of 24,000 ft-lb/lb. The optimum densities for larger cell sizes were found to yield lower specific energy absorption values. The stroke efficiency decreases somewhat in the higher density materials, but the increase in specific energy absorption per pound of material crushed greatly overshadows this small reduction.

Under angular impact the specific energy of the material decreases uniformly at the approximate rate of two percent per degree. Thus, for an impact angle of 30 degrees, the reduction is 60 percent from the maximum value at normal impact. Reliable conclusions indicate that this performance can be improved ten to fifteen percent by increasing the bond strength of the adhesive used to fabricate the honeycomb. This would also increase the reliability, or repeatability, of the material at the higher angles of impact. Dynamic tests with velocities up to 46 ft/sec verified the results obtained in static tests, and no effect of impact velocity on energy absorption was observed.

Forming of the honeycomb material into curved panels was considerably more difficult than anticipated. Fair results were obtained in singly curved panels and an R/t (Radius of Curvature/Material Thickness) ratio of three was obtained. Fair results were also obtained in forming the doubly curved panels and an R/t ratio of nine obtained. Because of the problems encountered in forming this material, a newly developed design which has a core pattern other than a hexagon, should be investigated for its suitability as an energy absorber. This design, which is fabricated by the corrugation method (Ref. Phase I Final Report, Section 5.2.3) can readily be formed into singly and doubly curved panels.

5. DESIGN AND MANUFACTURE OF STRUCTURAL ELEMENTS

5.1 INTRODUCTION

As discussed in the Phase I Final Report (Section 9.2.2), the contribution of the glass in the material to the energy absorption is negligible, and the primary energy absorber is the resin. Based on these findings, the specific energy can be increased by the addition of resin. This can be accomplished by repeated cycles of dipping the honeycomb in a resin bath and then curing. A ratio of resin to glass of 75 percent or greater was found to be favorable to high values of specific energy. In order to determine the optimum values of bulk density (for various cell sizes) which yield the highest value of specific energy while retaining the excellent crushing properties of the material, a series of specimens was fabricated and tested. These specimens were identical in configuration and differed in bulk density only. Additional specimens were fabricated from this optimized material, and specially cut shapes were used to determine the affect of angular impact on energy absorption.

A third series of specimens was fabricated for the purpose of determining the maximum radius to which this type of material could be formed. Details of the above three series of specimens will be found in the following paragraphs.

5.2 FABRICATION

All specimens fabricated in Phase II were made from a plain weave, Style 112 cloth, and Plaskon Laminating Varnish V-204 — a high-temperature phenolic resin. The resin is manufactured by the Plastics Division of Allied Chemical Corporation.

All specimens were prefailed on the end to be crushed by placing saw cuts through each cell in two perpendicular directions. The depth of these saw cuts varied from 1/8 to 1/4 inch. These saw cuts were necessary to prevent buckling failures of the specimens due to a high loading which occurs on non-prefailed specimens immediately prior to crushing of the material.

The expansion method, as described in Section 5.2.3 of the Phase I final report (Section 5.2.3), was used in fabricating all of the specimens.

5.3 OPTIMUM DENSITY SPECIMENS

As discussed in the Phase I Final Report (Section 9.2.2), the densities in which plastic honeycombs are commercially fabricated are not optimum for energy absorption purposes. Increasing the density of existing specimens increased the specimen's specific energy. Results of this investigation were summarized in the Phase I Final Report (Figure 9-2).

During the current phase of the program, the specimens in Table 5-1 were fabricated and tested to determine at what density, for a given cell size, the maximum specific energy is obtained. Two additional items considered in this investigation were manufacturing limitations and uniformity of the load during crushing. The 3/16 inch and 1/4 inch cell size specimens were fabricated to a size of 2 inches by 2 inches by 4 inches. This size was sufficiently large enough to prevent edge effects on good specimens and small enough to prevent overloading of the static testing machine.

TABLE 5-1. SPECIMEN SERIES OF OPTIMUM DENSITY DETERMINATION

Specimen Number	Cell Size (inches)	Specimen Size (inches)	Density (lb/cu-ft)
10Pa	3/16	2 x 2 x 4	12
10Pb	3/16	2 x 2 x 4	12
10Pc	3/16	2 x 2 x 4	12
11Pa	3/16	2 x 2 x 4	14
11Pb	3/16	2 x 2 x 4	14
11Pc	3/16	2 x 2 x 4	14
12Pa	1/4	2 x 2 x 4	10
12Pb	1/4	2 x 2 x 4	10
12Pc	1/4	2 x 2 x 4	10
13Pa	1/4	2 x 2 x 4	12
13Pb	1/4	2 x 2 x 4	12
13Pc	1/4	2 x 2 x 4	12
10Ra	3/8	2 x 2 x 2	12
10Rb	3/8	2 x 2 x 2	12
10Rc	3/8	2 x 2 x 2	12
11Ra	3/8	3 x 3 x 2	16
11Rb	3/8	2 x 3 x 2	16
11Rc	3/8	2 x 3 x 2	16
11Rd	3/8	2 x 2 x 2	16
11Re	3/8	2 x 2 x 2	16

NOTES: (1) Specimen Types 10P, 11P, 12P, and 13P are standard honeycomb fabrications except for density and tolerance on density which were ± 3% instead of the usual ± 10%. High-temperature phenolic resin, Plaskon V-204, was used with number 112 reinforcing cloth.

(2) Specimen Types 10R and 11R were fabricated from specimens remaining at General Electric from Phase I work by dipping in polyester resin, Plaskon 911, and curing a sufficient number of times to obtain the desired density.

(3) All specimens were fabricated by the expansion method.

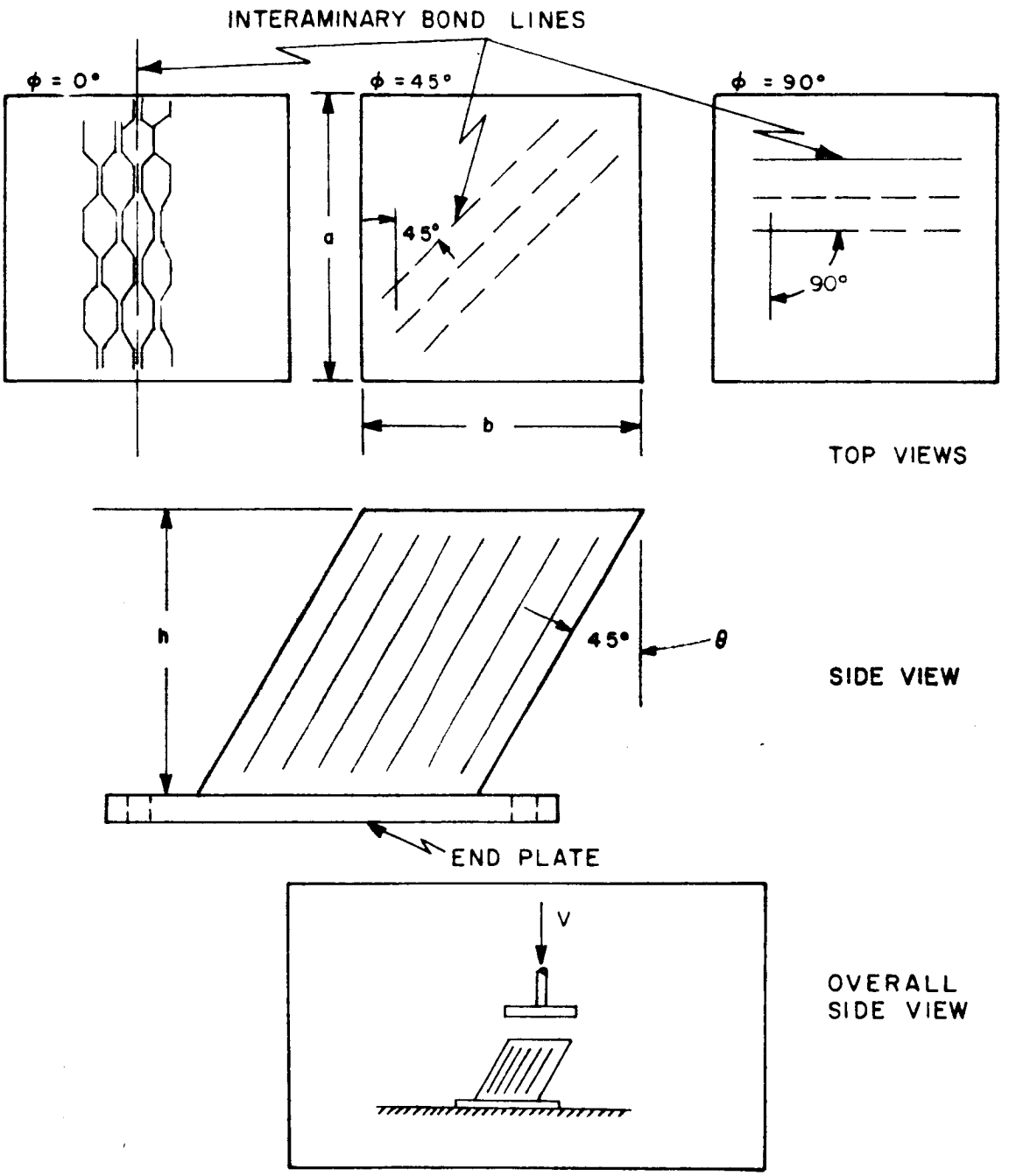

Figure 5-1. Impact Angle Orientation Specimen

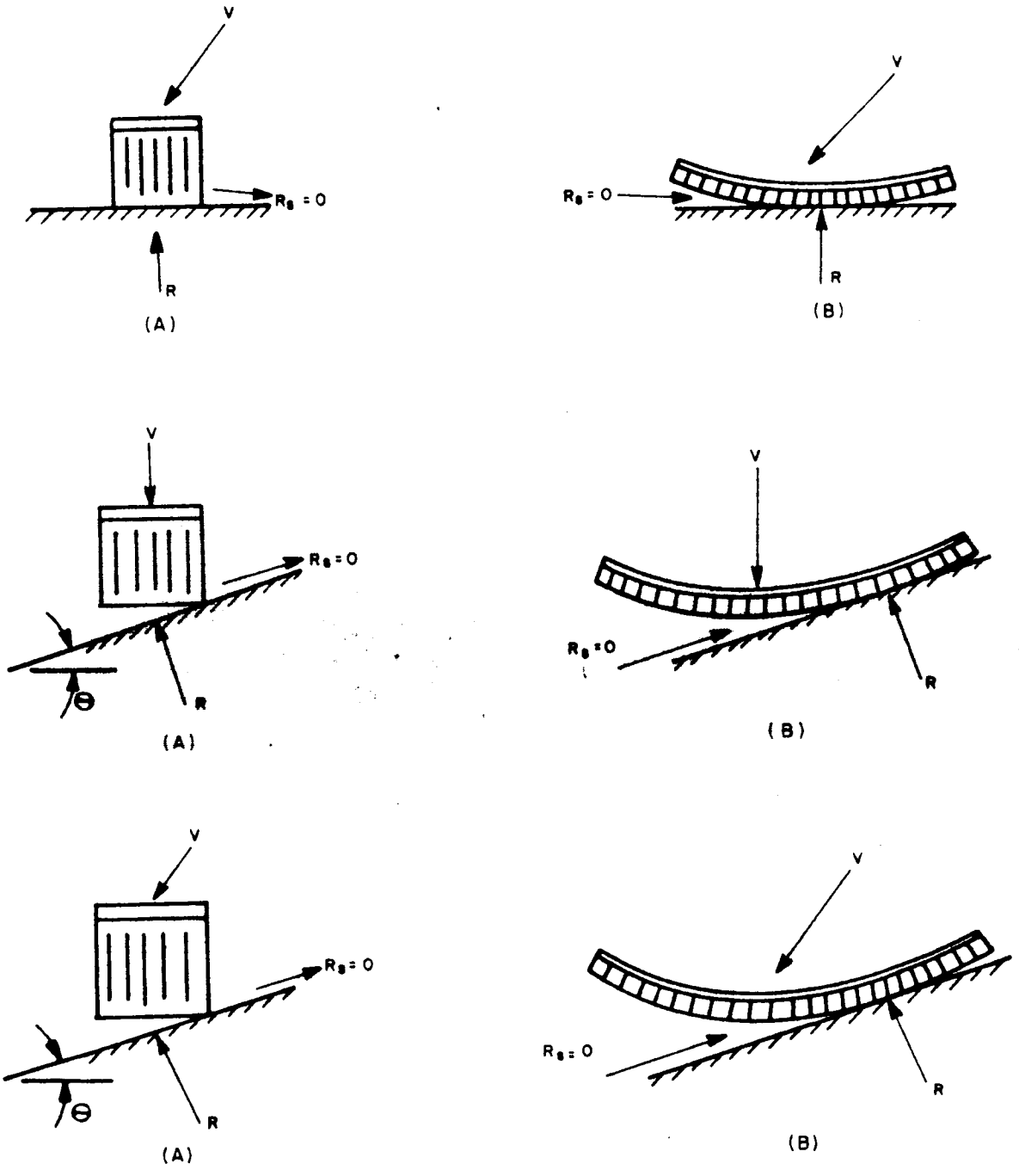

Figure 5-2. Angular Impact Cases

5.4 ANGULAR IMPACT SPECIMENS

A single configuration was used for all angular impact testing. The configuration yielding maximum specific energy was based on the test results summarized in Table 6-1. This was a 3/16 inch cell having a bulk density of 11 pounds per cubic foot. Each specimen was bonded to a metal end plate which permitted attachment of the specimen to the lower platen of the testing machine. The specimen design is described in Figure 5-1 and Table 5-2.

TABLE 5-2. ANGULAR IMPACT SPECIMENS

Specimen Type	Dimensions (Inches)*			Angles (Degrees)	
	a	b	h	θ	ϕ
AS-0-0	2	2	2	0	0
AS-10-0	2	2	2	10	0
AS-10-45	2	2	2	10	45
AS-10-90	2	2	2	10	90
AS-20-0	2	2	2	20	0
AS-20-45	2	2	2	20	45
AS-20-90	2	2	2	20	90
AS-30-0	2	2	2	30	0
AS-30-45	2	2	2	30	45
AS-30-90	2	2	2	30	90
AD-0-0	5	5	5	0	0
AD-10-0	5	5	5	10	0
AD-10-45	5	5	5	10	45
AD-10-90	5	5	5	10	90
AD-20-0	5	5	5	20	0
AD-20-45	5	5	5	20	45
AD-20-90	5	5	5	20	90
AD-30-0	5	5	5	30	0
AD-30-45	5	5	5	30	45
AD-30-90	5	5	5	30	90

NOTES: * See Figure 5-1

Specimens having θ angles of 0, 10, 20, and 30 degrees were manufactured. The angle, θ, is defined as the angle between the impact velocity vector and the cell axes (Figure 5-1). $\theta = 0$ corresponds to normal impact.

Because honeycomb is made up of parallel, corrugated strips which are bonded together, its shear strength varies with the angle between the shear plane and the bond lines. The complement of this angle to 90 degrees is denoted by ϕ (Figure 5-1). Three values of this angle, 0, 45, and 90 degrees were used to evaluate the effect of shear strength on bond line orientation.

Until tests were performed to determine the effect of angular impact on the specific energy of the specimen, the energy value available in a specimen could not be accurately predicted. Therefore, the dynamic impact tests specimens could not be accurately sized so that the entire specimen would be crushed. As shown in previous tests (Phase I), the energy values obtained in a specimen are repeatable, when the same specimen is crushed repeatedly, if no failure of the specimen occurs.

Angular impact tests were so planned that friction of the landing surface was assumed to be zero. This assumption established allowable or dictated test procedures which must be used to obtain data which are divorced from friction effects. Considering the three cases of angular impact that can occur (Figure 5-2), it can be shown that all desired data can be obtained from using the results of two types of tests for any combination of angles.

The two test types are: 1) a crushing test with the direction of force parallel to the axis of the honeycomb, and 2) a crushing test with the direction of force at some angle, θ, to the axis of the honeycomb.

In Case 1A (Figure 5-2) the only force being exerted on the specimen is a crushing force along the axis of the core. The horizontal component of the velocity vector (V) would remain constant and cause the specimen to continue at its original horizontal velocity, even after crushing. In Case 2A (Figure 5-2), assuming the direction of motion of the vehicle remained the same during crushing, this motion could be simulated by fixing the vehicle end of the specimen and exerting a force along R, at an angle θ with the core axis. By the same reasoning, the remaining four cases of Figure 5-2 can be calculated from the data obtained in these two tests. Therefore, specimens tested in this program were subjected to, first, a crushing force parallel to the core axis and, secondly, a force as shown in Figure 5-1.

In the testing of angular impact specimens, an end plate was bonded to one end of the specimens. This end plate was then rigidly attached to the base of the testing machine for both dynamic and static test set-ups. By using this end plate, the specimen was forced to remain in its original position as would be the case if the specimen were attached to a vehicle. This assumes that the vehicle would continue to move in the same direction after crushing had started and continue in that direction until the vehicle was stopped. Thus, tumbling of the vehicle is ruled out. A perforated plate was used on the dynamic specimens to eliminate the effect of air trapped inside the specimens during crushing.

Because it is necessary to prefail the specimen ends to prevent a high force impulse on contact (Section 5.2), there was no advantage to bonding an end plate to the end to be

crushed for this phase of the testing. Such an end plate would only serve as a base on which to crush and would no longer be connected to the specimen once crushing had begun. Such an end plate could be advantageous where a landing was being made on a rough surface with the impact velocity vector perpendicular to the surface. In the case of sliding angular impact on a flat surface, the plate would probably slide off the honeycomb material and not serve any useful function.

If the vehicle were spherical or cylindrical in shape and the cover was continuous and therefore prevented from coming loose, a gain in efficiency would probably occur provided the surface was relatively rough and therefore tended to rip the honeycomb material before it absorbed energy by crushing. Testing of the material on various types of surfaces would be required to establish these parameters. Because of these reasons end plates were not used on the end of the specimen to be crushed.

5.5 CURVED SPECIMENS

Honeycomb Products Inc., Mt. Vernon, Ohio, was chosen as the vendor to determine the manufacturing limitations in forming curved panels from the material developed under Phase I, because of their previous experience in curving reinforced plastic honeycomb cores for aircraft and aerospace applications. The curved material was five inches thick and curved in three directions. While the radius of curvature was on the order of 12 feet, it was felt that the experience gained in doing this work and the techniques developed should help in performing the work required for the present contract.

The vendor's procedure for curving honeycomb pieces is to apply weights to the material and then rapidly raise the temperature above the normal cure temperature. When this is done, there is a short period of approximately 20 seconds during which the material softens and creeps to the shape dictated by the weights. There is no decrease in the physical properties as a result of this temperature. The trick in performing this operation is in establishing the proper weight distribution and quantity. Too much or too little weight causes catastrophic results. In the case of forming cylindrical shapes, for example, more weight is required at the ends than in the center to prevent a saddle shape from forming.

Material ranging from one to twelve inches thick was used in determining an R/t (radius of curvature/material thickness) ratio limit. The material used was 1/4 inch cell, 10 pounds per cubic foot density, phenolic resin honeycomb. The following specimens were successfully obtained in this program.

Cylindrical Curvature		Remarks
C1)	5 inch thickness 18 inch radius	Fairly uniform

Cylindrical Curvature		Remarks
C2)	5 inch thickness 28 inch radius	Fairly uniform - Better than C1
Spherical Curvature		
S1)	1 inch thickness 36 inch radius	Good
S2)	2 inch thickness 36 inch radius	Good
S3)	3 inch thickness 36 inch radius	Good
S4)	4 inch thickness 36 inch radius	Fair

Pictures of the curved specimens are shown in Appendix E.

As the investigative program on curving neared completion, the vendors techniques were improving, and it appears that if a particular curvature and thickness were required which exceeded the above apparent limitations it may be possible to achieve such a curvature by repetition of the process many times on the given size specimen.

Although many specimens were tried in an attempt to establish a limiting R/t ratio, the results were not consistent when compared in this manner. As an example, a two inch thick specimen could not be formed successfully to an 18 inch spherical radius, while as indicated above, a four inch thick specimen was successfully curved to a 36 inch spherical radius. It is therefore recommended that the results obtained in this investigation be used only as a guide and not for their absolute value.

Cylindrical Curvature		Remarks
C2)	5 inch thickness 28 inch radius	Fairly uniform - Better than C1
Spherical Curvature		
S1)	1 inch thickness 36 inch radius	Good
S2)	2 inch thickness 36 inch radius	Good
S3)	3 inch thickness 36 inch radius	Good
S4)	4 inch thickness 36 inch radius	Fair

Pictures of the curved specimens are shown in Appendix E.

As the investigative program on curving neared completion, the vendors techniques were improving, and it appears that if a particular curvature and thickness were required which exceeded the above apparent limitations it may be possible to achieve such a curvature by repetition of the process many times on the given size specimen.

Although many specimens were tried in an attempt to establish a limiting R/t ratio, the results were not consistent when compared in this manner. As an example, a two inch thick specimen could not be formed successfully to an 18 inch spherical radius, while as indicated above, a four inch thick specimen was successfully curved to a 36 inch spherical radius. It is therefore recommended that the results obtained in this investigation be used only as a guide and not for their absolute value.

6. STATIC TESTING

6.1 GENERAL

Static load tests were performed on the specimens described in Section 5 to determine the energy absorption values of each specimen type. Measurements and observations were also made to determine stroke efficiency, and failure mode. A picture of each specimen was taken at the end of the test prior to removing the specimen from the testing machine. These pictures are shown in Appendix B.

6.2 FACILITY DESCRIPTION

All static tests were conducted on an Instron Tensile Testing Machine, Model TT-CM1-4.6 (Figure 6-1, Phase I Final Report). This model has a test capacity of 10,000 pounds and a crosshead speed varying from 0.02 to 20.0 inches per minute. All data were recorded on a high speed I eeds and Northrup graphic recorder.

6.3 TEST PROCEDURES

The honeycomb specimens were crushed between the two platens of the Instron testing machine. No venting or special fixtures were required for the optimum density specimens because of the low crosshead speed. In testing the angular specimens, the upper platen was greased with a Silicone grease to reduce the friction. The reason for this was discussed in Section 5.4. A cross sectional area of four square inches was used so that a crushing velocity of 0.5 inches per minute could be used without overloading the drive assembly motor.

Each specimen was weighed before being bonded to its base plate, and this weight was used in calculating the specific energy. This is necessary because the density of the material varies up to plus or minus ten percent within the block from which the specimens are cut.

6.4 TEST RESULTS

6.4.1 Optimum Density

Table 6-1 summarizes the results of all static tests on the optimum density specimens. The static tests are numbered by the specimen type designation, followed by a, b, c, etc., for the first, second, third, etc., test of this speci ic configuration. The P designates Phenolic and the R designates Redipped Polyester, and refers to the resin of which the honeycomb is fabricated.

Load-Deflection Diagrams and pictures of the specimens after crushing are shown in Appendix B and D.

TABLE 6-1. OPTIMUM DENSITY SPECIMENS
STATIC LOAD TESTS RESULTS

Specimen Number	Cell Size (inches)	Specimen Size (inches)	Density (lb cu-ft)	Nominal Crushing Force (lb)	Nominal Crushing Stress (psi)	Specific Energy Absorbed (ft-lb lb)*	Stroke Efficiency (percent)
10Pa	3 16	2 x 2 x 4	12	7500	1880	22.500	75
10Pb	3 16	2 x 2 x 4	12	7000	1750	21.000	50 tilted and sheared
10Pc	3 16	2 x 2 x 4	12	6300	1570	18.900	74
10Pd	3 16	2 x 2 x 4	12	8000	2000	24.000	24 tilted and sheared
11Pa	3 16	2 x 2 x 4	14	5000	1250	12.900	50 tilted
11Pb	3 16	2 x 2 x 4	14	5000	1250	12.900	75 multiple buckling
11Pc	3 16	2 x 2 x 4	14	4500	1120	11.600	50 tilted and multiple buckling
12Pa	1/4	2 x 2 x 4	10	4000	1000	14.400	87
12Pb	1 4	2 x 2 x 4	10	3800	950	13.700	87
12Pc	1 4	2 x 2 x 4	10	4000	1000	14.400	87
13Pa	1/4	2 x 2 x 4	12	4500	1120	13.500	87 multiple buckling
13Pb	1/4	2 x 2 x 4	12	4500	1120	13.500	87 multiple buckling
13Pc	1/4	2 x 2 x 4	12	4500	1120	13.500	87 multiple buckling
10Ra	3/8	2 x 2 x 2	12	4500	1120	13.500	85
10Rb	3/8	2 x 2 x 2	12	5000	1250	15.000	70
10Rc	3/8	2 x 2 x 2	12	5100	1280	15.300	75
10Ra	3/8	2 x 3 x 2	16				No test
10Rb	3/8	2 x 3 x 2	16	9500	1580	14.300	Failed
10Rc	3/8	2 x 3 x 2	16	10200+	1700	15.300	50
10Rd	3/8	2 x 2 x 2	16	6900	1720	15.500	60
10Re	3/8	2 x 2 x 2	16	7500	1870	16.900	60

Notes:

*The specific energy absorption is obtained by dividing the energy absorbed by the weight of the material crushed.

6.4.2 Angular Specimens

Table 6-2 summarizes the results of all static tests on the angular specimens. The tests are numbered by the specimen type designation, in the same manner as stated in Section 6.4.1 above. The symbols A and S designate a particular material configuration and static tests. The first number following AS designates the angle θ, and the second number designates the angle ϕ as shown in Figure 5-1 and Table 5-2 of Section 5.

Load-Deflection Diagrams and pictures of the specimens after crushing are shown in Appendix B and D.

6.4.3 Data Corrections

The nominal crushing stress as listed in Table 6-2 was corrected to account for the difference in specimen sizes. The static tests specimens were cut from a vendor-furnished block which was accurately cut to size and shape. These blocks were then cut into approximately four equal pieces. To account for the difference in sizes, since the specimens were not measured prior to testing, the measured weight of each specimen was compared with that of a specimen of the theoretical size having a density equal to the average of all the specimens (except the ϕ = 90 degrees specimens) furnished by the honeycomb vendor. Using these weight ratios, corrected specimen areas were calculated, and these areas were used to determine the nominal crushing stress. Specific energy absorption values were then calculated using this stress and the average density.

Because the specimens for ϕ = 90 degrees were fabricated from a different portion of the log (honeycomb stock according to vendor terminology) than the other specimens, and because the average density of these specimens was higher, the average density used in the calculations for the 90 degree specimens was 12.8 pounds per cubic foot rather than 11.2 pounds per cubic foot used for all other specimens.

As discussed in Section 5, all specimens were prefailed to an average depth of approximately 3/16 inch. To keep the specific energy data meaningful, the area under the load-deflection curve, (Appendix D) corresponding to the initial 3/16 inch deflection, was not used in calculating specific energy, because this length is a constant regardless of the thickness of the specimen and specific energy should be independent of specimen size. This 3/16 inch thickness of material should, however, be added to the total required material thickness.

TABLE 6-2. ANGULAR TEST SPECIMEN STATIC LOAD TESTS RESULTS

Specimen	Weight (Gram)	Density (lb/cu-ft.)	Nominal Crushing Force (lb)	Nominal Crushing Stress(2) (psi)	Specific Energy(1) Absorption (ft-lb/lb)	Energy Absorption Density (ft-lb/cu-in)	Stroke Efficiency (percent)
AS 0-0-a	29.0	11.2	9350	1900	24,400	158	75
b	24.1	11.2	7750	1900	24,400	158	79
c	24.9	11.2	7750	1840	23,600	153	79
10-0-a	21.3	11.2	4700	1300	16,700	108	87
b	26.9	11.2	6820	1500	19,300	125	84
c	21.8	11.2	4650	1260	16,200	105	84
10-45-a	26.7	11.2	7720	1710	22,000	143	83
b	28.9	11.2	7850	1600	20,600	134	83
c	26.4	11.2	7630	1710	22,000	143	83
10-90-a	28.3	12.8	7540	1800	20,200	150	85
b	29.8	12.8	7300	1650	18,600	138	85
c	30.1	12.8	8120	1820	20,500	152	86
20-0-a	27.6	11.2	5840	1250	16,100	105	75
b	24.7	11.2	5080	1210	15,500	101	81
c	27.9	11.2	5650	1200	15,400	100	80
20-45-a	20.8	11.2	4080	1160	14,900	97	82
b	21.3	11.2	4380	1210	15,500	101	80
c	21.4	11.2	4220	1160	14,900	97	80
20-90-a	24.2	12.8	2010	560	6,300	47	90
b	26.0	12.8	4680	1210	13,600	101	88
c	24.4	12.8	2680	740	8,300	62	90
30-0-a	20.6	11.2	2100	600	7,700	50	79
b	21.5	11.2	2320	640	8,200	53	76
c	20.2	11.2	1980	580	7,500	49	79
30-45-a	24.1	11.2	2970	730	9,400	61	76
b	22.4	11.2	3150	830	10,700	69	76
c	22.1	11.2	3770	1000	12,900	84	76
30-90-a	24.3	12.8	1140	316	3,600	27	91
b	27.4	12.8	2940	725	8,200	61	88
c	27.3	12.8	4340	1070	12,000	89	88

Notes:

(1) Value based on quantity of material crushed, not entire specimen.
(2) Nominal crushing stress corrected for ratio of actual to theoretical weight to account for variations in specimen size. (See Section 6.4.2.)

7. DYNAMIC TESTING

7.1 DYNAMIC TESTING

7.1.1 Drop Test Facility

The tests described herein were conducted on a modified version of the precision drop tester of the Space Sciences Laboratory. This facility, utilizes a one-inch diameter shaft, 40 feet in length to guide a freely falling impact heat assembly in its downward travel. The shaft is made from selected lengths of Thompson 60 Case shaft material and has a diametral tolerance of .001 in. and a straightness tolerance of from .0005 to .001 inch per foot along the entire length. The guide shaft is held under tension through spherical bearing seats at each end and, as a result, is extremely straight. The impact head assembly slides along the shaft via two ball bushings which assure low friction movement and excellent fixity on the shaft. The impact head assembly consists of three major parts: (1) the bearing housing which contains the ball bushings and has provisions for adjusting the inclination of the impact head assembly with respect to the shaft, (2) the support beam, a heavy 8 in. aluminum "I" beam, which connects the bearing housing with the impact head, and (3) the impact head, a hardened and ground steel disc having a diameter of ten inches and a thickness of two inches. The entire weight of the impact head assembly is 73.7 lb.

At the bottom of the shaft a solid sheet base, 20 inches in diameter and eight inches in thickness, is mounted centrally around the shaft. The base is mounted on three equally spaced adjustment bolts; the base can be adjusted precisely in the horizontal plane or in any plane several degrees from the horizontal.

The impact head assembly is raised and lowered by means of an electrically powered winch via an electromagnet and may be released at any height from zero to 34 feet above the base merely by opening the electromagnet circuit. By means of the adjustments on the impact head assembly and the base, the impact head can be adjusted precisely with the impact end of the specimen to be tested.

7.1.2 Mounting Fixture

The specimens tested in this program were mounted to a fixture which was specially designed to allow venting of the air from within the honeycomb cells. The purpose of the fixture was twofold: (1) to eliminate the contribution of air compression from the total energy absorbed by the specimen; (2) to prevent internal pressure differentials across the cell walls which, in an unvented specimen could cause internal stresses and blowout. The fixture, shown in Figure 7-1 features a plate of4130 alloy steel, 8 x 8 x 3/4 inches in dimension which contains a five inch square center array of 1/8 in. diameter through-holes located on 3/16 inch centers. The plate was heat-treated to a hardness of 35° C

Rockwell in order to obtain adequate strength to resist a uniform pressure loading of 1500 psi. The plate is bolted to a heavy steel channel beam over a central five inch square cut-out around which reinforcements are welded. The honeycomb specimens, each bonded to a steel sheet which is perforated with the same pattern of holes as the vent plate, is mounted directly on the vent plate. In this situation, air from within the rapidly decreasing volume in the cell walls exits through the vent plate, the cut-out in the channel, and finally the opening between the channel flanges. The mounting fixture itself is clamped to the steel base of the drop tester after the center of the mounted specimen is aligned accurately with the center of gravity of the impact head assembly.

7.2 INSTRUMENTATION

7.2.1 Accelerometer and Recording

The impact head assembly was instrumented with a Statham A5-500-350 strain gage type accelerometer of 2000 cps natural frequency. This unit was found to be the most useful and trouble-free of all the various instruments previously used for this type of testing. The output from the accelerometer was channeled through a type Q Tektronix transducer to a Tektronix type 530 oscilloscope. Photographic records of the accelerometer traces were made by means of a Polaroid camera mounted on the oscilloscope. They are shown in Appendix C.

7.2.2 Trigger Device

The oscilloscopes were run on a single sweep which was initiated by a trigger device immediately before impact. This device consisted of a pivoting rod which made electrical contact with the impact head when struck by the latter. The trigger was set at a specified distance above the impact end of the specimen depending on the impact velocity. This served to initiate a reference base for acceleration or the oscilloscope trace.

7.3 PROCEDURE

All specimens were individually bonded at their bases to perforated steel plates as previously described in Section 7.1.2 and tested in the vented fixture. The epoxy bond prevented penetration of the specimen into the holes of the vent plate in most cases. As a precaution, the first test of each type of specimen was conducted at a lower than maximum velocity in order to avoid the excessive shock to the apparatus which a catastrophic failure of the specimen would produce. This initial velocity chosen was 36 ft/sec in most cases. Of the 34 tests conducted, 17 were at 46 ft/sec, eight at 36 ft/sec, and nine at 31 ft/sec.

Prior to raising the impact head assembly to the test height, the parallelism and center of gravity alignment between the lower surface of the impact head and the upper end of the specimen were checked and adjusted where necessary. This resulted in acceptably

flat impacts as evidenced by the post-test specimen photographs (Appendix C). The instrumentation trigger was set to provide a zero reference for deceleration approximately one millisecond before impact.

7.4 EXPERIMENTAL DATA

Accelerometer records of all tests are shown in Figures C-9 through C-43 in Appendix C. The data presented are un-retouched photographs of the original records obtained from the tests, except for those from test nos. AD-0-0-b1 and AD-10-90-c which were too faint to be published effectively. Photographs of the corresponding specimens are shown on the same pages as the accelerometer records. The results of all the impact tests are summarized in Table 7-1. The table is arranged according to specimen number, with the following nomenclature scheme: AD-θ-ϕ-S where the first and second numbers are the values of θ and ϕ respectively (in degrees) and the final letter specifies the individual specimen of each type, D denotes dynamic test and A, a particular specimen design.

7.5 TEST RESULTS

Table 7-1 lists the specimen designation, impact velocity, energy absorbed, weight of crushed material, the individual and specimen type average ratios of the absorbed energy to the crushed weight, and the initial and final lengths of the specimens and the description of the specimens after test. The weights of all specimens except those marked with the superscript (1) were obtained by individual measurement prior to bonding the specimens to the perforated sheets. The weights of specimens marked with the superscript were determined from the average density obtained from the individually weighed specimens. This density was found to be 12.3 lb/ft^3. The average energy/weight ratios of specimens of a common type were highest for the non-inclined specimens, as expected. The average values of all specimens with the same θ angle were 17290, 12720, 9680 and 7570 lb ft/lb for θ = 0, 10, 20 and 30° respectively. A plot of this appears in Figure 6-10 as a smooth concave curve. Within a set of specimens having the same angular impact angle θ, those with ϕ = 45° consistently showed the least energy/weight ratios although the values for ϕ = 0° were not much higher. Within a set of specimens having the same ϕ, the energy weight ratios invariably decreased with θ. These values are shown in Tables 7-2 and 7-3.

Selected measured deceleration curves were subjected to detailed double integration to determine the force-stroke characteristics. The resulting force-stroke curves are shown in Figures C-1 to C-8 in Appendix C inclusive. The oscilloscope traces were first smoothed to eliminate spurious vibrations which were due to the impact head. In certain cases, such as test numbers AD-10-90-b and AD-30-0-c the negative deceleration portions of the curve are probably due to overshoot in the impact head response when an abrupt

TABLE 7-1. SUMMARY OF RESULTS OF IMPACT TESTS

Specimen No.	Absorbed Energy (ft-lb)	Impact Velocity ft/sec)	Weight of Crushed Material (lb)	Specific Energy (ft-lb/lb)	Specific Energy Avg. (ft-lb/lb)	Initial Length (in)	Final Length (in)	Condition of Specimen After Test
AD-0-0-a	2432	46	.1235	19700	-	5	4.38	Crushed from top, excellent final condition
AD-0-0-b1	2432	46	.156	15600	- 17290	5	4.06	Crushed from top, shear failure near bottom
AD-0-0-b2	2432	46	.1493	16300	-	4.06	3.16	Some slicing action at shear failure interface. One bond interface separated
AD-0-0-c1	1474	36	.0890	16570(1)	-	5	4.50	Crushed from top, shear failure near bottom
AD-0-0-c2	1474	36	.189	7810(1)	-	4.5	3.44	Slicing action at shear failure interface contributed to stroke
AD-10-0-a	2432	46	.1985	12240	-	5	3.94	Shear failure near bottom, moderate interlaminate bond separation. Angle θ changed to 18°
AD-10-0-b1	2432	46	.2024	12000	- 12080	5	3.88	Shear failure near bottom
AD-10-0-b2	2432	46				3.88	Collapsed	Collapsed due to interlaminate bond separation
AD-10-0-c	1474	36	.1229	12000(1)	-	5	4.32	Separated from base plate; good final condition
AD-10-45-a	1474	36	.1408	10480	-	5	4.06	Crushed from top, slight shear failure at bottom end
AD-10-45-b	2432	46	.211	11520	- 11370	5	3.88	Crushed at both ends, specimen separated from base plate by fracture along the bottom surface
AD-10-45-c1	2432	46	.201	12100	-	5	3.94	
AD-10-45-c2	2432	46	.215	11310(1)		3.94	2.81	Similar to No. AD-10-45-b but with moderate degree of interlaminate bond separation
AD-10-90-a	1474	36	.0890	16600	-	5	4.56	Crushed from top, shear failure near bottom
AD-10-90-b	2432	46	.212	11400	- 14700	5	3.88	Crushed from top, no shear failure
AD-10-90-c	2432	46	.151	16100	-	5	4.12	Crushed at both ends, no shear failure
AD-20-0-a	1747	36		10390(1)	-	5	4.25	Specimen separated into two pieces along a bond line. Separated from base plate
AD-20-0-b	1106	31	.1207	9100	- 9750	5	4.38	Crushed from top, shear failure at bottom, one bond separation at edge
AD-20-0-c	1474	36				5	-	Similar to No. AD-20-0-a
AD-20-45-a	2432	46			-	5	Collapsed	Collapsed due to interlaminate bond separation
AD-20-45-b	2432	46	.284	8550(1)	- 8290	5	3.50	Separated from base plate due to gross fractures at bottom
AD-20-45-c	2432	46	.292	8330	-	5	3.62	Partial separation from base plate accompanied by increased θ - moderate interlaminate bond separation
AD-20-90-a	2432	46	.234	10400	-	5	3.69	Separated from base plate by material fracture
AD-20-90-b	2432	46	.250	9720	- 11010	5	3.75	Multiple delaminations accompanied by increased θ.
AD-20-90-c	2432	46	.188	12920	-	5	4	Partial separation from base plate, good final condition
AD-30-0-a	1106	31	.195	5670	-	5	4.19	Crushed from top, separated into two sections
AD-30-0-b	1106	31	.169	6540	- 6020	5	4.31	Similar to No. AD-30-0-a
AD-30-0-c	1106	31	.189	5840	-	5	4.25	Similar to No. AD-30-0-a
AD-30-45-a	1106	31	.1870	5920	-	5	4.25	
AD-30-45-b	1106	31	.193	5730	- 5920	5	4.12	Crushed from top, moderate interlaminate bond separation
AD-30-45-c	1106	31	.181	6110	-	5	4.25	Crushed from top, shear failure near bottom, partial separation from base plate due to local crushing
AD-30-90-a	1474	36	.1274	11600(1)	-	5	4.38	Multiple interlaminate bond separations throughout specimen, separated from base plate
AD-30-90-b	1106	31	.1028	11480(1)	- 10770	5	4.50	Crushed from top
AD-30-90-c	1106	31	.1198	9230	-	5	4.50	Crushed from top, separated from base plate, several interlaminate bond separations

(1) W obtained from avg. density of 12.3 lb/ft^3 determined from average of all specimen weights. Then $\Delta W = \Delta \ell \times \text{Area} \times \text{Density} \times \cos\theta$ where $\Delta \ell$ is change of length.

All other ΔW's obtained from $\Delta W = W_i \frac{\Delta \ell}{\ell_i}$, where W_i is the particular weight of the specimen before test, ℓ_i is initial length.

TABLE 7-2. VARIATION OF E ∠ W with θ

Specimen Type θ - ϕ	Specific Energy (ft-lb/lb)
0	17290
10-90	14700
20-90	11010
30-90	10770
0	17290
10-45	11370
20-45	8290
30-45	5920
0	17290
10-0	12080
20-0	9750
30-0	6020

θ = Angle between impact velocity and honeycomb cell axis, see Figure 5-1.
ϕ = Orientation angle between honeycomb bond lines and impact angle, see Figure 5-1.

TABLE 7-3. VARIATION OF E/ω W with ϕ

Specimen Type θ - ϕ	Specific Energy (ft-lb/lb)
0	17290
10-90	14700
10-45	11370
10-0	12080
20-90	11010
20-45	8290
20-0	9750
30-90	10770
30-45	5920
30-0	6020

θ = Angle between impact velocity and honeycomb cell axis, see Figure 5-1.
ϕ = Orientation angle between honeycomb bond lines and impact angle, see Figure 5-1.

failure of the specimen occurred. This would result in a sudden reduction of the axial force experienced by the impact head and a subsequent overshoot.

Listed in Table 7-4 are values for average deceleration and stress both with respect to time and stroke, as well as the stress corresponding to the peak deceleration.

NOTE: All data presented in this section is as recorded. Refer to Section 8.2 before using this data.

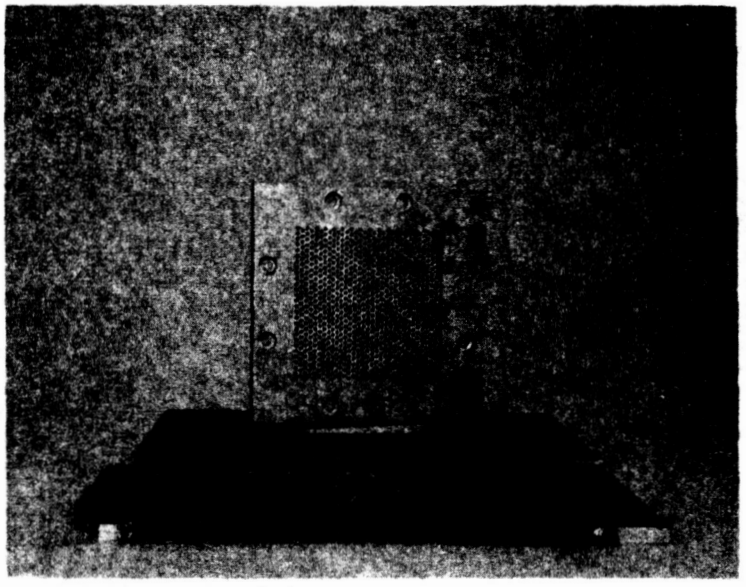

Figure 7-1. Mounting Fixture

TABLE 7-4. VALUES FOR AVERAGE ACCELERATION AND STRESS DURING TIME, STROKE, AND AT PEAK STRESS

SPECIMEN	AVERAGE DURING TIME		AVERAGE DURING STROKE		PEAK STRESS (psi)
	DECELERATION (g)	STRESS (psi)	DECELERATION (g)	STRESS (psi)	
AD-0-0-c	263	776	224	661	1050
AD-0-0-b	400	1180	367	1080	1590
AD-10-90-a	328	954	330	960	1600
AD-10-90-b	283	822	297	863	1750
AD-10-90-c	386	1120	359	1042	1480
AD-10-45-b	325	958	293	864	1630
AD-10-0-a	313	909	321	932	1080
AD-20-90-c	272	754	294	815	1320
AD-30-0-c	95.4	243	145	369	619

8. ANALYSIS AND DISCUSSION OF TEST RESULTS

8.1 OPTIMUM DENSITY SPECIMENS

The test results for the optimum density specimens are shown in Table 6-1. These results are plotted in Figures 8-1 and 8-2. Figures 8-3 and 8-4 were plotted from the same data and are included for use as working graphs for those applications where either energy absorbed per cubic inch (energy absorption density) as a function of bulk density or crushing stress as a function of core density is required. All the specific energy values used throughout this report are referred to the amount of material actually crushed and not to the total amount of material in the specimen.

It was intended to use the dynamic test non-tilted angular impact specimens for proof of the conclusion drawn in Phase I that there is no effect on energy absorption efficiency with changing velocities up to 46 ft/sec. Unfortunately, the zero degree angular specimens used for dynamic tests were higher in density than the optimum value of 11 lb/cu-ft, and hence partially failed during testing, as had the higher density optimum density test specimens.

As can be seen in Figure 8-1, a particular cell size yields increasing specific energy values up to a certain density. When the density is raised above this optimum value, the specific energy drops off rapidly, because the material then fails in a catastrophic manner, and large pieces of the material break off. It can be noted from Figure 8-2 that the stroke efficiency is somewhat lower for the higher density specimens, but this is more than compensated for by the increase in specific energy.

While specimens Type 10P yielded the highest value of specific energy, two of these static specimens failed at approximately 50% of the total stroke. This failure occurred due to movement of the specimen on the platen which caused the specimen to tilt. This movement was caused by a multiple buckling phenomenon in which the load built up to a maximum value and then dropped to a value of about 50% of the maximum. As this drop took place, a loud report was heard, and an obvious buckling or breaking up of the material occurred locally directly under the upper (moving) platen. This loading and unloading cycle occurred at approximately every 0.05 inch of head travel. This behavior leads to the conclusion that the density was slightly higher than optimum. It was also shown on a separate test that the specimen did not tilt and fail catastrophically when it was bonded to a base plate which prevented the specimen from tilting and hence shearing down the middle (see Table 6-1).

The 16 lb/cu-ft density, 3/8 inch cell polyester resin specimens Type 11R also failed, but in a different manner. Rather than crushing, the material broke apart at the interlaminary

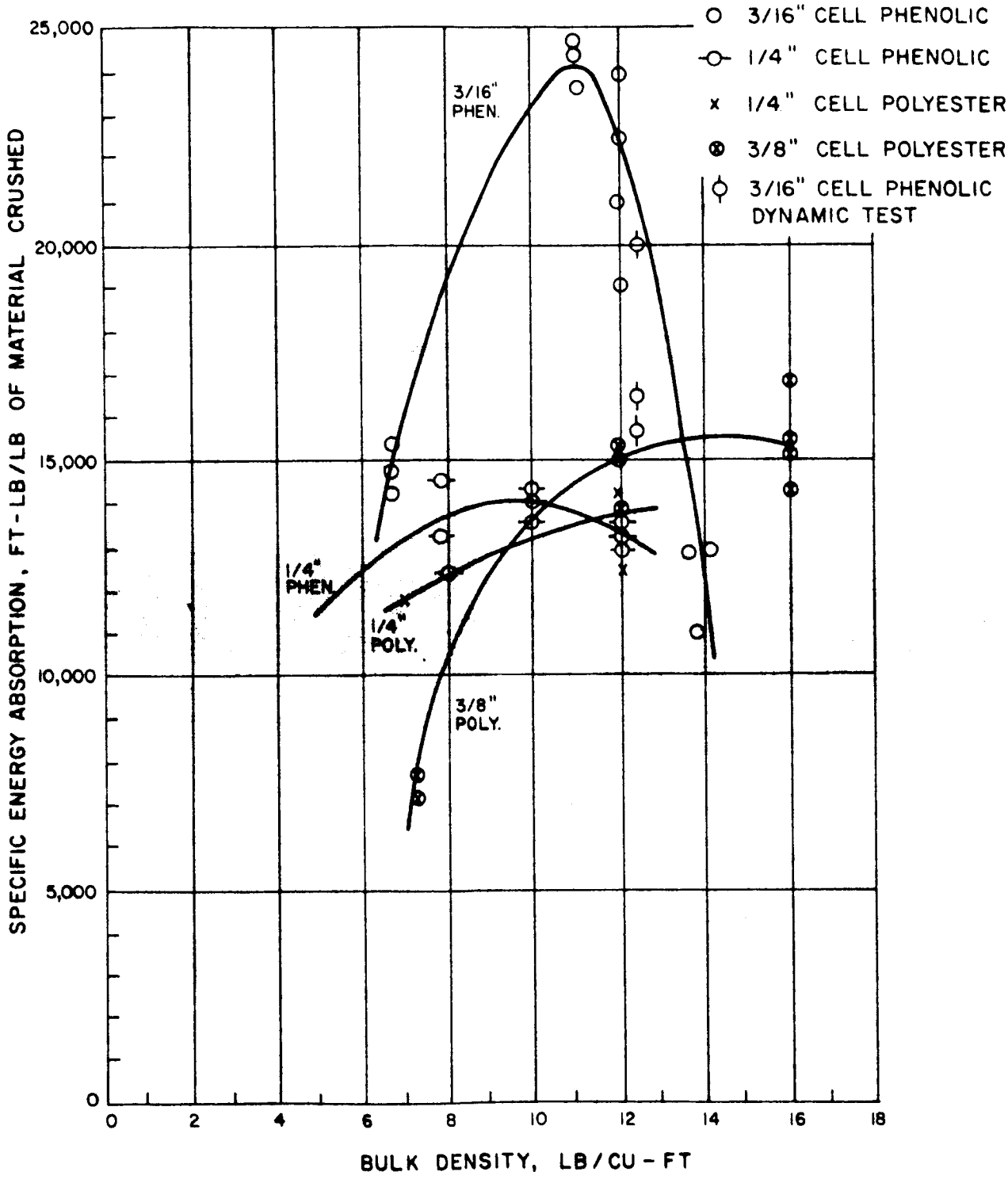

Figure 8-1. Specific Energy vs. Bulk Density

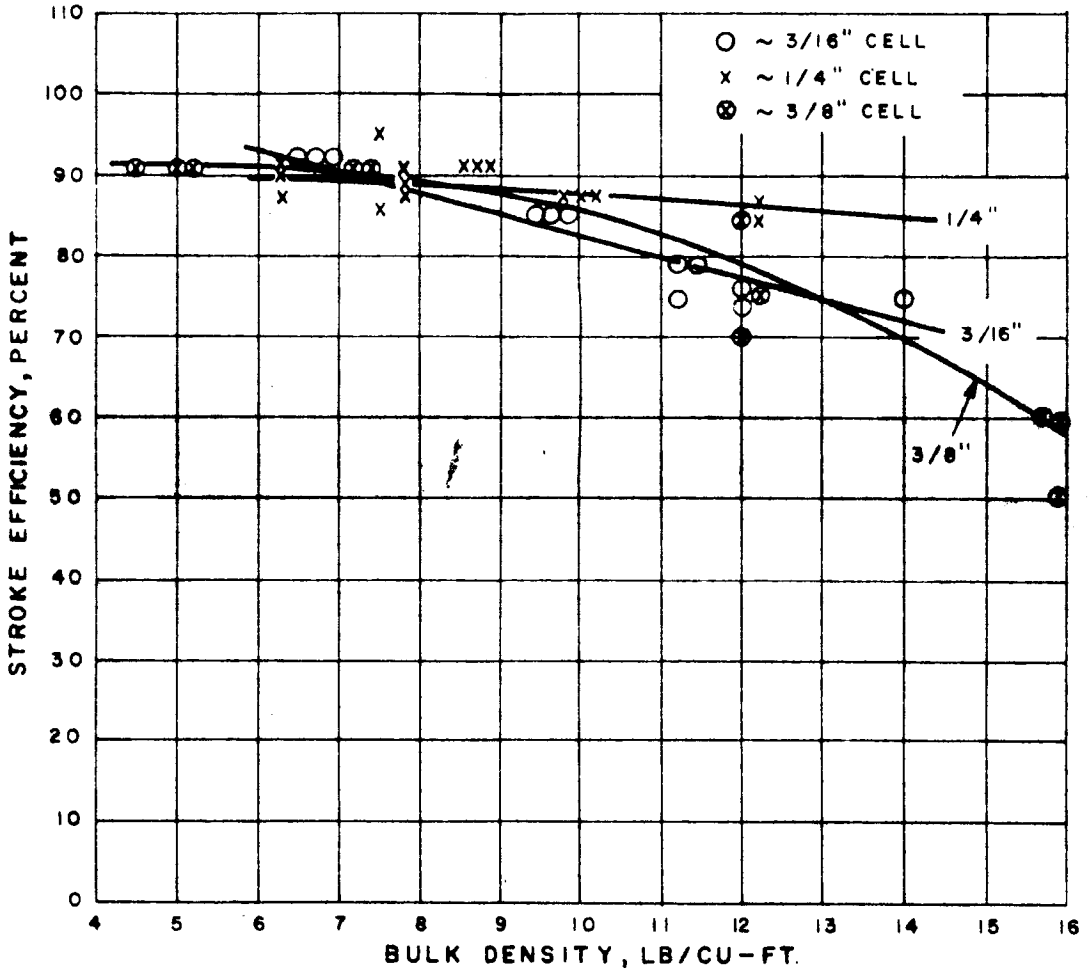

Figure 8-2. Stroke Efficiency vs. Bulk Density

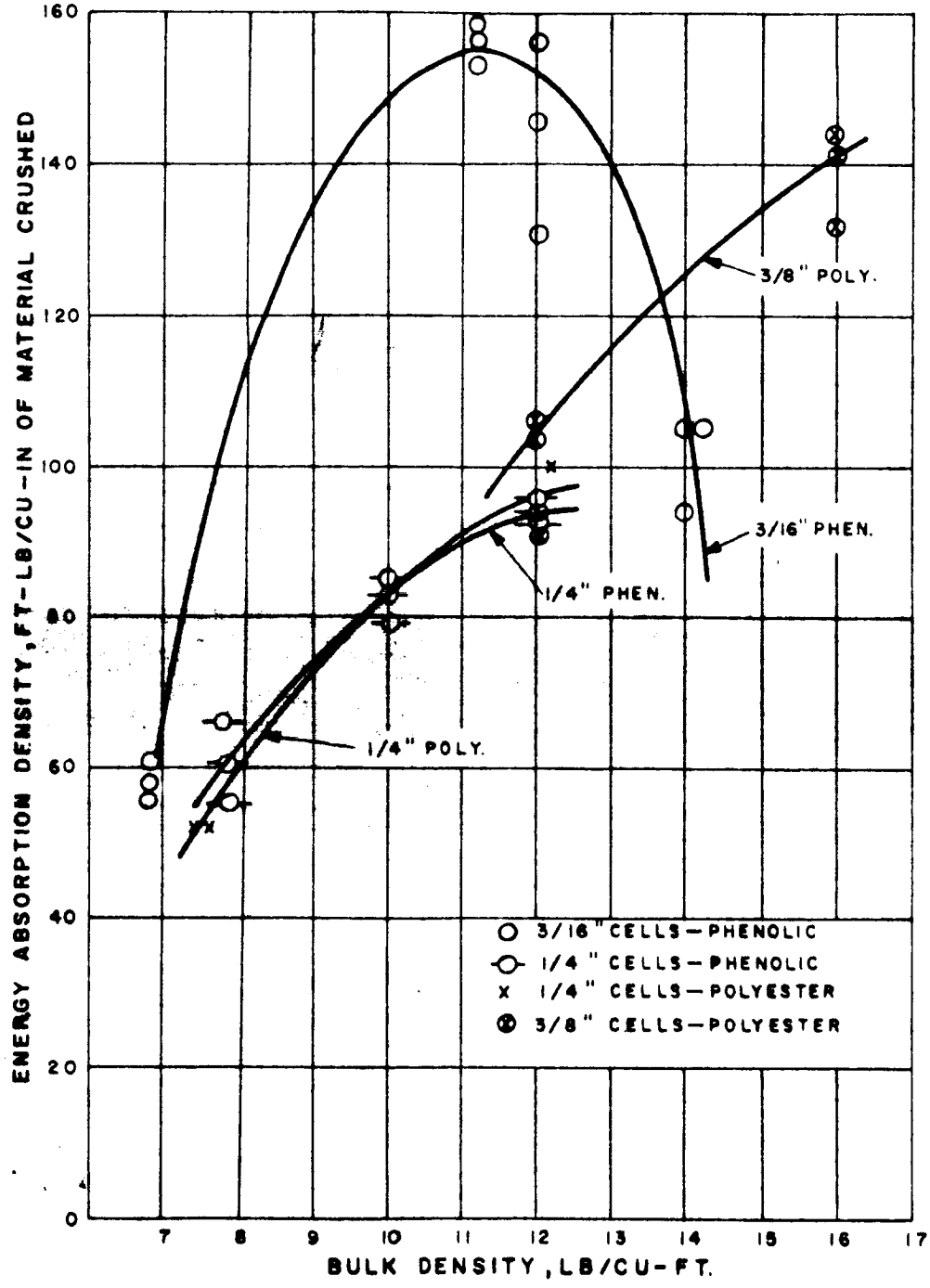

Figure 8-3. Energy Absorption Density vs. Bulk Density

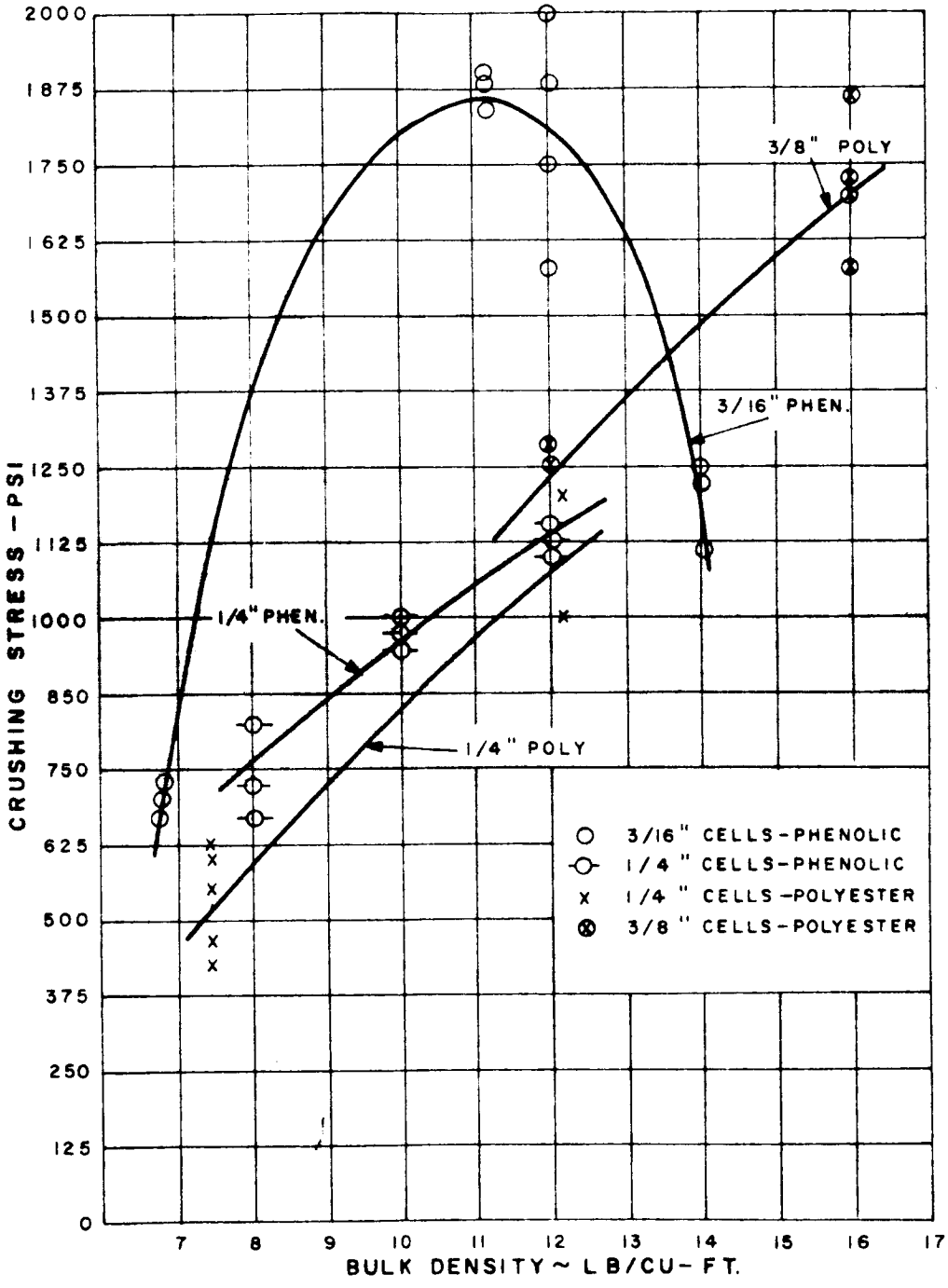

Figure 8-4. Crushing Stress vs. Bulk Density

bond lines and opened at the lower end of the specimen in a fan-like manner. The crushing load was therefore not uniform and became smaller as the stroke progressed. A different interlaminary bond material having a higher strength would make this material more useful in these higher density ranges.

The failure mechanism of the glass reinforced plastic honeycomb is the localized, brittle crushing of the cell walls at the impacted end. The contribution of the glass to the total energy absorption is negligible. The failed particles are small, which accounts for the high specific energy and the high stroke efficiency. As the bulk density is increased by adding resin, the failed particles increase slightly in size which explains the small decrease in stroke efficiency (see Figure 8-2). As the bulk density is further increased, a point is reached at which the interlaminary bond between the corrugated strips is no longer strong enough to hold the cell walls in position for crushing. As the bond fails, relatively large pieces of cell wall separate, bend, and snap off. Since the bending failure mode absorbs less energy than the crushing failure mode, the result is a drastic reduction in specific energy (see Figures 8-1, 8-3, 8-4).

It appears that further improvement in the specific energy of this material can be made by increasing the strength of the interlaminary adhesive load which joins the corrugated strips to form the honeycomb geometry.

8.2 ANGULAR IMPACT

As in Phase I of this program, both static and dynamic tests were performed on the angular test specimens to evaluate any difference in energy absorption properties in the velocity range of zero to fifty feet per second. Data obtained during Phase I of this contract showed no apparent connection between impact velocity and specific energy absorbed. This fact was reasonably well confirmed during the present Phase II of the contract. Since this conclusion is not obvious from the raw static and dynamic test data, an explanation of the probable causes for the apparent discrepancy in the raw data is contained in the following paragraphs.

As discussed in Sections 5, 6 and 7 all specimens were prefailed by placing sawcuts in one end of the specimen. These sawcuts performed very well in the static test specimens and prevented the load from becoming excessive during initial crushing. In the dynamic tests, the force-stroke curves obtained from the double integration of the deceleration traces showed that in most instances the resistance of the specimens was low during the initial part of the stroke. This is in contrast to much of the reported initial behavior of honeycomb materials under dynamic crushing loads. This is undoubtedly due chiefly to the presence of the sawcuts. The effect of the sawcuts, in addition to reducing the probability of initial failure at impact, reduced the calculated energy absorption of the material, since the depth of cut

(up to 1/4 inch) was a substantial percentage of the actual stroke in the impact tests. This explains, in part, why the energy/weight ratios obtained from the impact test were generally lower than those from the static tests.

The reason that the sawcut depths accounted for such a large percentage of the stroke in the dynamic specimens was that the specimens were deliberately made large in cross sectional areas to prevent the overturning moment, resulting from the angular configurations of the specimens, from becoming so large as to affect the stress distribution across the face of the material to be crushed.

Another contribution, admissible only for those few cases which experienced it, may be due to penetration of the material into the vent plate holes. This effect is probably minor since, in the previous program in which the specimens were not sawcut, the deceleration traces showed much steeper initial rises and penetration into the vent plate was common.

A factor which undoubtedly greatly influenced the effectiveness of the material, as tested in the dynamic tests, was the failure of the bond material which was used to bond the specimens to the perforated base plate. When this bond fails, the overturning moment increases the shear stress in the honeycomb at the interlaminary bond joint which joins the corrugated layers that make up the honeycomb material. In a continuous honeycomb structure, such as would be found on a vehicle design, this condition would not exist because of the continuity of the material. This is therefore an example of size effect encountered in testing which would not occur elsewhere in practice.

In contrast to the lower density specimens tested in Phase I of this program, the Phase II specimens exhibited a strong tendency to fail in what appeared to be a shear mode in the region well beyond the crushed zone. This has been previously observed in higher strength metal honeycombs which possessed high compression strength and relatively low shear strength (Reference 11.1). Under crushing loading, the honeycomb tends to shorten axially by slipping along a diagonal plane. This failure mode occurred in the normal as well as the angular impact specimens. Under normal impact the shear mode failure is explained by the fact that the present specimens had considerably higher density and therefore higher compression strength than the ones tested in Phase I. The interlaminate bond strength, on the other hand, is not measurably increased because the greater density of these specimens was obtained by redipping the expanded honeycomb in resin. Under compression loading, a local bond separation can trigger buckling or fracture of adjacent cell walls and this in turn causes other adjacent regions to fail as more load is shifted to them. The shear mode failure in the inclined specimens occurs through a combination of the above mechanism and the addition of external shear loading.

Using the acceleration stroke curves in Appendix C, values for the peak crushing stresses of the dynamic specimens were calculated. Table 8-1 shows these values compared with the average values of crushing stress obtained from static tests. Peak values were used for this comparison because they should more realistically represent the potential of the material, had the specimens not been subjected to the perturbing conditions discussed in the preceeding paragraphs. These stresses are graphically compared in Figure 8-5.

TABLE 8-1. COMPARISON OF CRUSHING STRESS VS. ANGLE OF IMPACT FOR STATIC AND DYNAMIC LOADING

SPECIMEN TYPE	CRUSHING STRESS (psi)	
	Static Tests	Dynamic Tests
A-0-0-a	1900	1510
-b	1900	
-c	1840	
A-10-0-a	1300	1070
-b	1500	
-c	1260	
A-10-45-a	1710	1600
-b	1600	
-c	1710	
A-10-90-a	1800	1600
-b	1650	1570
-c	1820	1450
A-20-0-a	1250	
-b	1210	
-c	1200	
A-20-45-a	1160	
-b	1210	
-c	1160	
A-20-90-a	560	
-b	1210	
-c	740	
A-30-0-a	600	600
-b	640	
-c	580	
A-30-45-a	730	
-b	830	
-c	1000	
A-30-90-a	316	
-b	725	
-c	1070	

The largest differences (20%) between static and dynamic stresses occur on normal impact and for an impact angle of 10^{o} combined with an interlaminary bond line orientation angle of 0^{o}. For an impact angle of 10^{o}, the difference is 4% for $\theta = 45^{o}$ and 12.5% for $\theta = 90^{o}$. The dynamic stresses are consistently below the static stresses for the reasons previously discussed, except for the 30^{o} impact angle where they are the same.

The crushing stresses are between 1500 and 1900 psi at normal impact, and they decrease approximately linearly to a value of 0 at an impact angle of 50^{o}, if an extrapolation beyond the measured data is made.

Figure 8-6 is a plot of specific energy absorption vs. angle of impact vs. interlaminary bond line orientation as obtained from static tests. Specific energy absorption was calculated as described in Section 6.4. The two low values shown at the 20^{o} impact angle and the one shown at 30^{o} are specimens which failed in interlaminary bond. Figure 8-7 shows the same data in terms of volume density of energy absorption.

The most consistent variation of energy absorbed with impact angle occurs for $\phi = 45^{o}$. If the interlaminary bond lines are unfavorably oriented with respect to the impact angle ($\theta = 0$) severe shear loads cause premature bond failures. This leads to a drastic reduction in energy absorption from normal impact to impact under a 10^{o} inclination.

Contrary to expectations, the specimens in which the interlaminary bond lines were at an angle of $\phi = 90^{o}$ (see Figure 5-1, page 5-3), did not perform best except at small impact angles. When this angle exceeded 10^{o}, two out of three specimens split apart because the interlaminary bond was not strong enough to prevent shear buckling failure of the individual corrugated strips. It is apparent that a stronger bond would raise the average energy absorption of these specimens at least to the highest values obtained at the 20^{o} and 30^{o} impact angles; refer to Table 6-2, page 6-4.

In general, the values of energy vs. impact angle look like curves of buckling load vs. slenderness ratio of compression members. This lends additional weight to the explanation of the honeycomb failure mechanism by interlaminary bond rupture and subsequent shear buckling failure.

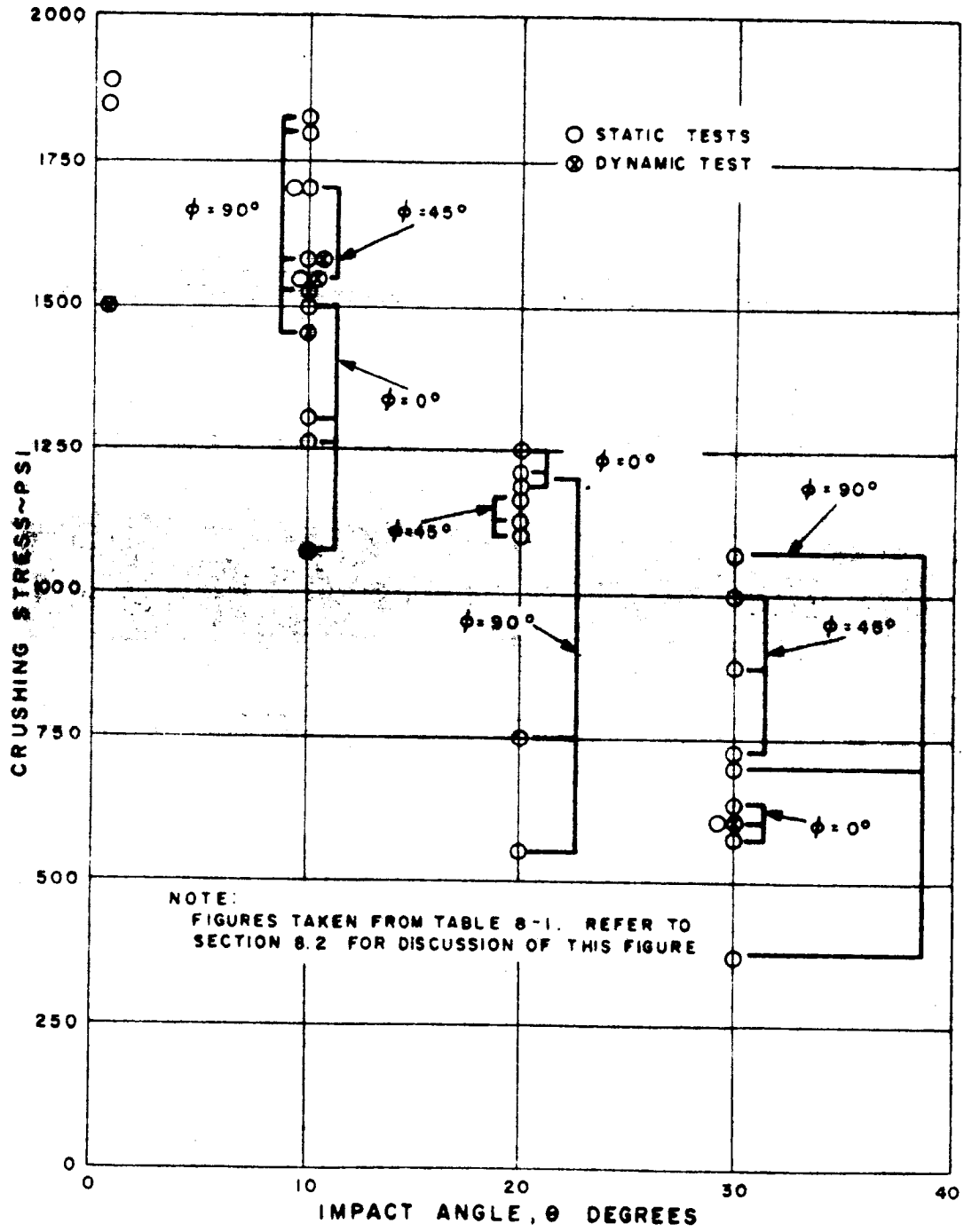

Figure 8-5. Comparison of Crushing Stress vs. Angle of Impact for Static and Dynamic Loading

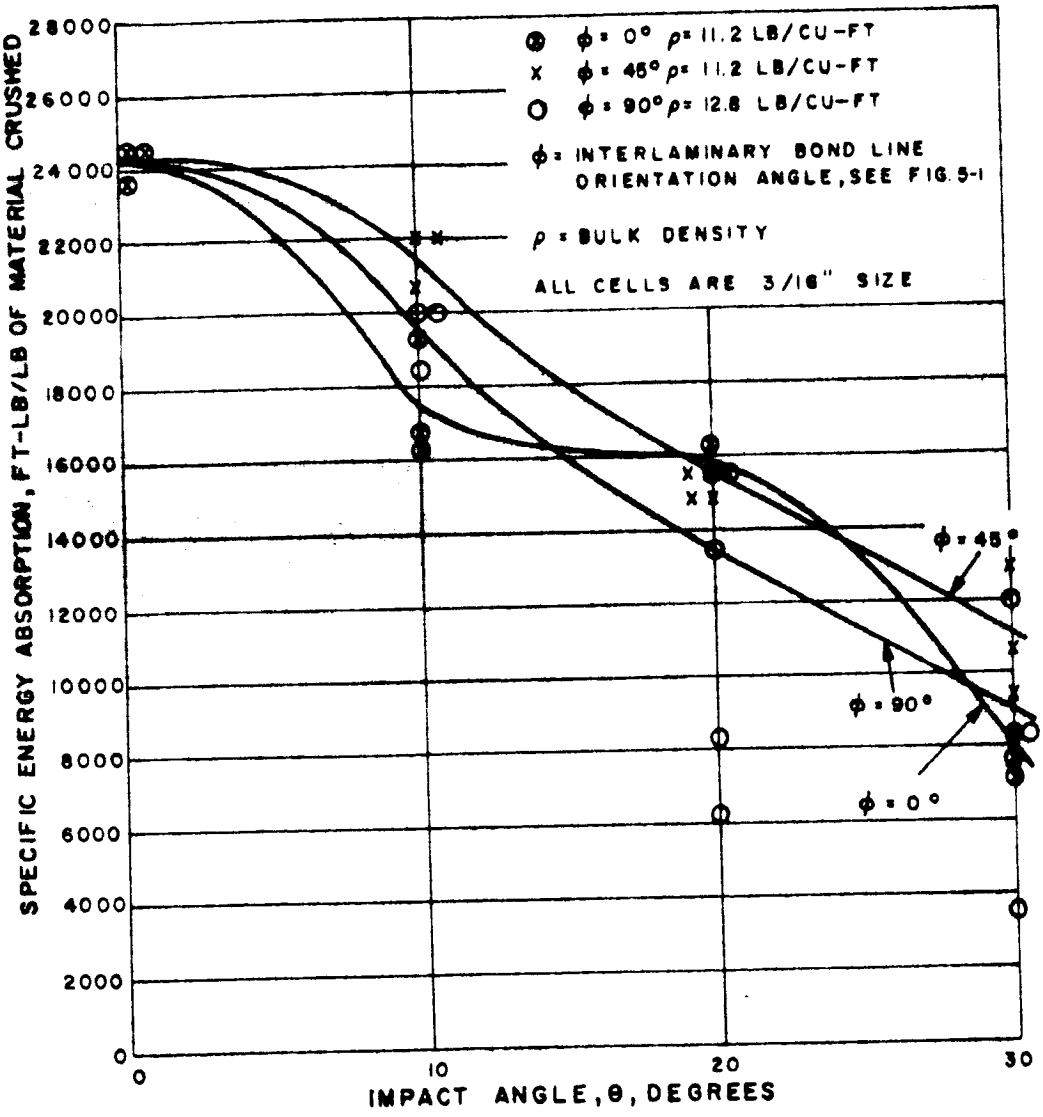

Figure 8-6. Specific Energy Absorption vs. Angle of Impact vs. Honeycomb Bond Line Orientation Angle

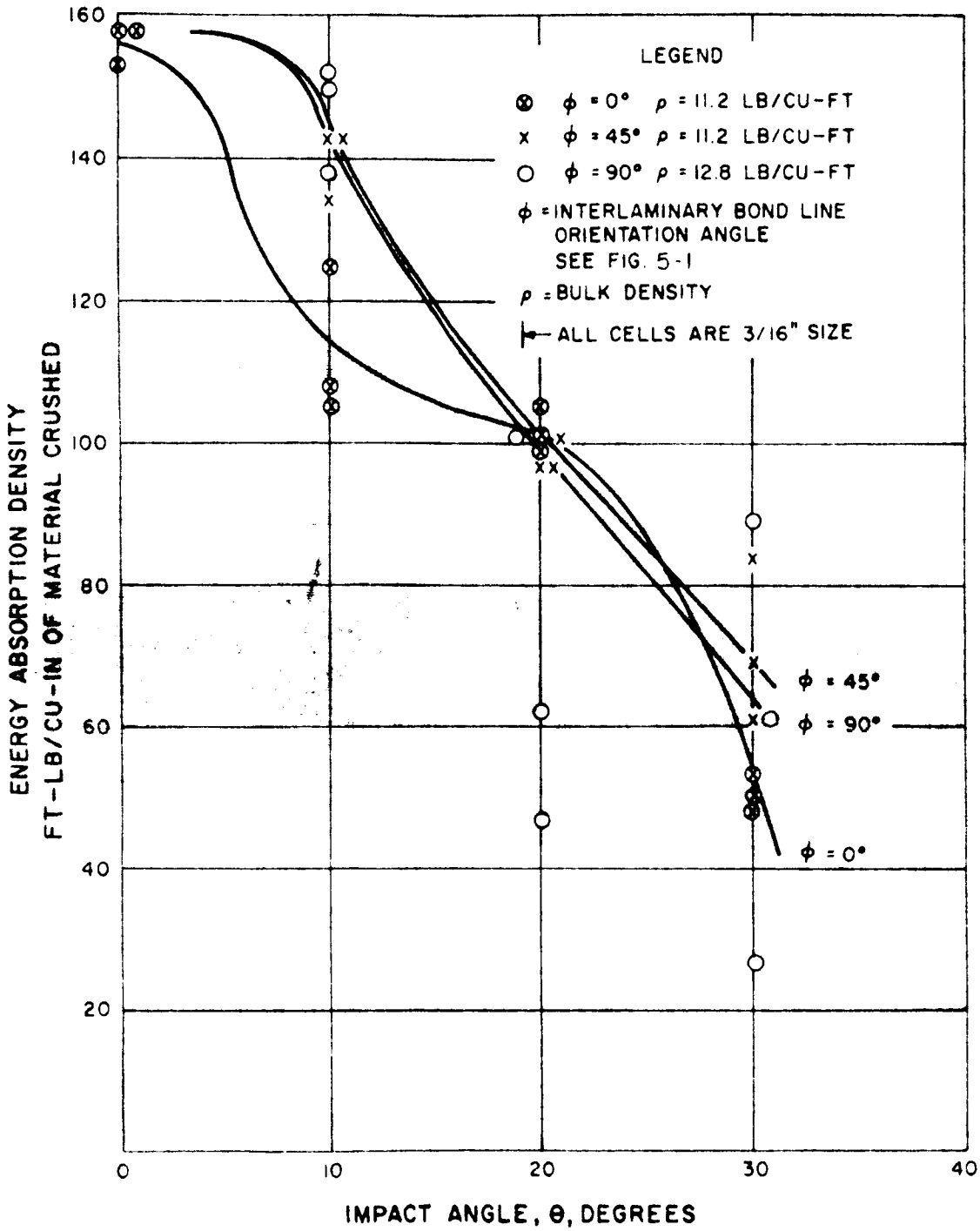

Figure 8-7. Specific Energy Absorption Density vs. Angle of Impact vs. Honeycomb Bond Line Orientation Angle

Figure 8-8 shows crushing stress vs. impact angle vs. interlaminary bond line orientation as obtained from static tests. The stress values used are taken from Table 6-2. The graphs are similar to Figures 8-6 and 8-7, and the previous discussion also applies.

Figure 8-9 is a plot of stroke efficiency vs. impact angle vs. interlaminary bond line orientation as obtained from static tests. The highest efficiency of approximately 90% is obtained for large impact angles and $\theta = 90°$. Generally it appears that the efficiency of angular impact is higher than that of normal impact. It may be expected that the stroke efficiency curve would remain at a value of 80 to 85% if the interlaminary bond failures were eliminated by increasing the bond strength. The large pieces of material which are broken off as the bond fails causes the material to build up to a greater thickness which reduces the thickness efficiency.

Figure 8-10 compares the reduction in efficiency of static and dynamic specimens under angular impact. It is noticeable that, while the absolute numbers of energy absorption are not identical, the relative decrease in efficiency or angular impact is essentially the same for both static and dynamic tests. It is approximately a linear relation which decreases at the rate of 2% for each degree of impact angle.

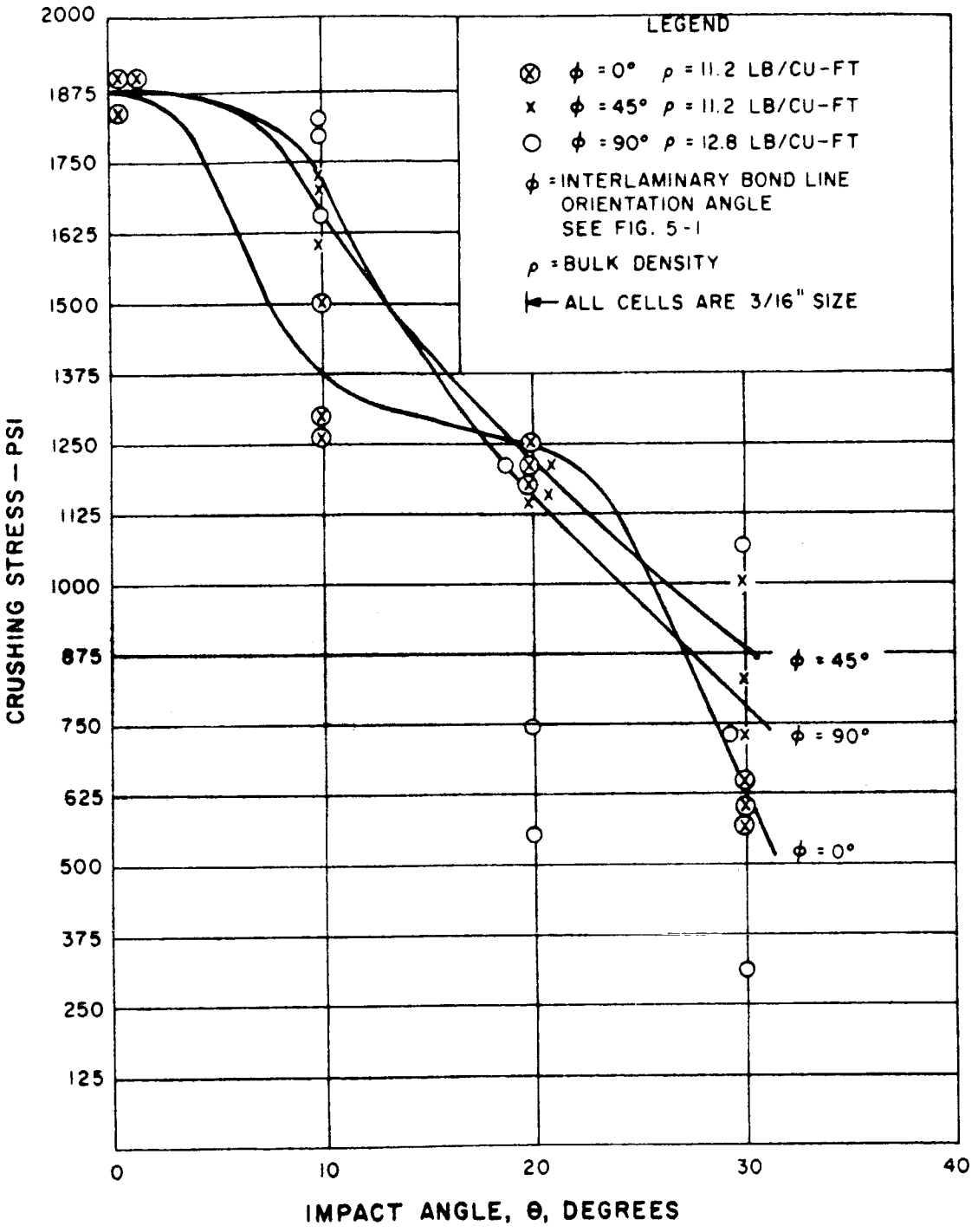

Figure 8-8. Crushing Stress vs. Angle of Impact vs. Honeycomb Bond Line Orientation Angle

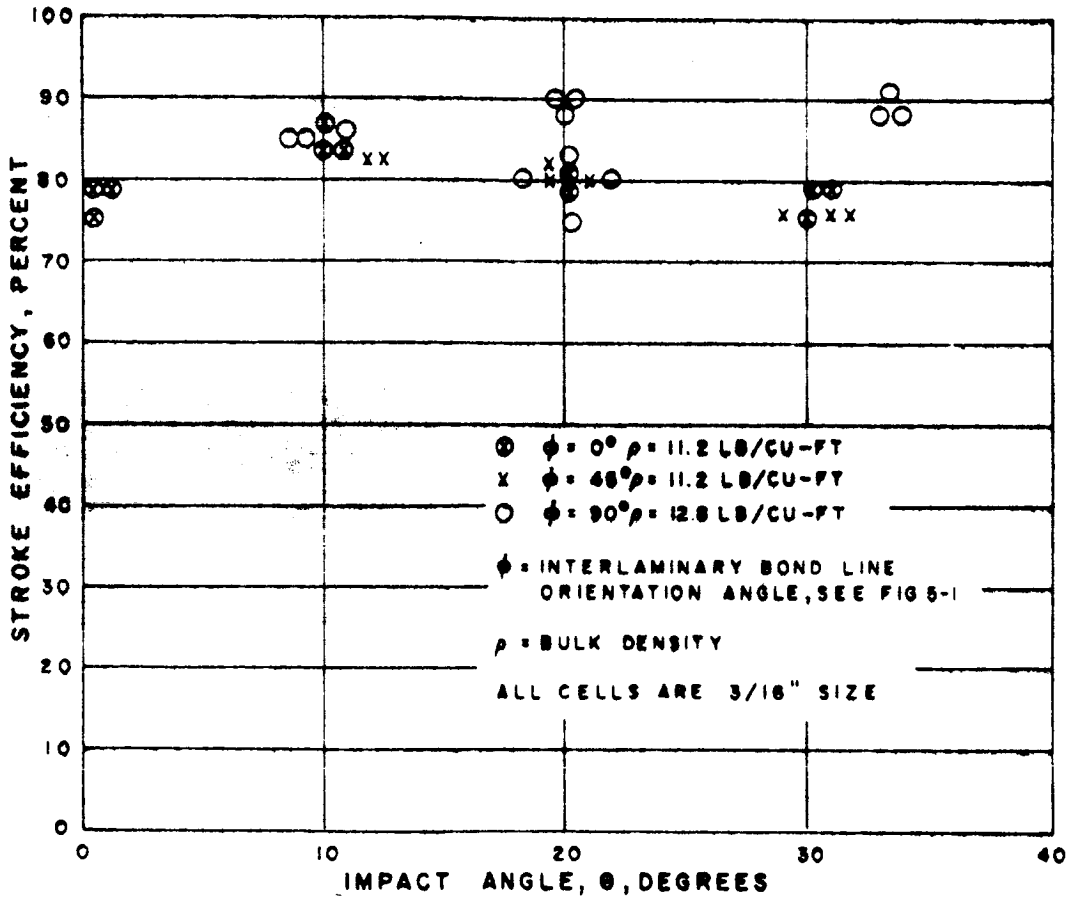

Figure 8-9. Stroke Efficiency vs. Angle of Impact vs. Honeycomb Bond Line Orientation Angle

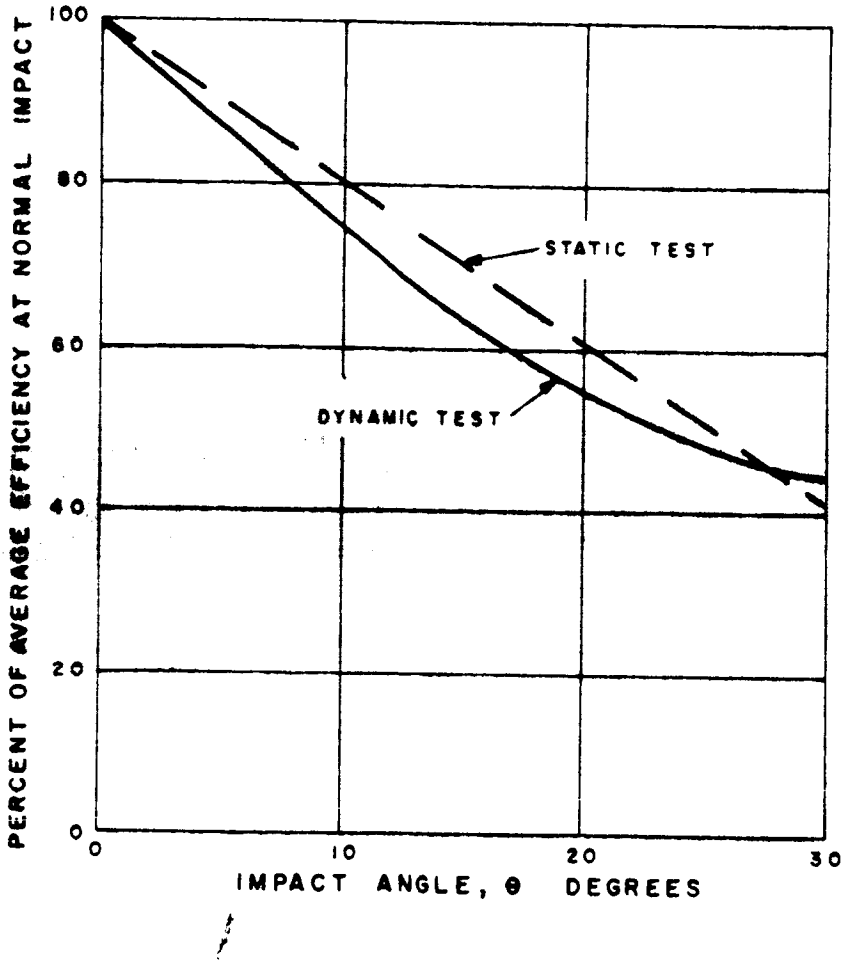

Figure 8-10. Comparison of Efficiencies vs. Angles of Impact for Static and Dynamic Loading

9. CONCLUSIONS AND RECOMMENDATIONS

The design objective of improving the specific energy absorption properties of plastic reinforced honeycomb has been met and exceeded. A value of 24,000 ft-lb/lb was achieved for the 3/16" cell, 11 lb/cu-ft configuration. This value makes the material superior to any known radio frequency transparent energy absorber. The average RF attenuation equals 0.35 db/ft of thickness. The material is readily available and can be manufactured by state-of-the-art methods.

At the present time, the smallest cells absorb the highest specific energies. This may not hold true for very high bulk densities if the interlaminar bonding material can be significantly improved. The specific energy and the energy density can be lowered to meet special requirements by reducing the resin content, increasing the cell size, changing the resin formulation or any combination of these variables.

As in Phase I testing, comparison of static and dynamic tests showed that the material properties are relatively constant for velocities from 0 to 46 ft/sec. The structural elements tested fractured progressively by break-up of the cell-wall material into small fragments. The succession of small brittle fractures at the near-microscopic level yields a macroscopic, quasi-plastic, constant fracture force, ideally suited to the cushioning of landing impact shocks. The honeycomb configuration developed is highly conducive to the formation of small fracture particles which leads to high specific energy values. The primary contributor to the energy absorption process is the resin, not the glass. Increasing the resin ratio of the specimens, therefore, increases the specific energy, and vice versa.

Test results indicate that a stronger interlaminary bond between the honeycomb corrugations would raise the specific energy absorption for the larger cell sizes. It would prevent the bending failure of large fragments of cell wall which absorbs less energy than the orderly compressive crushing. By the same reasoning, the stroke efficiency would improve.

Angular impact tests, performed on the optimized 3/16-inch - 11 lb density material, yielded specific energies which decreased linearly from 100% to40% of specific energy for normal impact as the angle of impact was changed from 0 to 30 degrees. The mode of failure for angular impact was the same as for vertical impact except in cases of interlaminary bond failure. For these honeycombs of higher than commercial density, a stronger bond material would significantly raise the energy absorption and also increase the reliability. This increase is estimated to be 10 to 15 percent.

All of the angular impact tests performed under this contract attempted to simulate impact

on frictionless surfaces. Since this is not a realistic condition for lunar or planetary impact, it would be logical to perform a succeeding series of tests on surfaces having varying bulk and friction properties in order to determine the behavior of the material developed under those conditions.

The hexagonally shaped honeycomb design is not the best configuration for curved panels. Another configuration, recently developed on work not connected with this contract, which can be readily curved in one or more planes, appears to be desirable from a fabrication standpoint for singly and doubly curved panels. Evaluation of the mechanical properties of this new configuration would be required before it could be used as an energy absorber. While the properties would probably be very similar to the present hexagonal configuration for forces along the cell axis, there is no sure way of predicting the effect of angular impact on this configuration.

For immediate applications of the hexagonal material to cylindrical or spherically shaped vehicles requiring a small R/t (radius to thickness ratio) ratio, the material should be applied in pieces so that the angle between the cell axis and a line radiating from the center of curvature does not exceed 30 degrees. Limiting R/t ratios, based on experiments carried out in this program are three for cylindrical panels and nine for spherically shaped panels. The material used for this evaluation was 1/4 inch cell, 10 lb/cu-ft density.

The following recommendations for future studies are made:

a. Determine the effect of temperature range which could be encountered in lunar or planetary landings on the behavior of the material developed.

b. Undertake a material development program aimed at improving the strength the adhesive now used for the interlaminary bonding of the corrugated honeycomb strips to each other.

c. Fabricate singly and doubly curved honeycomb panels by a new process recently developed on work not connected with this contract.

d. Evaluate the improved adhesive and the new honeycomb configuration by performing angular impact tests similar to those carried out under the present contract.

e. Evaluate the effect of the mechanical properties of the landing surfaces on the behavior of this material, particularly under angular impact.

10. DESIGN DATA

Using the test data obtained in Phase II, the data presented in Section II in the Phase I Final Report has been extended to include the higher values of specific energy absorption attained during the Phase II program. For convenience, some of the data presented in the Phase I Report is repeated.

These graphs enable the user quickly to determine the detail requirements of honeycomb-cell size and density for a given set of conditions, and obtain the total system weight for an energy absorbing system based on vehicle weight and impact velocity only.

10.1 REQUIRED STROKE LENGTH

Figure 10-1 is a graphical representation of the formula,

$$v_o^2 = 2as,$$

and can be used to determine the required stroke length, or depth of honeycomb, s, required for given impact velocity, v_o, and allowable deceleration, a, on the vehicle. The assumption of constant deceleration is justified by the constant deceleration curves obtained during the dynamic tests. The theoretical stroke length obtained from Figure 10-1 should be increased by a suitable factor of safety of about 50%.

With the stroke established, the following items must be considered to arrive at a final design:

a. Total energy to be absorbed

b. Available surface area for mounting energy absorbing material

c. Manufacturing limitations of honeycomb material

d. Column limitation (buckling) of honeycomb material.

10.2 CHOICE OF AREA AND HONEYCOMB CONFIGURATION

The total vehicle energy, E, to be absorbed can be calculated from the kinetic energy formula,

$$E = m\frac{v^2}{2}.$$

where

m = vehicle mass,

$m = \frac{W}{g}$,

v = impact velocity,

W = vehicle weight, in any system

g = acceleration of gravity.

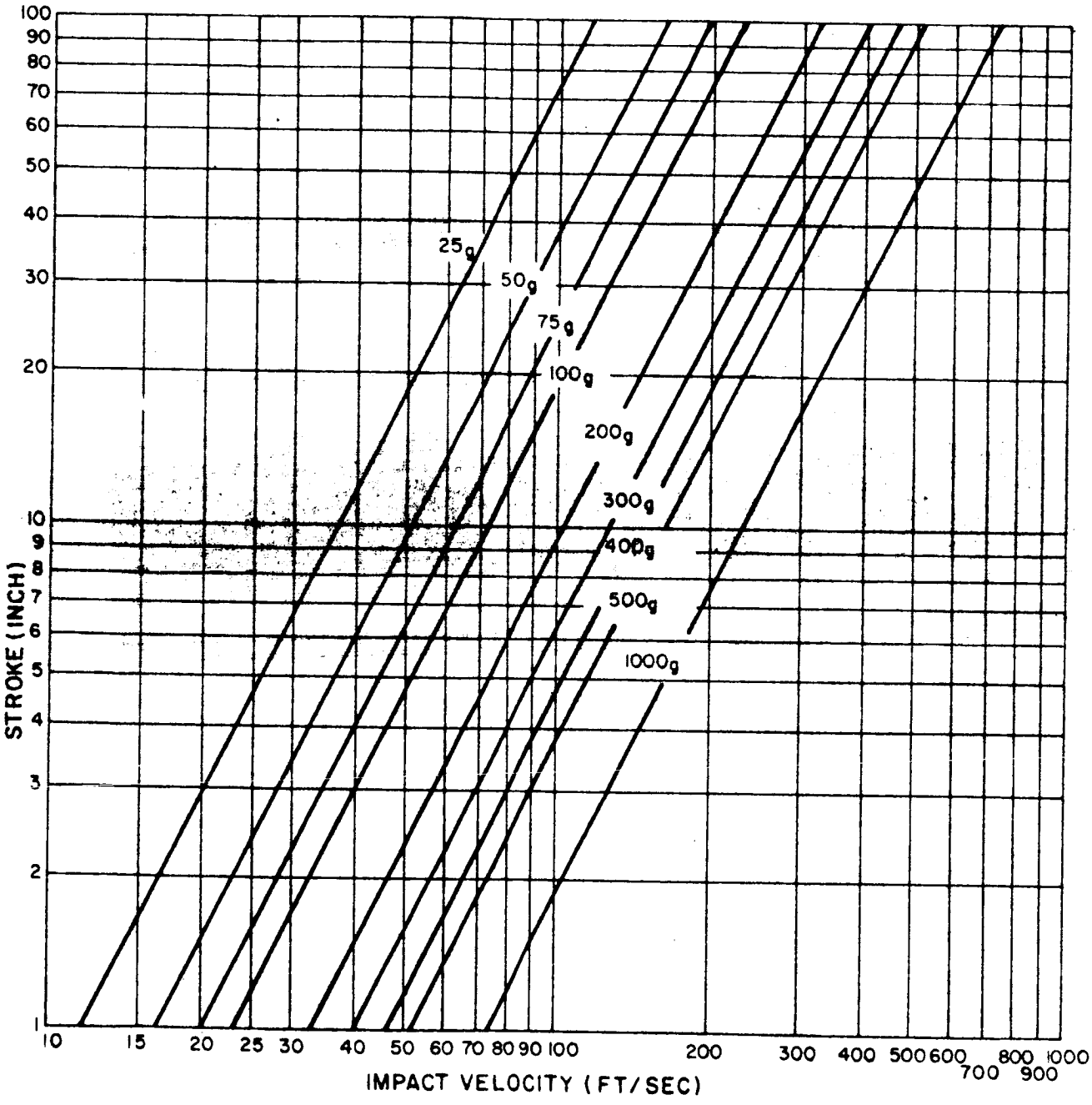

Figure 10-1. Stroke Length as a Function of Impact Velocity and Allowable (Constant) Deceleration

Using the stroke obtained from Figure 10-1, Figure 10-2 shows energy densities (energy per square foot of impact area) for various honeycomb configurations. Dividing the energy density from Figure 10-2 into the total vehicle energy obtained from the last equation yields the required impact area. This is the theoretically required area of the vehicle over which the energy absorbing material must be distributed.

In choosing the required surface area the 3/16-in. cell should always be given preference and tried first, since it will yield the lightest weight system. If, because of manufacturing limitations, such as curving of honeycomb panels, a 1/4-in. instead of 3/16-in. material is required, the highest value of ft lb sq ft for the 1/4-in. material at the given stroke should be used for the lightest configuration.

10.3 DESIGNING FOR ANGULAR IMPACT

Figure 10-3 is a curve of Specific Energy Absorption versus Angle of Impact. This curve was estimated from Figure 8-5 and is the best approximation available from tests results for use in designing landing systems which are fabricated from 3/16 inch cell, 11 lb/cu-ft density, phenolic resin honeycomb. While a few test specimens fell outside the limits of these curves, it is felt that these causes, which are known, can and will be corrected in future specimen designs.

10.4 TOTAL SYSTEM WEIGHT

Using Figure 10-4, it is possible to determine the total weight of an energy absorbing system required for a given weight vehicle and a given impact velocity. No further details of the system must be known to use the graph. The indicated spread of weights required, for a given impact velocity, is based upon two values of specific energy. In preparing this graph an additional factor of five has been used to account for the additional material required because the point of impact on the vehicle is not exactly defined and the energy absorbing material must therefore be "wrapped around" the lander. Thus, only a fraction of the material, approximately 20%, can be effective. If a very good orientation system is used, this fraction can be increased and the factor of five decreased, since normal factors of safety and material efficiency have already been included. All things considered, this graph is considered to be a realistic, slightly conservative estimate of total energy absorbing system weight.

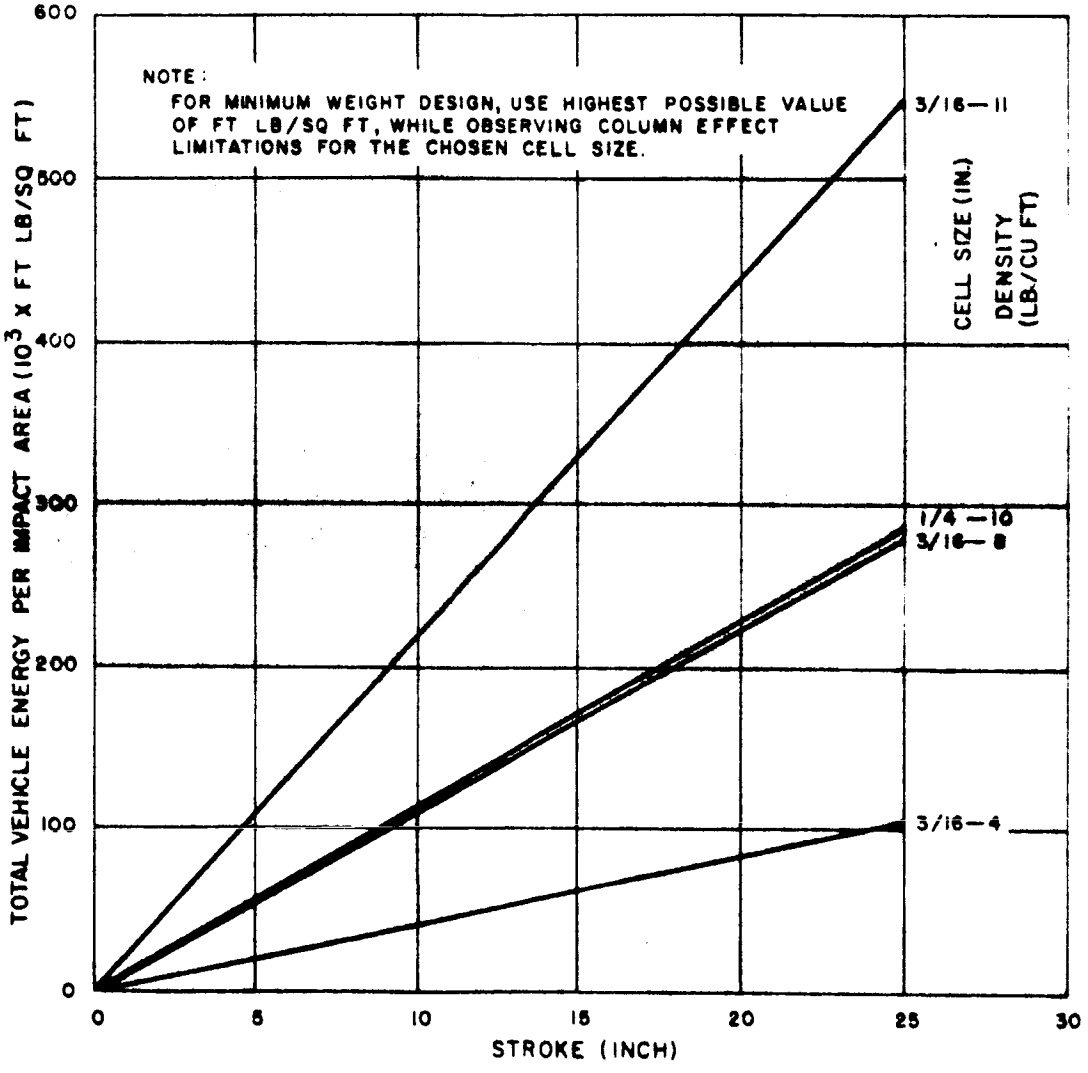

Figure 10-2. Energy Available Per Square Foot at a Given Stroke for 3/16 in. and 1/4" in. Cell Sizes

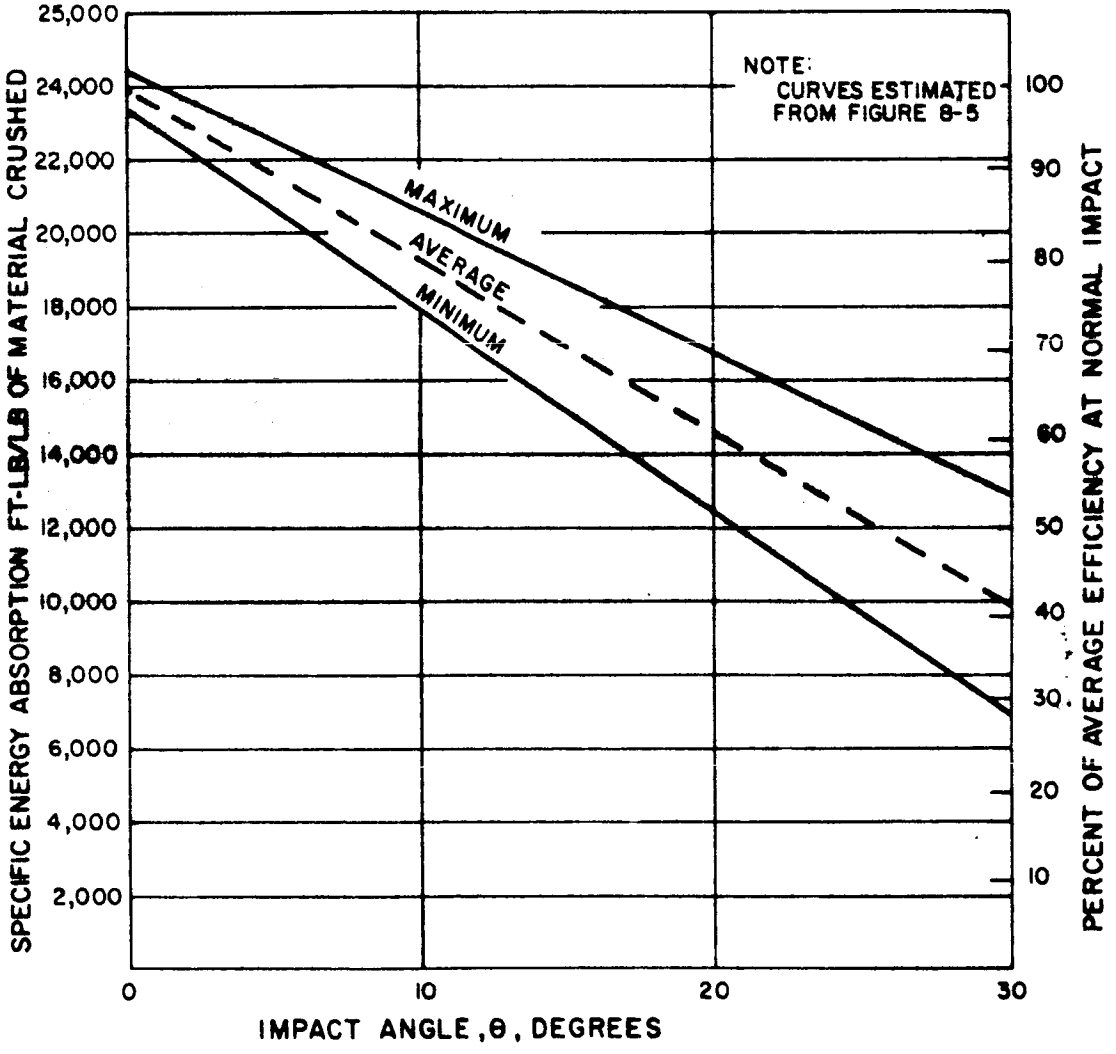

Figure 10-3. Specific Energy Absorption vs. Angle of Impact

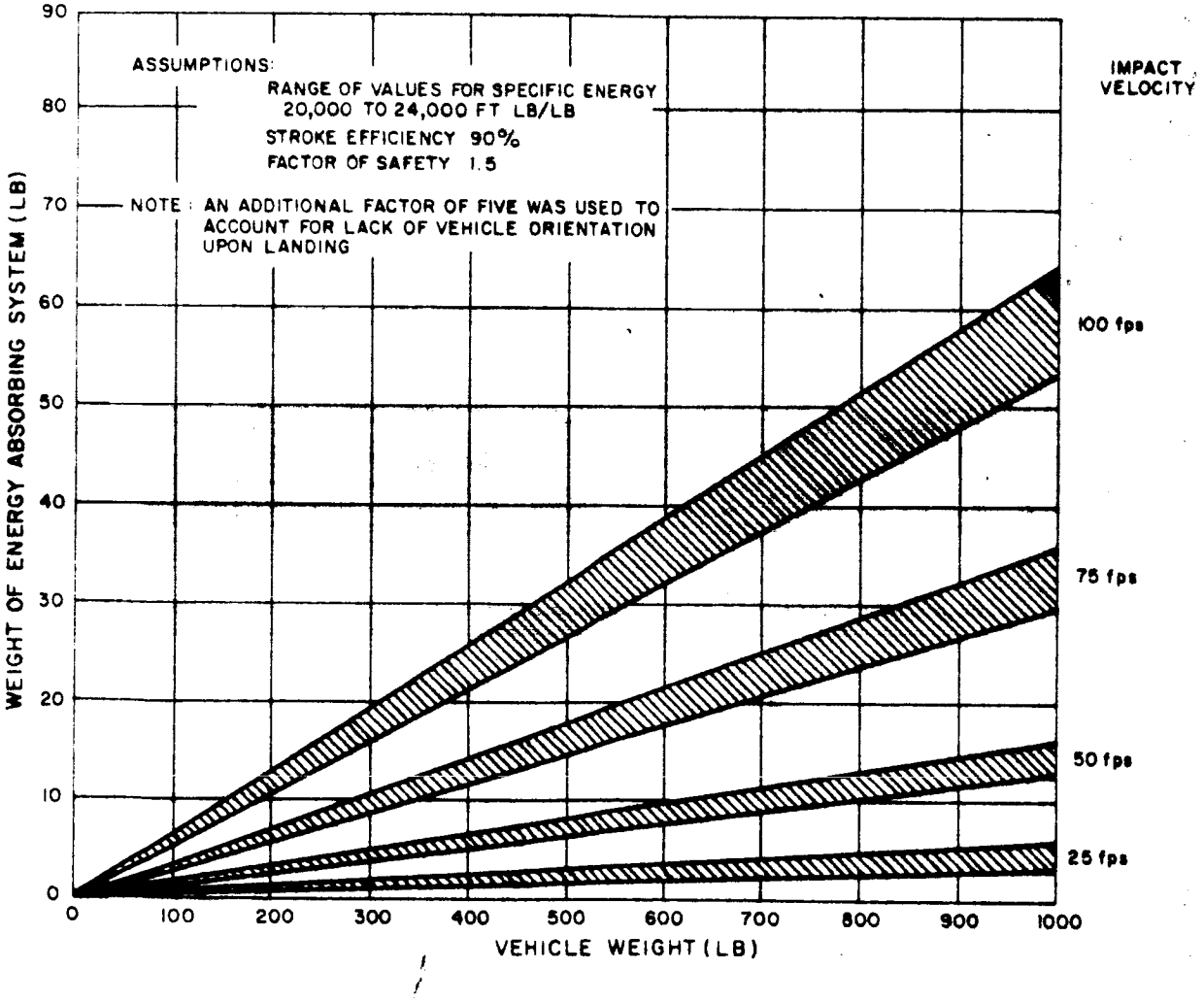

Figure 10-4. Weight of Energy Absorbing System Required for Given Vehicle Weight and Impact Velocity

11. REFERENCES

11.1 McFarland Jr., R.K., "A Limit Analysis of the Collapse of Hexagonal Cell Structure Under Axial Load," Jet Propulsion Laboratory, TR No. 32186, December, 1961.

11.2 "RF Transparent, Energy Absorbing, Structural Elements, Phase I, Final Report," GE-MSD Document No. 64SD565, March 16, 1964.

APPENDICES

APPENDIX A

ORIGINAL CALCULATIONS

APPENDIX A. ORIGINAL CALCULATIONS

Copies of the original calculation sheets are presented in this Appendix. They cover the following topics:

Figure A-1. Planimeter interpretation of static test data.

Figure A-2. Crushing stress corrections for static test data.

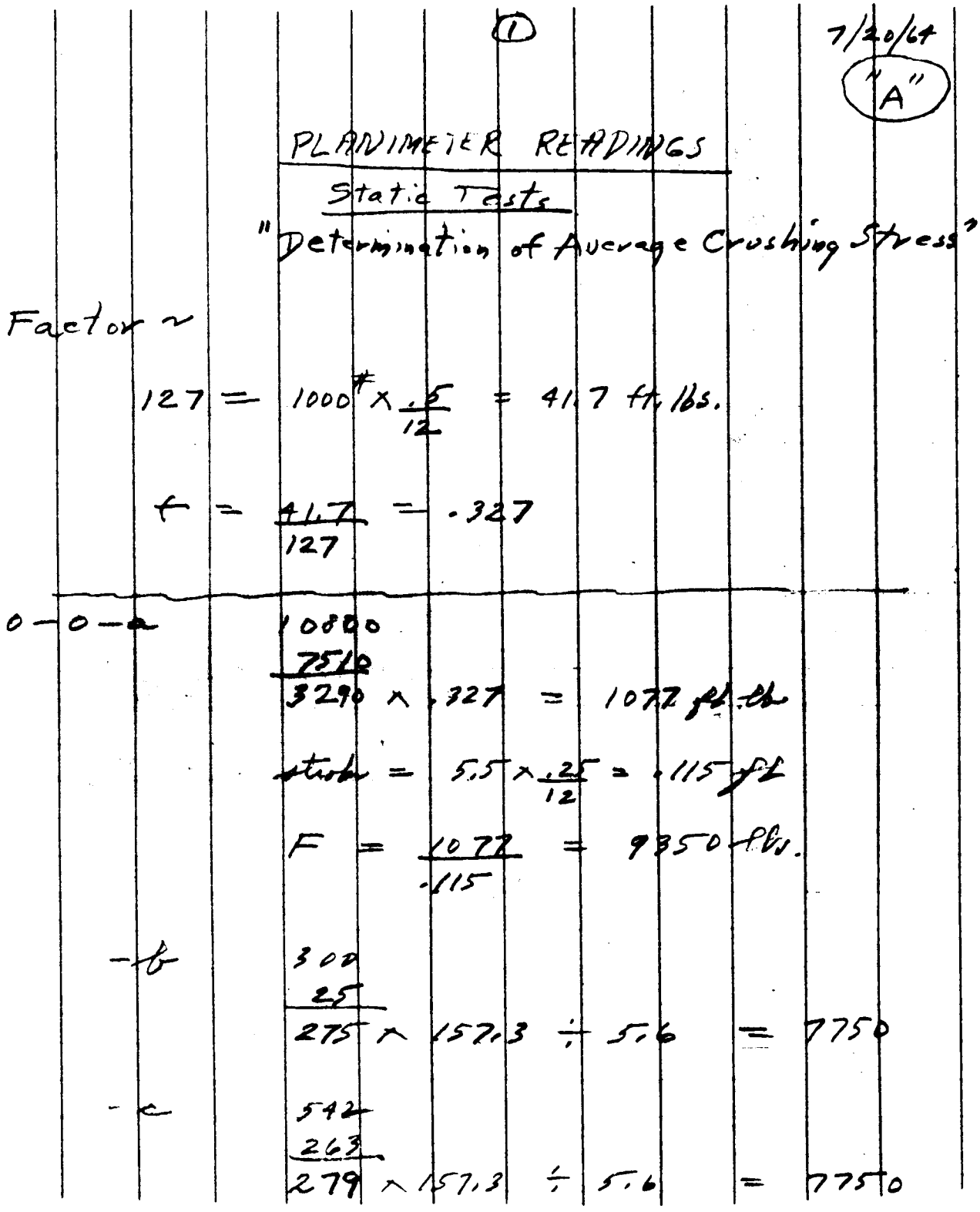

Figure A-1a. Planimeter Interpretation Of Static Test Data.

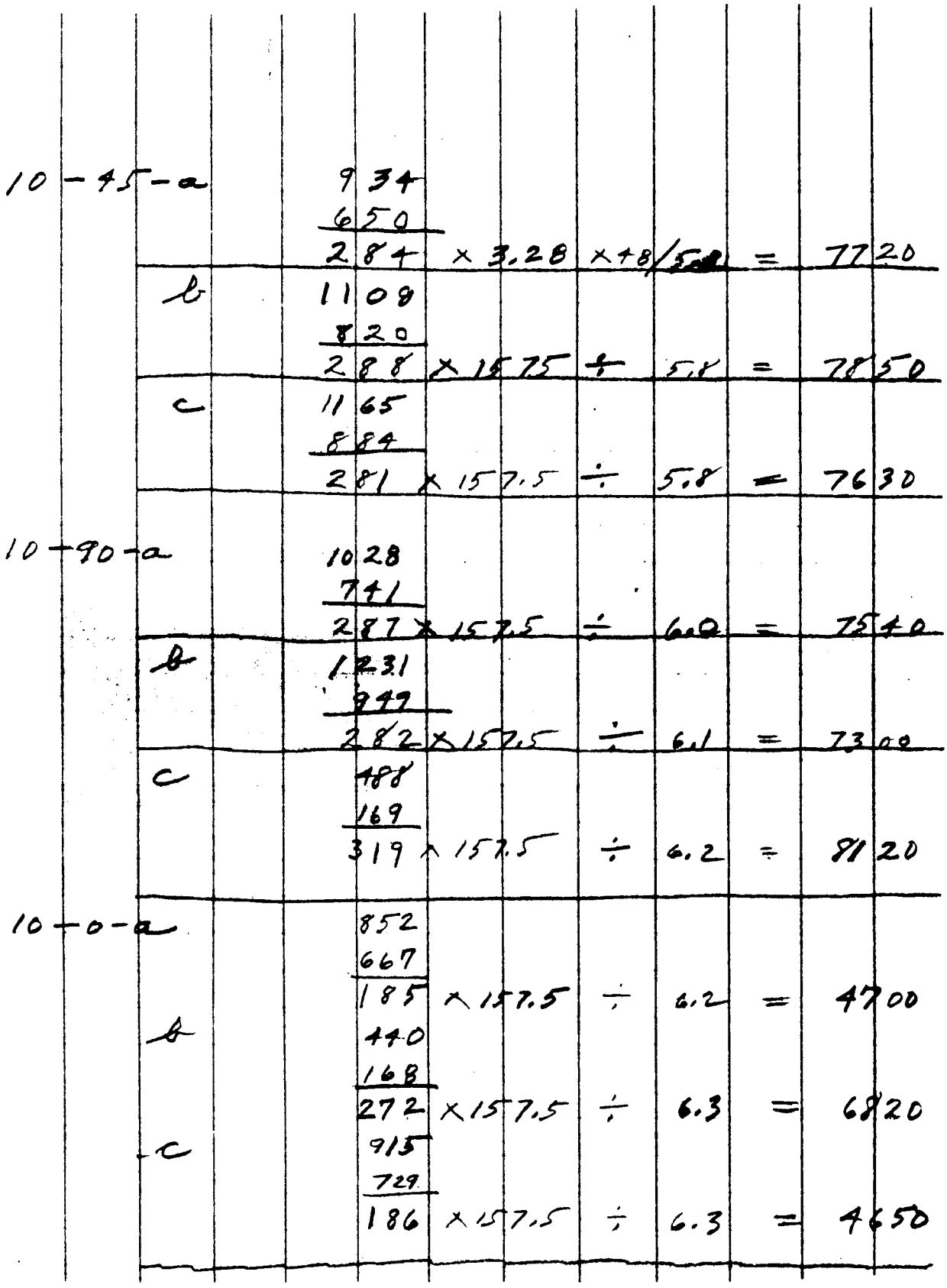

10-45-a	934 − 650 = 284	× 3.28	× 48/5	=	7720
b	1108 − 820 = 288	× 1575	÷	5.8	=	7850
c	1165 − 884 = 281	× 157.5	÷	5.8	=	7630
10-90-a	1028 − 741 = 287	× 157.5	÷	6.0	=	7540
b	1231 − 949 = 282	× 157.5	÷	6.1	=	7300
c	488 − 169 = 319	× 157.5	÷	6.2	=	8120
10-0-a	852 − 667 = 185	× 157.5	÷	6.2	=	4700
b	440 − 168 = 272	× 157.5	÷	6.3	=	6820
c	915 − 729 = 186	× 157.5	÷	6.3	=	4650

Figure A-1b. Planimeter Interpretation Of Static Test Data.

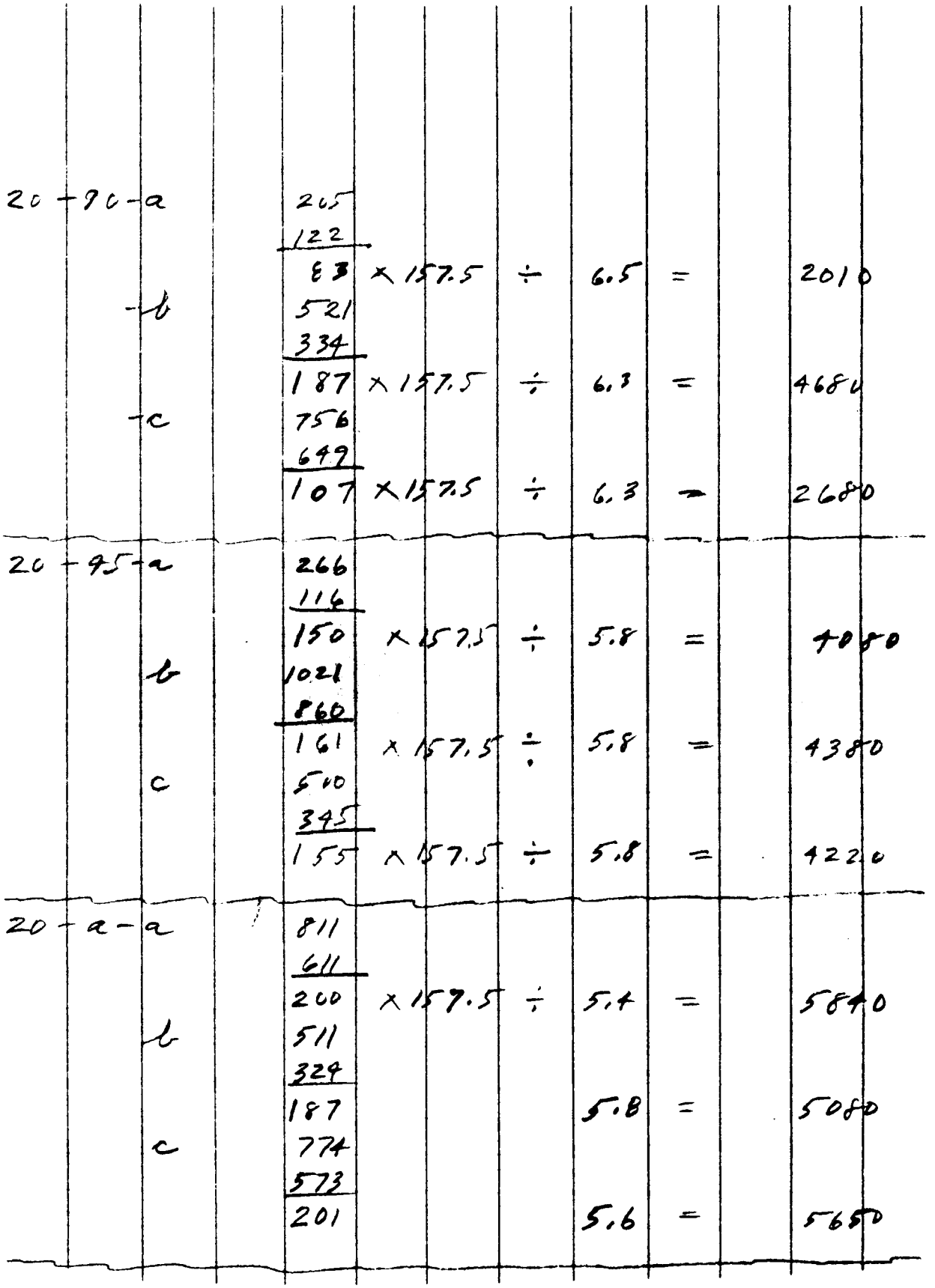

20 + 90 - a		205						
		122						
		83	× 157.5	÷	6.5	=		2010
	- b	521						
		334						
		187	× 157.5	÷	6.3	=		4680
	- c	756						
		649						
		107	× 157.5	÷	6.3	=		2680
20 + 95 - a		266						
		116						
		150	× 157.5	÷	5.8	=		4080
	b	1021						
		860						
		161	× 157.5	÷	5.8	=		4380
	c	510						
		345						
		155	× 157.5	÷	5.8	=		4220
20 + a - a		811						
		611						
		200	× 157.5	÷	5.4	=		5840
	b	511						
		329						
		187			5.8	=		5080
	c	774						
		573						
		201			5.6	=		5650

Figure A-1c. Planimeter Interpretation Of Static Test Data.

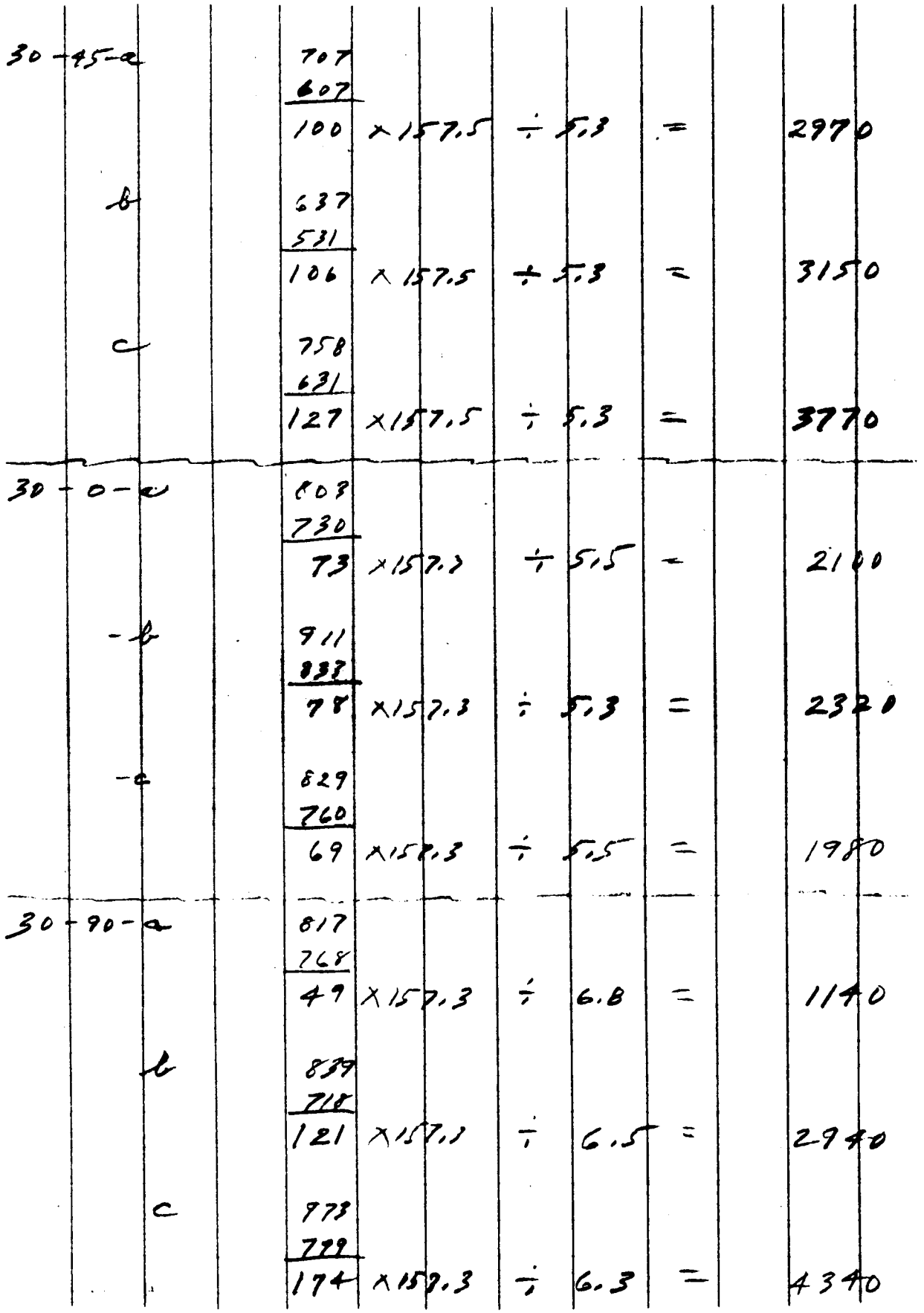

30 - 45 - a	707					
	607					
	100	× 157.5	÷ 5.3	=	2970	
b	637					
	531					
	106	× 157.5	÷ 5.3	=	3150	
c	758					
	631					
	127	× 157.5	÷ 5.3	=	3770	
30 - 0 - a	803					
	730					
	73	× 157.3	÷ 5.5	=	2100	
b	911					
	833					
	78	× 157.3	÷ 5.3	=	2320	
c	829					
	760					
	69	× 157.3	÷ 5.5	=	1980	
30 - 90 - a	817					
	768					
	49	× 157.3	÷ 6.8	=	1140	
b	859					
	718					
	121	× 157.3	÷ 6.5	=	2940	
c	973					
	729					
	174	× 157.3	÷ 6.3	=	4340	

Figure A-1d. Planimeter Interpretation Of Static Test Data.

APPENDIX B

TEST SPECIMENS

7/21/64

A-2a

Pressure corrections —

Wt of 2×2×2 specimens:

at $\rho = 11.2$ $\quad \frac{11.2 \times 8}{1728} \times 1\# = 23.6$ grams

at $\rho = 12.8$ $\quad = 27.0$ grams

example: $\frac{\text{Force}}{\text{area}} \times \frac{P_T}{P_A}$

$\frac{9350}{4} \times \frac{23.6}{29.0}$

$\frac{F \times 5.9}{P_A}$ (for $\rho = 11.2$)

$\frac{F \times 6.75}{P_A}$ (for $\rho = 12.8$)

Ke calculations from average crushing stress:

$\frac{\rho \times 1\#}{P} = Ke$

Figure A-2. Crushing Stress Corrections For Static Test Data.

APPENDIX B. TEST SPECIMENS

The Figures in this Appendix show the test specimens used for static testing after crushing.

Figure B-1 shows the specimens from the optimum density tests. Figures 1 through 10 show the angular test specimens after crushing before they were removed from the testing machine.

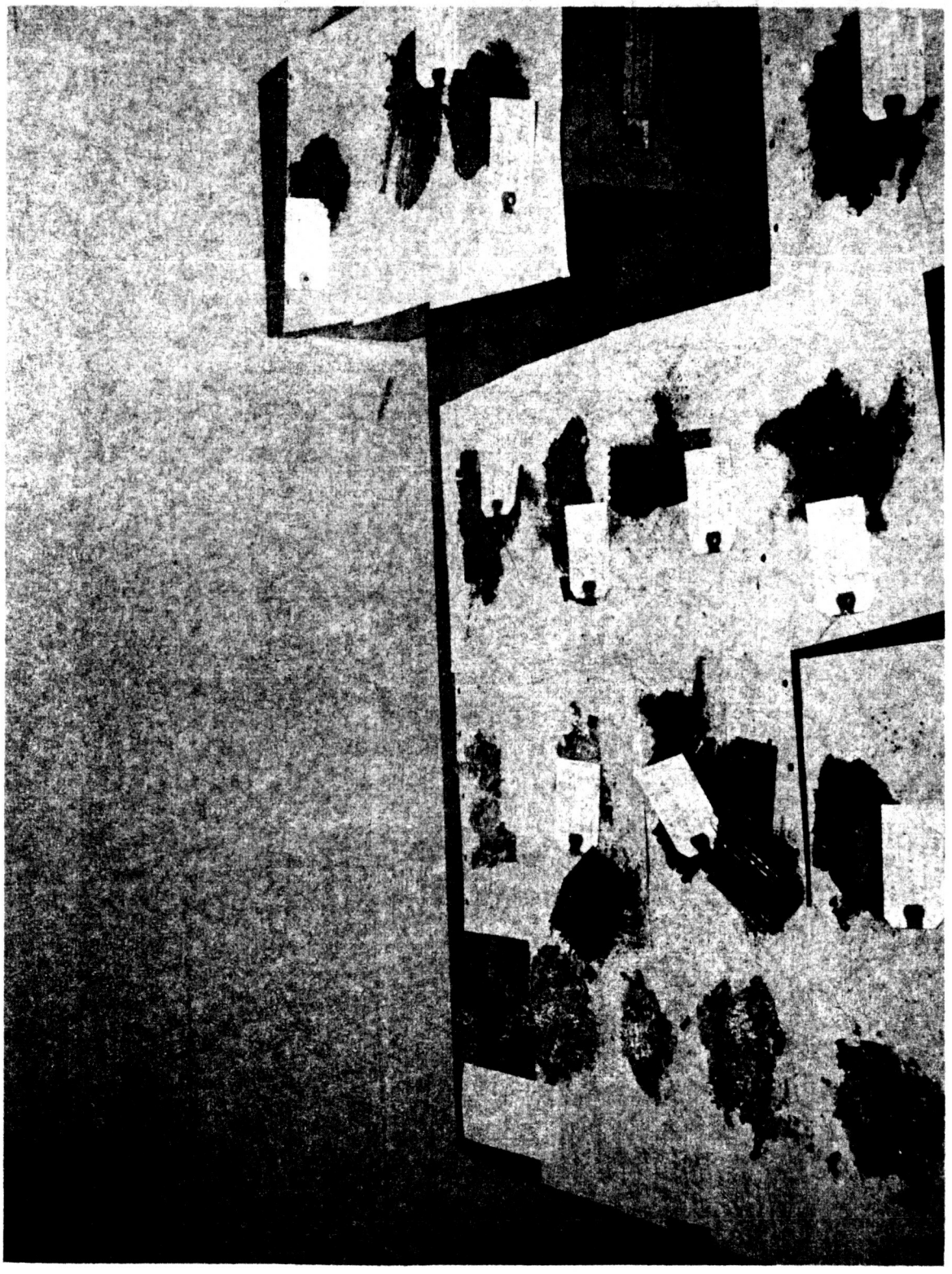

Figure B-1. Specimens From the Optimum Density Tests

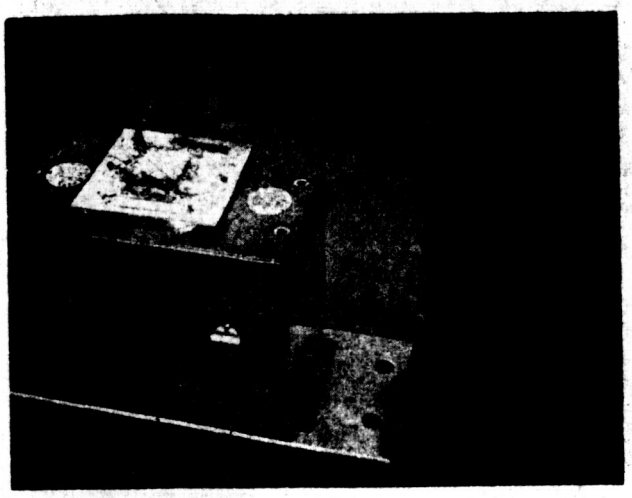

Figure 1-a. AS-0-0-a

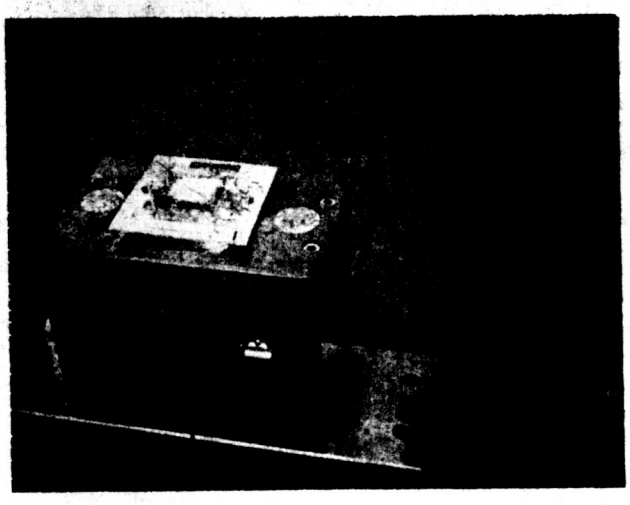

Figure 1-b. AS-0-0-b

Figure 1-c. AS-0-0-c

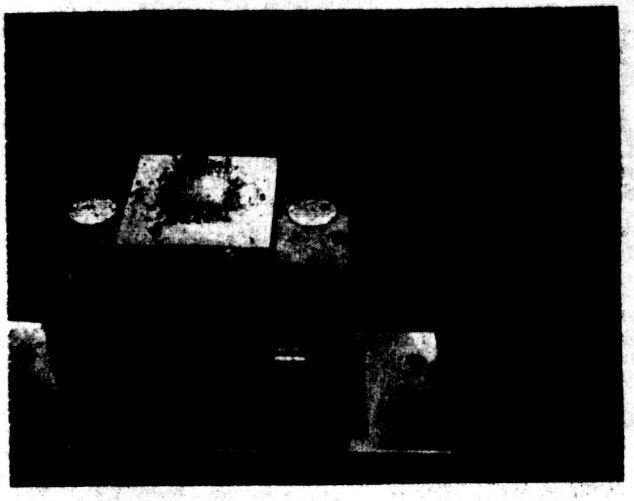

Figure 2-a. AS-10-0-a

Figure 2-b. AS-10-0-b

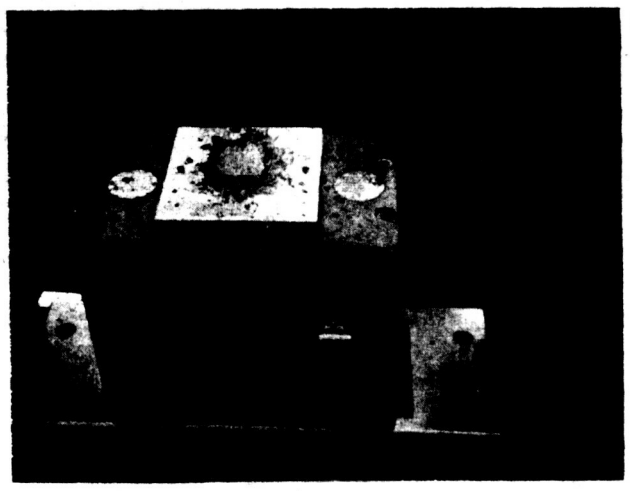

Figure 2-c. AS-10-0-c

Figure 3-a. AS-10-45-a

Figure 3-b. AS-10-45-b

Figure 3-c. AS-10-45-c

Figure 4-a. AS-10-90-a

Figure 4-b. AS-10-90-b

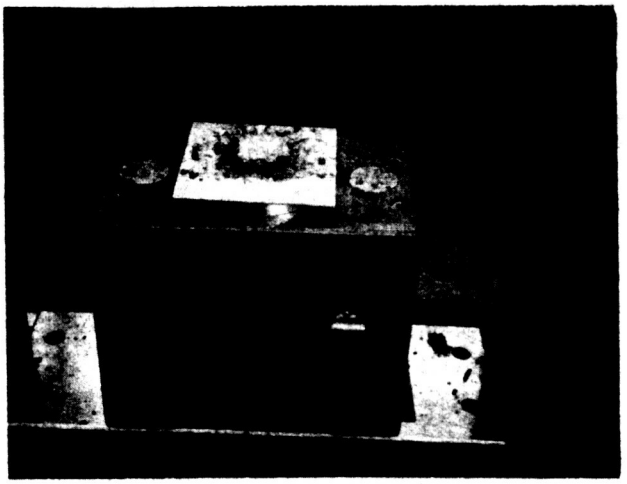

Figure 4-c. AS-10-90-c

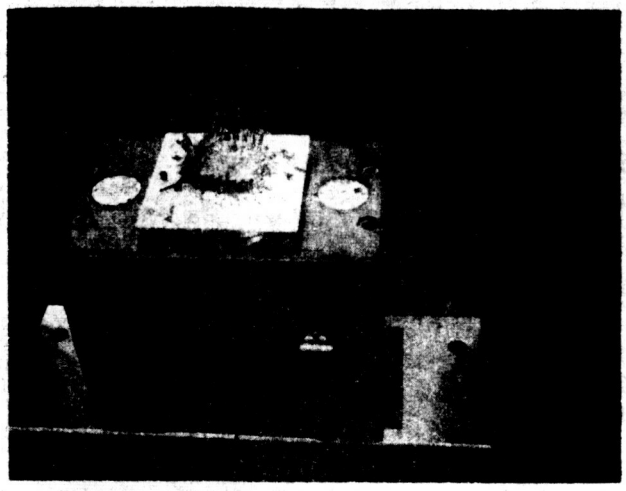

Figure 5-a. AS-20-0-a

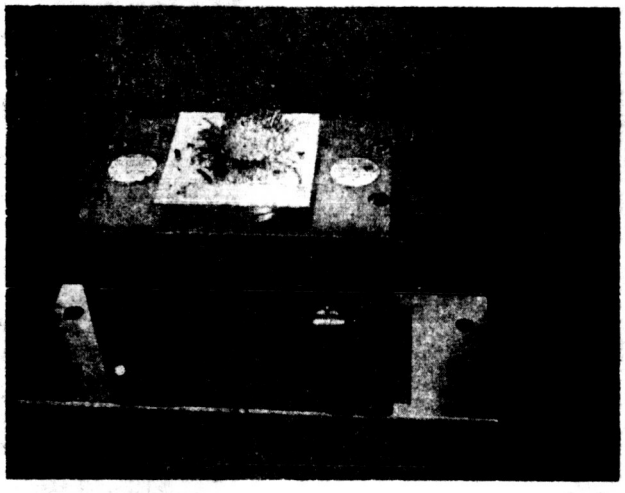

Figure 5-b. AS-20-0-b

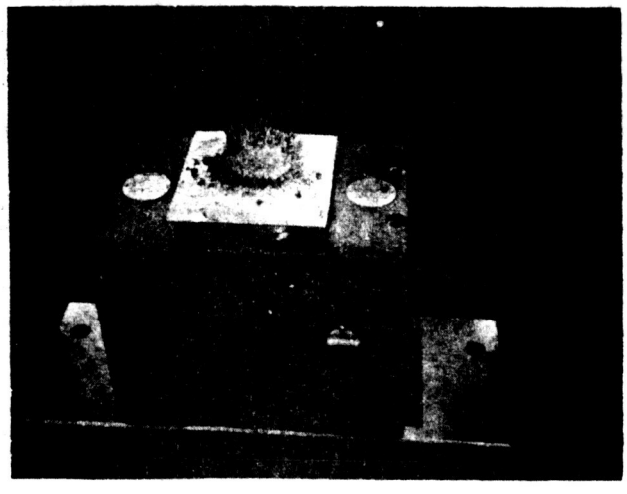

Figure 5-c. AS-20-0-c

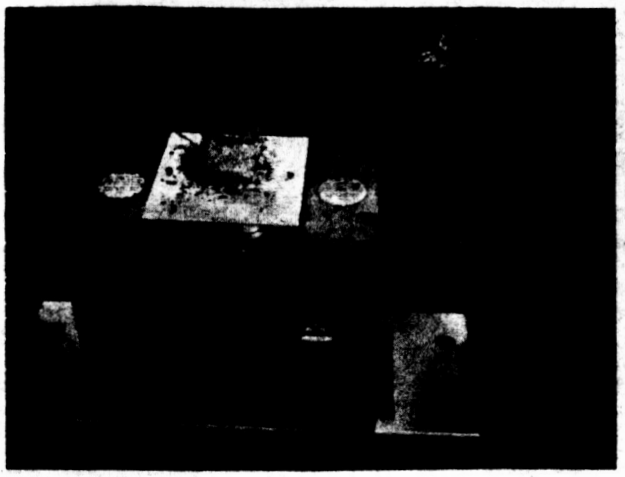

Figure 6-a. AS-20-45-a

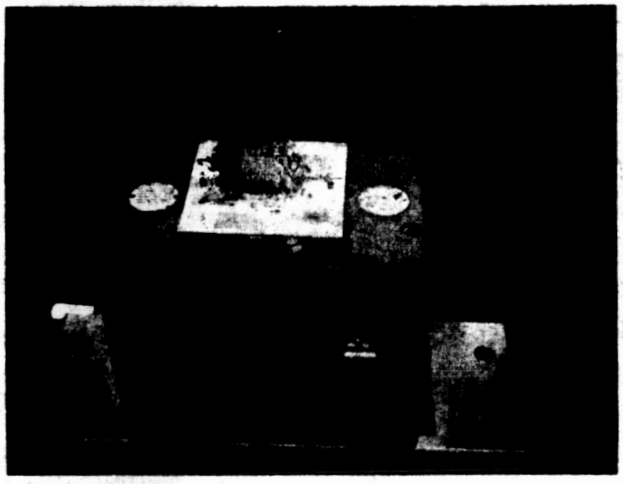

Figure 6-b. AS-20-45-b

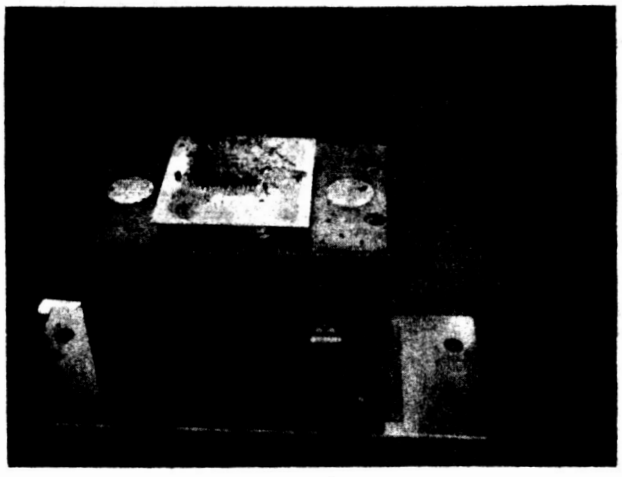

Figure 6-c. AS-20-45-c

Figure 7-a. AS-20-90-a

Figure 7-b. AS-20-90-b

Figure 7-c. AS-20-90-c

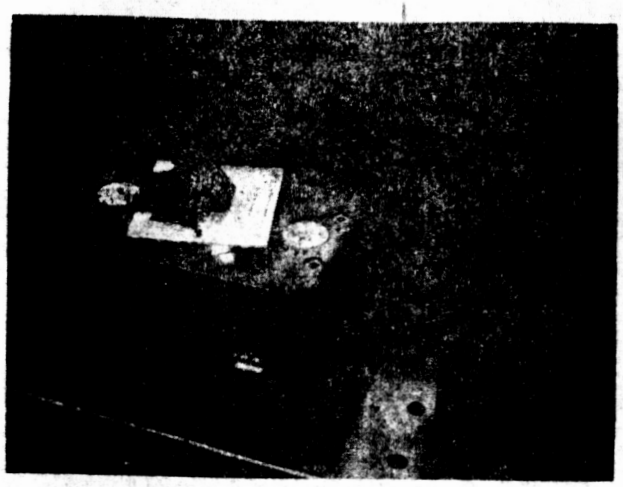

Figure 8-a. AS-30-0-a

Figure 8-b. AS-30-0-b

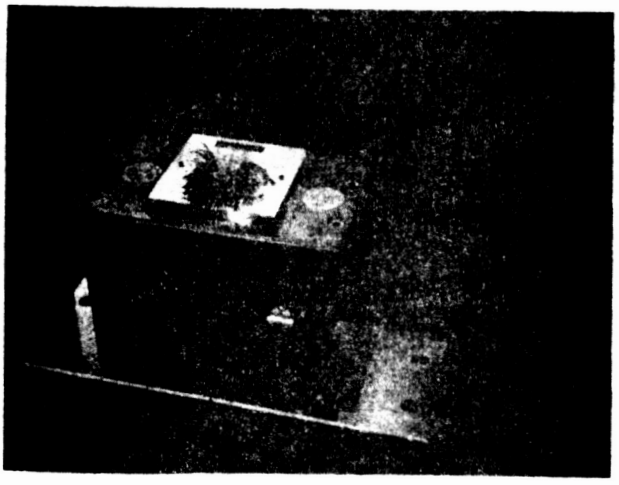

Figure 8-c. AS-30-0-c

Figure 9-a. AS-30-45-a

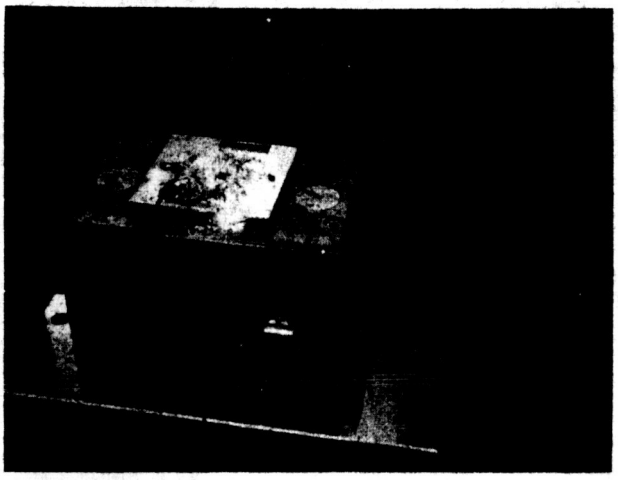

Figure 9-b. AS-30-45-b

Figure 9-c. AS-30-45-c

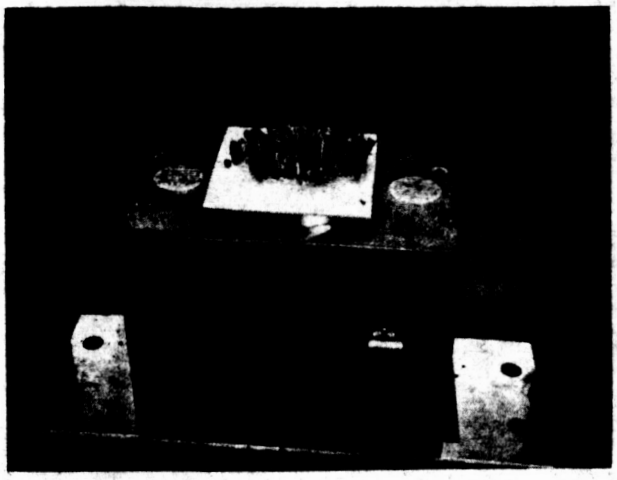

Figure 10-a. AS-30-90-a

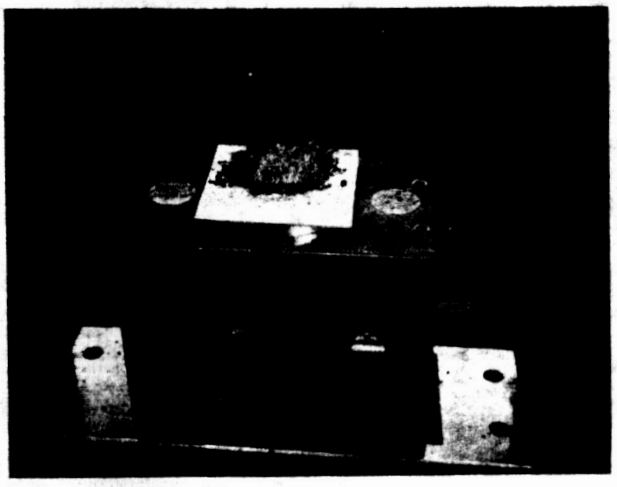

Figure 10-b. AS-30-90-b

Figure 10-c. AS-30-90-c

APPENDIX C

DYNAMIC IMPACT TESTS

APPENDIX C. DYNAMIC IMPACT TESTS

Force-stroke curves obtained by double integration of the accelerometer traces are shown in Figures C-1 through C-8. Figures C-9 through C-42 are copies of experimental data covering the dynamic impact tests. Photographs of the accelerometer trace and the specimen after impact for each test are presented on the same page for easy reference.

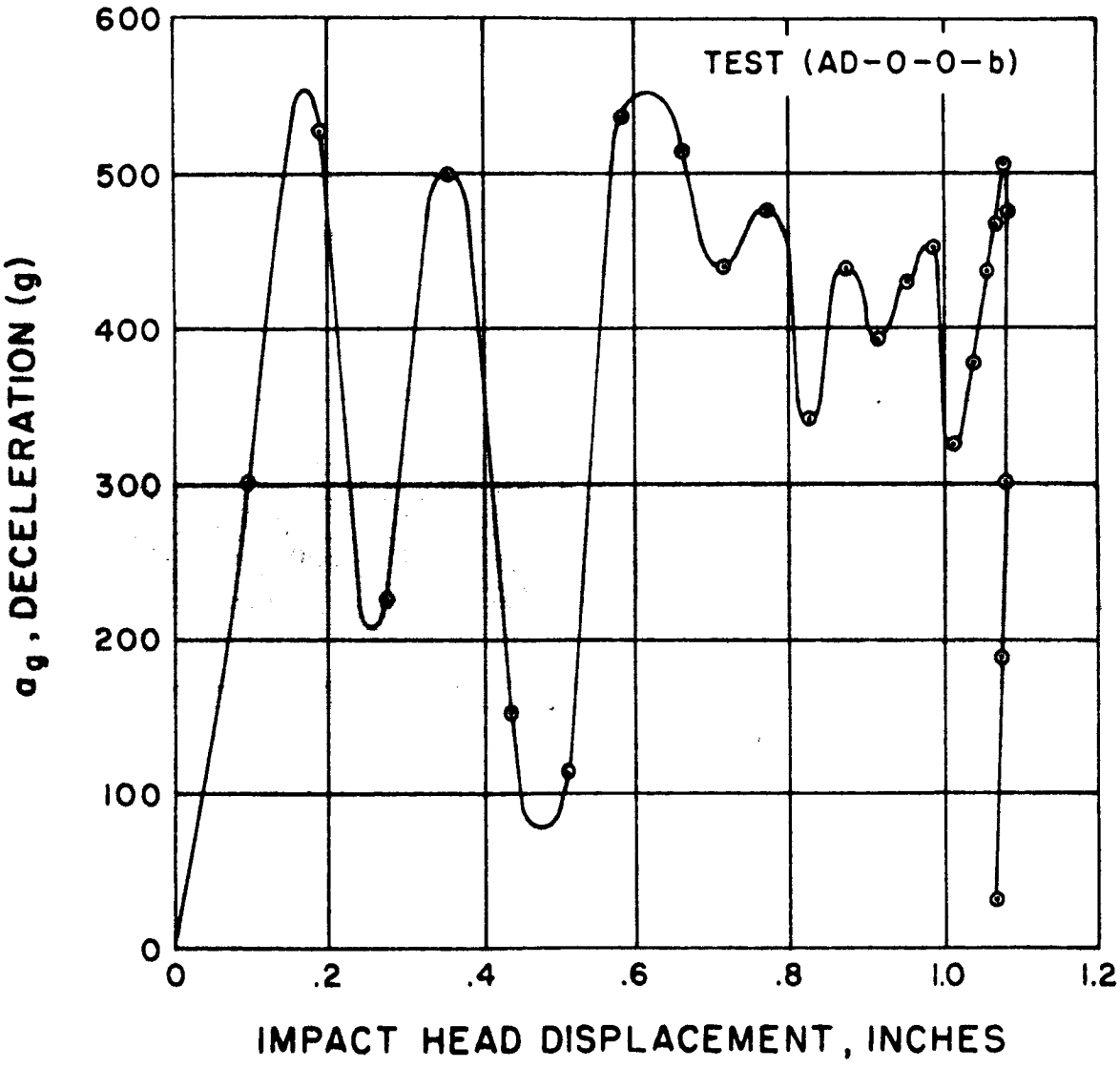
TEST (AD-O-O-b)
600
500
400
300
200
100
0
0
.2
.4
.6
.8
1.0
1.2
a_g, DECELERATION (g)
IMPACT HEAD DISPLACEMENT, INCHES

Figure C-1.

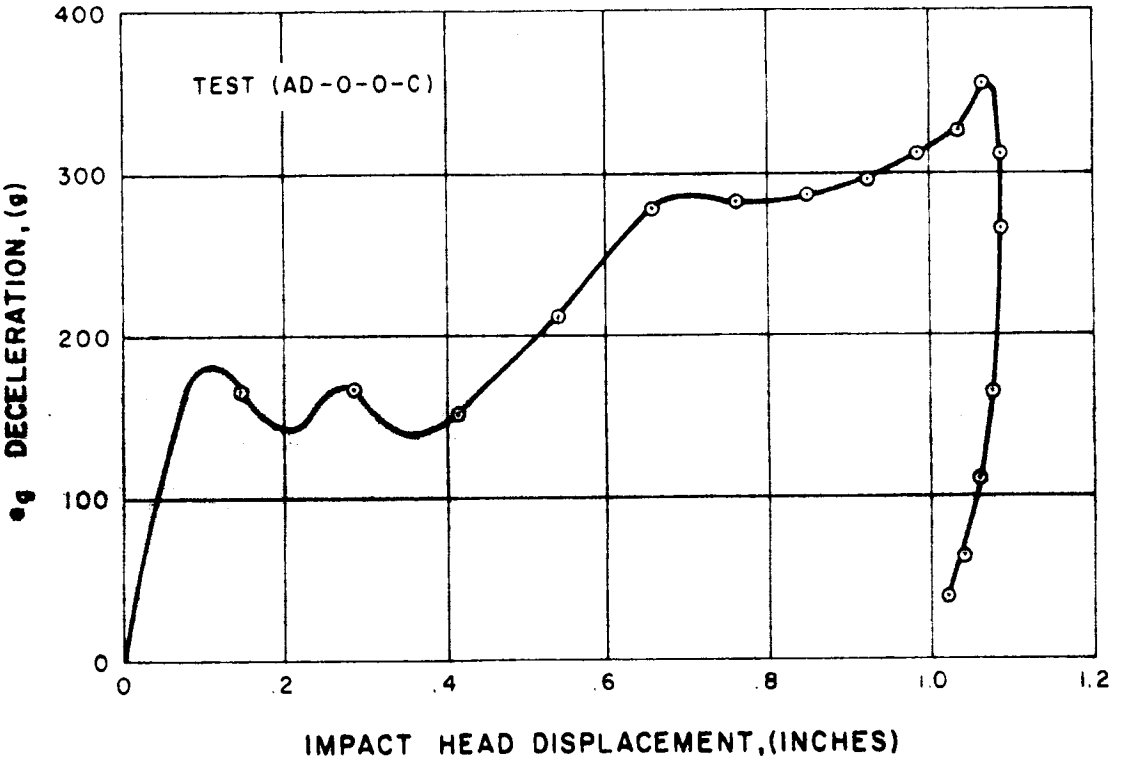

Figure C-2.

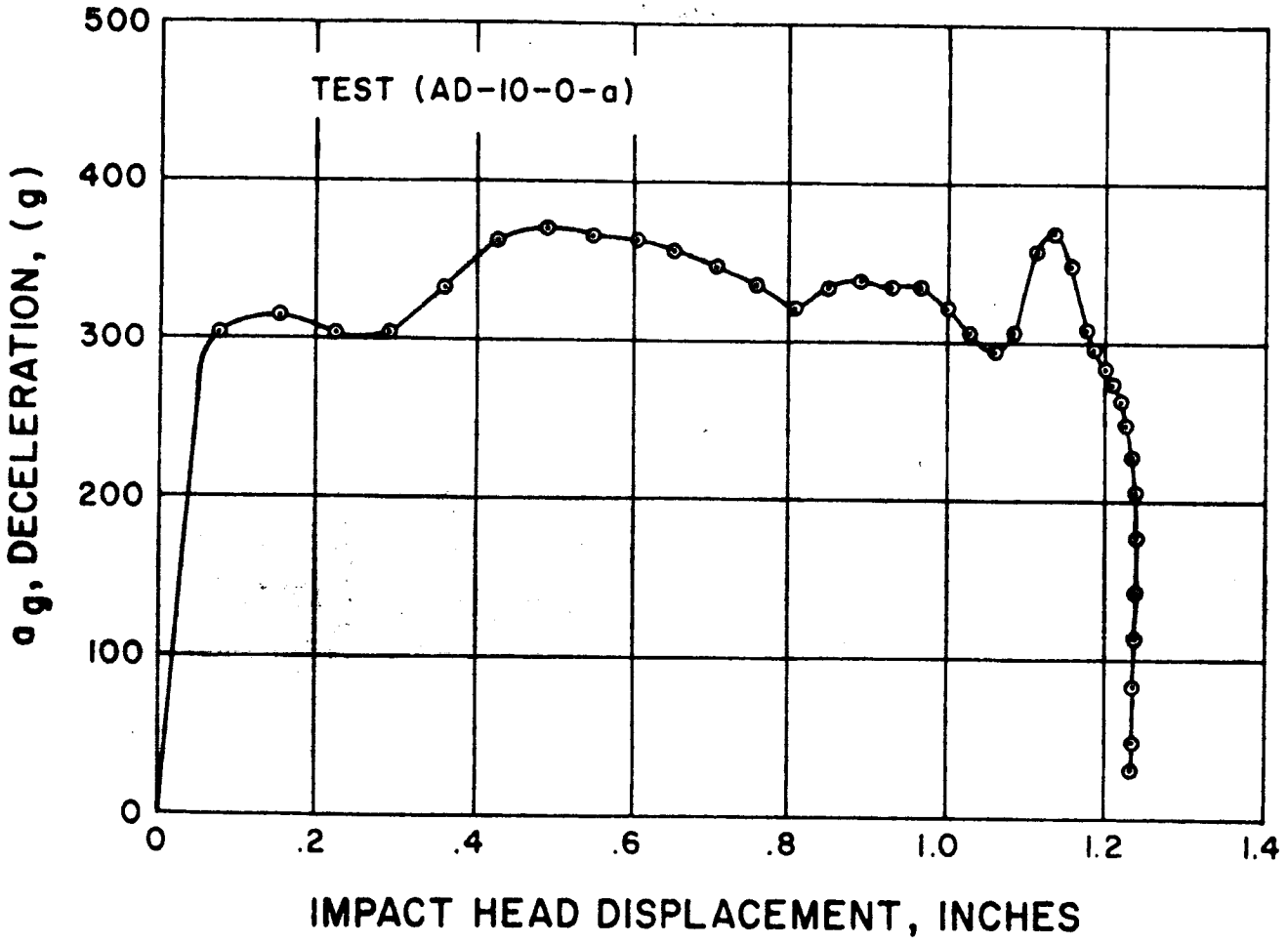
TEST (AD-10-0-a)
500
400
300
200
100
0
0
.2
.4
.6
.8
1.0
1.2
1.4
a g, DECELERATION, (g)
IMPACT HEAD DISPLACEMENT, INCHES

Figure C-3.

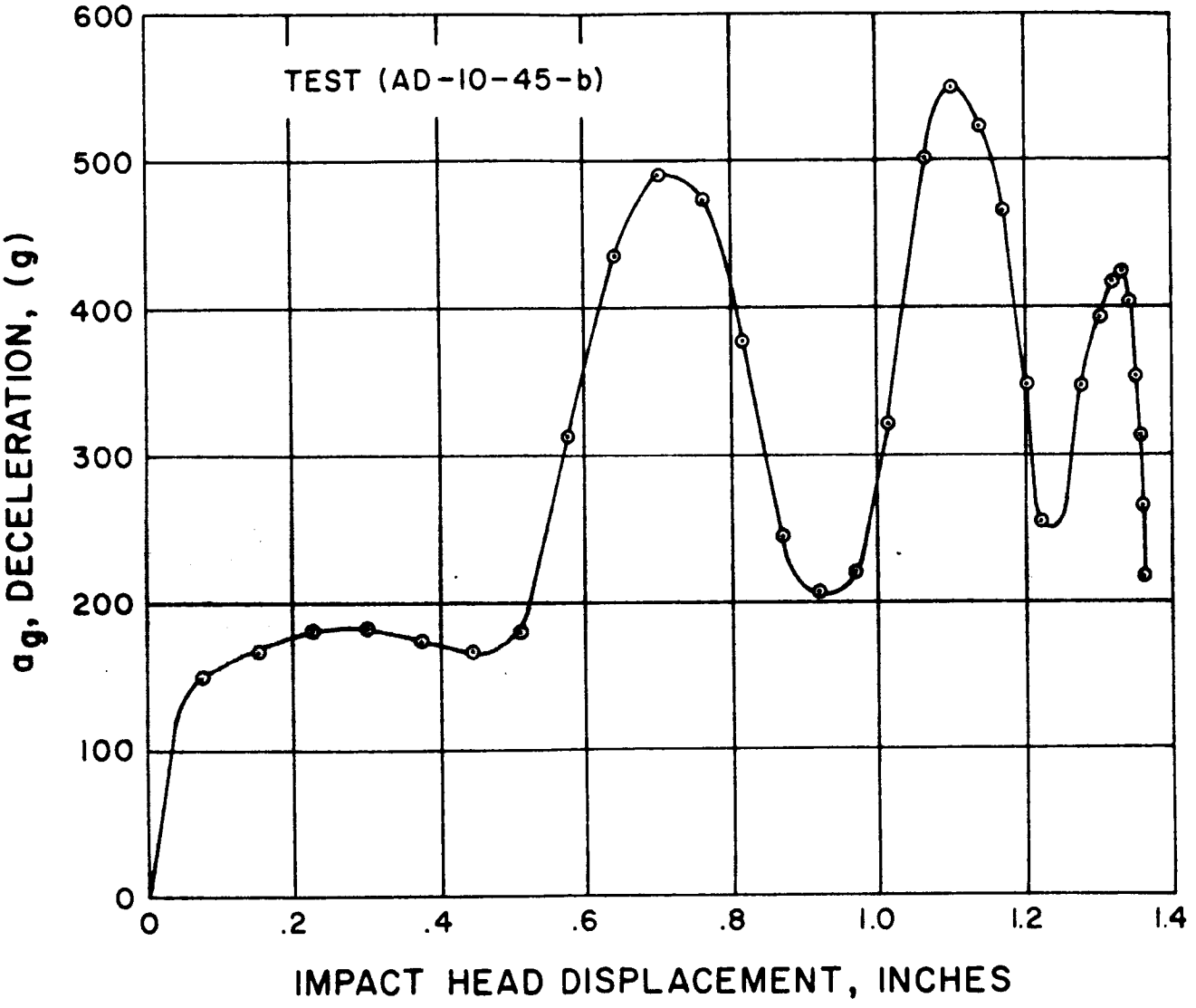
TEST (AD-10-45-b)
600
500
400
300
200
100
0
a_g, DECELERATION, (g)
0
.2
.4
.6
.8
1.0
1.2
1.4
IMPACT HEAD DISPLACEMENT, INCHES

Figure C-4.

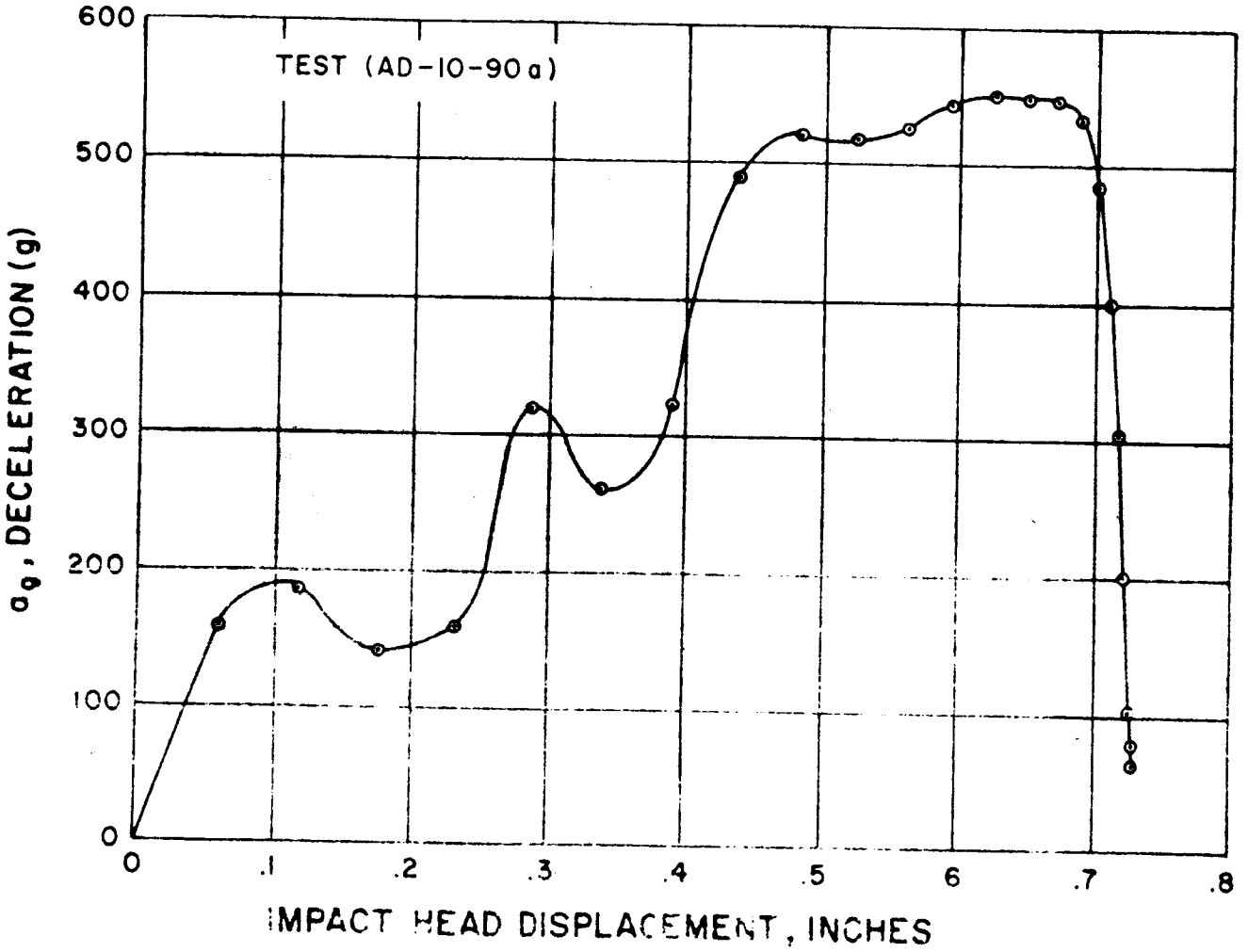

Figure C-5.

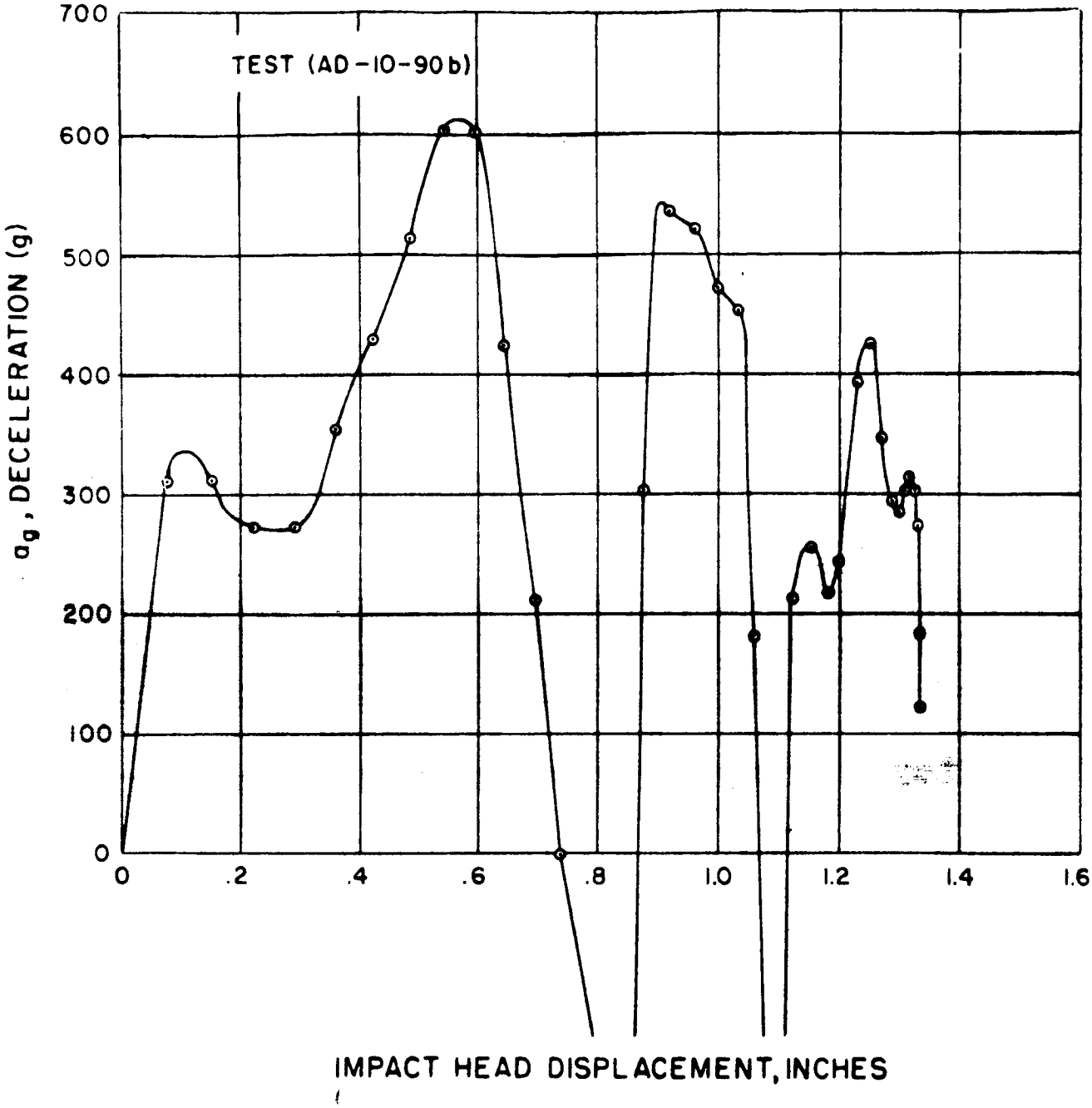

Figure C-6.

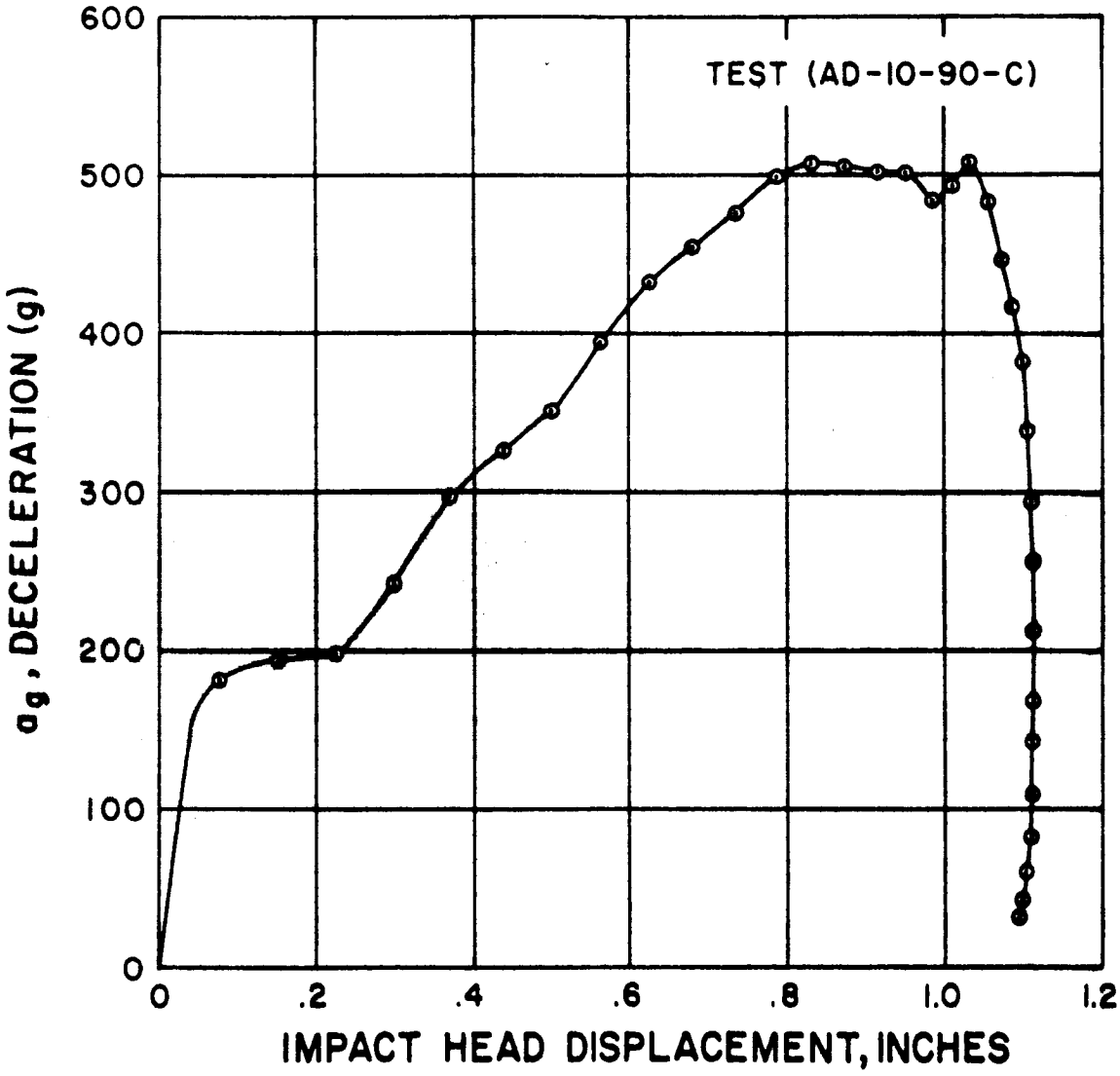

Figure C-7.

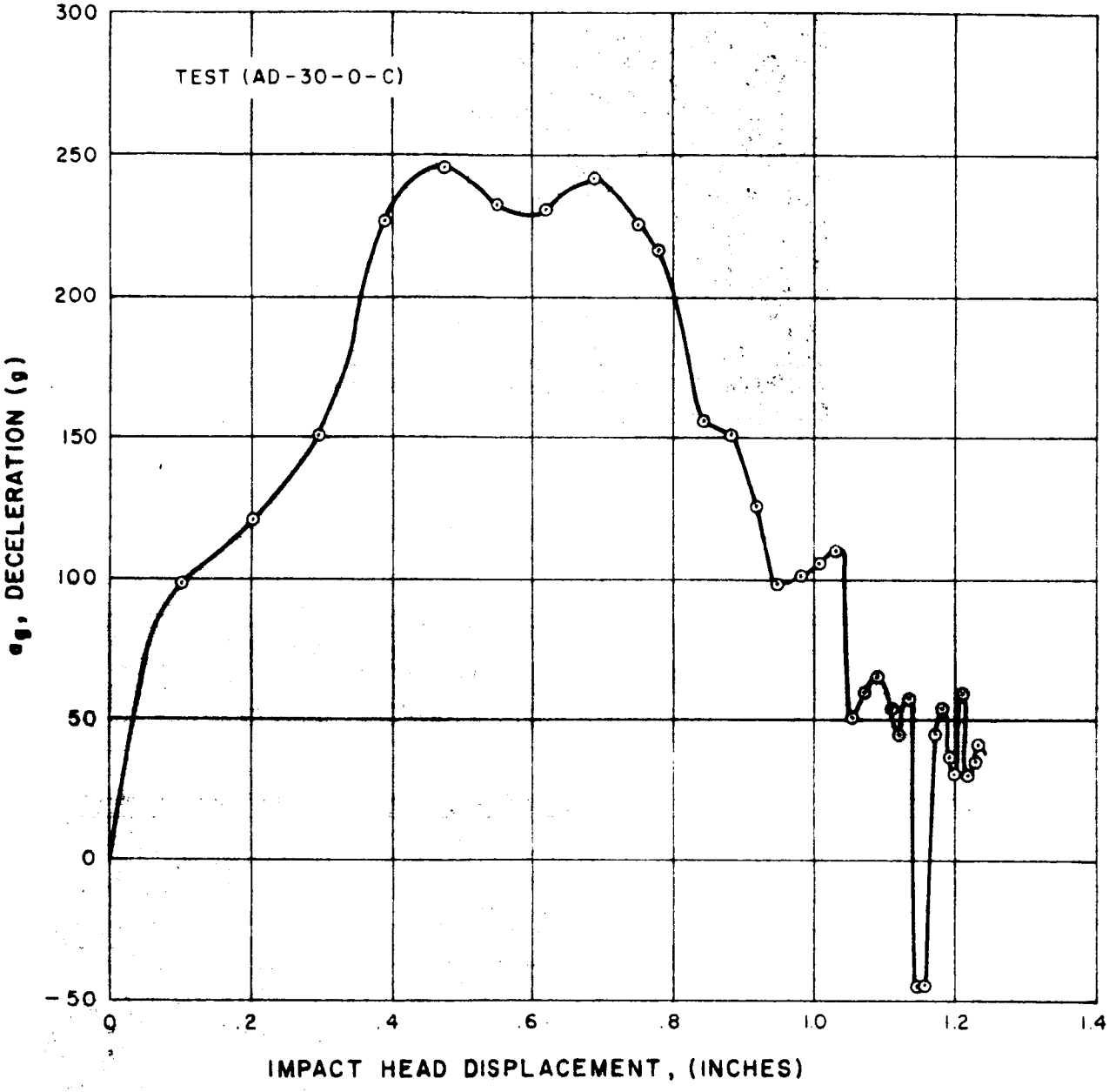
TEST (AD-30-0-C)
300
250
200
150
100
50
0
-50
0
.2
.4
.6
.8
1.0
1.2
1.4
g, DECELERATION (g)
IMPACT HEAD DISPLACEMENT, (INCHES)

Figure C-8.

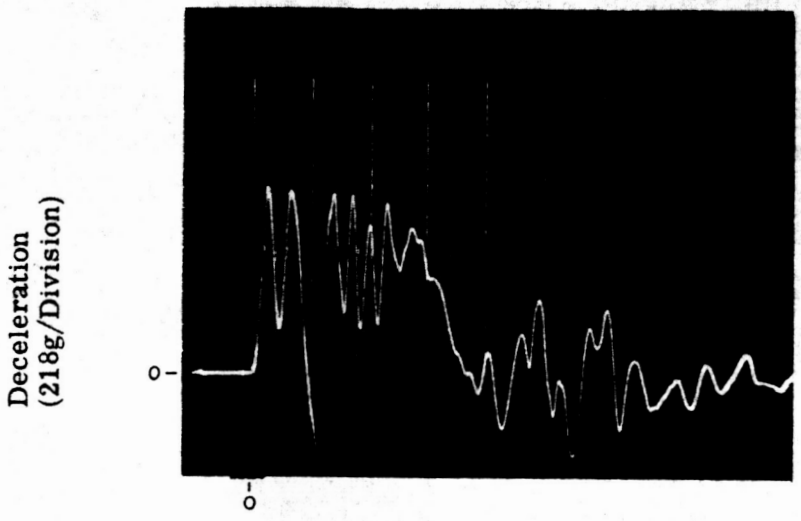

Time After Response Initiation
(1 Millisecond/Division)

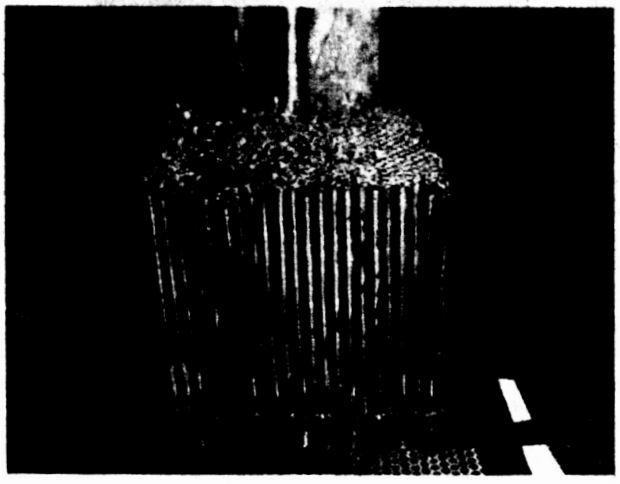

Impact Velocity - 46 ft/sec
Energy Absorbed - 2432 lb.ft
Initial Length - 5 in.
Final Length 4.38 in.

Figure C-9. Accelerometer Record (Statham A5-500-350) and Specimen After Impact (AD-0-0-a)

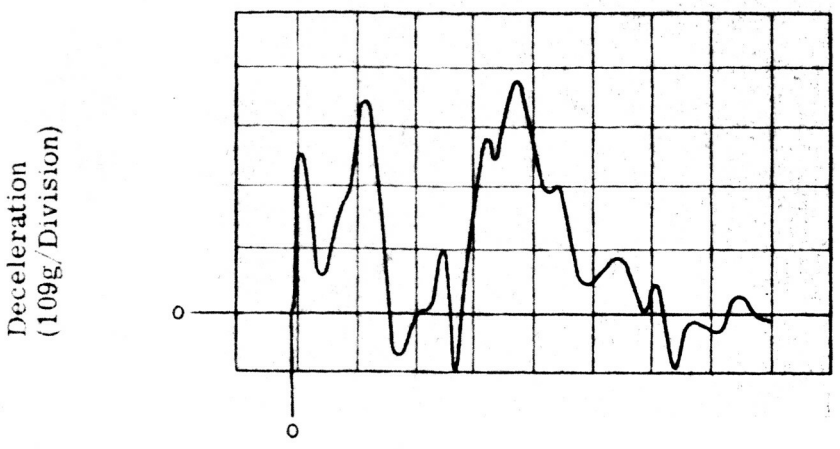

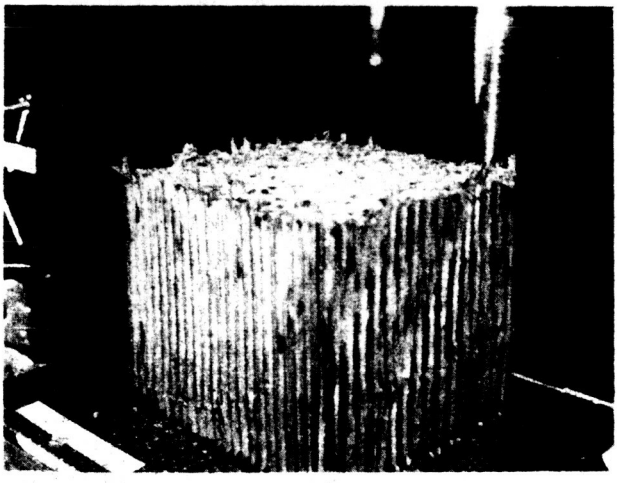

Impact Velocity - 46 ft/sec
Energy Absorbed - 2432 lb. ft.
Initial Length - 5 in.
Final Length 4.06 in.

Figure C-10. Accelerometer Record (Statham A5-500-350) and Specimen After Impact (AD-0-0-b1)

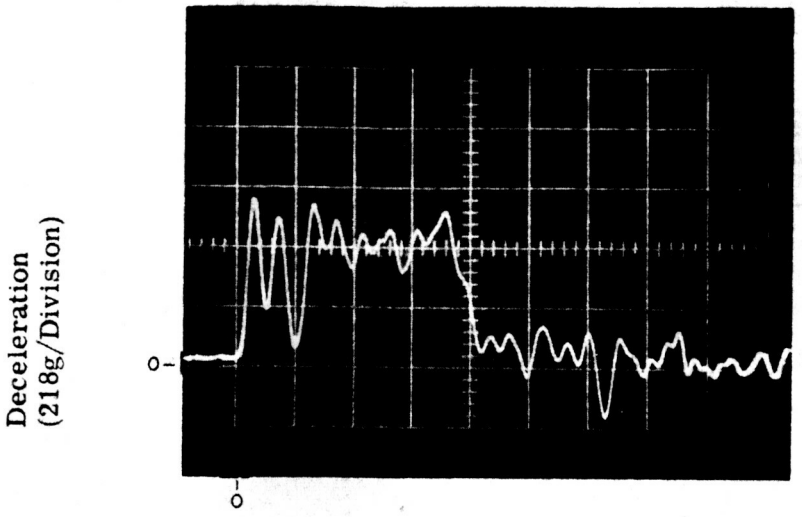

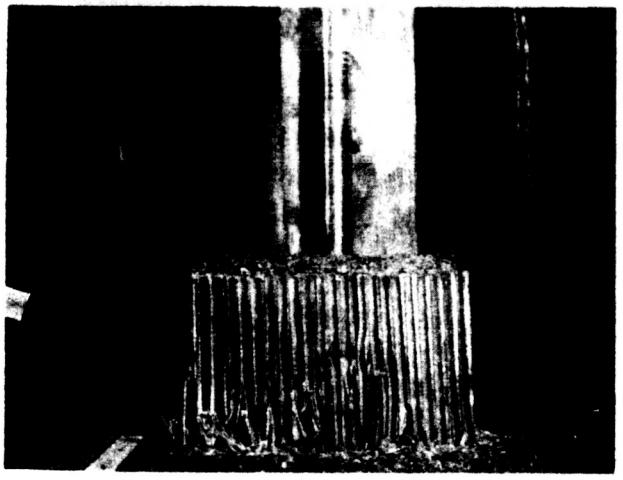

Impact Velocity - 46 ft/sec
Energy Absorbed - 2432 lb.ft.
Initial Length - 4.06 in.
Final Length 3.16 in.

Figure C-11. Accelerometer Record (Statham A5-500-350) and Specimen After Impact (AD-0-0-b2)

Deceleration
(- g/Division)

NOT
AVAILABLE

Time After Response Initiation
(- Millisecond/Division)

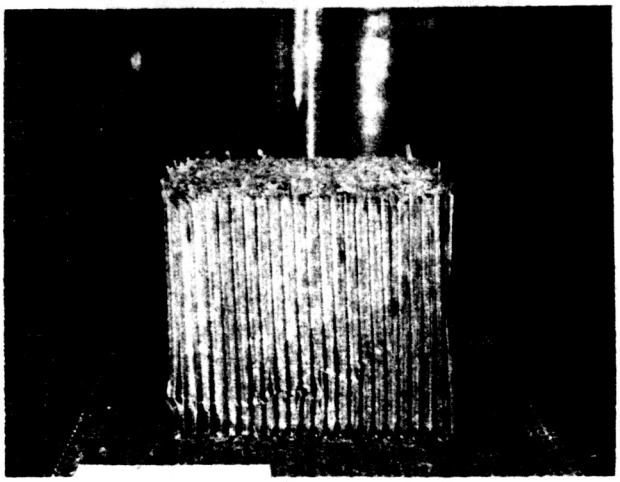

Impact Velocity - 36 ft/sec
Energy Absorbed - 1474 lb. ft.
Initial Length - 5 in.
Final Length 4.50 in.

Figure C-12. Accelerometer Record (Statham A5-500-350) and Specimen After Impact (AD-0-0-c)

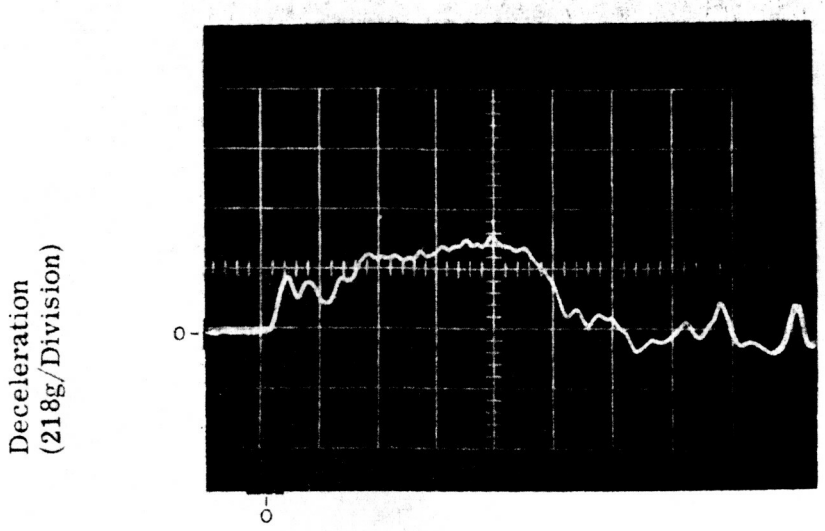

Time After Response Initiation
(1 Millisecond/Division)

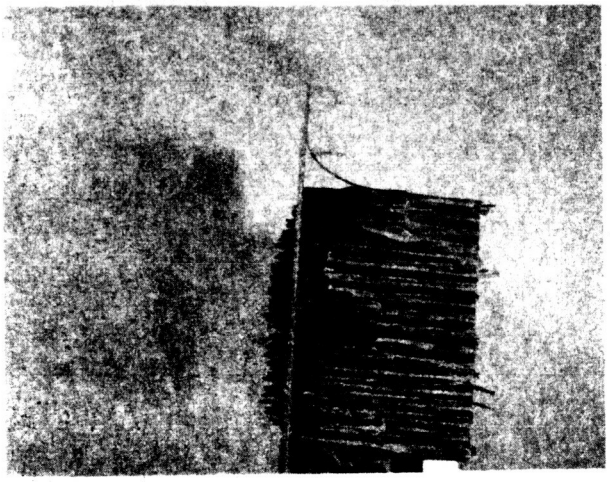

Impact Velocity - 36 ft/sec
Energy Absorbed - 1474 lb. ft.
Initial Length - 4.5 in.
Final Length 3.44 in.

Figure C-13. Accelerometer Record (Statham A5-500-350) and Specimen After Impact (AD-0-0-c)

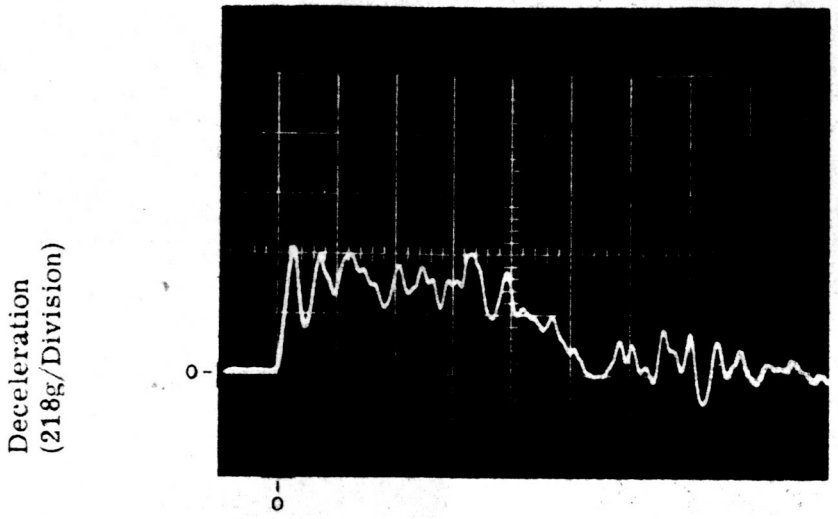

Time After Response Initiation
(1 Millisecond/Division)

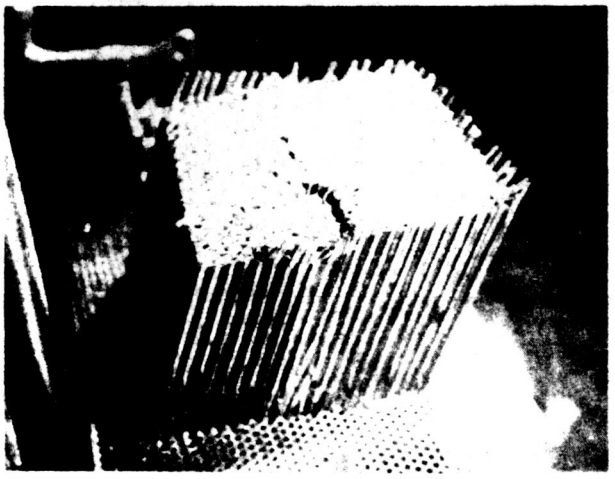

Impact Velocity - 46 ft/sec
Energy Absorbed - 2432 lb. ft.
Initial Length - 5 in.
Final Length - 3.94 in.

Figure C-14. Accelerometer Record (Statham A5-500-350) and Specimen After Impact (AD-10-0-a)

Deceleration
(-g/Division)

NOT
AVAILABLE

Time After Response Initiation
(- Millisecond/Division)

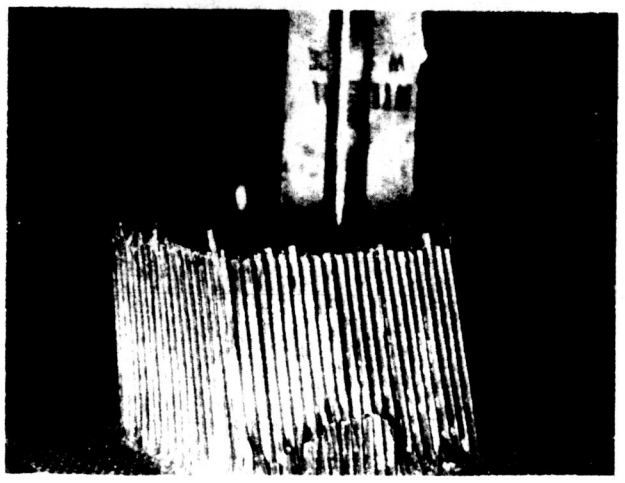

Impact Velocity - 46 ft/sec
Energy Absorbed - 2432 lb. ft.
Initial Length - 5 in.
Final Length - 3.88 in.

Figure C-15. Accelerometer Record (Statham A5-500-350) and Specimen After Impact (AD-10-0-b1)

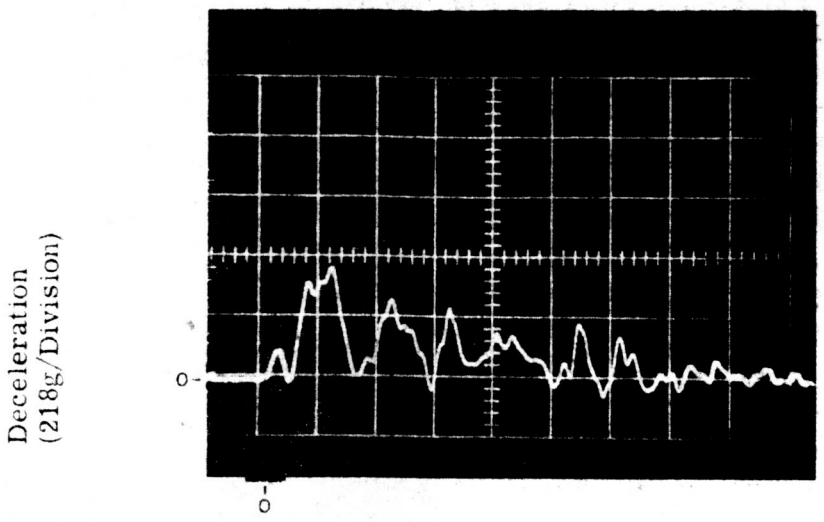

Time After Response Initiation
(1 Millisecond/Division)

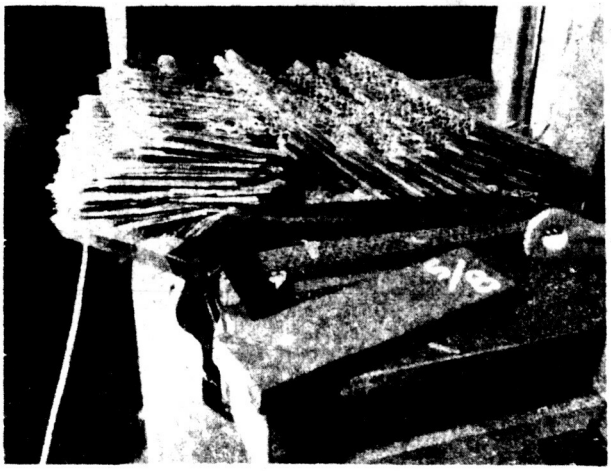

Impact Velocity - 46 ft/sec
Energy Absorbed - 2432 lb. ft.
Initial Length - 3.88 in.
Final Length - Collapsed

Figure C-16. Accelerometer Record (Statham A5-500-350) and Specimen After Impact (AD-10-0-b2)

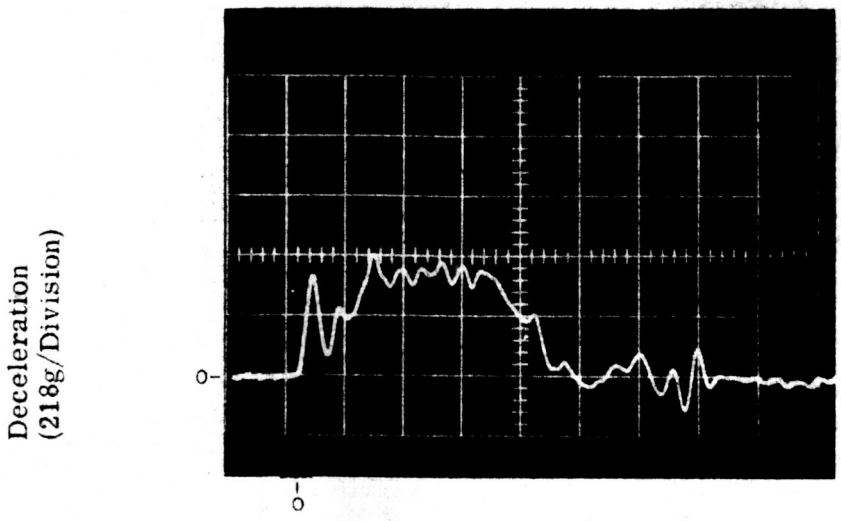

Time After Response Initiation
(1 Millisecond/Division)

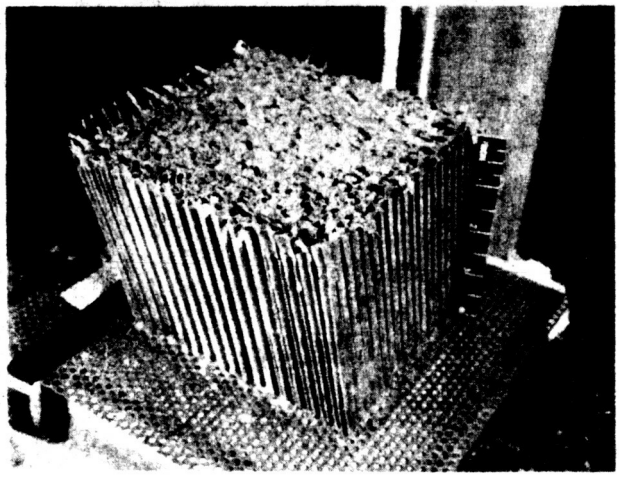

Impact Velocity - 36 ft/sec
Energy Absorbed - 1474 lb. ft.
Initial Length - 5 in.
Final Length - 4.32 in.

Figure C-17. Accelerometer Record (Statham A5-500-350) and Specimen After Impact (AD-10-0-c)

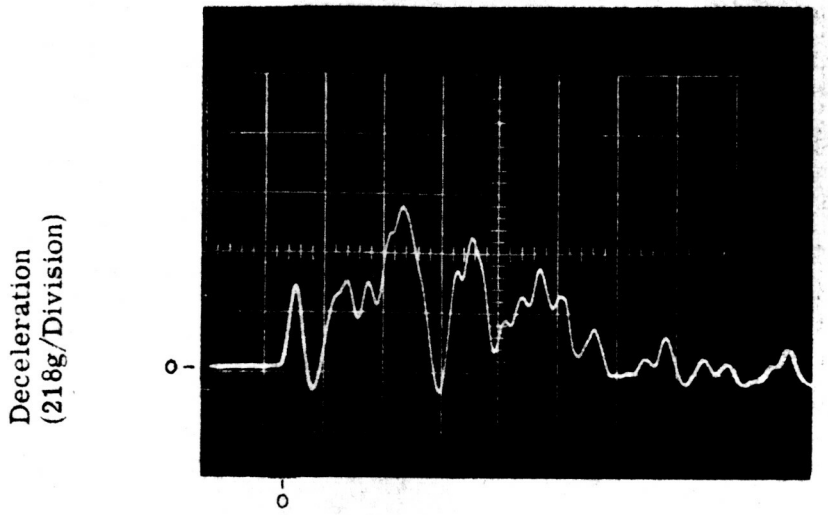

Time After Response Initiation
(1 Millisecond/Division)

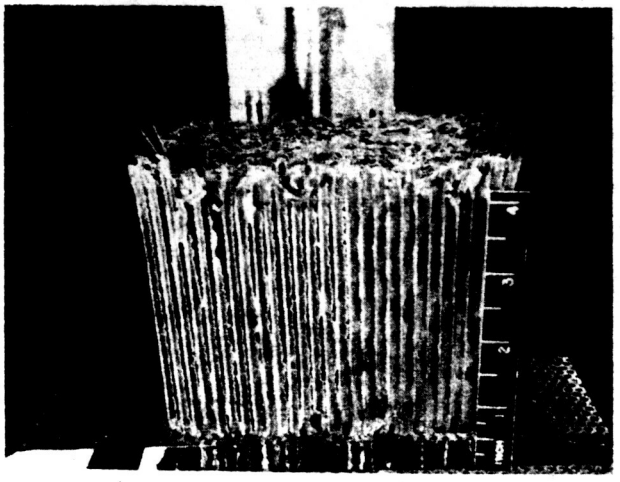

Impact Velocity - 36 ft/sec
Energy Absorbed - 1474 lb. ft.
Initial Length - 5 in.
Final Length - 4.06 in.

Figure C-18. Accelerometer Record (Statham A5-500-350) and Specimen After Impact (AD-10-45-a)

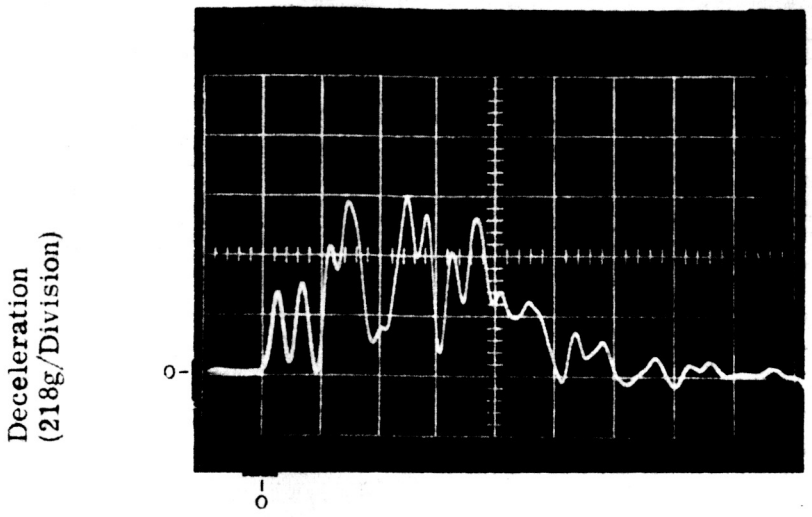

Time After Response Initiation
(1 Millisecond/Division)

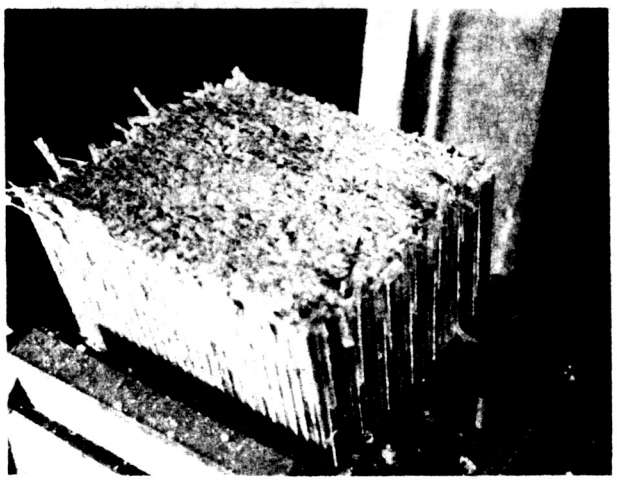

Impact Velocity - 46 ft/sec
Energy Absorbed - 2432 lb. ft.
Initial Length - 5 in.
Final Length - 3.88 in.

Figure C-19. Accelerometer Record (Statham A5-500-350) and Specimen After Impact (AD-10-45-b)

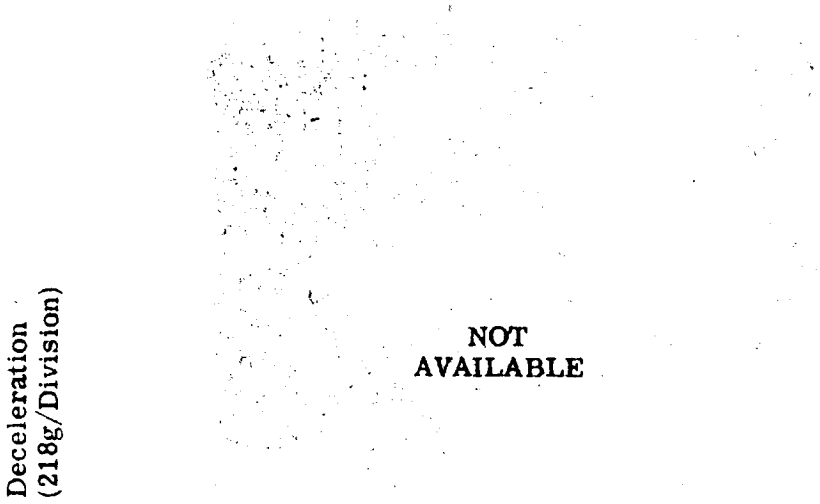

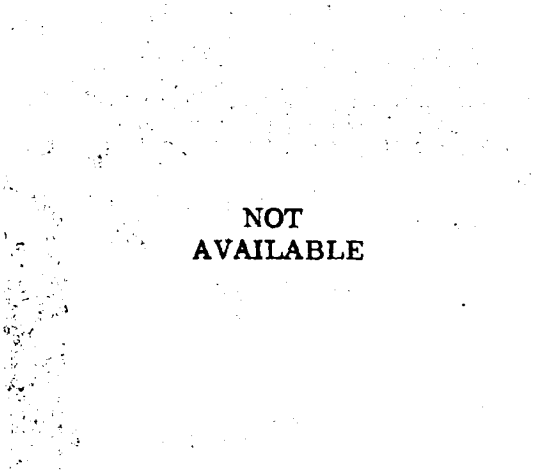

Impact Velocity - 46 ft/sec
Energy Absorbed - 2432 lb. ft.
Initial Length - 5 in.
Final Length - Collapsed

Figure C-20. Accelerometer Record (Statham A5-500-350) and Specimen After Impact (AD-20-45-a)

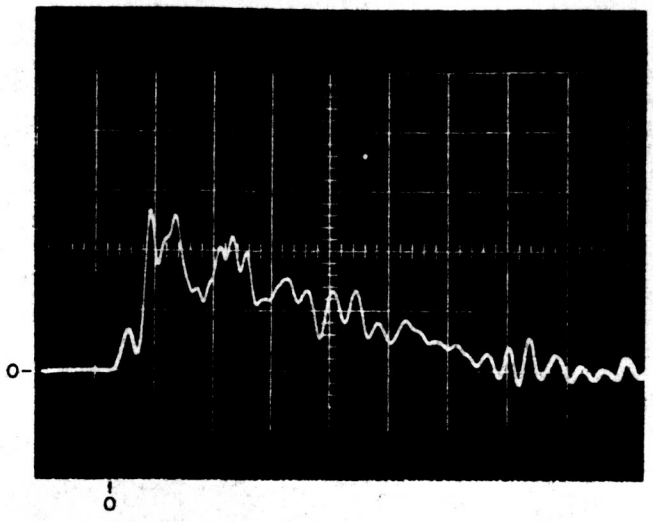

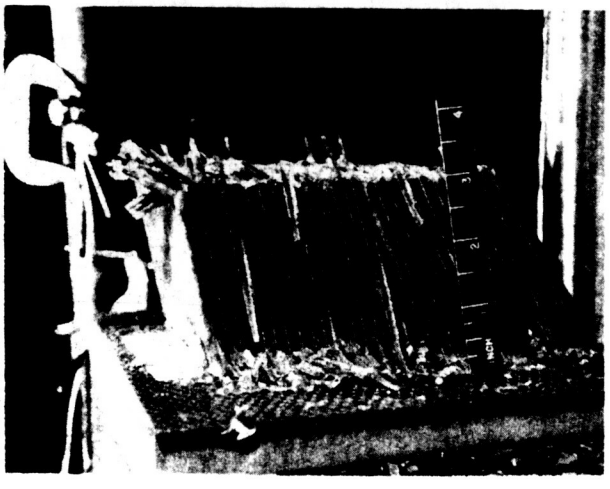

Impact Velocity - 46 ft/sec
Energy Absorbed - 2432 lb. ft.
Initial Length - 3.94 in.
Final Length - 2.81 in.

Figure C-21. Accelerometer Record (Statham A5-500-350) and Specimen After Impact (AD-10-45-c2)

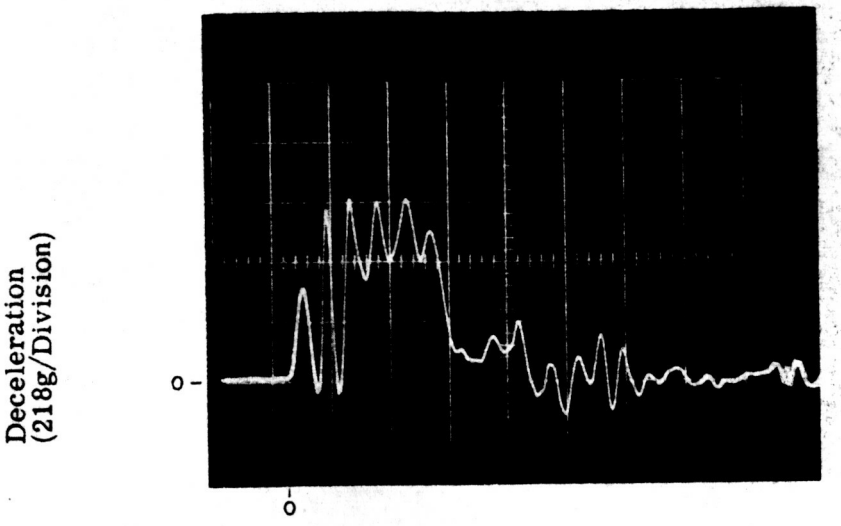

Time After Response Initiation
(1 Millisecond/Division)

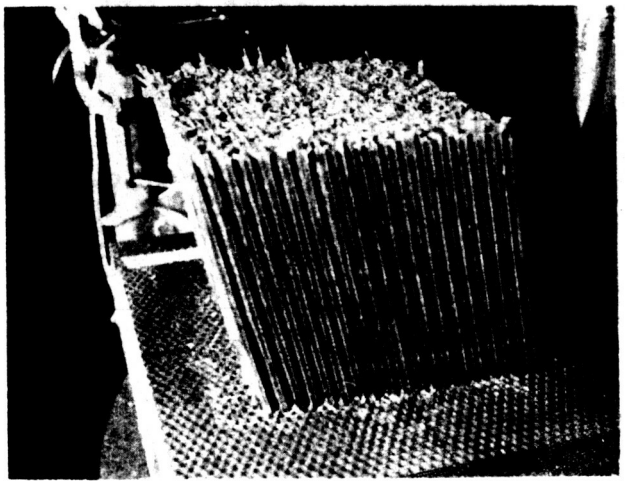

Impact Velocity - 36 ft/sec
Energy Absorbed - 1474 lb. ft.
Initial Length - 5 in.
Final Length - 4.56 in.

Figure C-22. Accelerometer Record (Statham A5-500-350) and Specimen After Impact (AD-10-90-a)

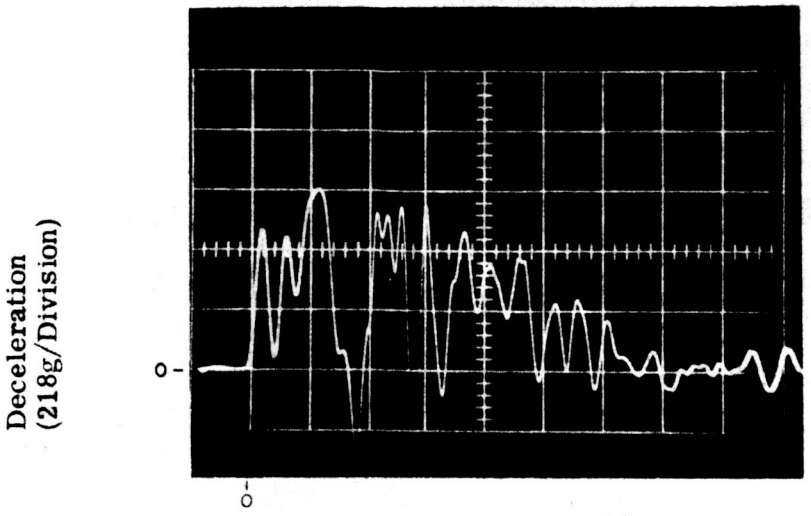

Time After Response Initiation
(1 Millisecond/Division)

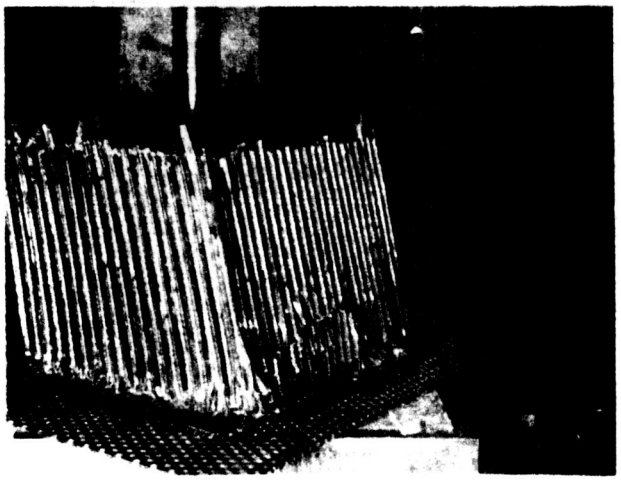

Impact Velocity - 46 ft/sec
Energy Absorbed - 2432 lb. ft.
Initial Length - 5 in.
Final Length - 3.88 in.

Figure C-23. Accelerometer Record (Statham A5-500-350) and Specimen After Impact (AD-10-90-b)

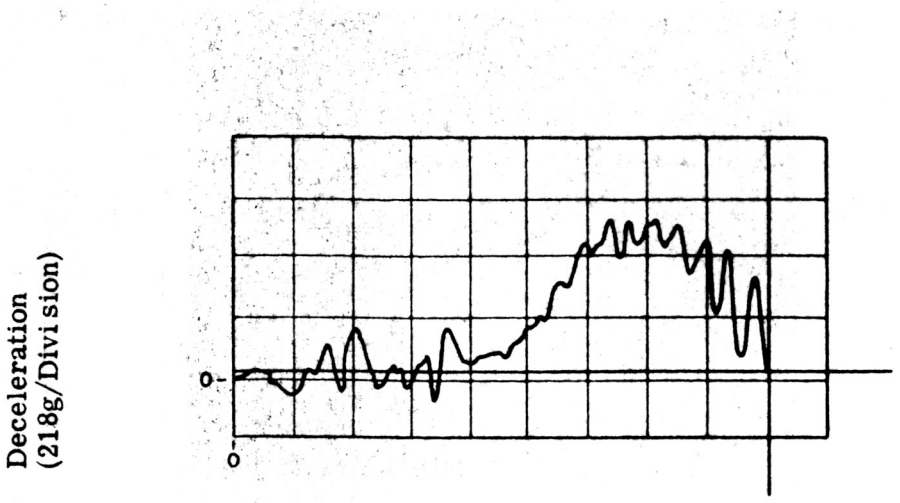

Time After Response Initiation
(1 Millisecond/Division)

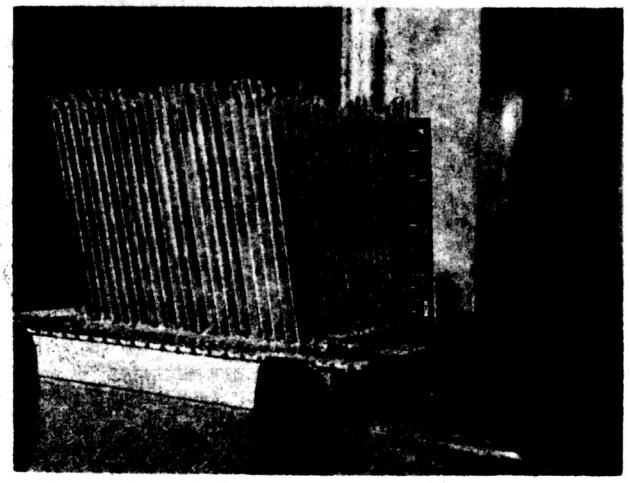

Impact Velocity - 46 ft/sec
Energy Absorbed - 2432 lb. ft.
Initial Length - 5 in.
Final Length 4.12 in.

Figure C-24. Accelerometer Record (Statham A5-500-350) and Specimen After Impact (AD-10-90-c)

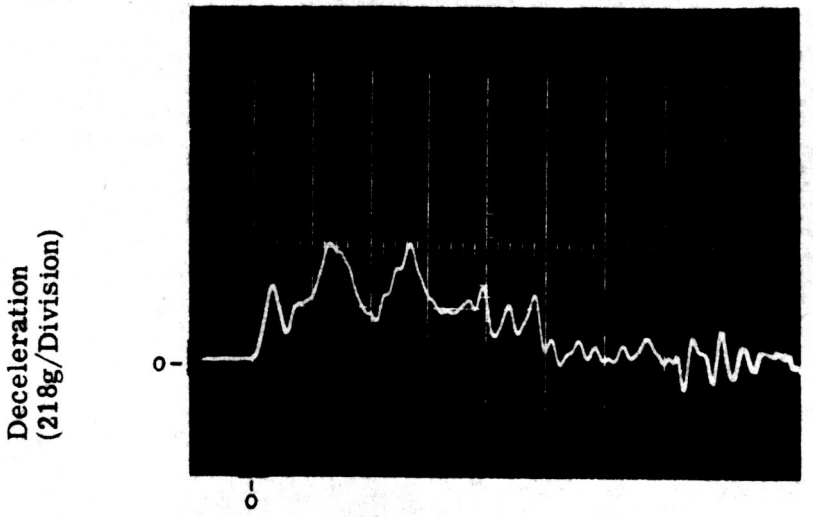

Time After Response Initiation
(1 Millisecond/Division)

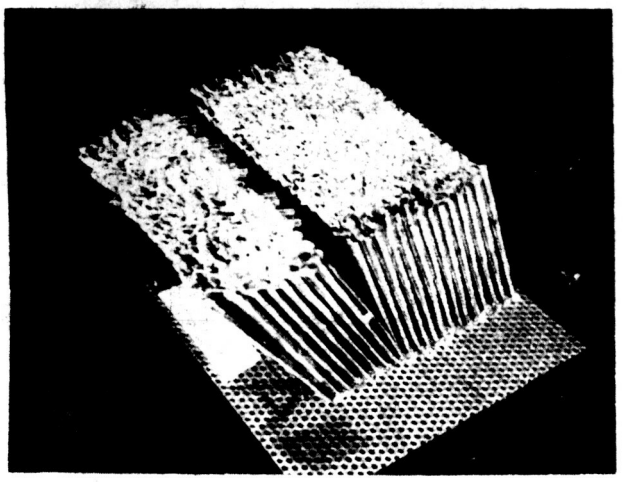

Impact Velocity - 36 ft/sec
Energy Absorbed - 1474 lb. ft.
Initial Length - 5 in.
Final Length - 4.25 in.

Figure C-25. Accelerometer Record (Statham A5-500-350) and Specimen After Impact (AD-20-0-a)

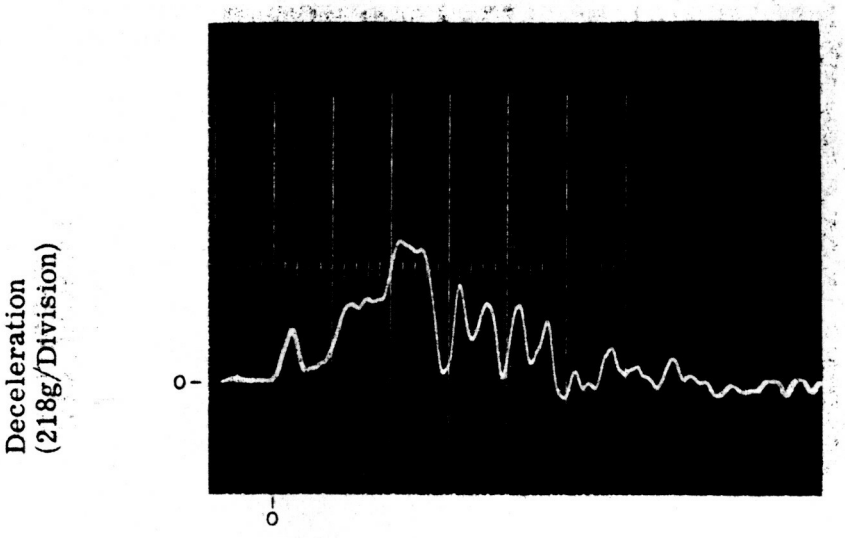

Time After Response Initiation
(1 Millisecond/Division)

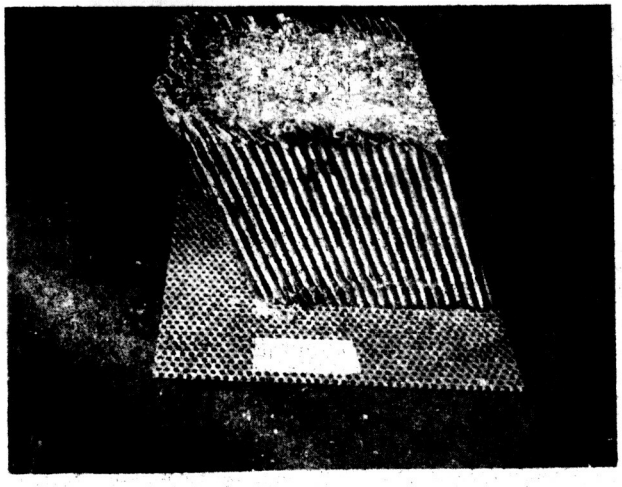

Impact Velocity - 31 ft/sec
Energy Absorbed - 1106 lb. ft.
Initial Length - 5 in.
Final Length - 4.38 in.

Figure C-26. Accelerometer Record (Statham A5-500-350) and Specimen After Impact (AD-20-0-b)

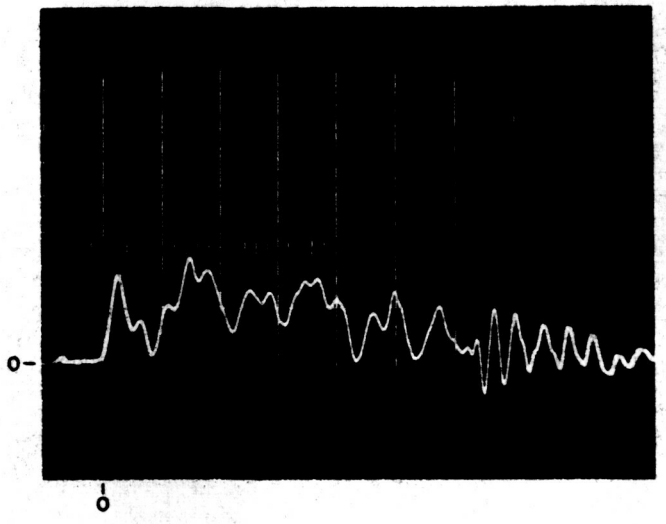

Time After Response Initiation
(1 Millisecond/Division)

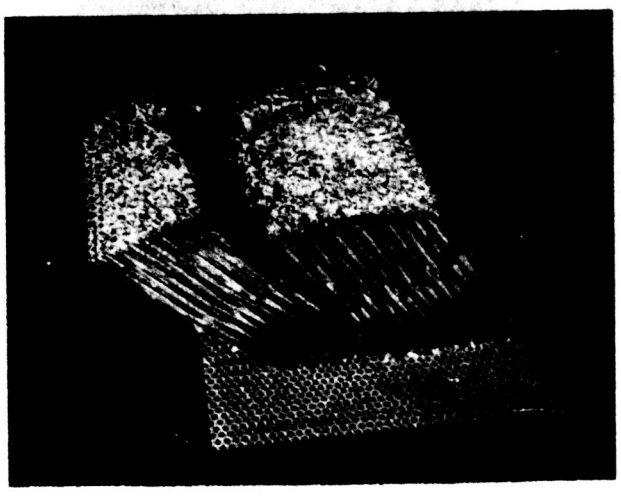

Impact Velocity - 36 ft/sec
Energy Absorbed - 1474 lb. ft.
Initial Length - 5 in.
Final Length -

Figure C-27. Accelerometer Record (Statham A5-500-350) and Specimen After Impact (AD-20-0-c)

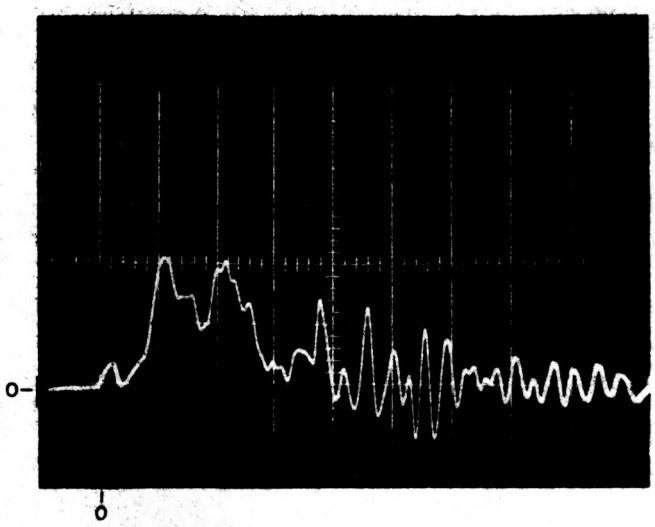

Time After Response Initiation
(1 Millisecond/Division)

Impact Velocity - 46 ft/sec
Energy Absorbed - 2432 lb. ft.
Initial Length - 5 in.
Final Length - Collapsed

Figure C-28. Accelerometer Record (Statham A5-500-350) and Specimen After Impact (AD-20-45-a)

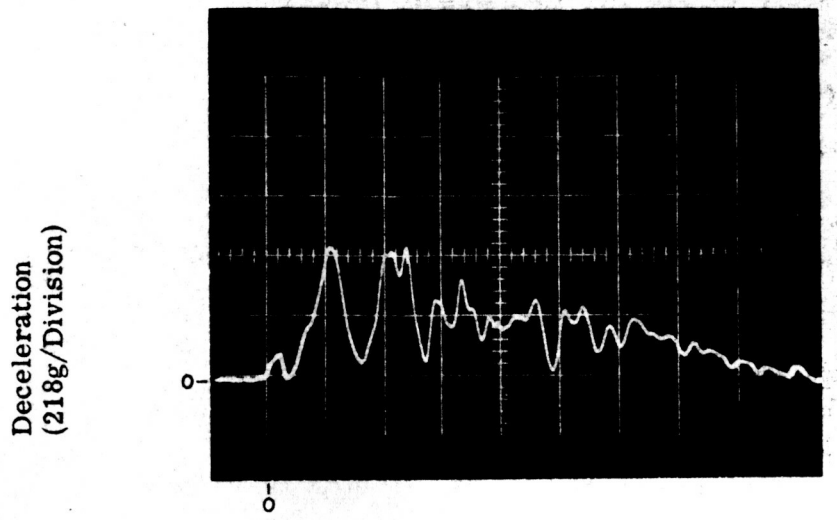

Time After Response Initiation
(1 Millisecond/Division)

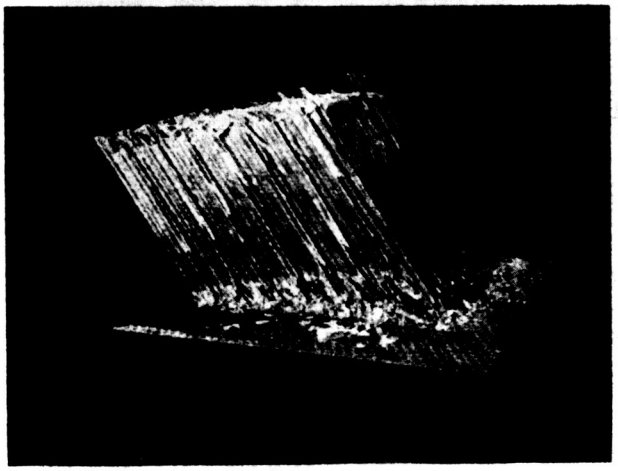

Impact Velocity - 46 ft/sec
Energy Absorbed - 2432 lb. ft.
Initial Length - 5 in.
Final Length - 3.50 in.

Figure C-29. Accelerometer Record (Statham A5-500-350) and Specimen After Impact (AD-20-45-b)

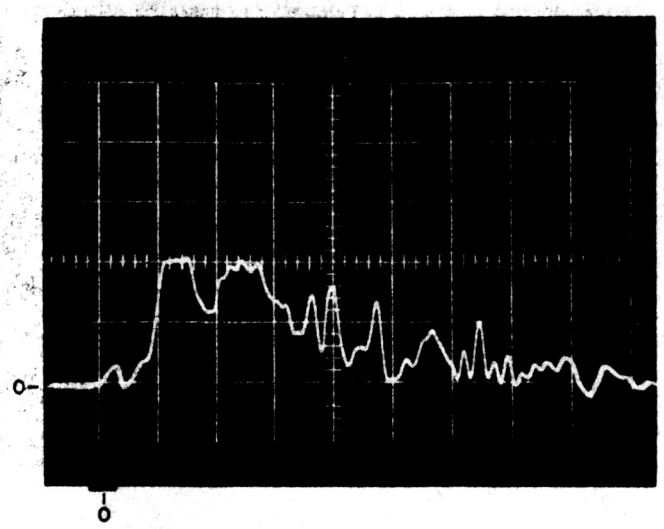

Impact Velocity - 46 ft/sec
Energy Absorbed - 2432 lb. ft.
Initial Length - 5 in.
Final Length - 3.62 in.

Figure C-30. Accelerometer Record (Statham A5-500-350) and Specimen After Impact (AD-20-45-c)

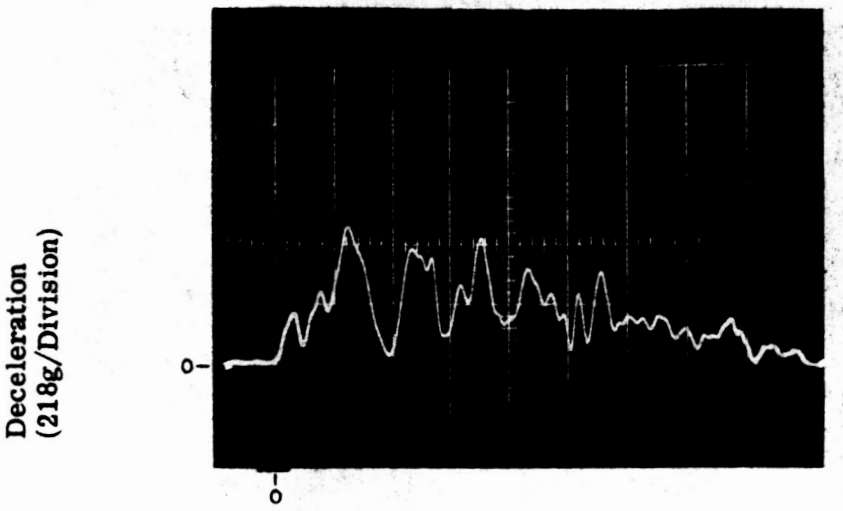

Time After Response Initiation
(1 Millisecond/Division)

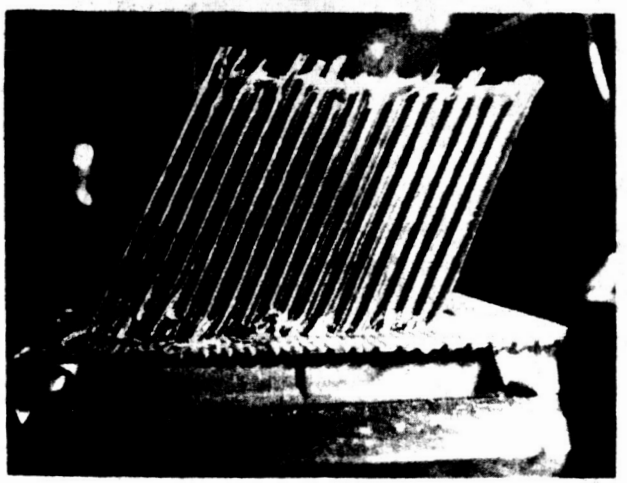

Impact Velocity - 46 ft/sec
Energy Absorbed - 2432 lb. ft.
Initial Length - 5 in.
Final Length - 3.69 in.

Figure C-31. Accelerometer Record (Statham A5-500-350) and Specimen After Impact (AD-20-90-a)

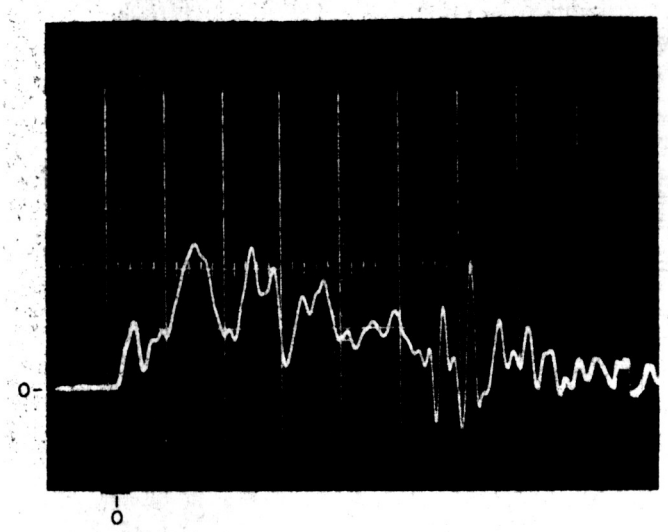

Time After Response Initiation
(1 Millisecond/Division)

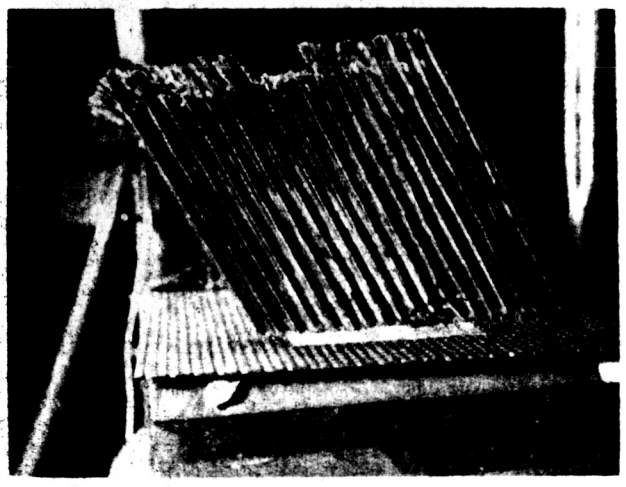

Impact Velocity - 46 ft/sec
Energy Absorbed - 2432 lb. ft.
Initial Length - 5 in.
Final Length - 4 in.

Figure C-32. Accelerometer Record (Statham A5-500-350) and Specimen After Impact (AD-20-90-c)

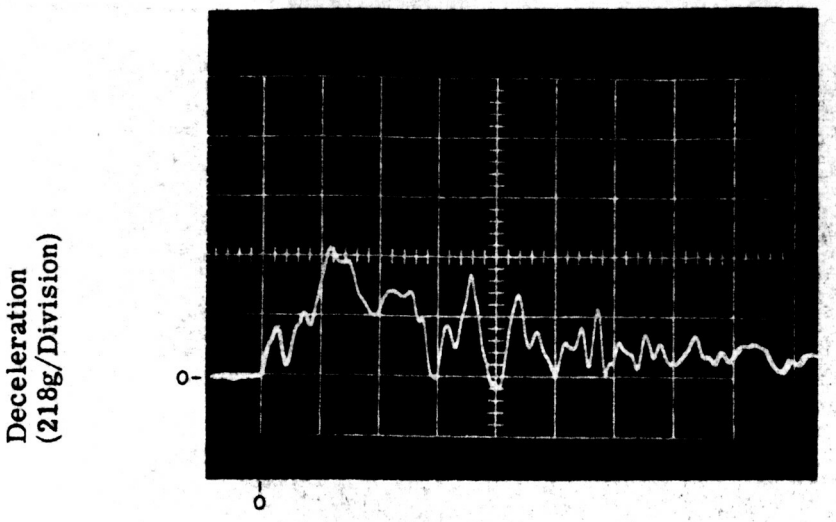

Time After Response Initiation
(1 Millisecond/Division)

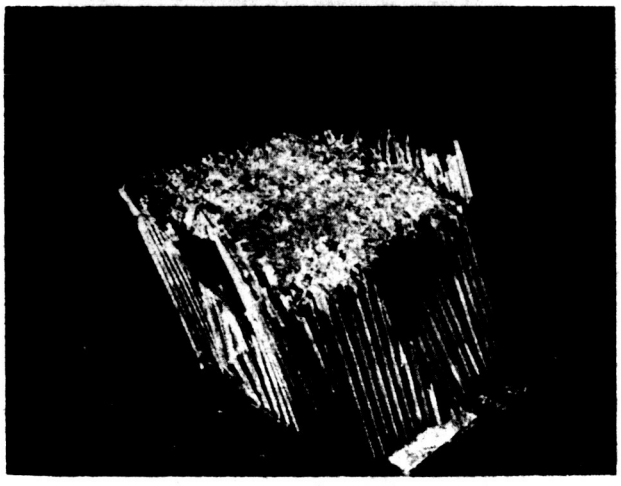

Impact Velocity - 46 ft/sec
Energy Absorbed - 2432 lb. ft.
Initial Length - 5 in.
Final Length - 3.75 in.

Figure C-33. Accelerometer Record (Statham A5-500-350) and Specimen After Impact (AD-20-90-b)

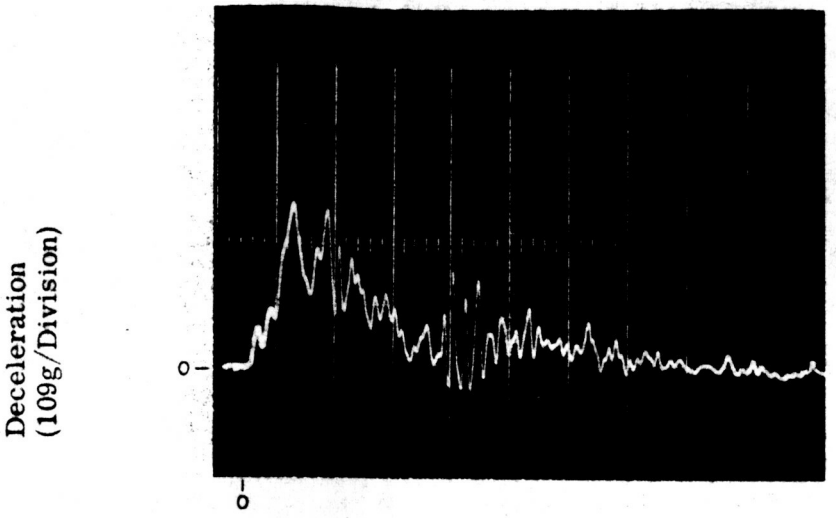

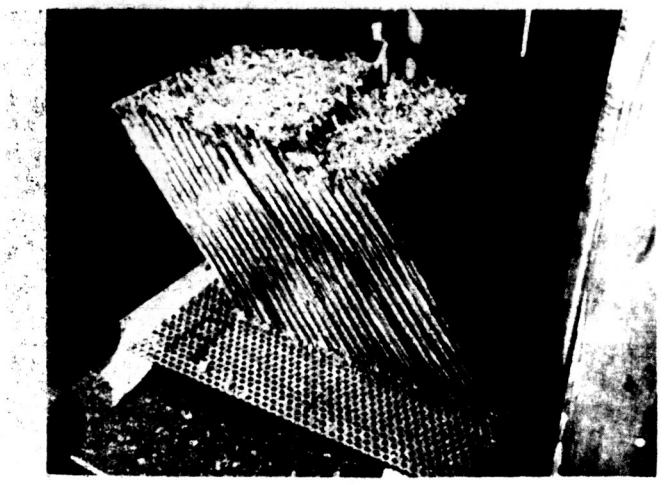

Impact Velocity - 31 ft/sec
Energy Absorbed - 1106 lb. ft.
Initial Length - 5 in.
Final Length - 4.19 in.

Figure C-34. Accelerometer Record (Statham A5-500-350) and Specimen After Impact (AD-30-0-a)

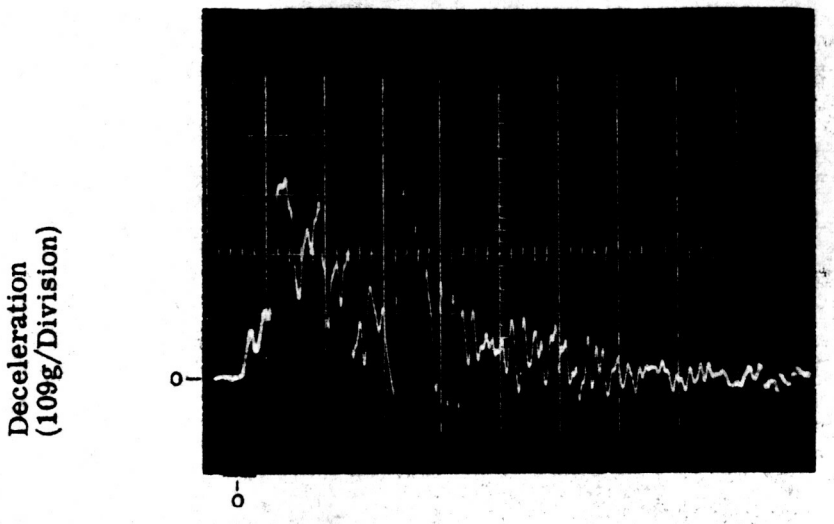

Time After Response Initiation
(2 Millisecond/Division)

Impact Velocity - 31 ft/sec
Energy Absorbed - 1106 lb. ft.
Initial Length - 5 in.
Final Length - 4.31 in.

Figure C-35. Accelerometer Record (Statham A5-500-350) and Specimen After Impact (AD-30-0-b)

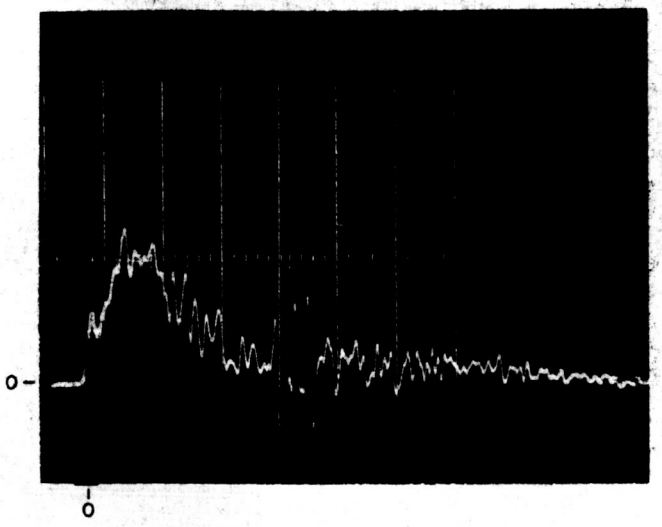

Time After Response Initiation
(2 Millisecond/Division)

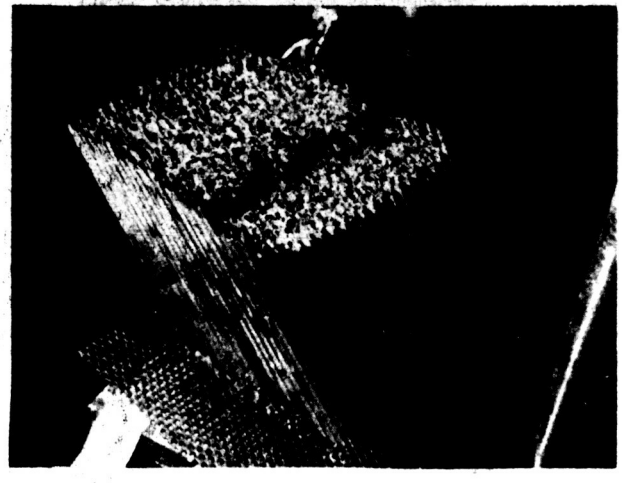

Impact Velocity - 31 ft/sec
Energy Absorbed - 1106 lb. ft.
Initial Length - 5 in.
Final Length - 4.25 in.

Figure C-36. Accelerometer Record (Statham (A5-500-350) and Specimen After Impact (AD-30-0-c)

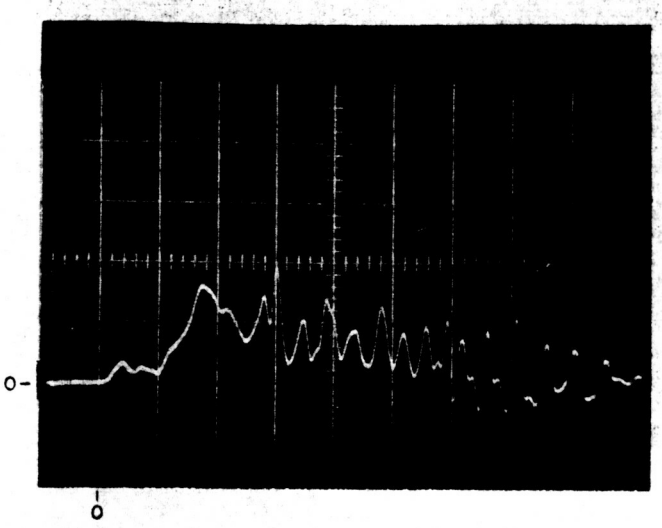

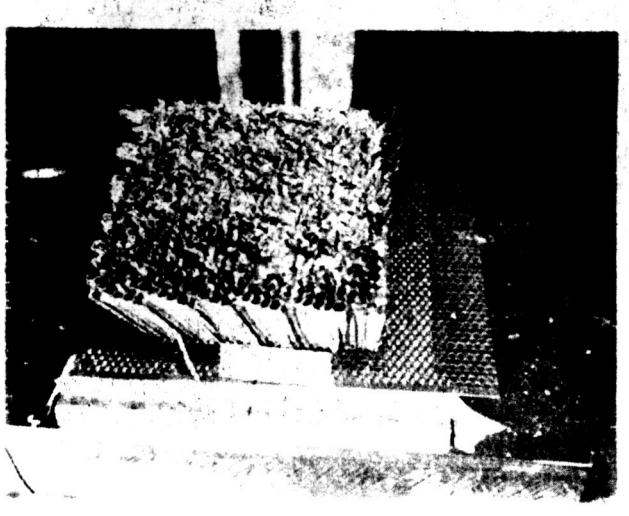

Impact Velocity - 31 ft/sec
Energy Absorbed - 1106 lb. ft.
Initial Length - 5 in.
Final Length - 4.25 in.

Figure C-37. Accelerometer Record (Statham A5-500-350) and Specimen After Impact (AD-30-45-a)

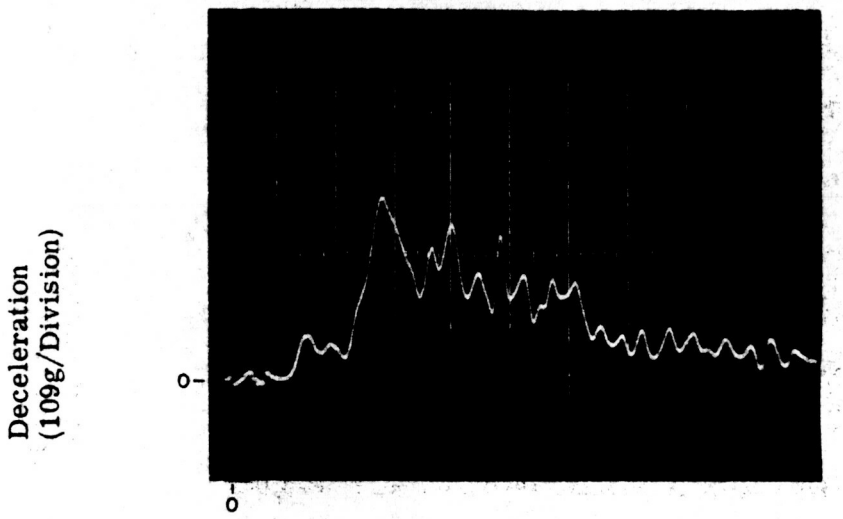

Time After Response Initiation
(1 Millisecond/Division)

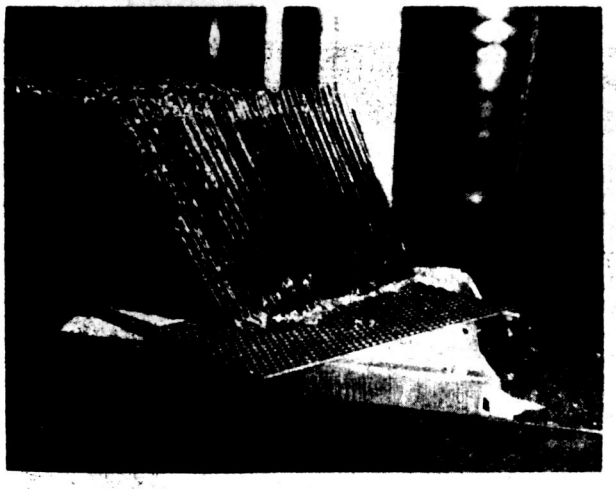

Impact Velocity - 31 ft/sec
Energy Absorbed - 1106 lb. ft.
Initial Length - 5 in.
Final Length - 4.12 in.

Figure C-38. Accelerometer Record (Statham A5-500-350) and Specimen After Impact (AD-30-45-b)

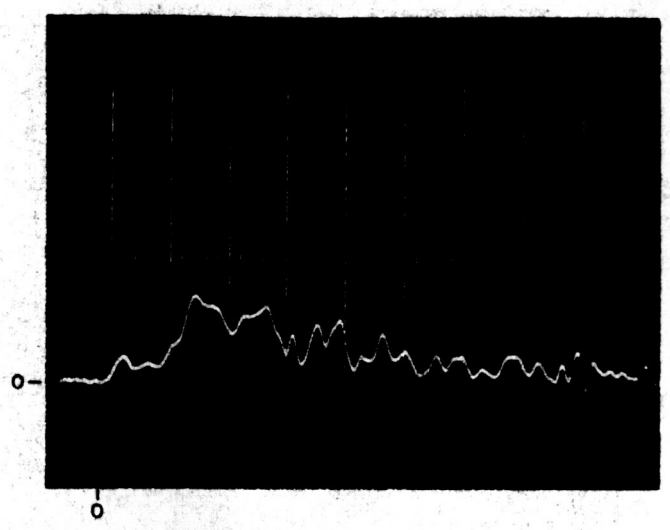

Impact Velocity - 31 ft/sec
Energy Absorbed - 1106 lb. ft.
Initial Length - 5 in.
Final Length - 4.25 in.

Figure C-39. Accelerometer Record (Statham A5-500-350) and Specimen After Impact (AD-30-45-c)

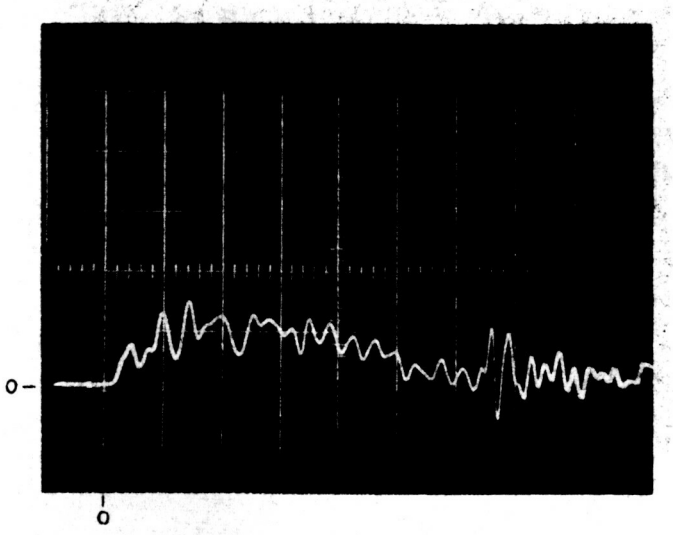

Time After Response Initiation
(1 Millisecond/Division)

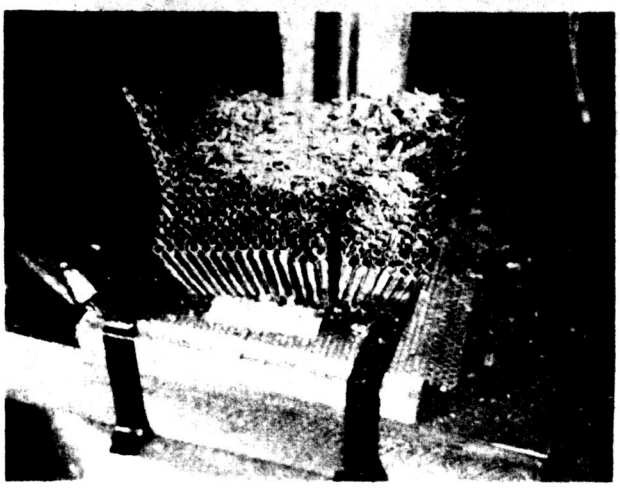

Impact Velocity - 36 ft/sec
Energy Absorbed - 1474 lb. ft.
Initial Length - 5 in.
Final Length - 4.38 in.

Figure C-40. Accelerometer Record (Statham A5-500-350) and Specimen After Impact (AD-30-90-a)

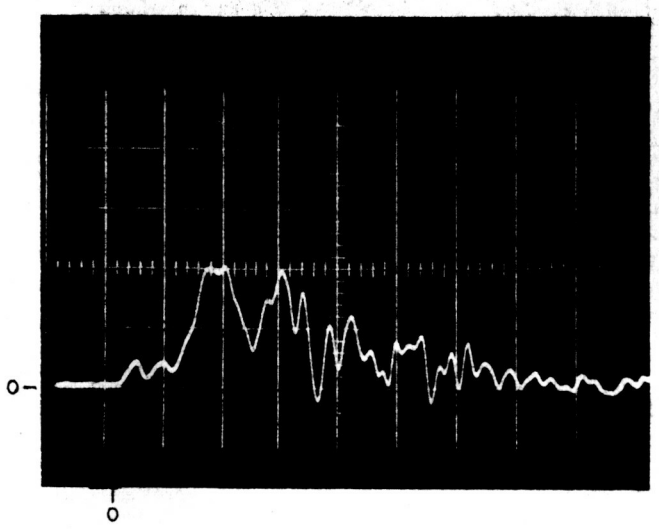

Time After Response Initiation
(1 Millisecond/Division)

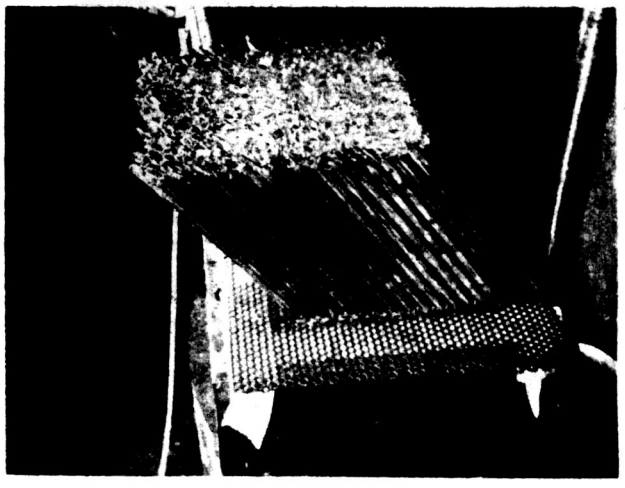

Impact Velocity - 31 ft/sec
Energy Absorbed - 1106 lb. ft.
Initial Length - 5 in.
Final Length - 4.50 in.

Figure C-41. Accelerometer Record (Statham A5-500-350) and Specimen After Impact (AD-30-90-b)

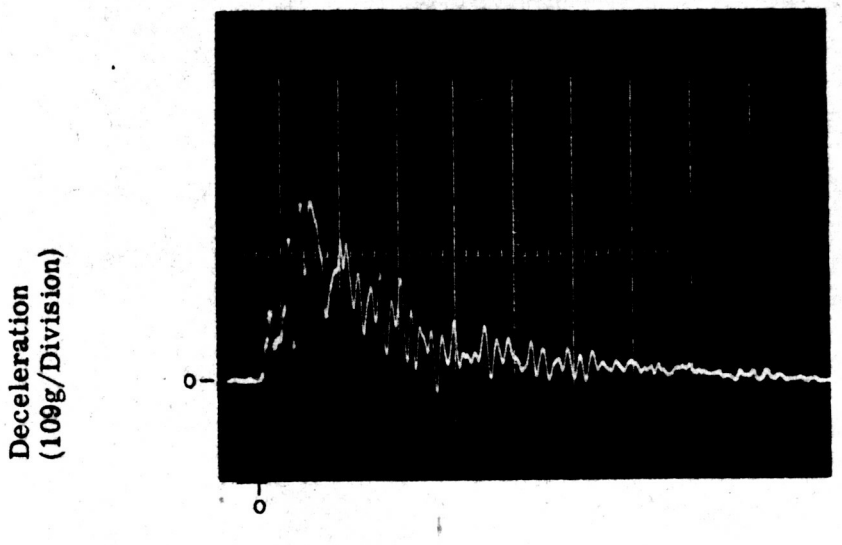

Time After Response Initiation
(2 Millisecond/Division)

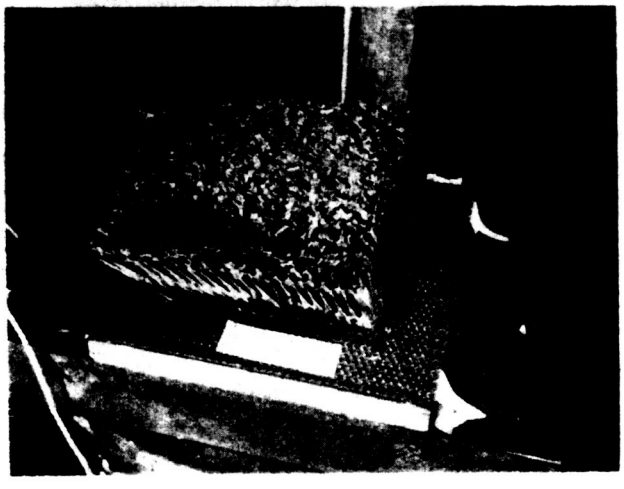

Impact Velocity - 31 ft/sec
Energy Absorbed - 1106 lb. ft.
Initial Length - 5 in.
Final Length - 4.50 in.

Figure C-42. Accelerometer Record (Statham A5-500-350) and Specimen After Impact (AD-30-90-c)

APPENDIX D

STATIC TEST LOAD-DEFLECTION DIAGRAMS

APPENDIX D. STATIC TEST LOAD-DEFLECTION DIAGRAMS

Included in this section are unretouched reproductions of the load-deflection diagrams (Figures D-1 to D-30) as recorded on the Instron Testing Machine.

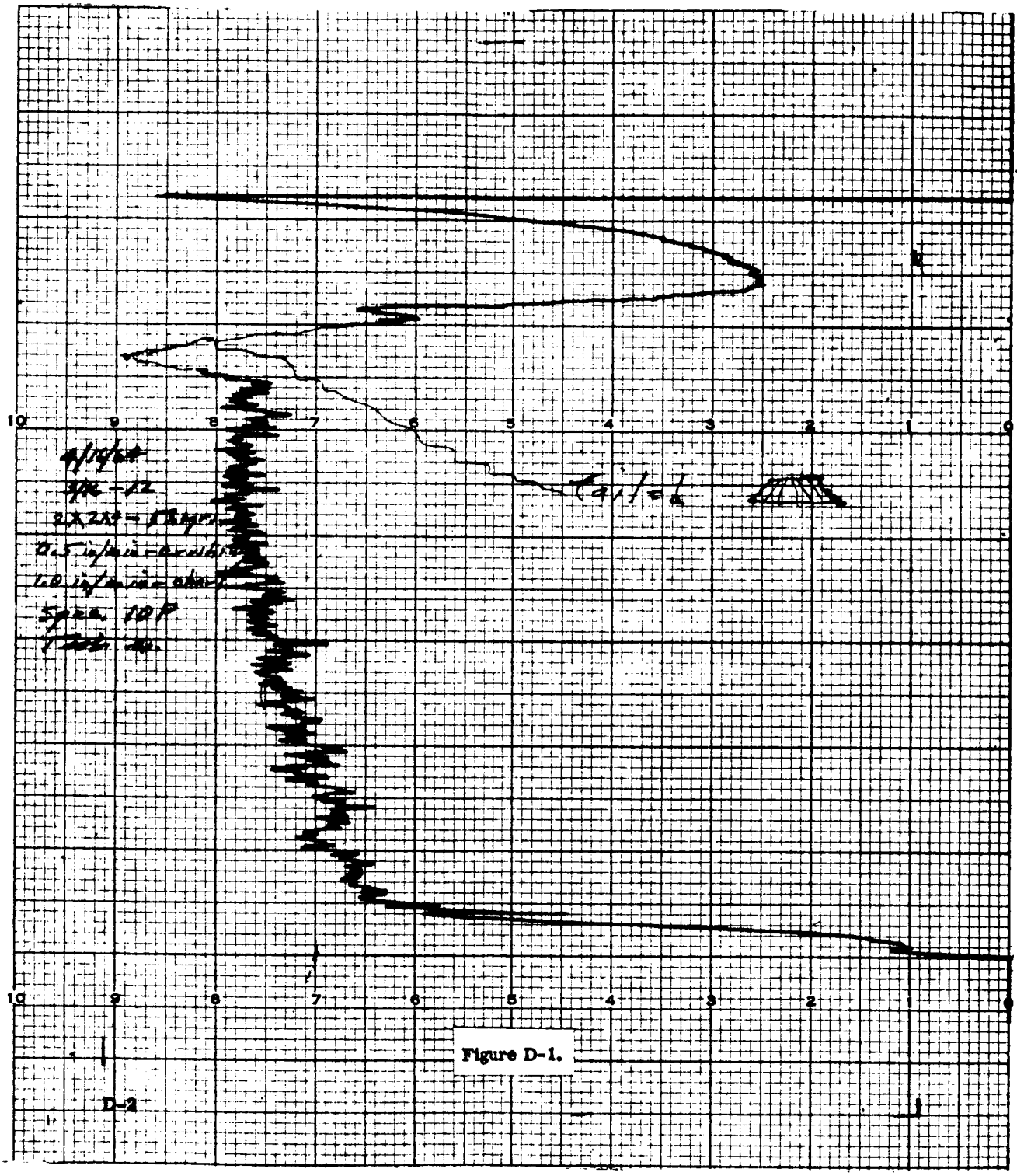

Figure D-1.

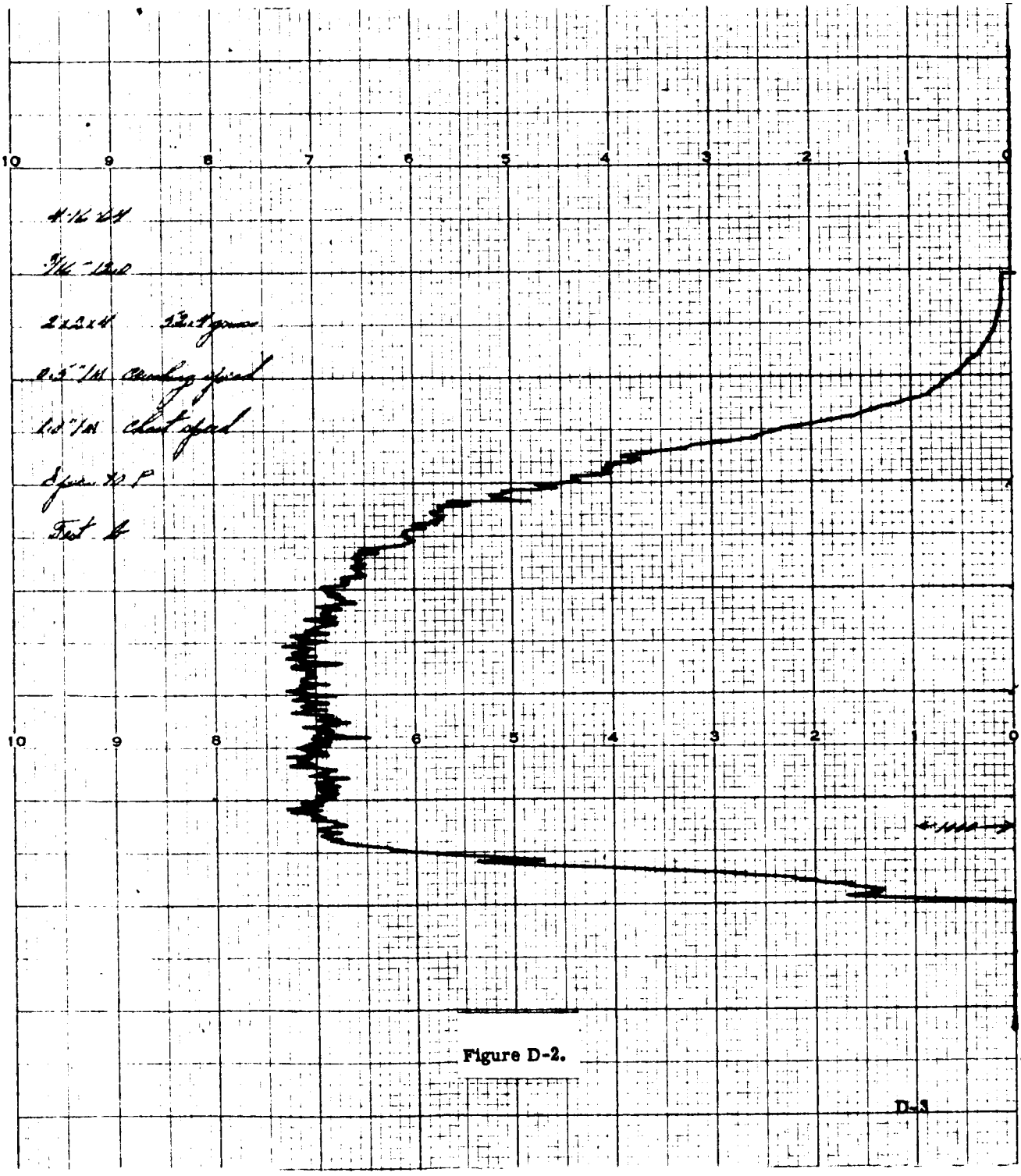
10
9
8
7
6
5
4
3
2
1
0
4-16-24
Pile Load
2x8x4 12 ft span
0.5" Ht Cantilevered
1.0" Ht Cantilevered
Span to P
Test #

Figure D-2.

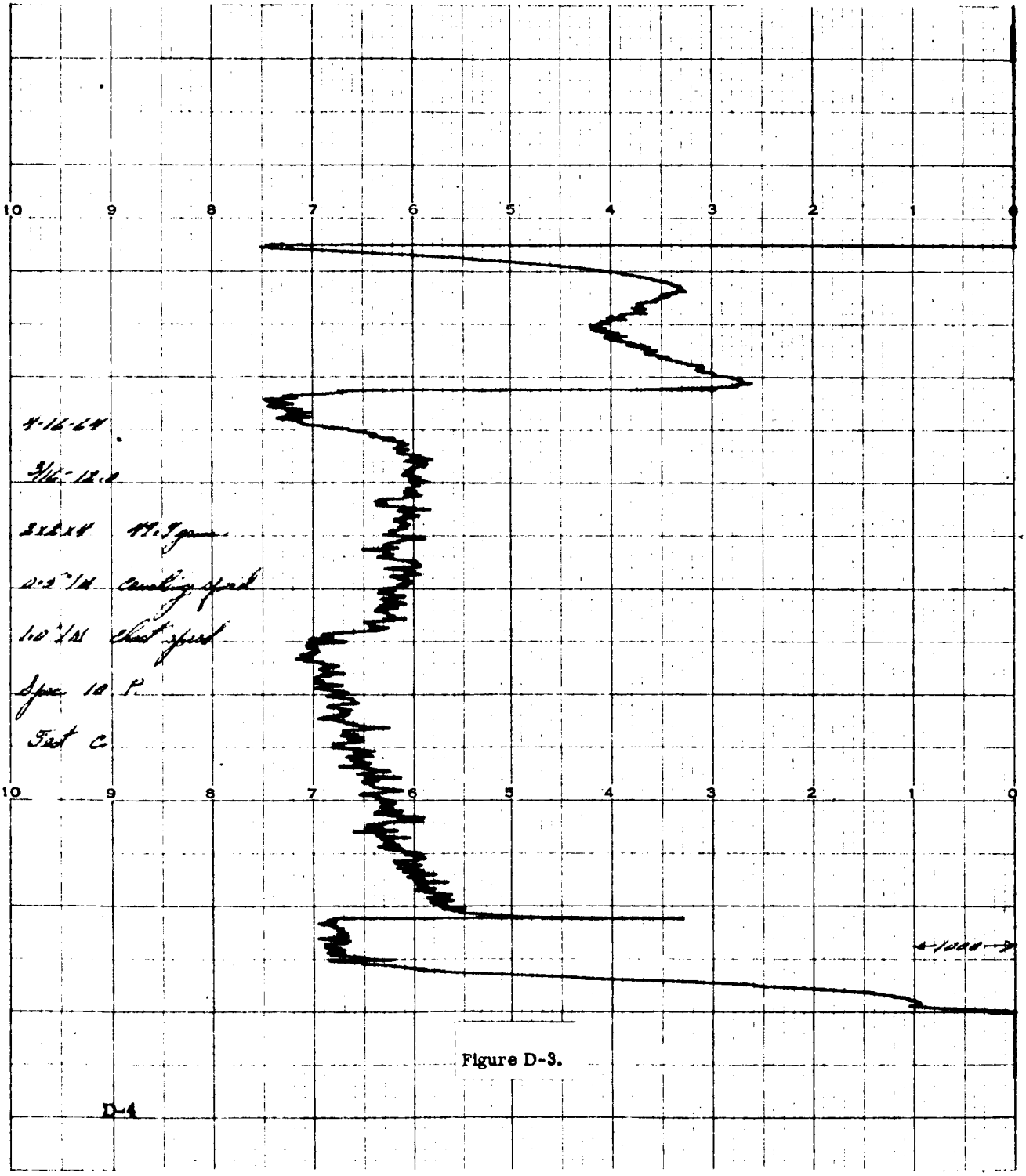
10
9
8
7
6
5
4
3
2
1
0
4-16-64
3/16-12.0
3x8x4 11.3 gpm
2-2 1/2 Centrifugal
10 1/2 Centrifugal
Span 10 P.
Test C
←1000→

Figure D-3.

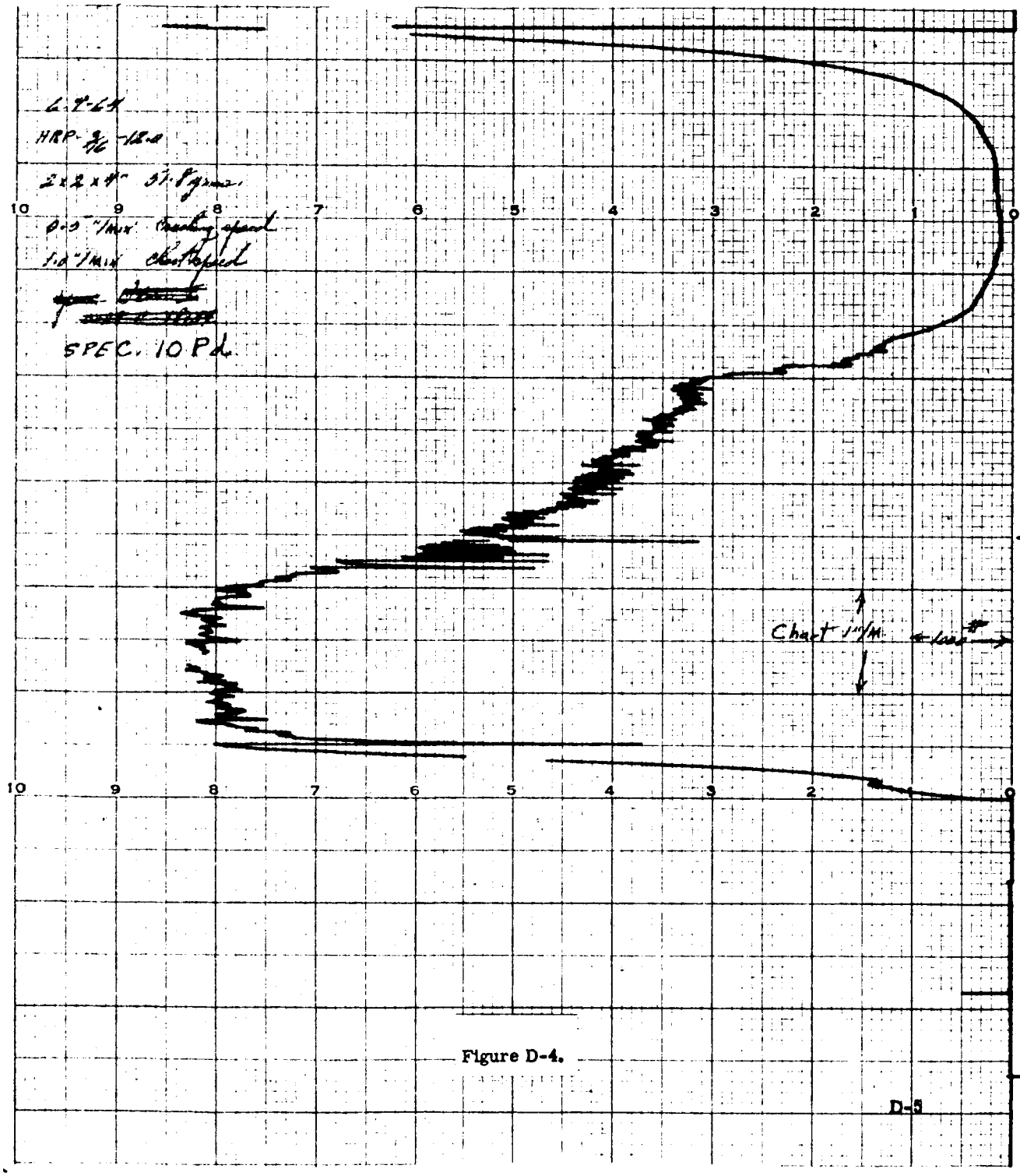
6-2-64
HRP-3/16-12.0
2x2x4" 37 figure.
10 9 8 7 6 5 4 3 2 1 0
0.9 "/min Reading speed
5.0 "/min Chart speed
SPEC. 10 Pd.
Chart 1"/M
Load
10 9 8 7 6 5 4 3 2 1 0

Figure D-4.

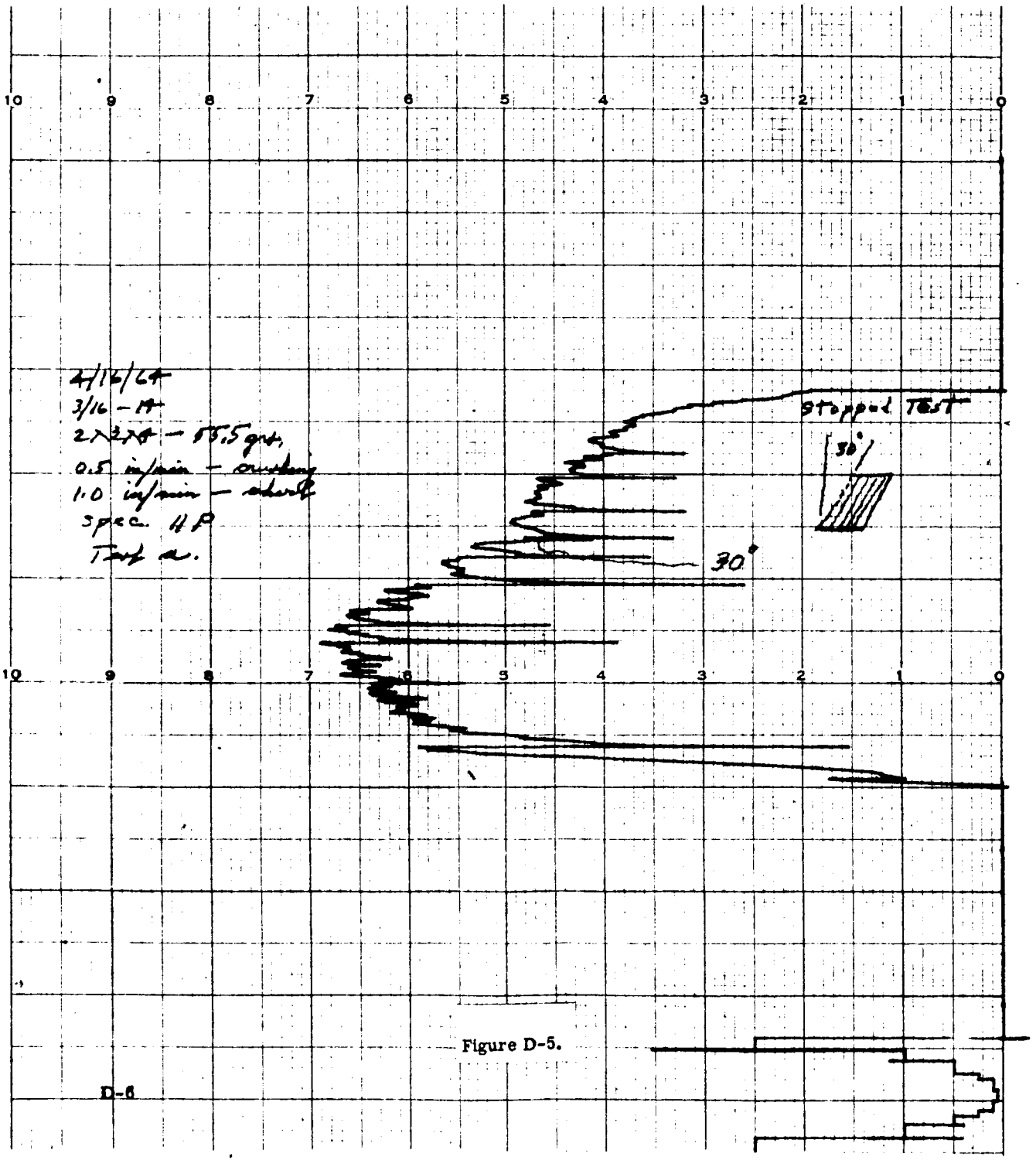

Figure D-5.

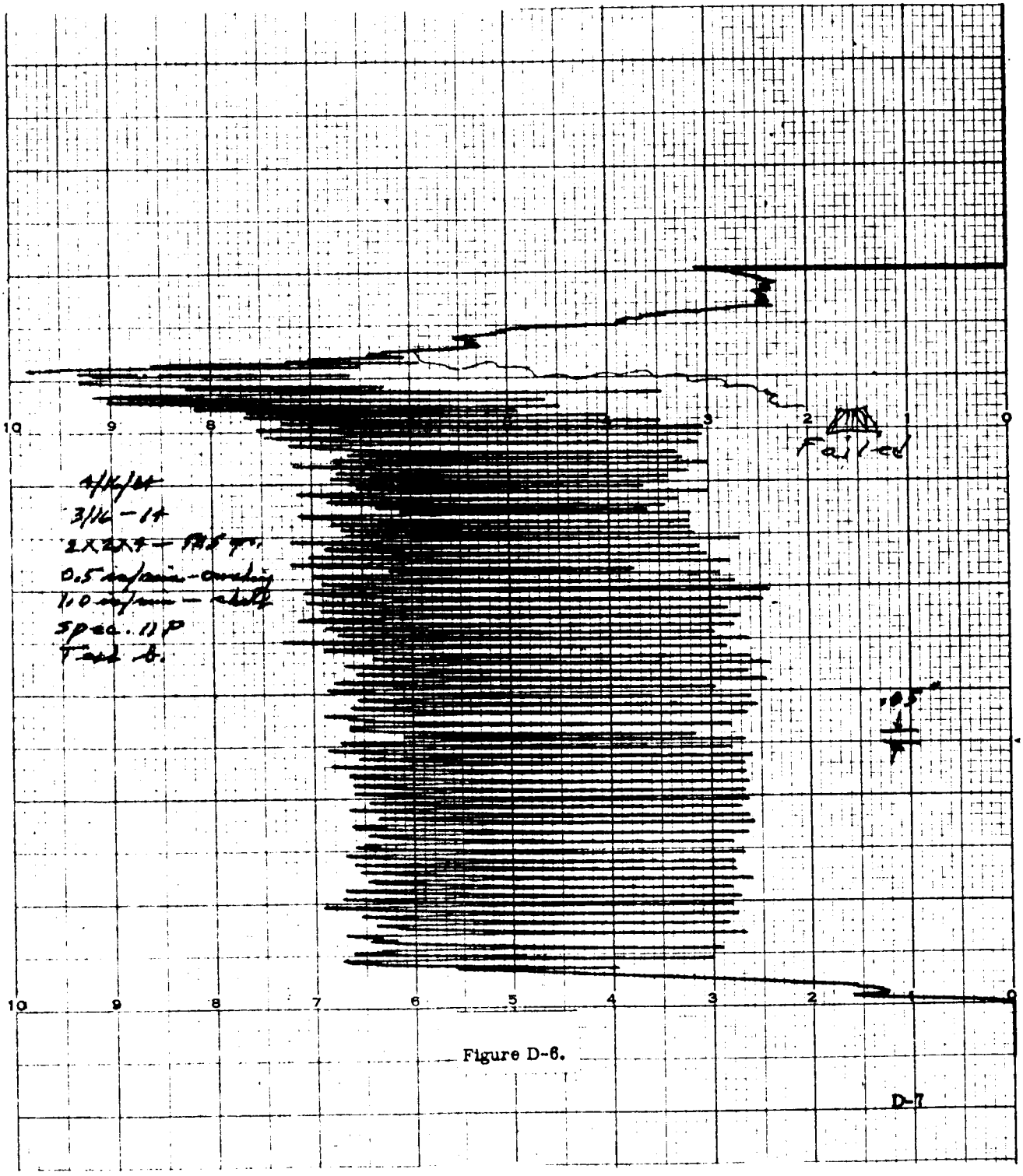

Figure D-6.

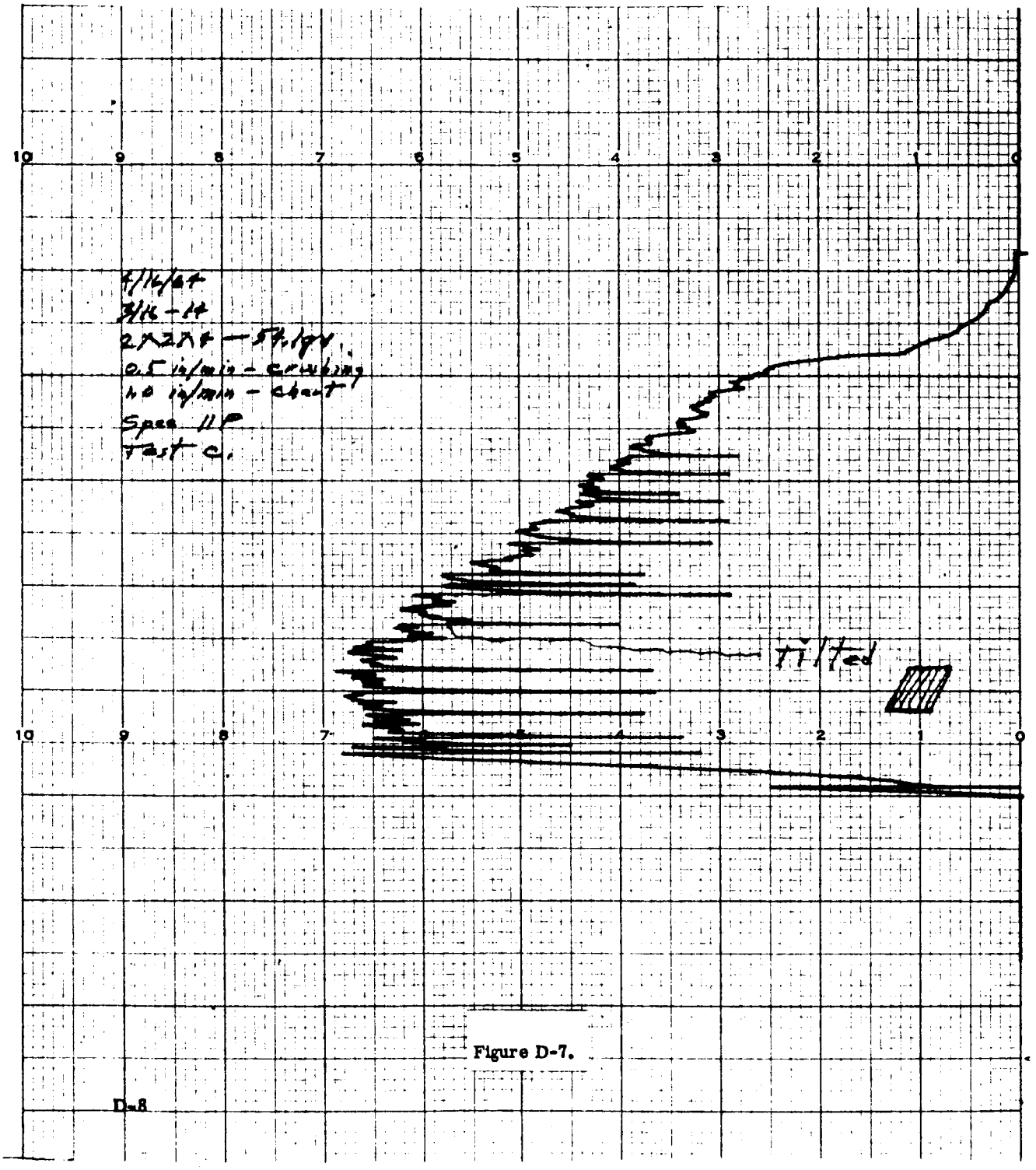

Figure D-7.

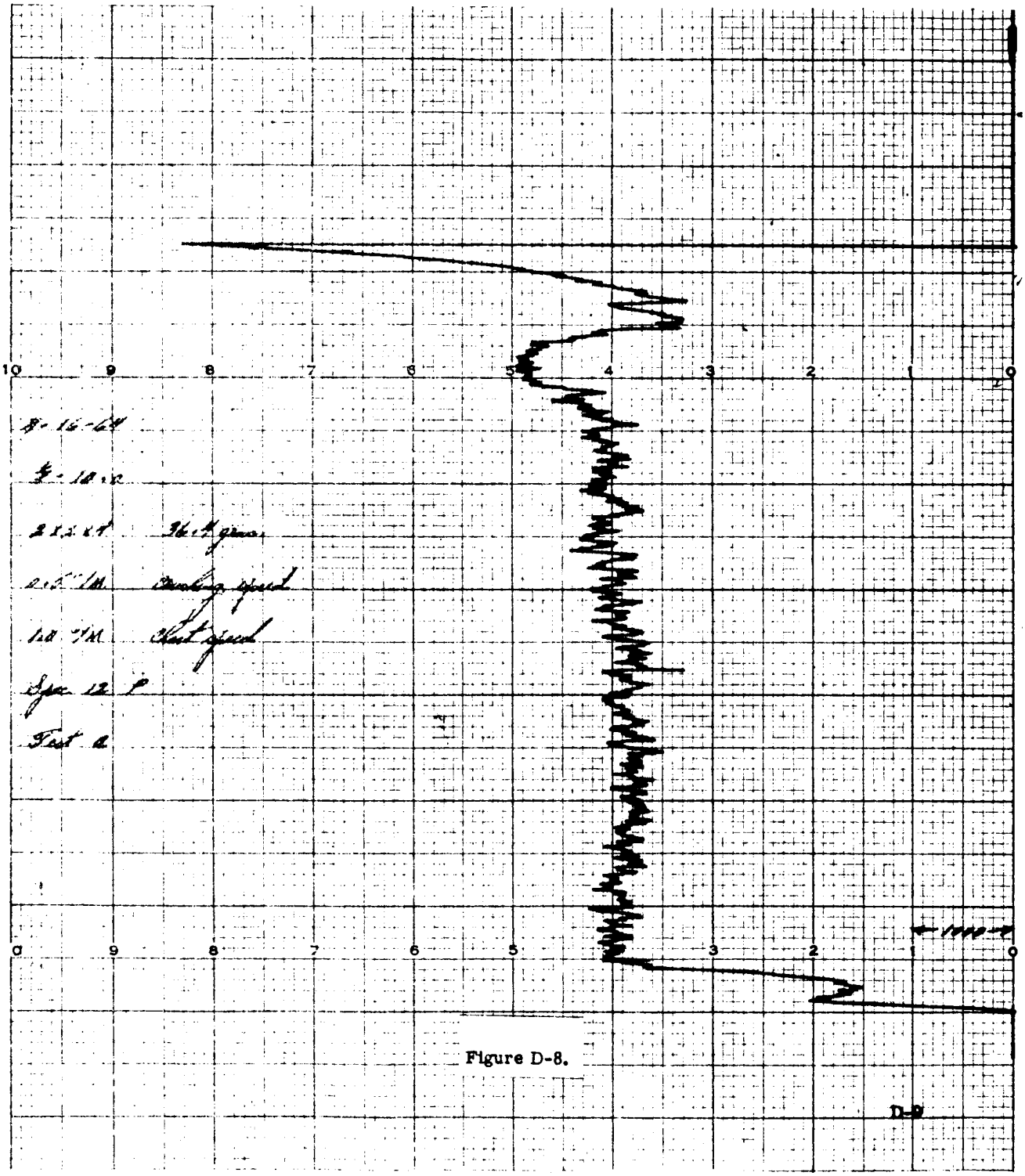
10 9 8 7 6 5 4 3 2 1 0
8-15-64
F-18 x
2 x 2 x 4 96 Hydra.
2 x 2 x 4 Analog feed
2 x 2 x 4 Heat feed
Spec 12 P
Test 2
0 9 8 7 6 5 4 3 2 1 0

Figure D-8.

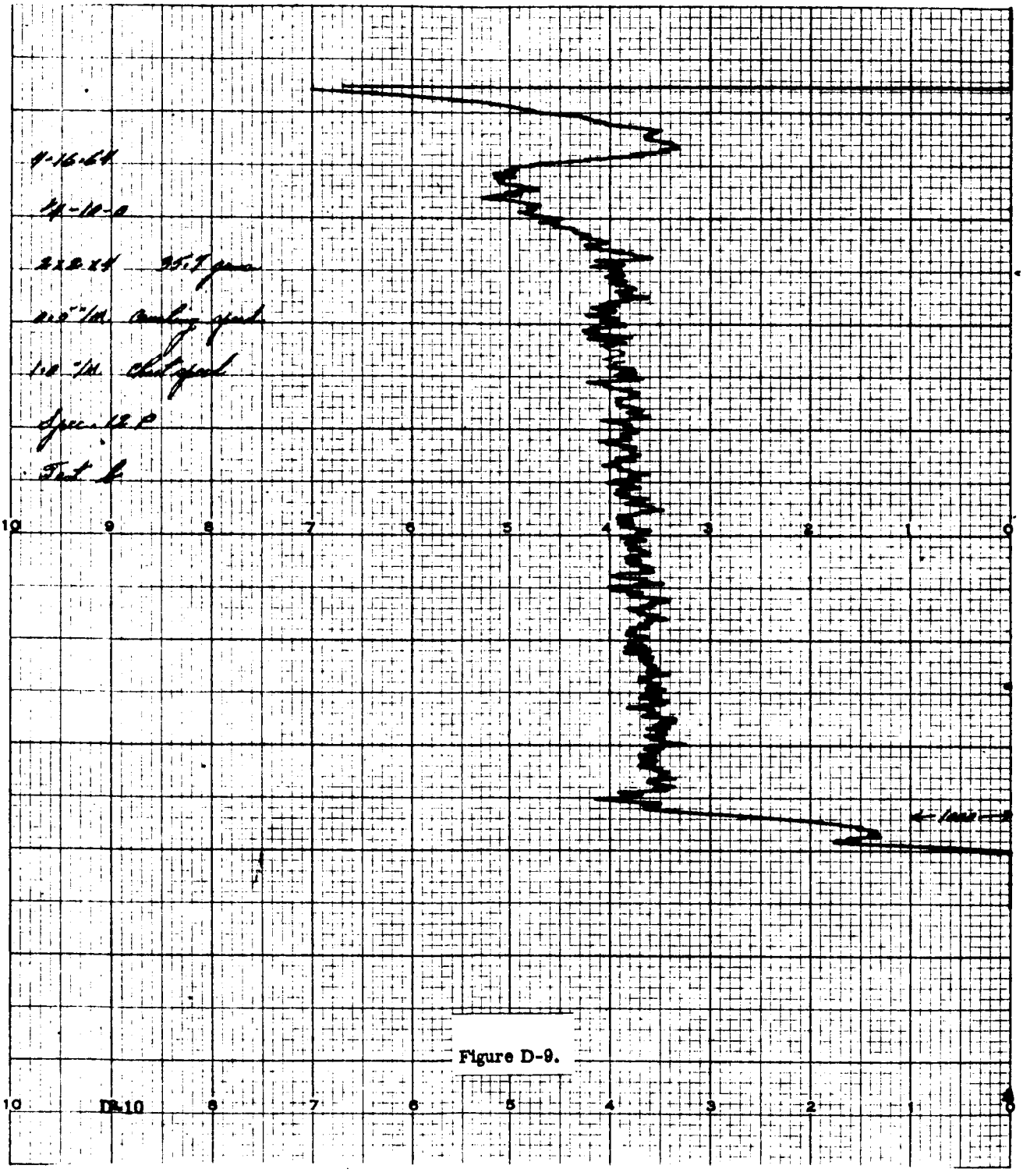

Figure D-9.

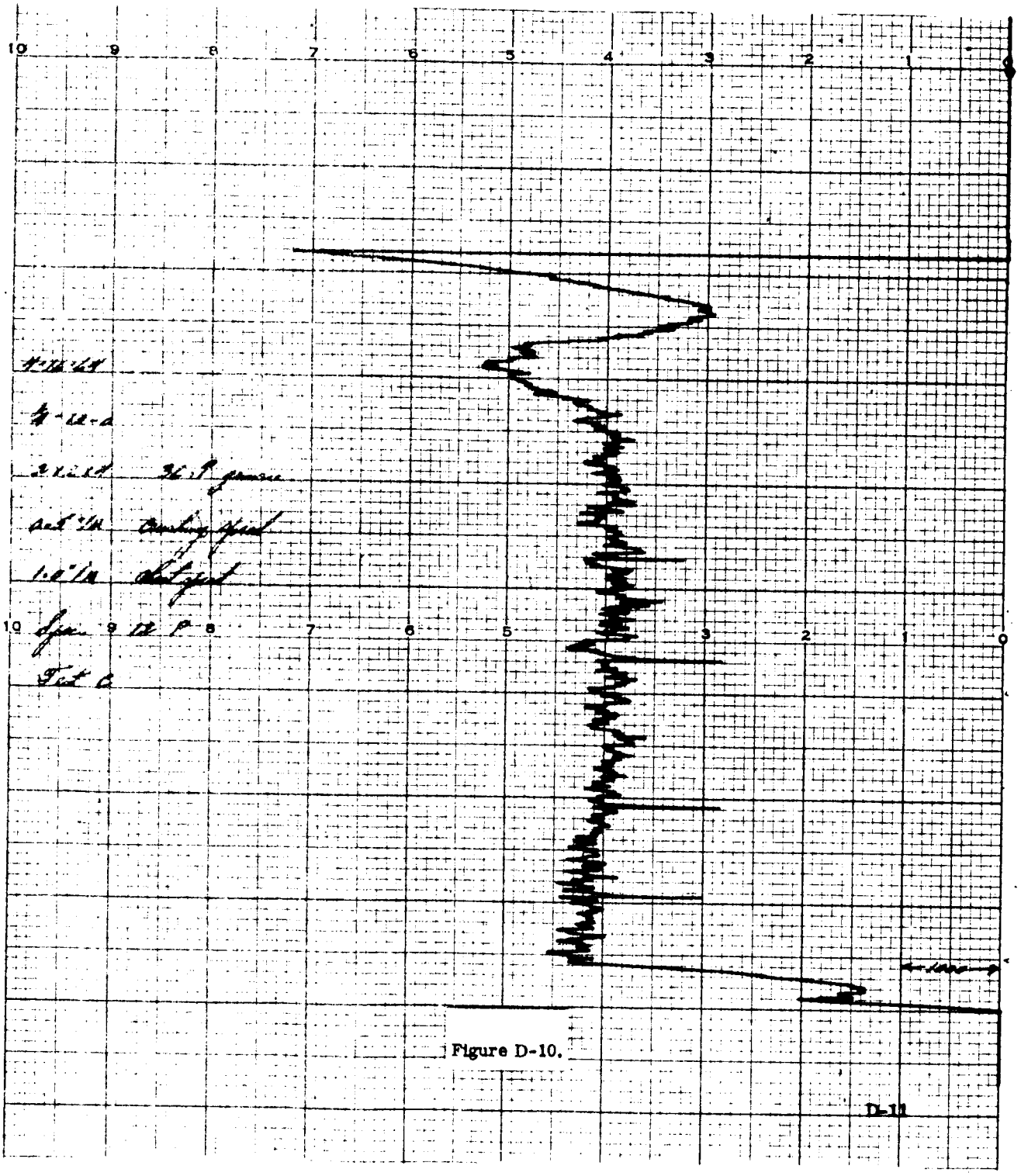

Figure D-10.

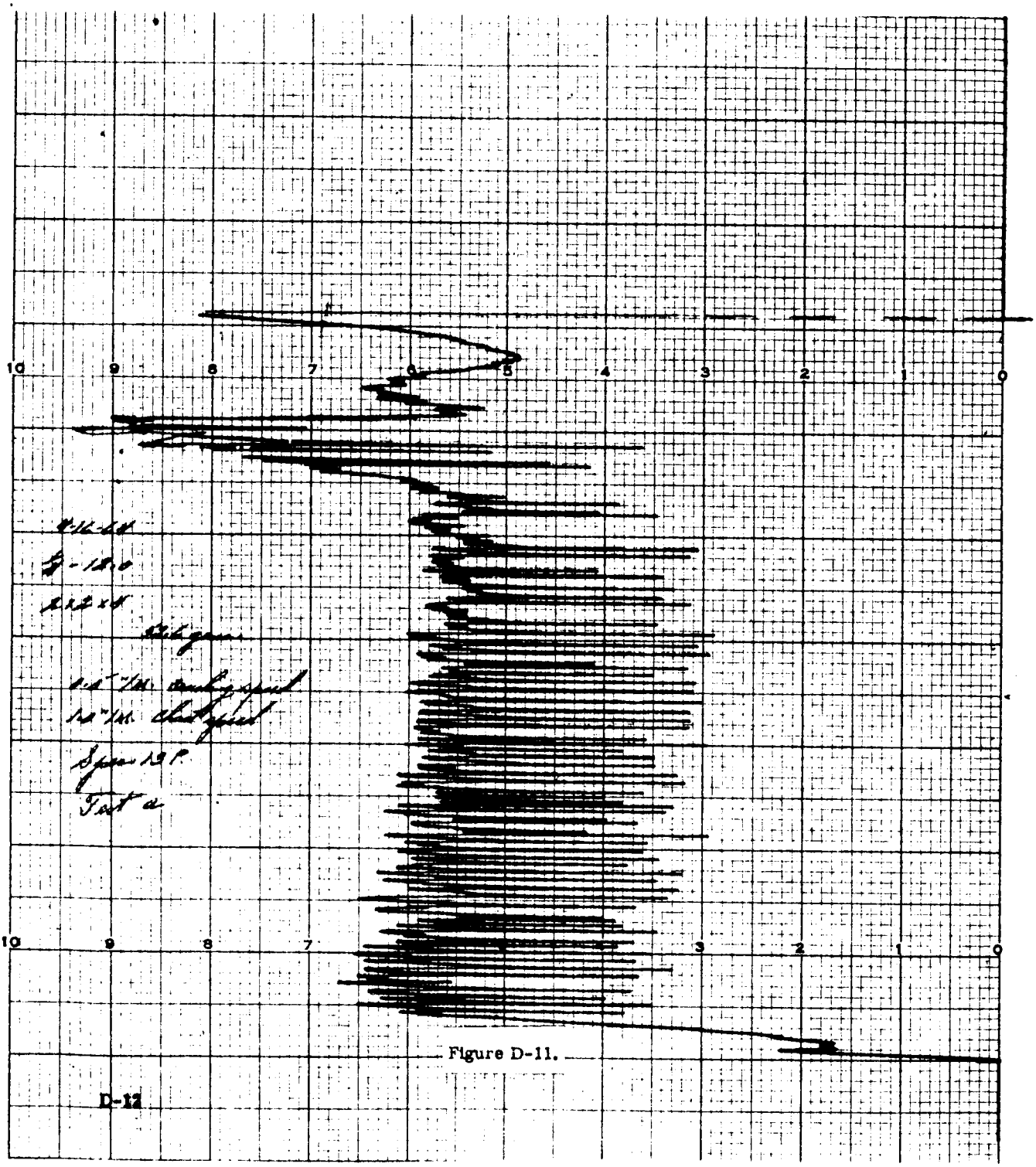

Figure D-11.

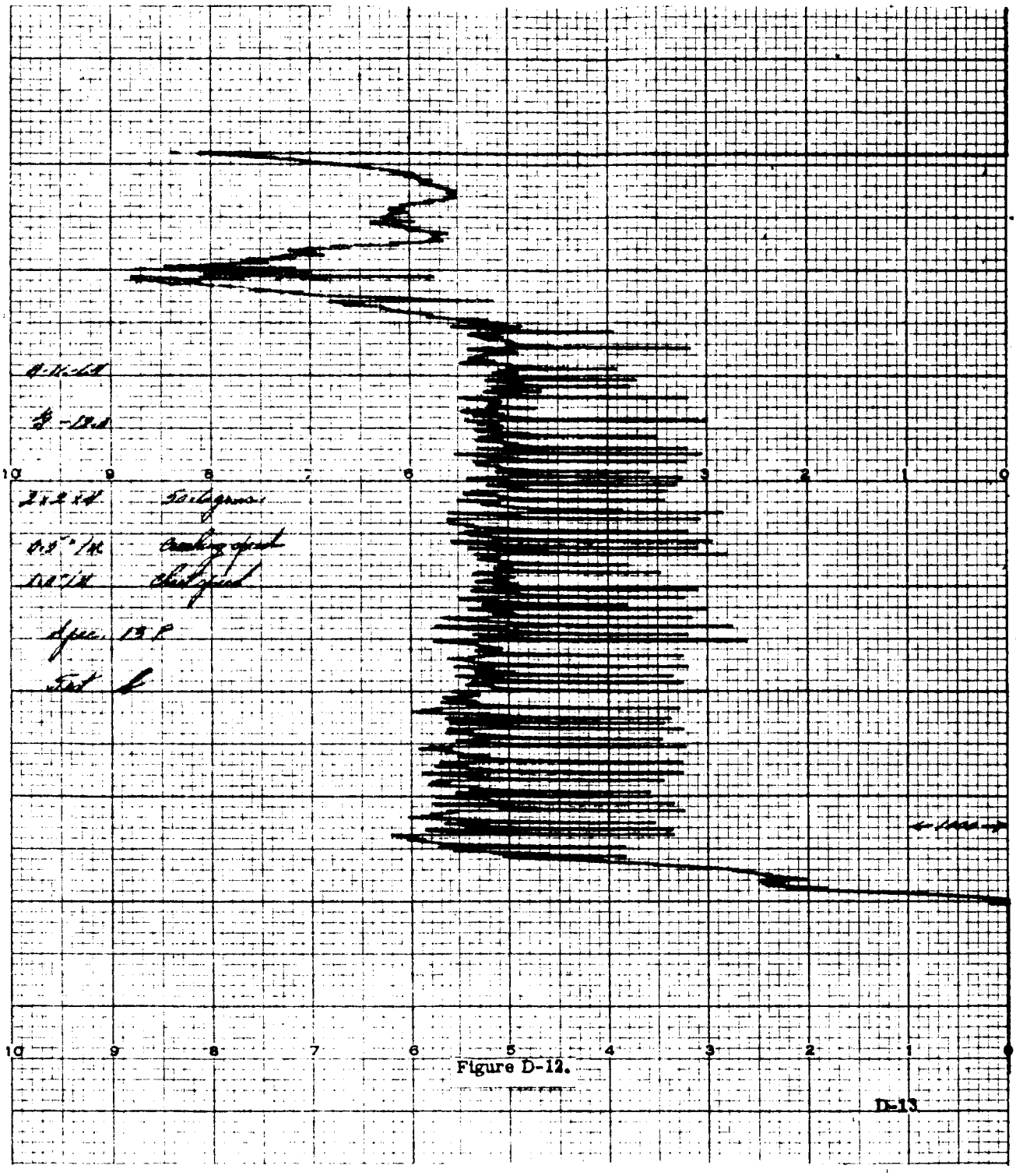

Figure D-12.

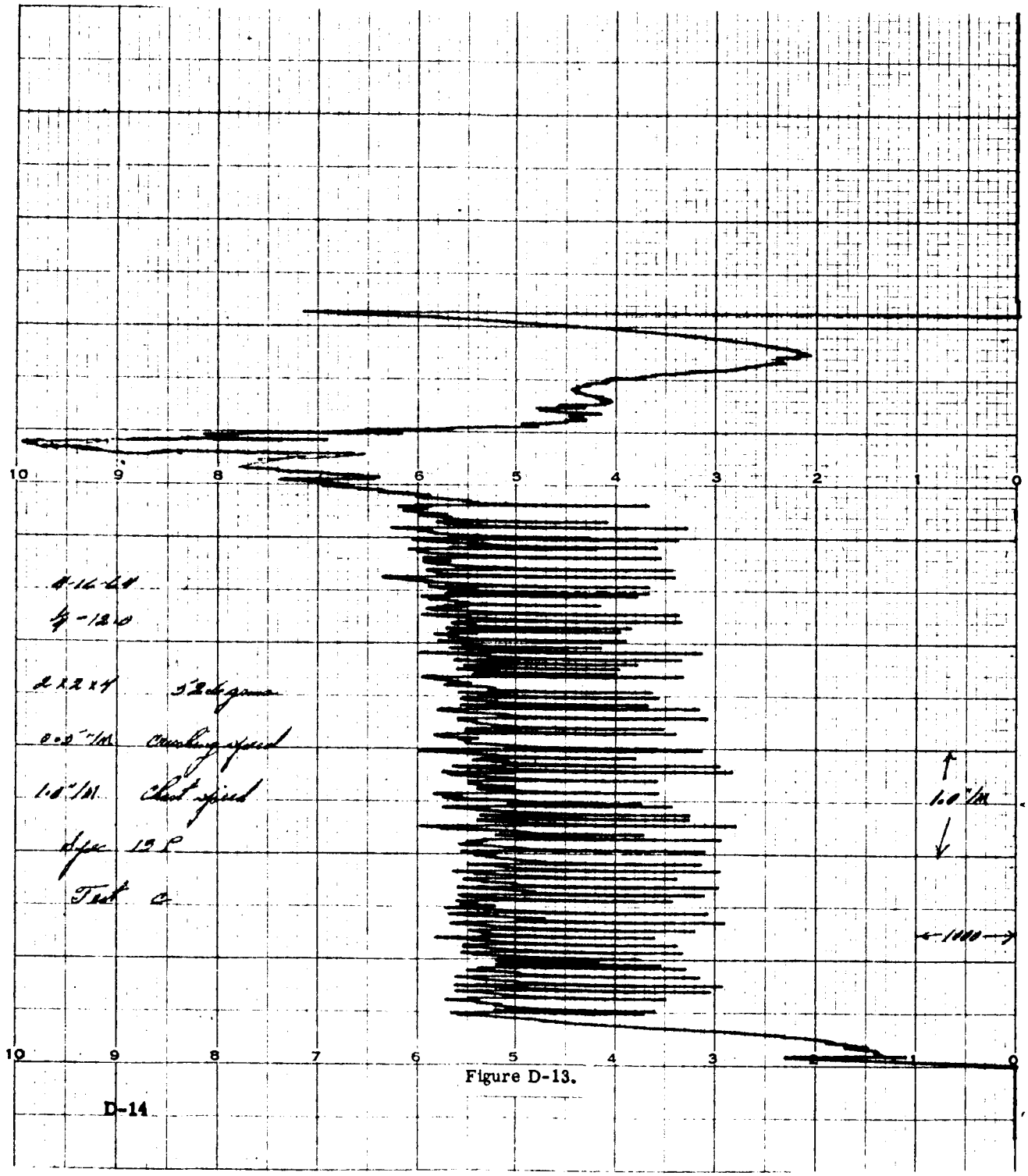

Figure D-13.

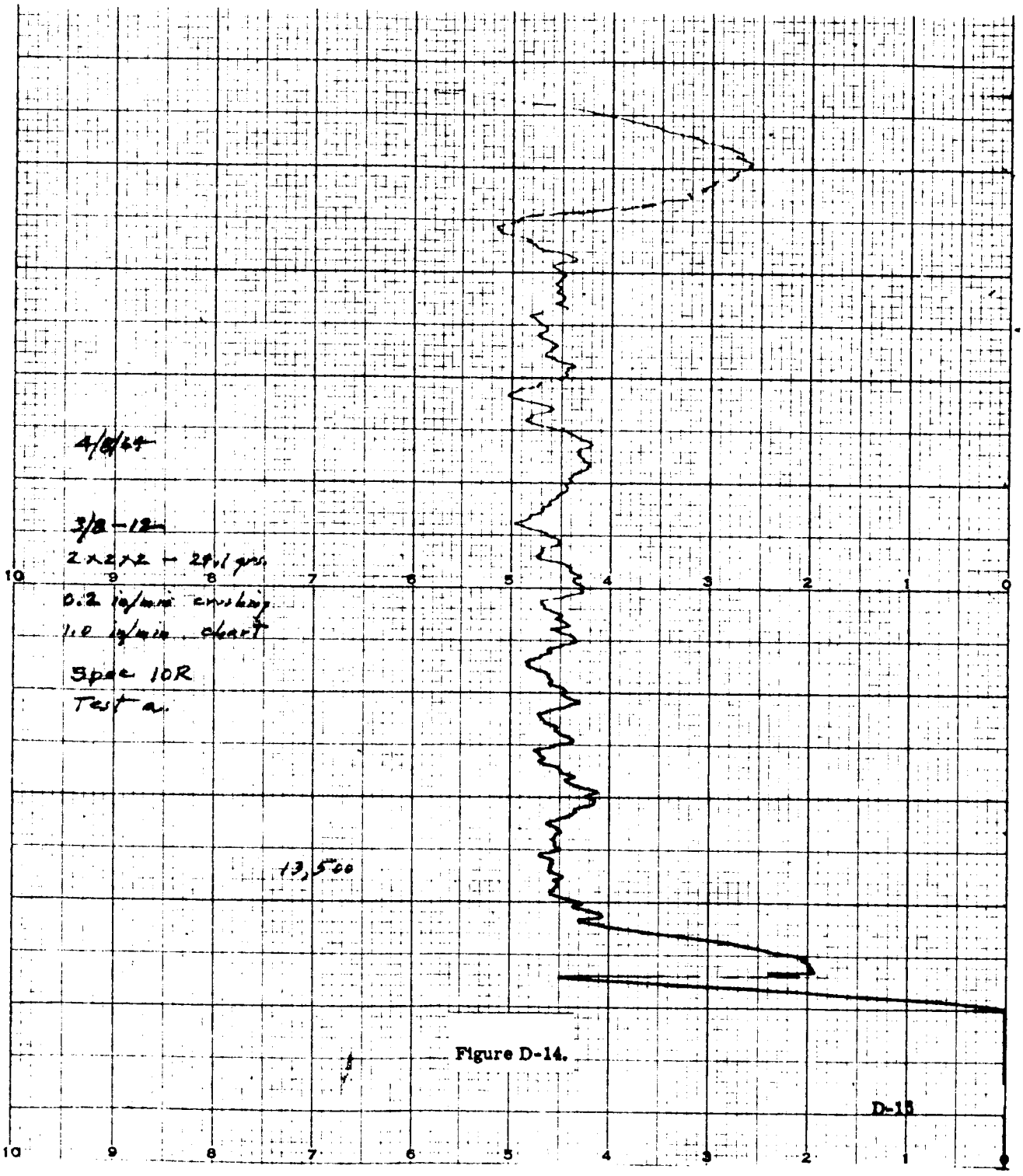
4/8/64
3/8 - 12
2 x 2 x 2 - 24 l/gm
0.2 lg/min crushing
1.0 lg/min chart
Spec 10R
Test a.
13,500
10
9
8
7
6
5
4
3
2
1
0

Figure D-14.

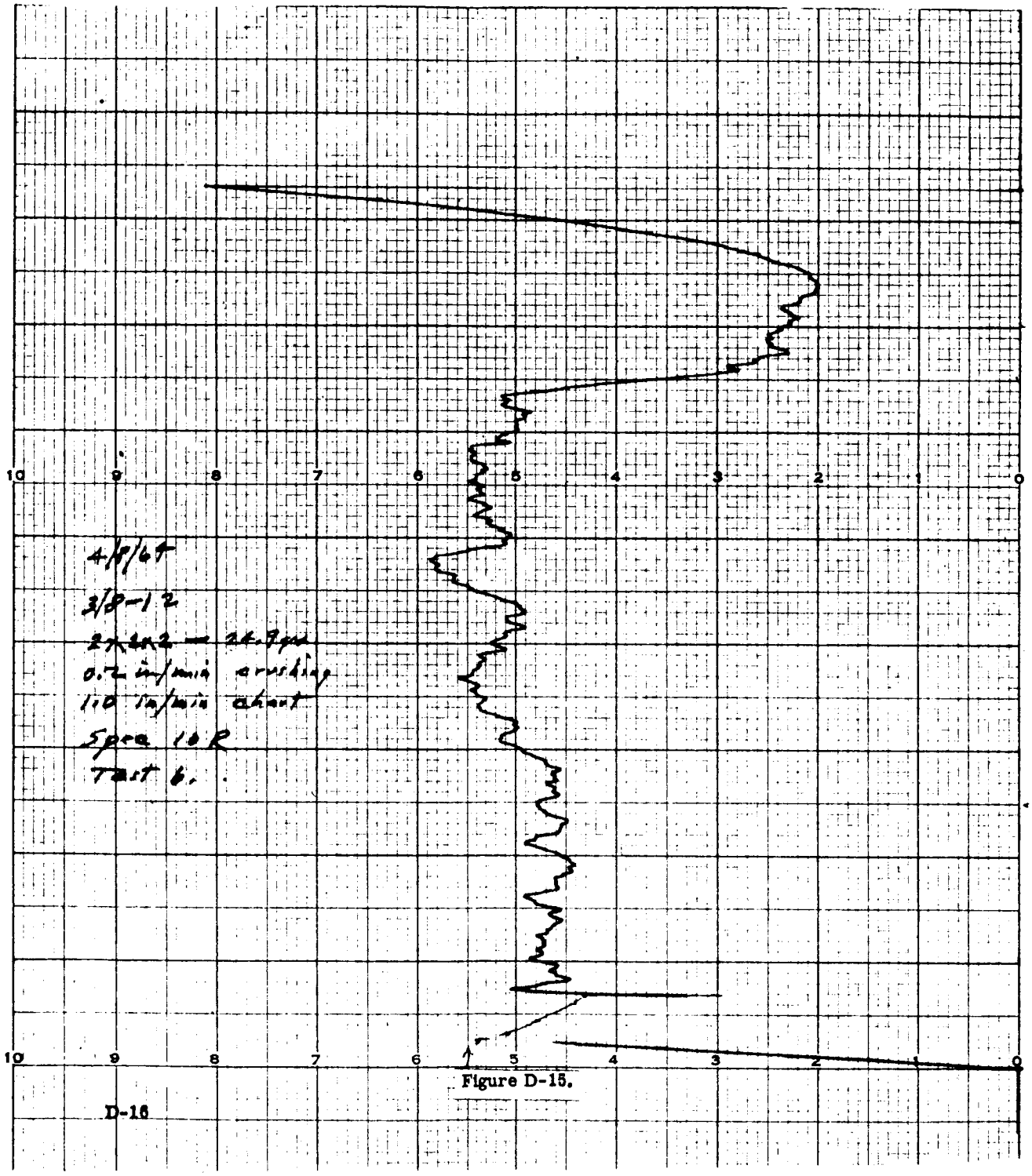
10
9
8
7
6
5
4
3
2
1
0
4/8/54
3/8-12
2x4x2 — 24.8 gpm
0.2 in/min corroding
1.0 in/min about
Spec 10R
Test 6.

Figure D-15.

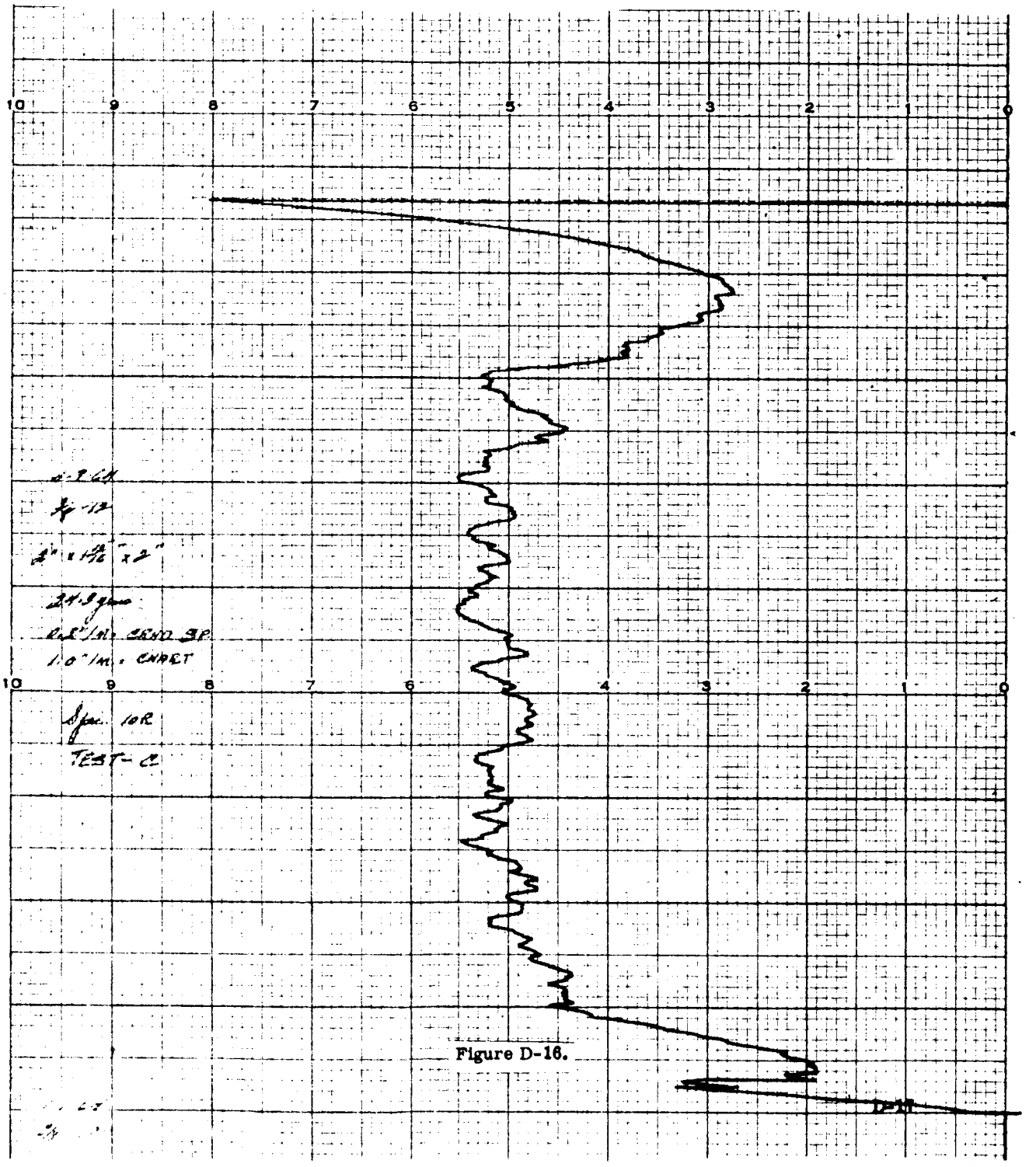

Figure D-16.

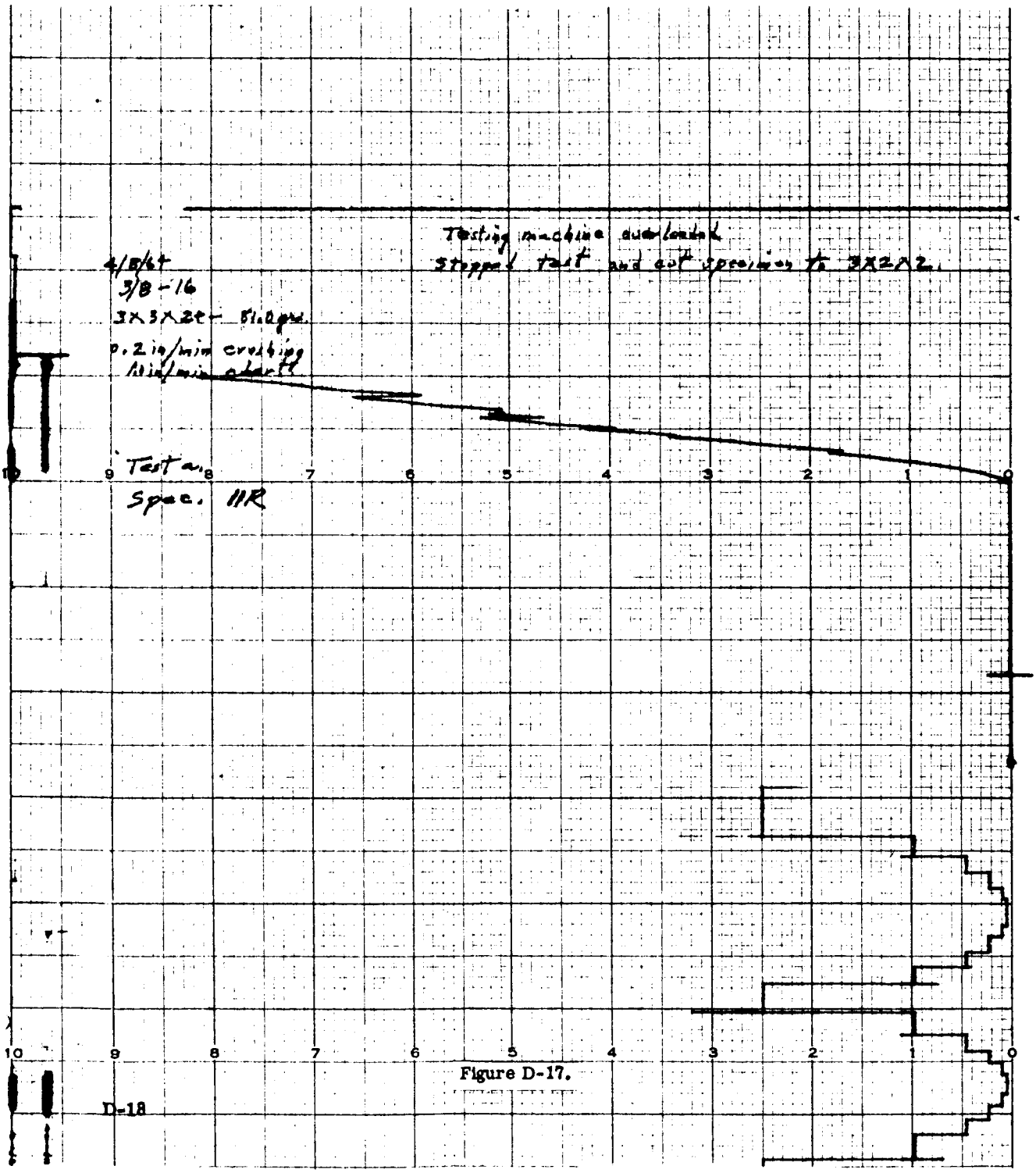
4/8/64
3/8-16
3X3X2t- Bl. Age.
0.2 in/min crosshead
A in/min chart
Testing machine overloaded
Stopped test and cut specimen to 3X2X2.
Test a.
Spec. 11R
10
9
8
7
6
5
4
3
2
1
0

Figure D-17.

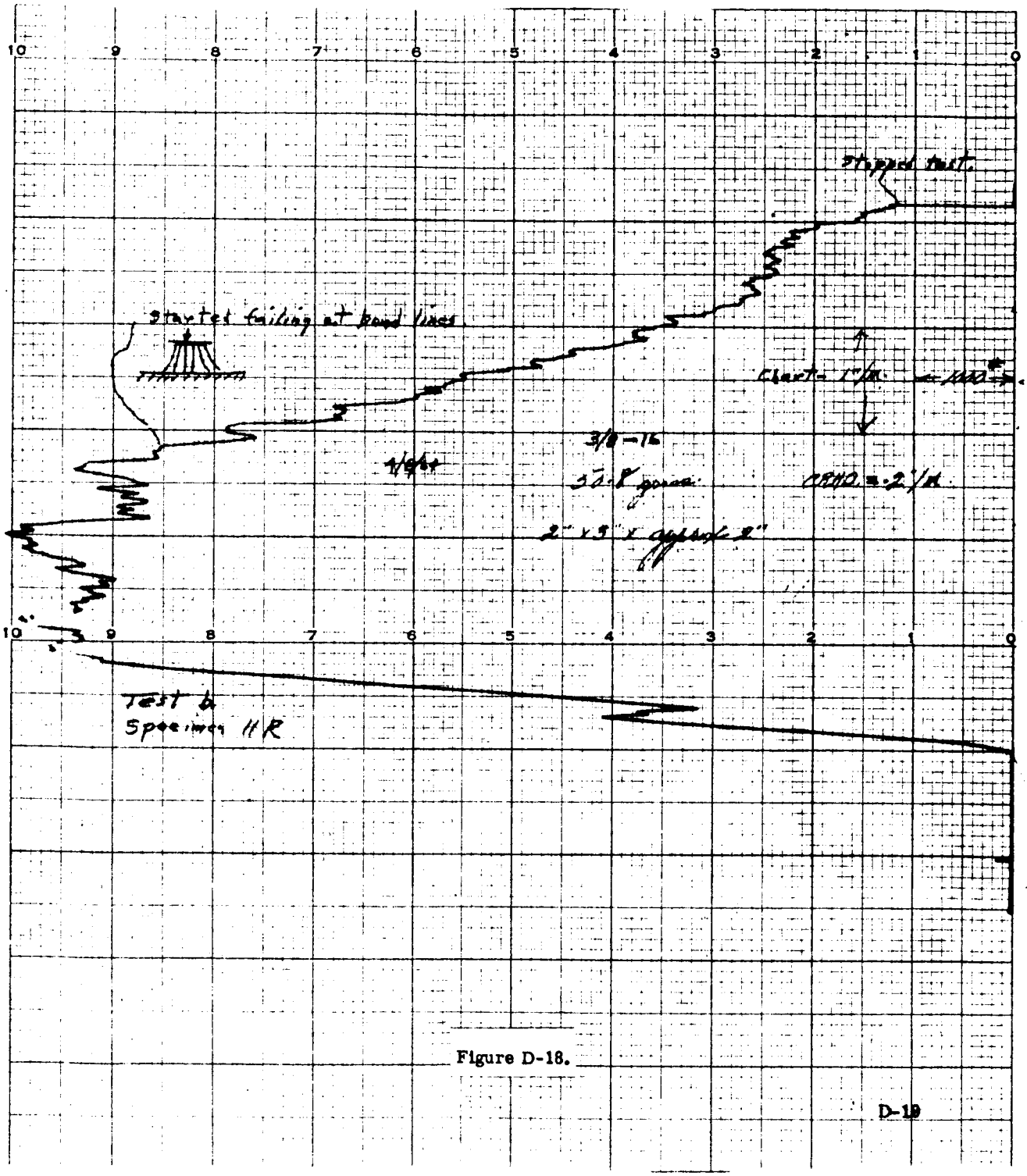
10
9
8
7
6
5
4
3
2
1
0
Stopped test.
Started failing at bond lines
Chart = 1"/hr.
3/8-16
1/4"
35.8 grams
2" x 9" x approx 2"
Test b
Specimen 11R

Figure D-18.

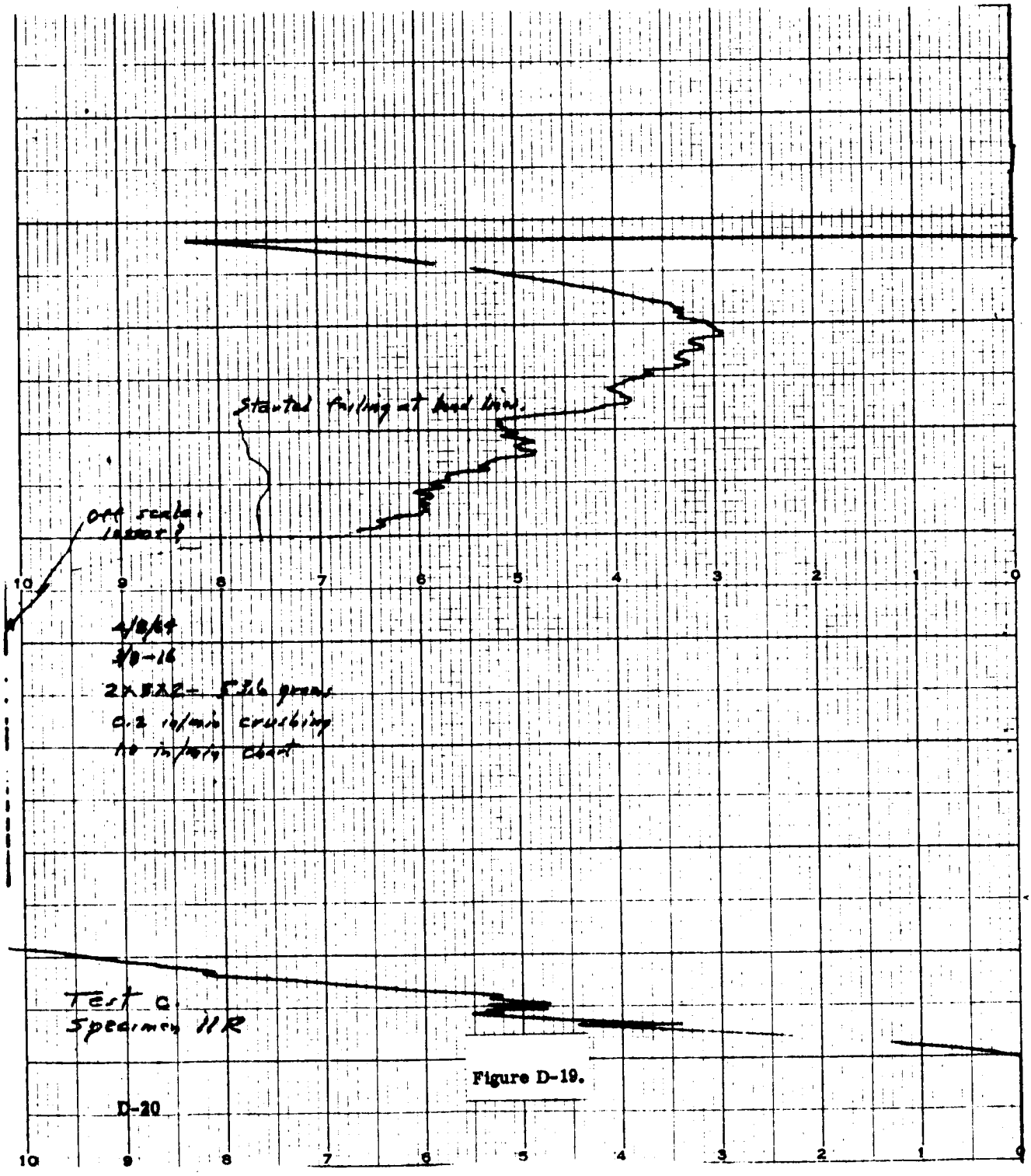

Figure D-19.

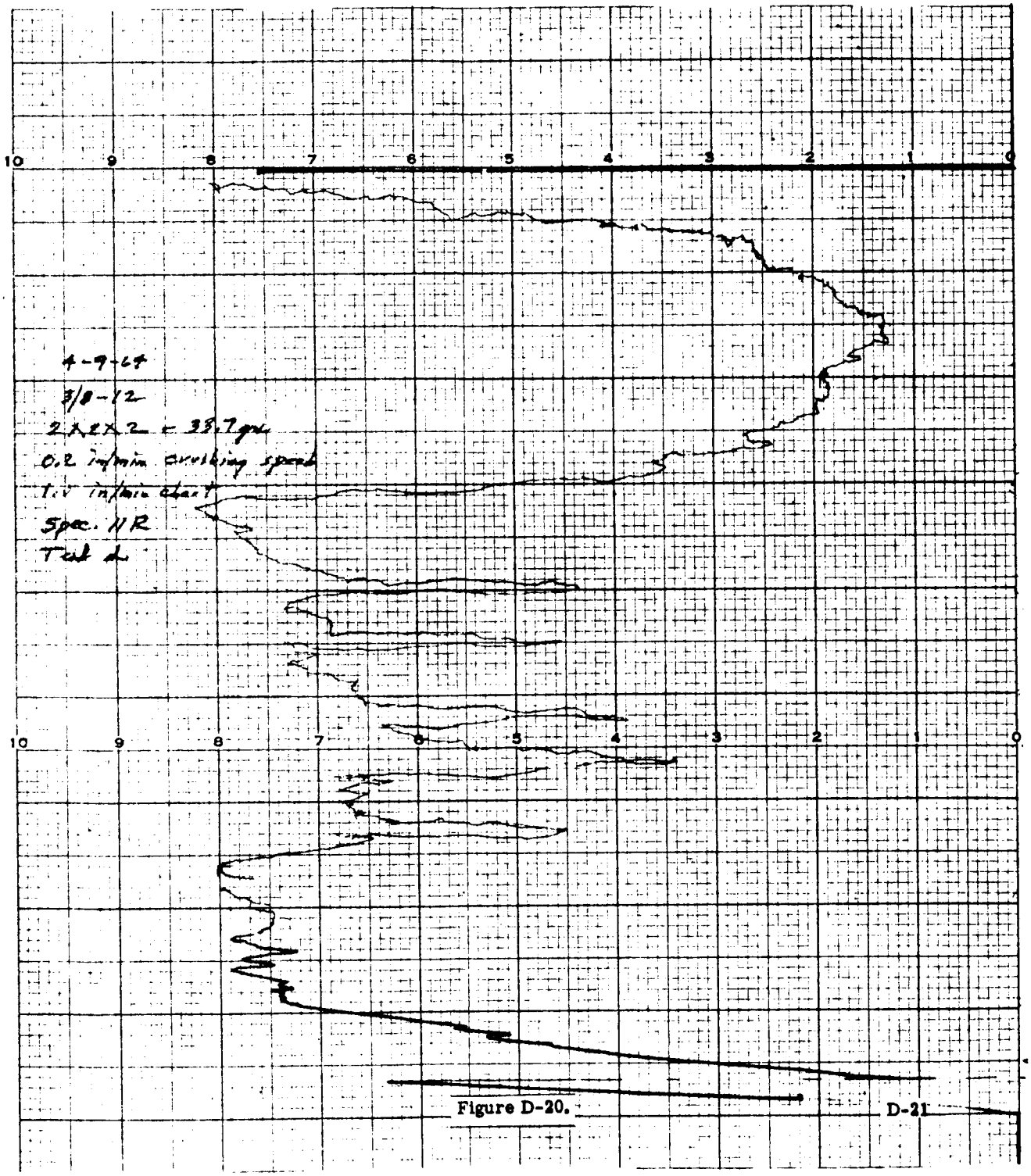

Figure D-20.

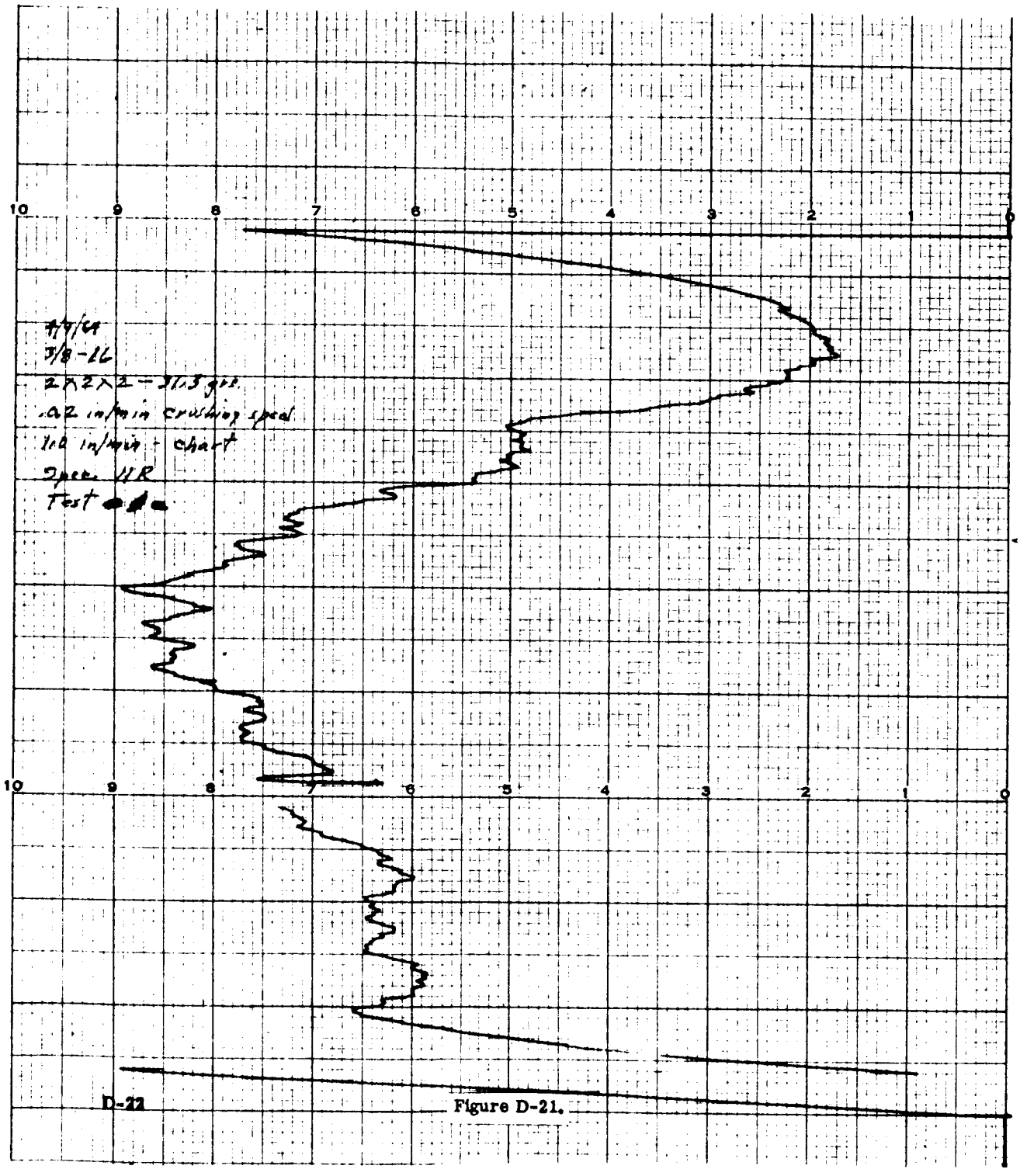
10
9
8
7
6
5
4
3
2
1
0
4/9/64
3/8-2L
2x2x2 - 31.3 gpf.
.02 in/min crushing speed
1.0 in/min chart
Spec. HR
Test #4

Figure D-21.

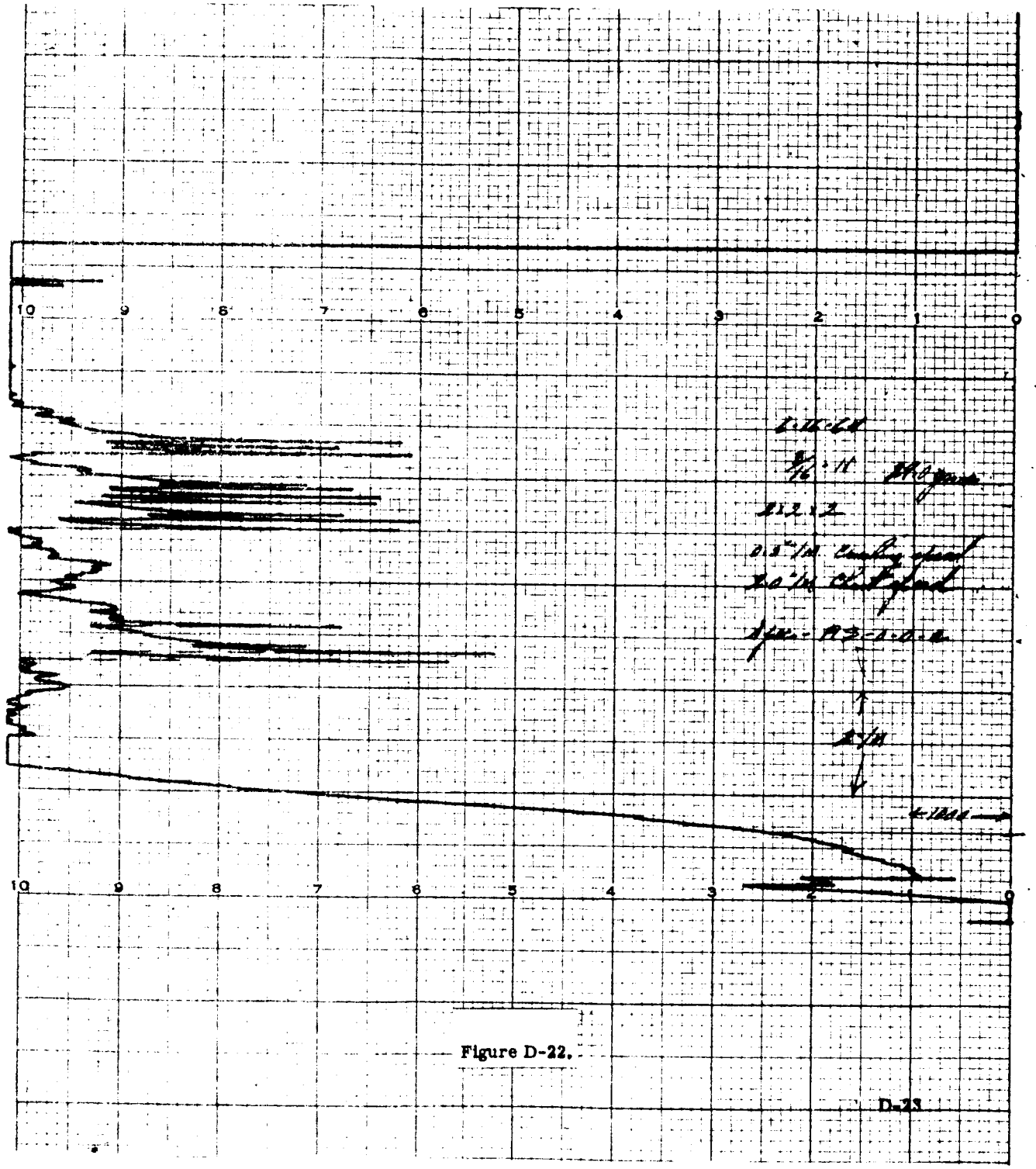

Figure D-22.

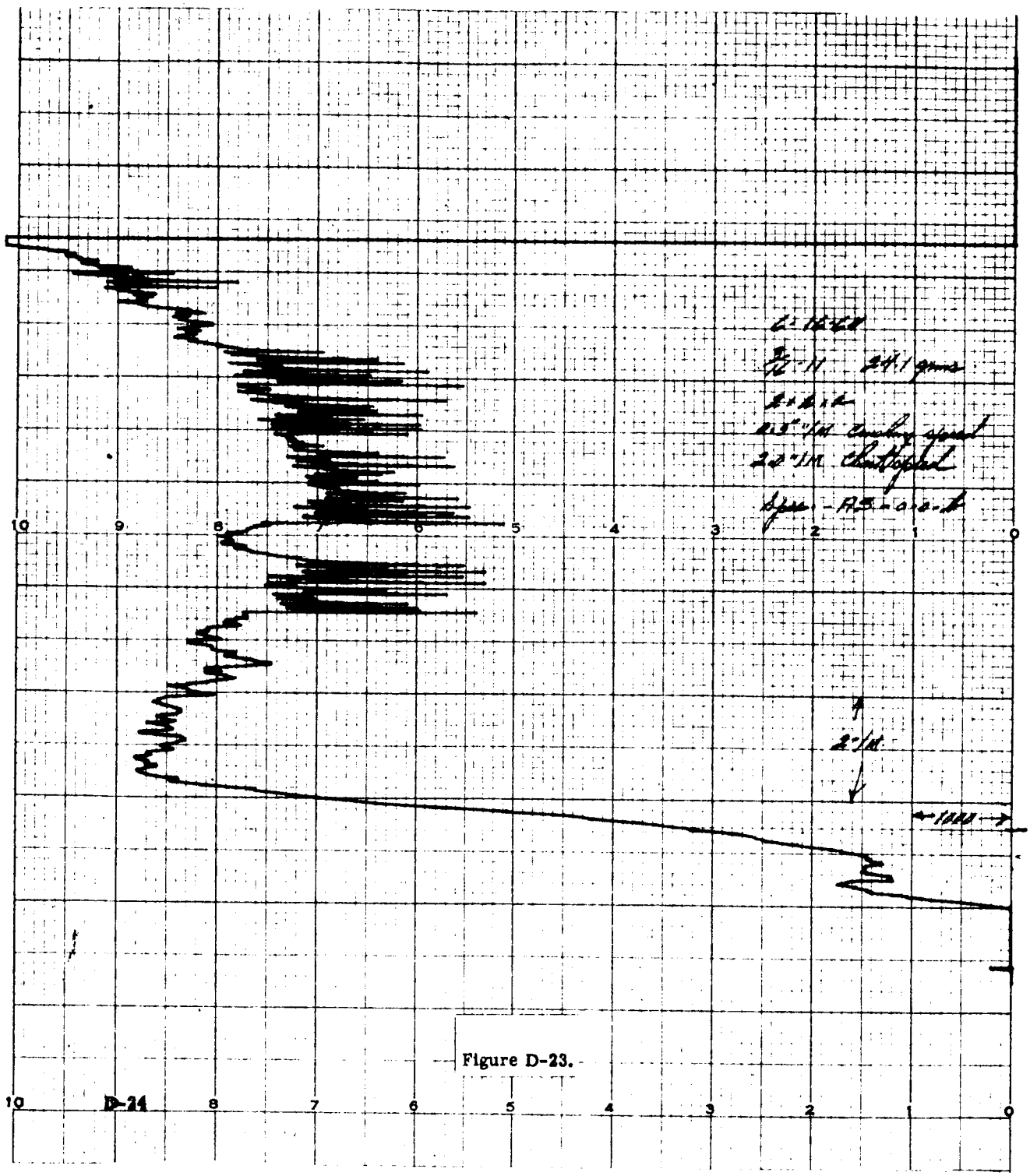

Figure D-23.

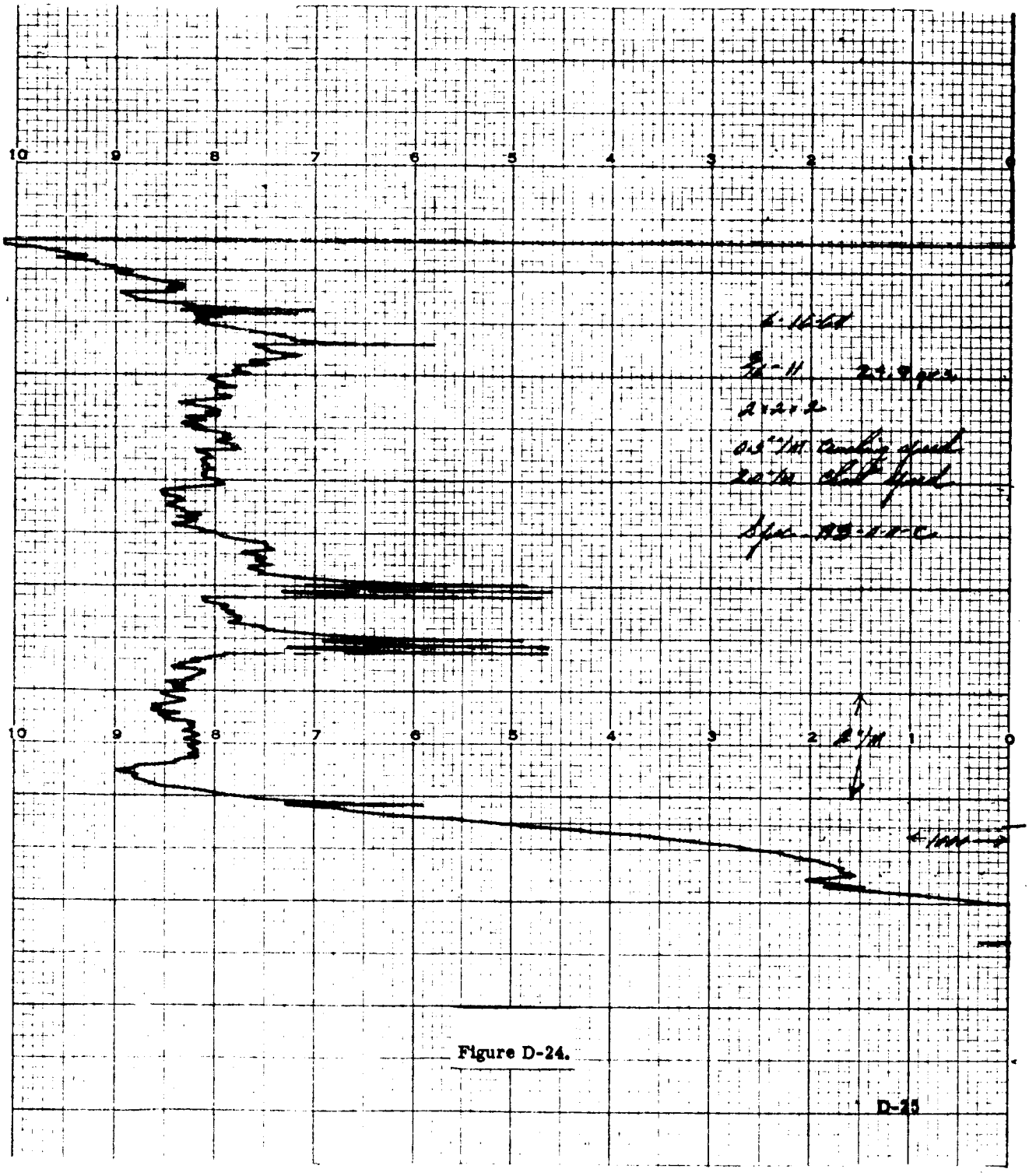

Figure D-24.

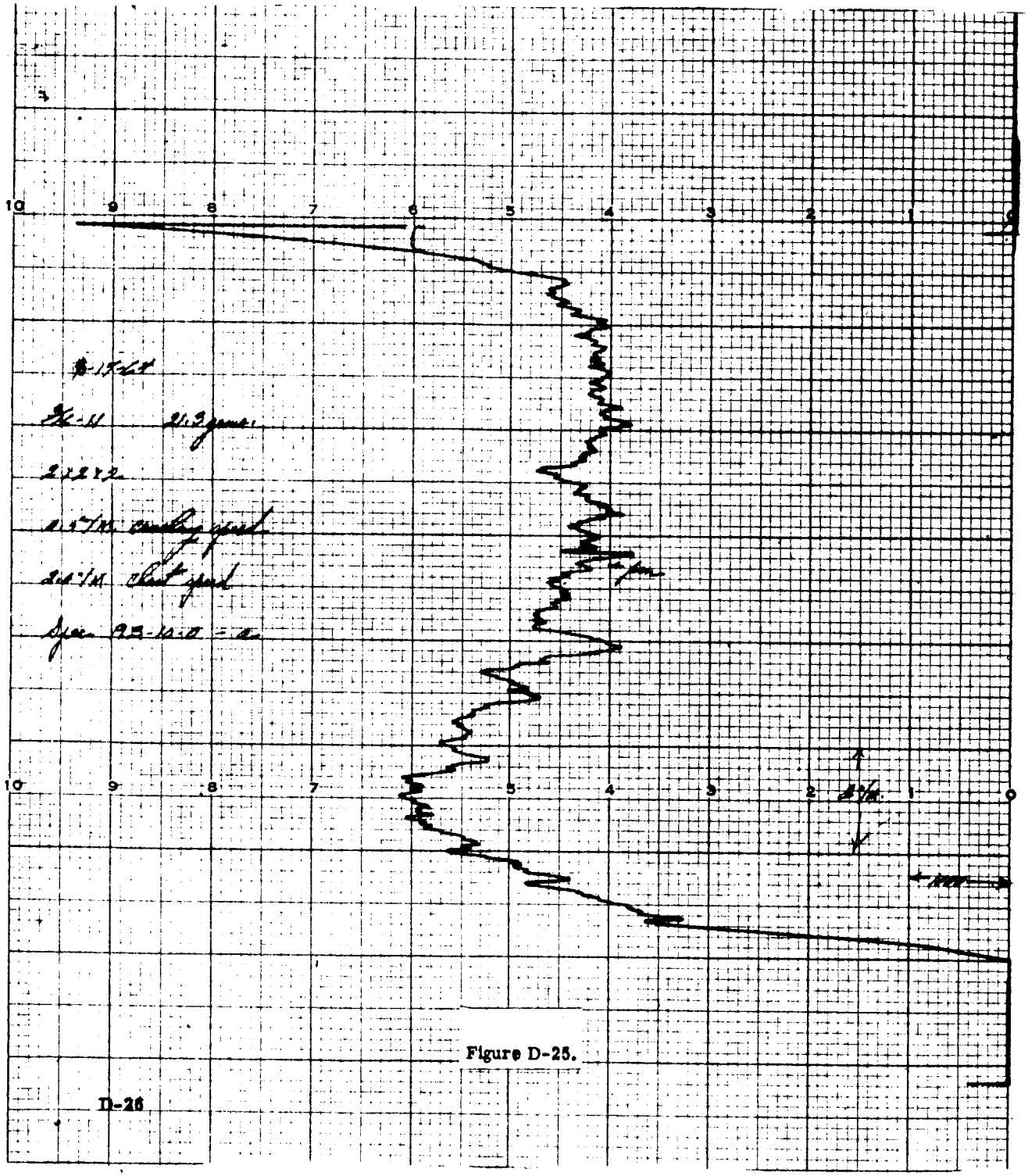

Figure D-25.

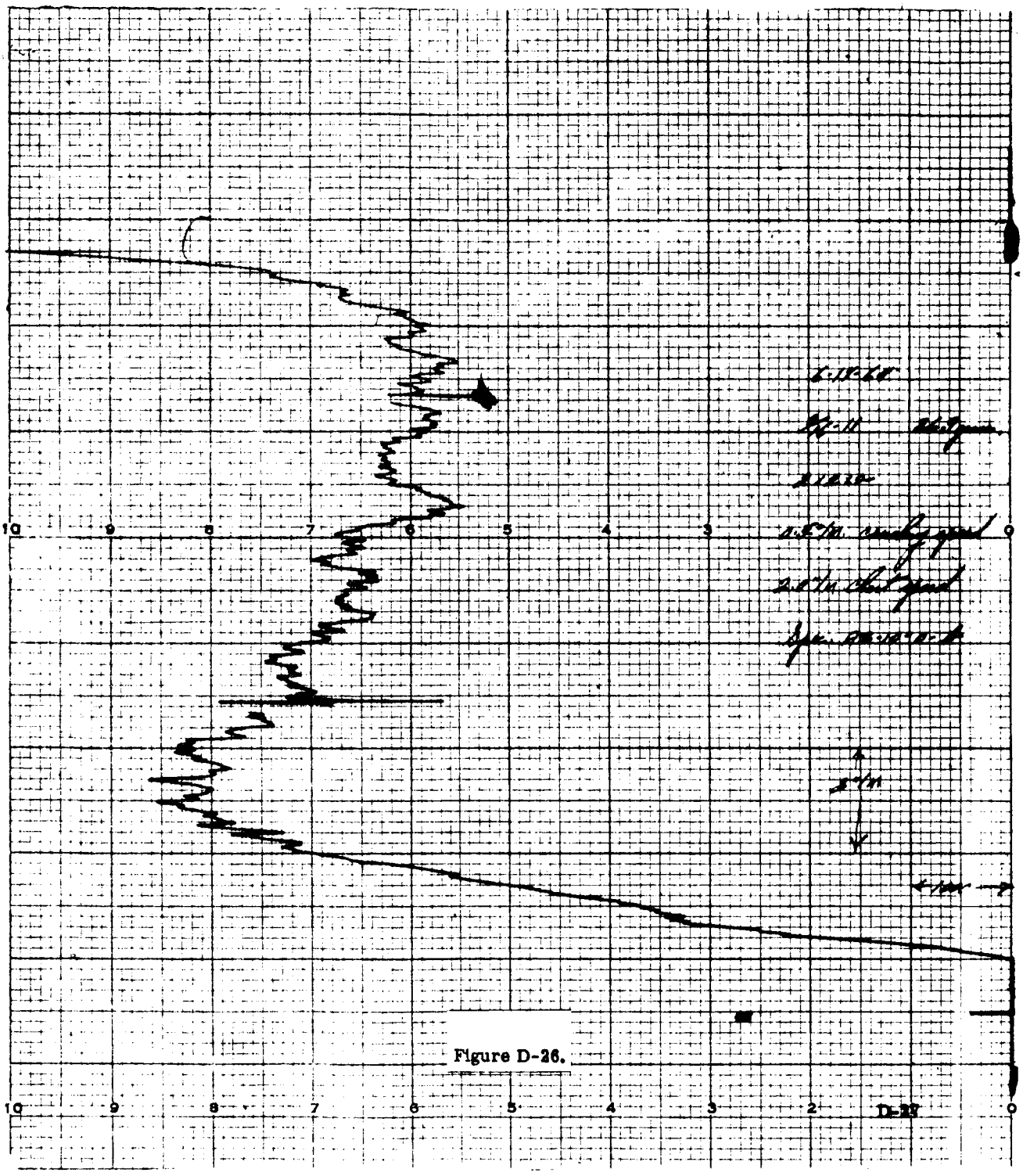

Figure D-26.

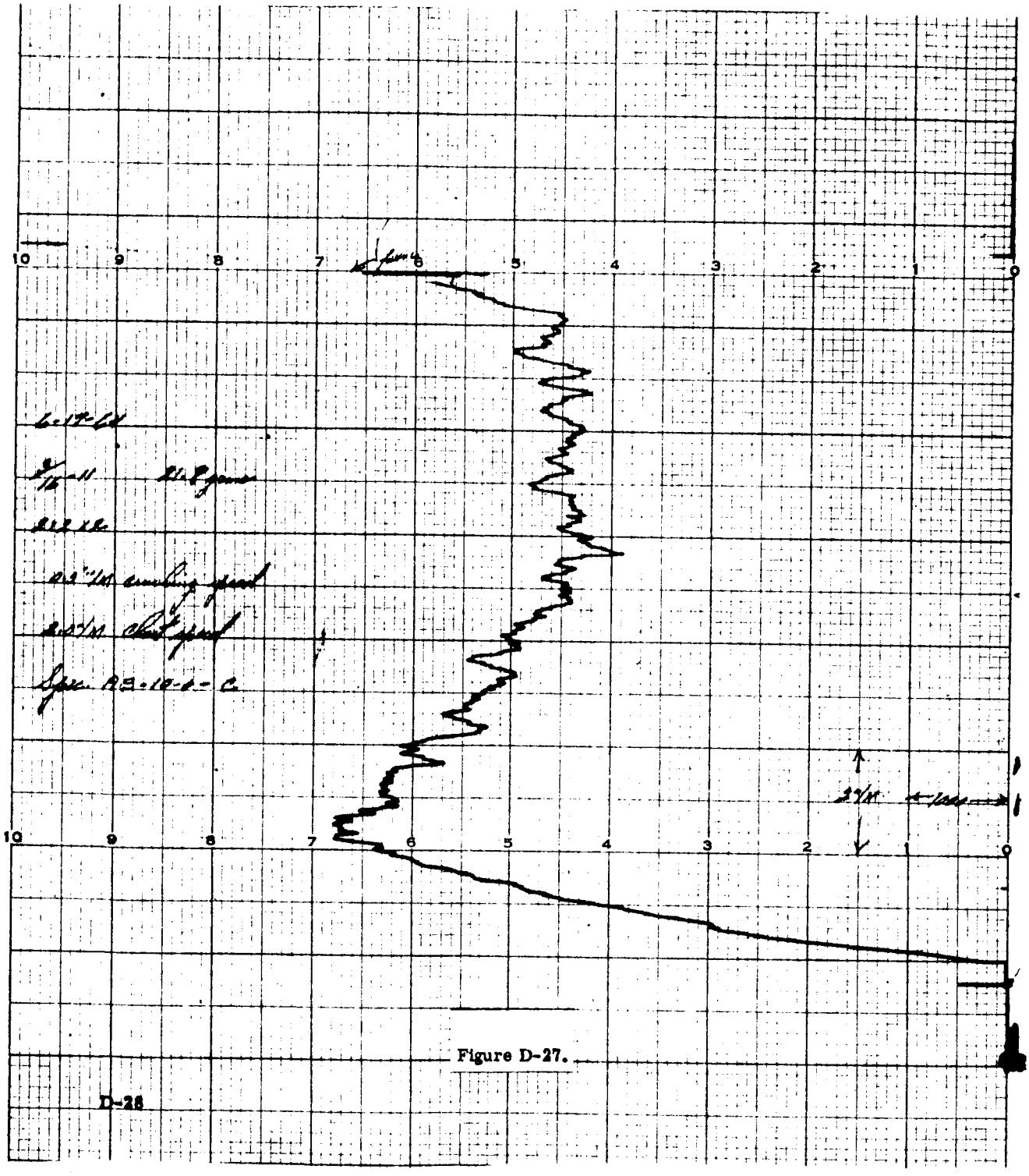

Figure D-27.

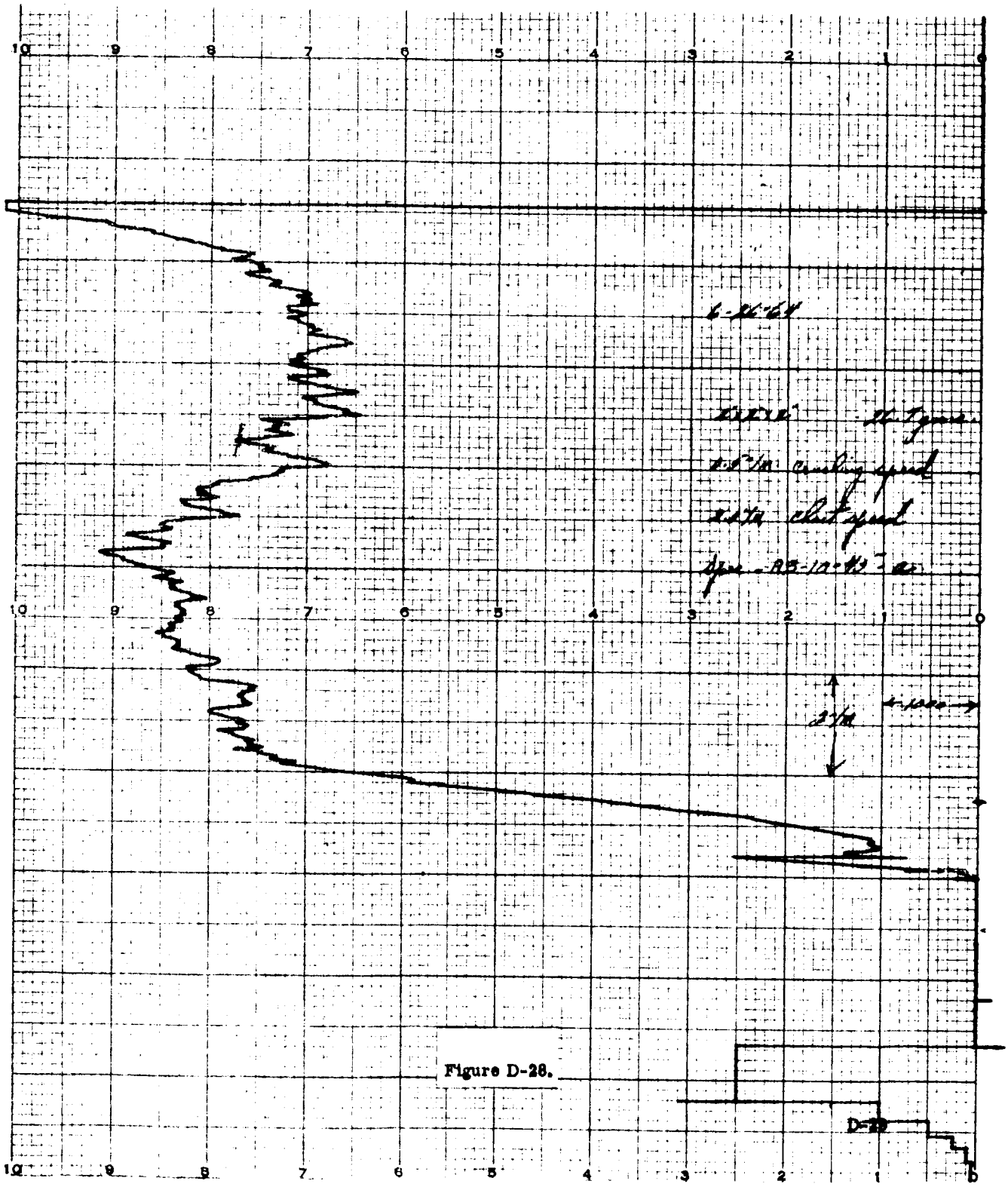

Figure D-28.

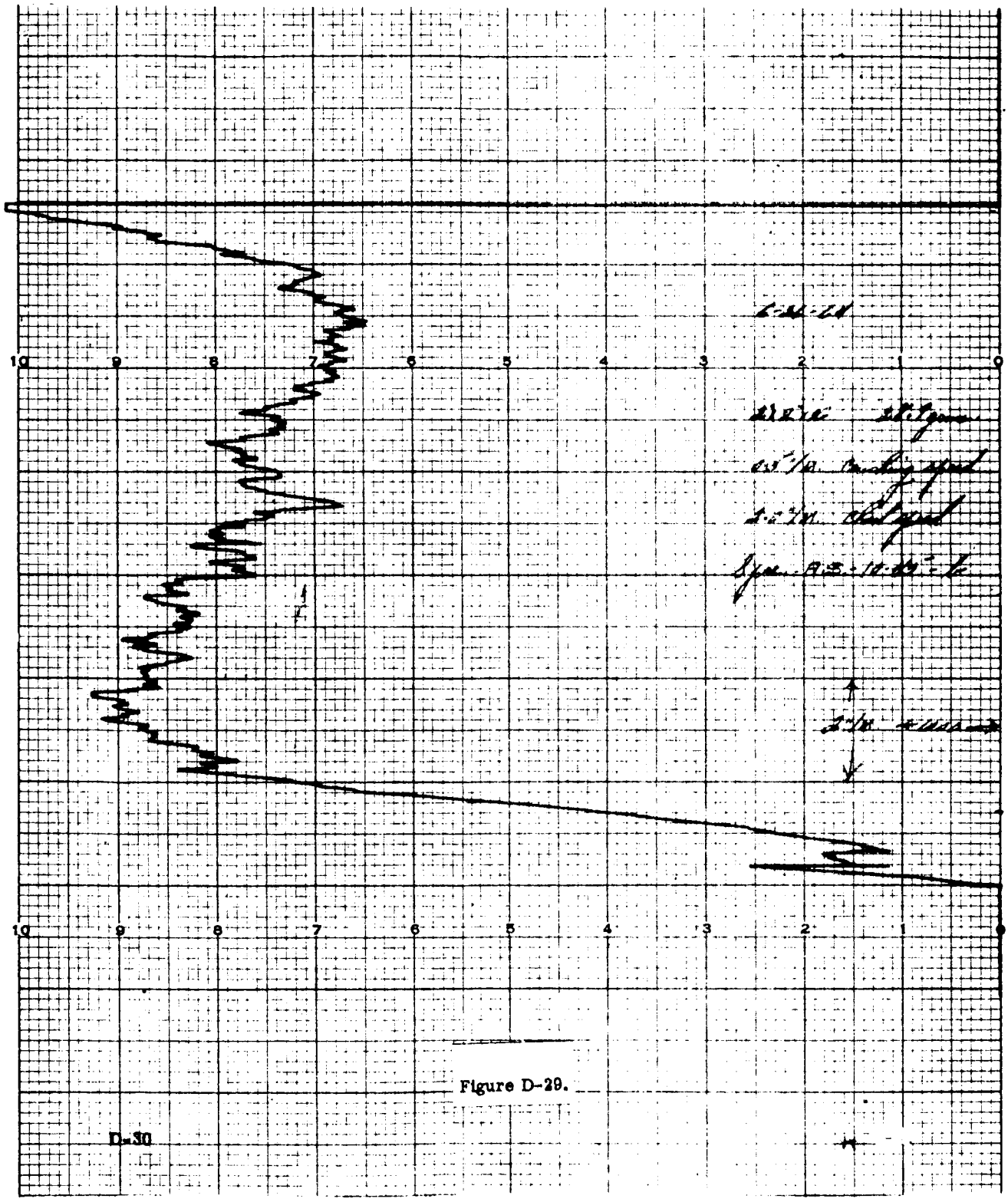

Figure D-29.

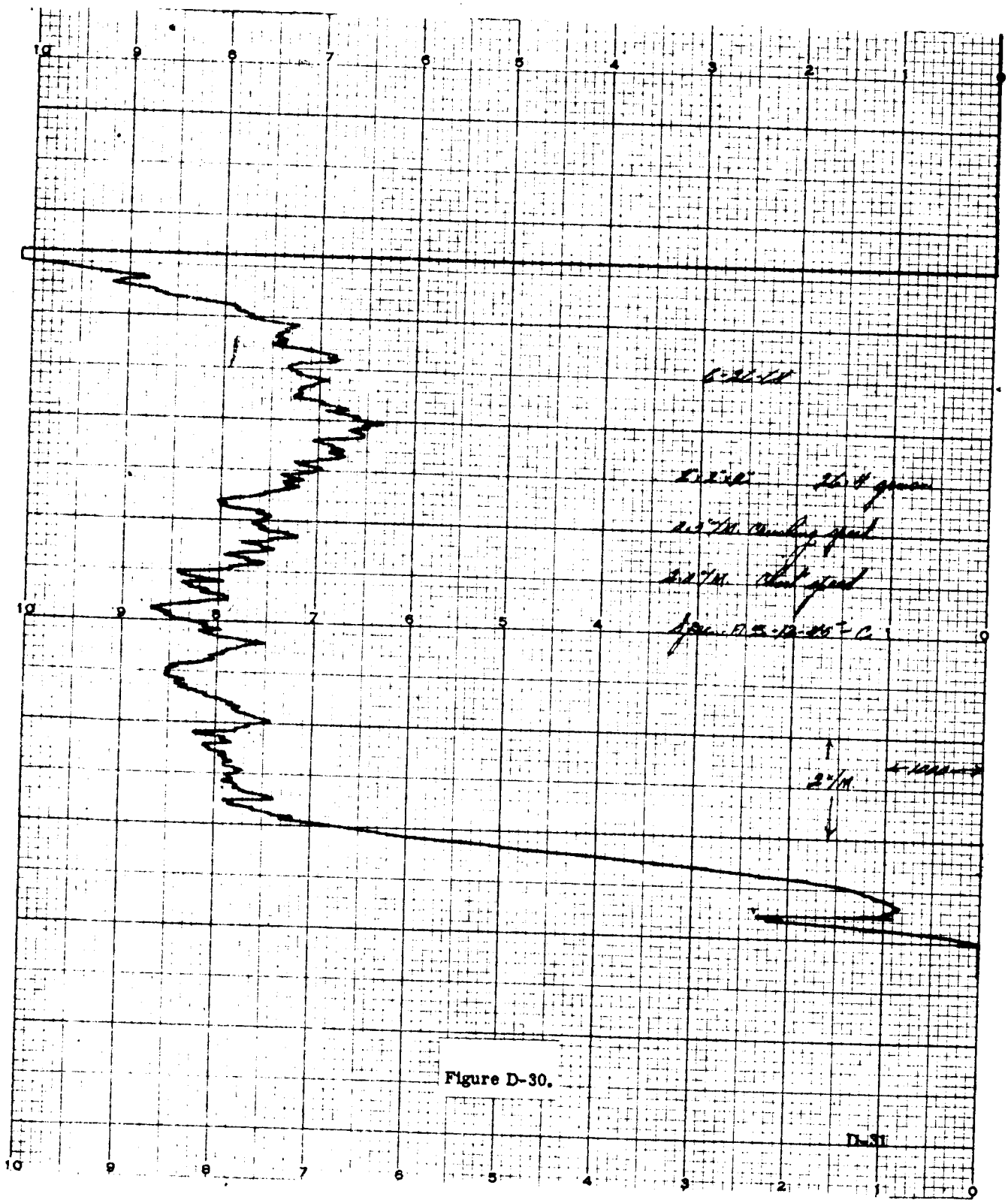

Figure D-30.

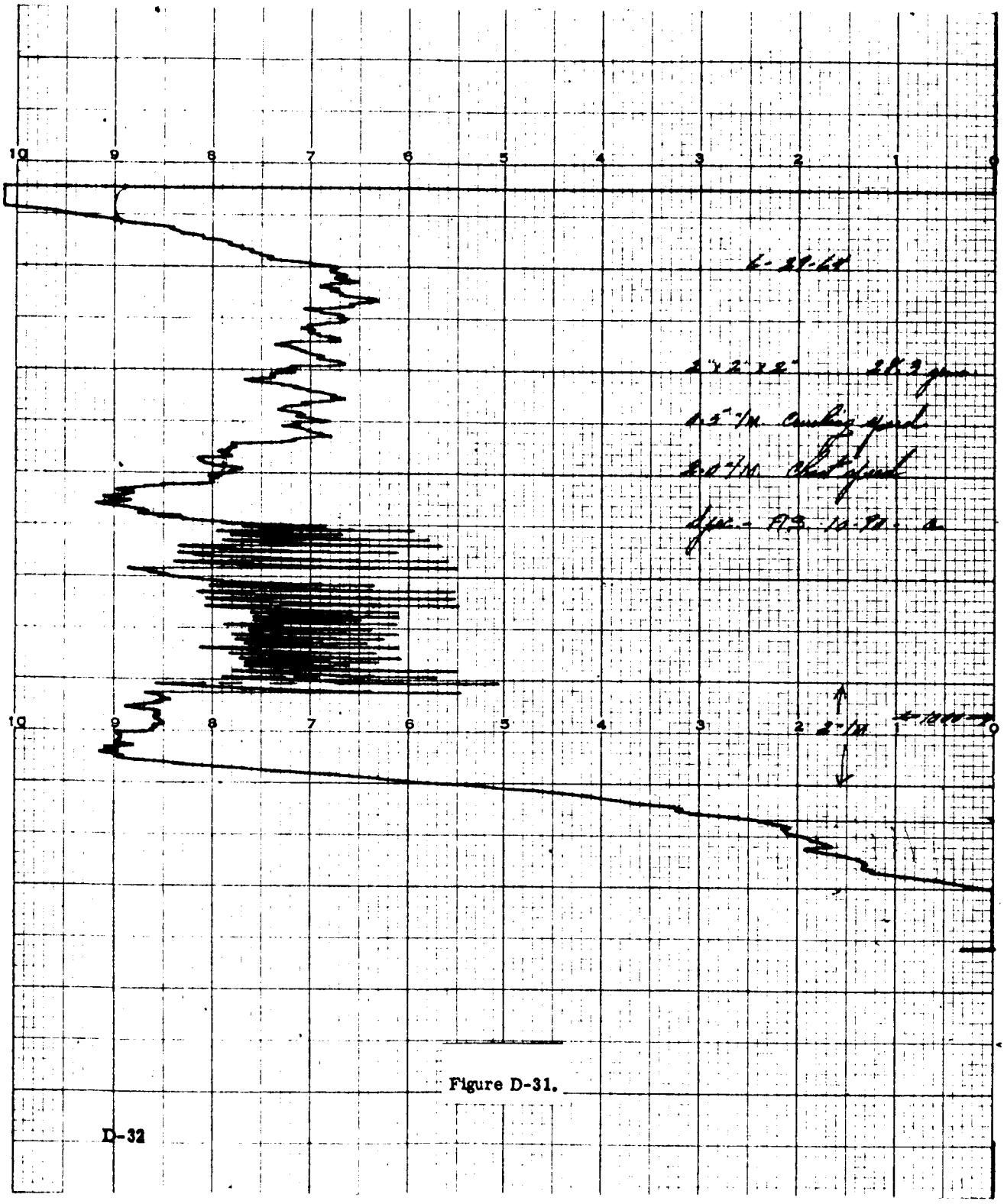

Figure D-31.

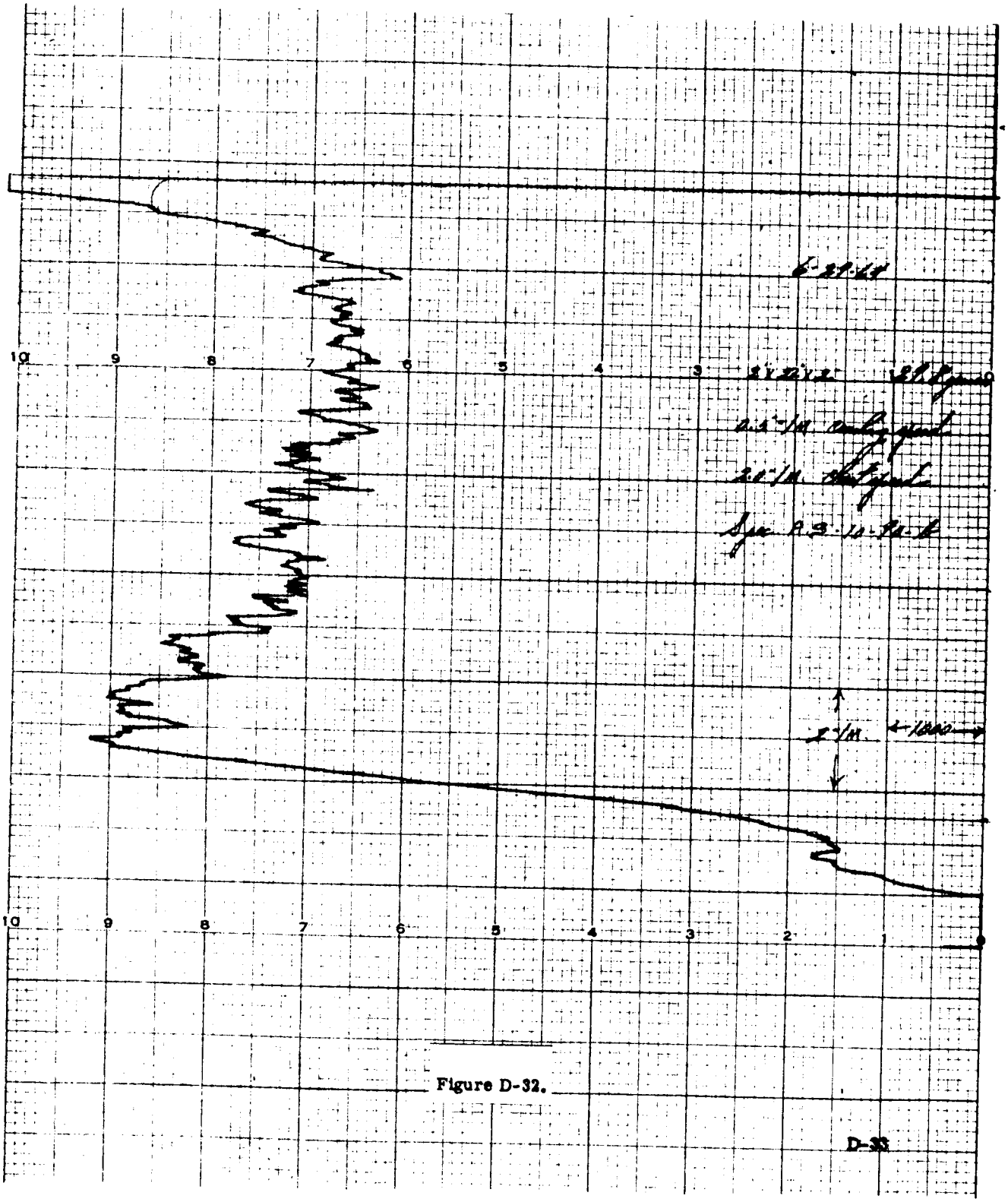

Figure D-32.

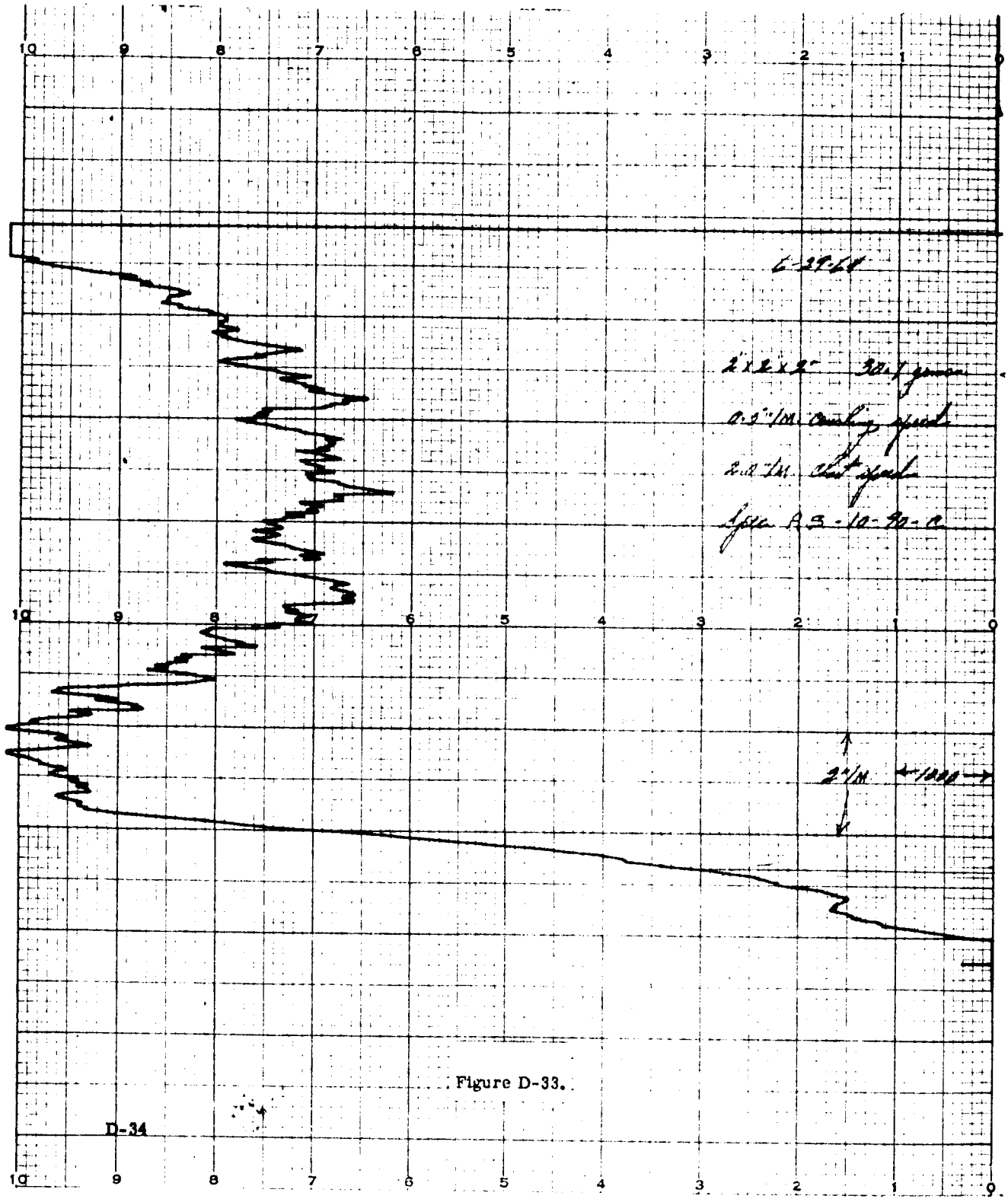

Figure D-33.

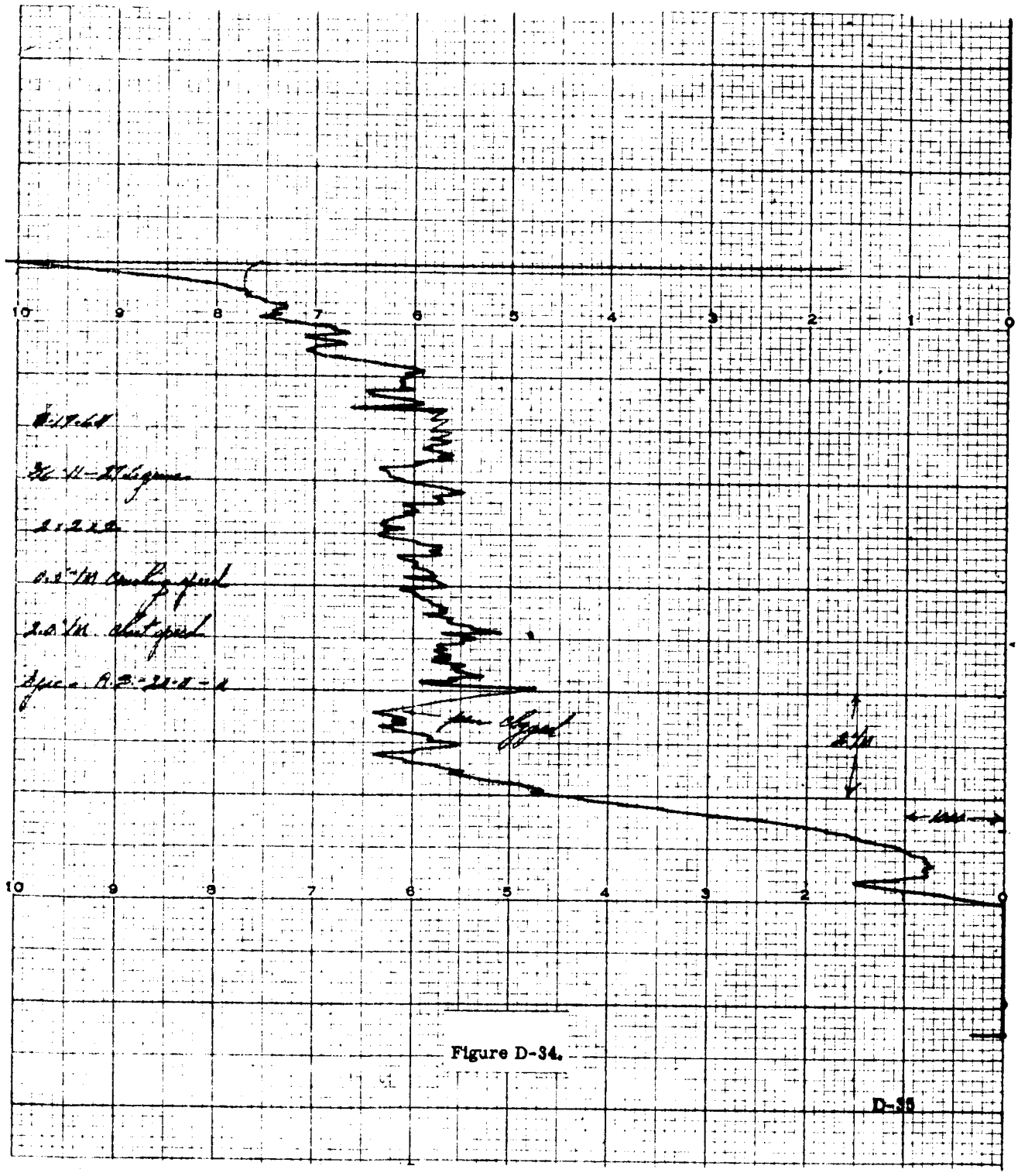

Figure D-34.

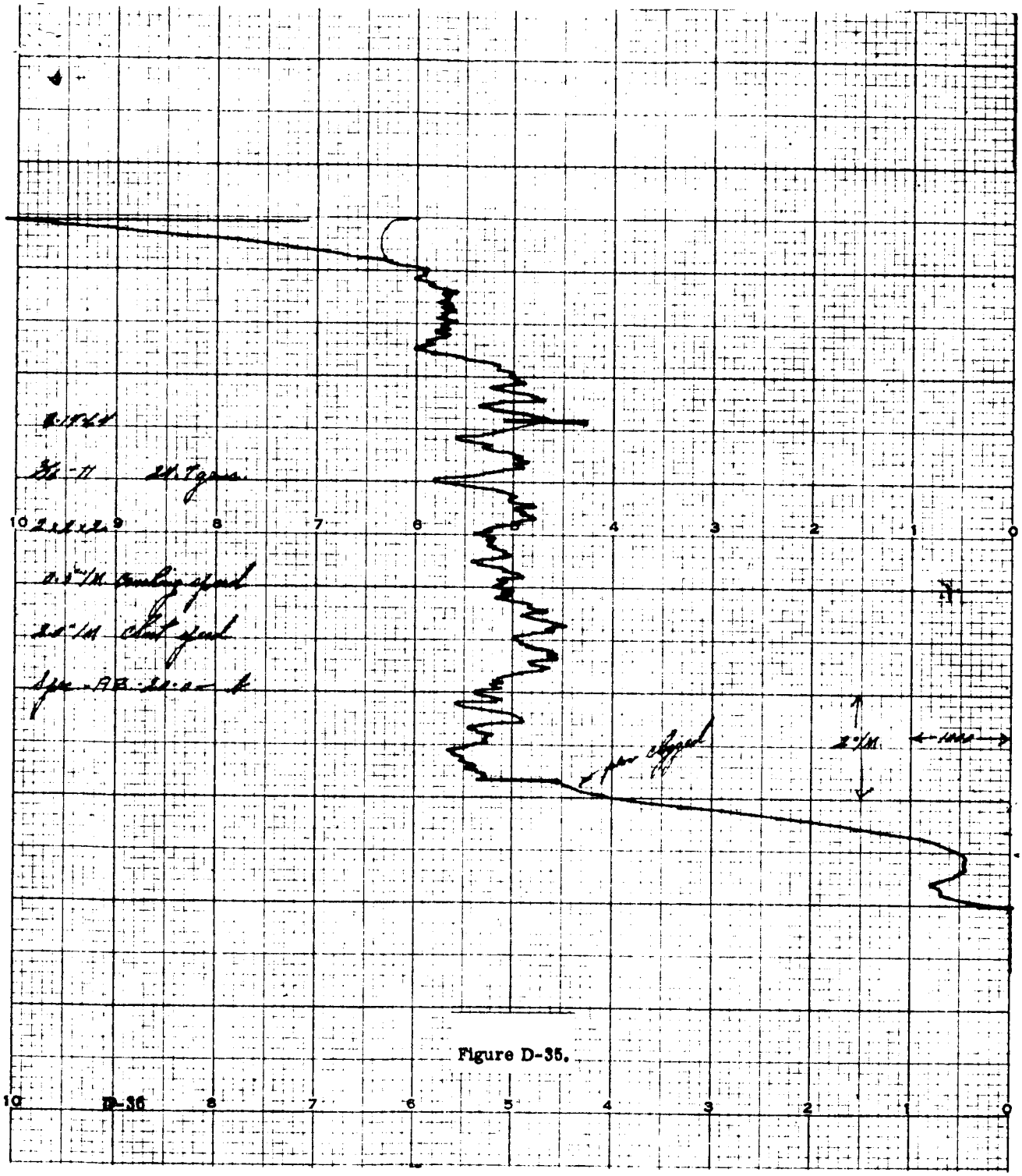

Figure D-35.

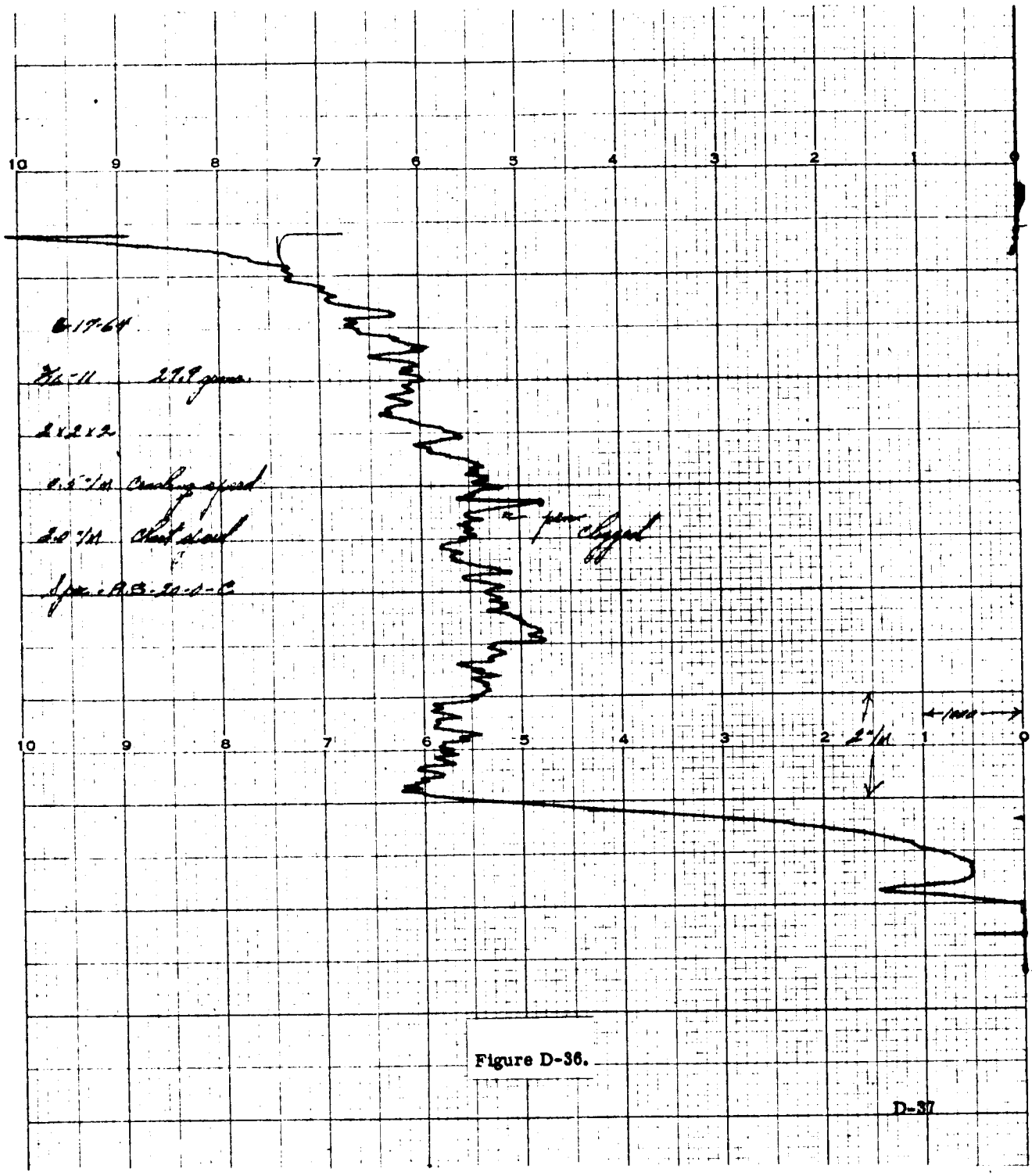
10
9
8
7
6
5
4
3
2
1
0
6-17-64
Ba-11 27.9 grams
2 x 2 x 2
0.2 %/M Cracking speed
2.0 %/M Shear speed
Spec. RB-20-2-C
2"/M
1 mm

Figure D-36.

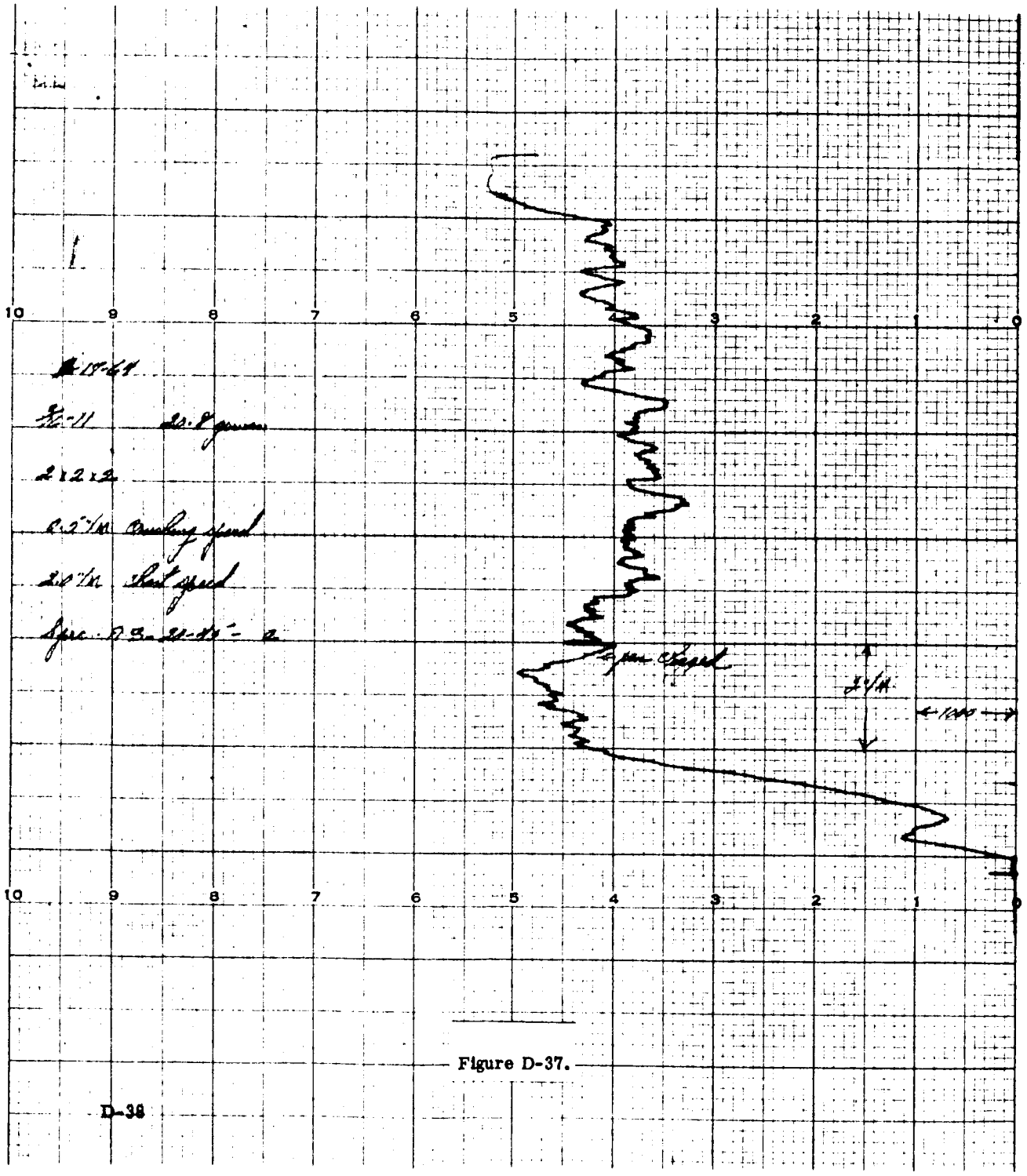
10
9
8
7
6
5
4
3
2
1
0
18-64
11
2 1/2 x 2
2.3"/M Running speed
2.0"/M Haul speed
4 per cent
1"/M
1000

Figure D-37.

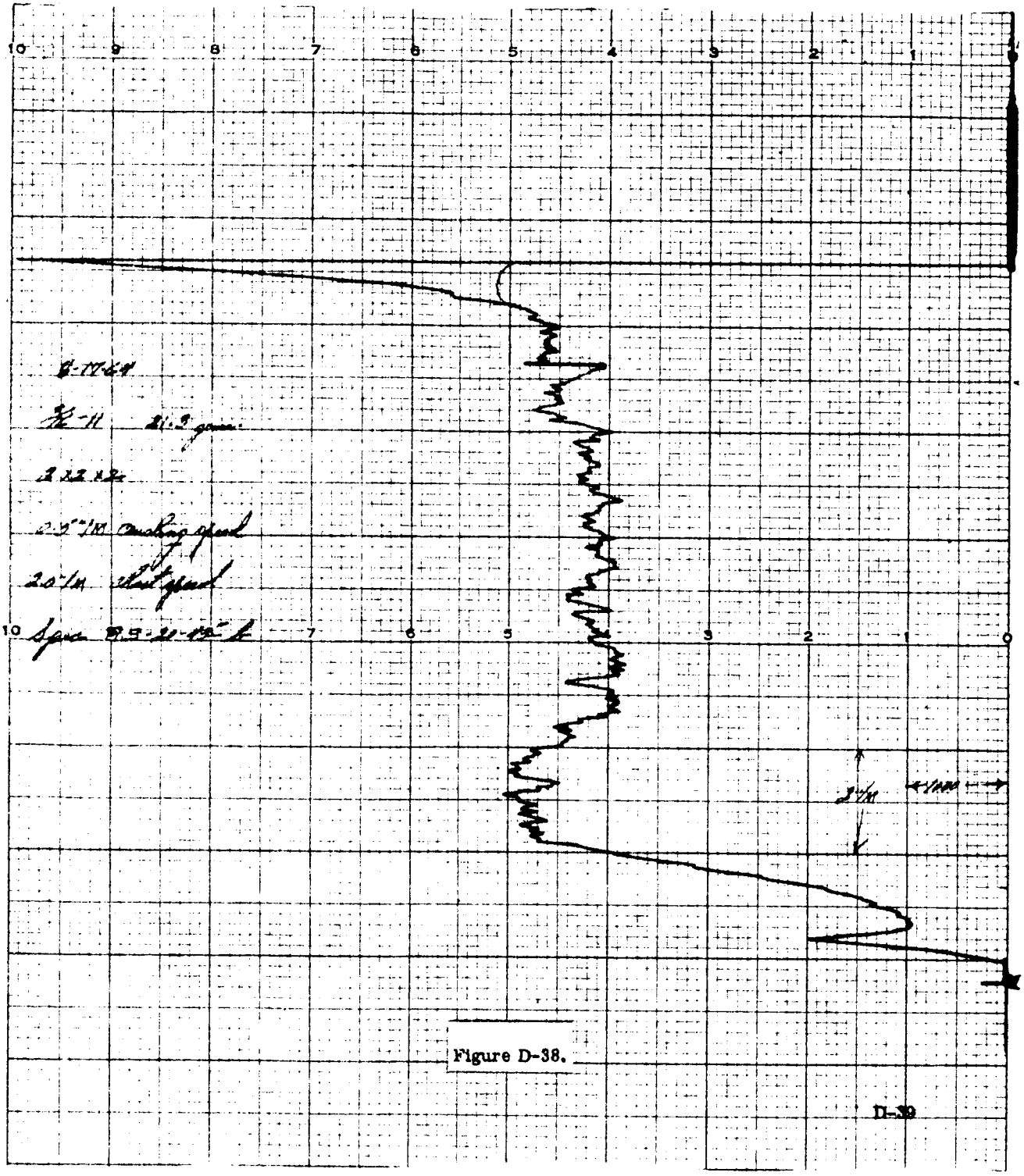

Figure D-38.

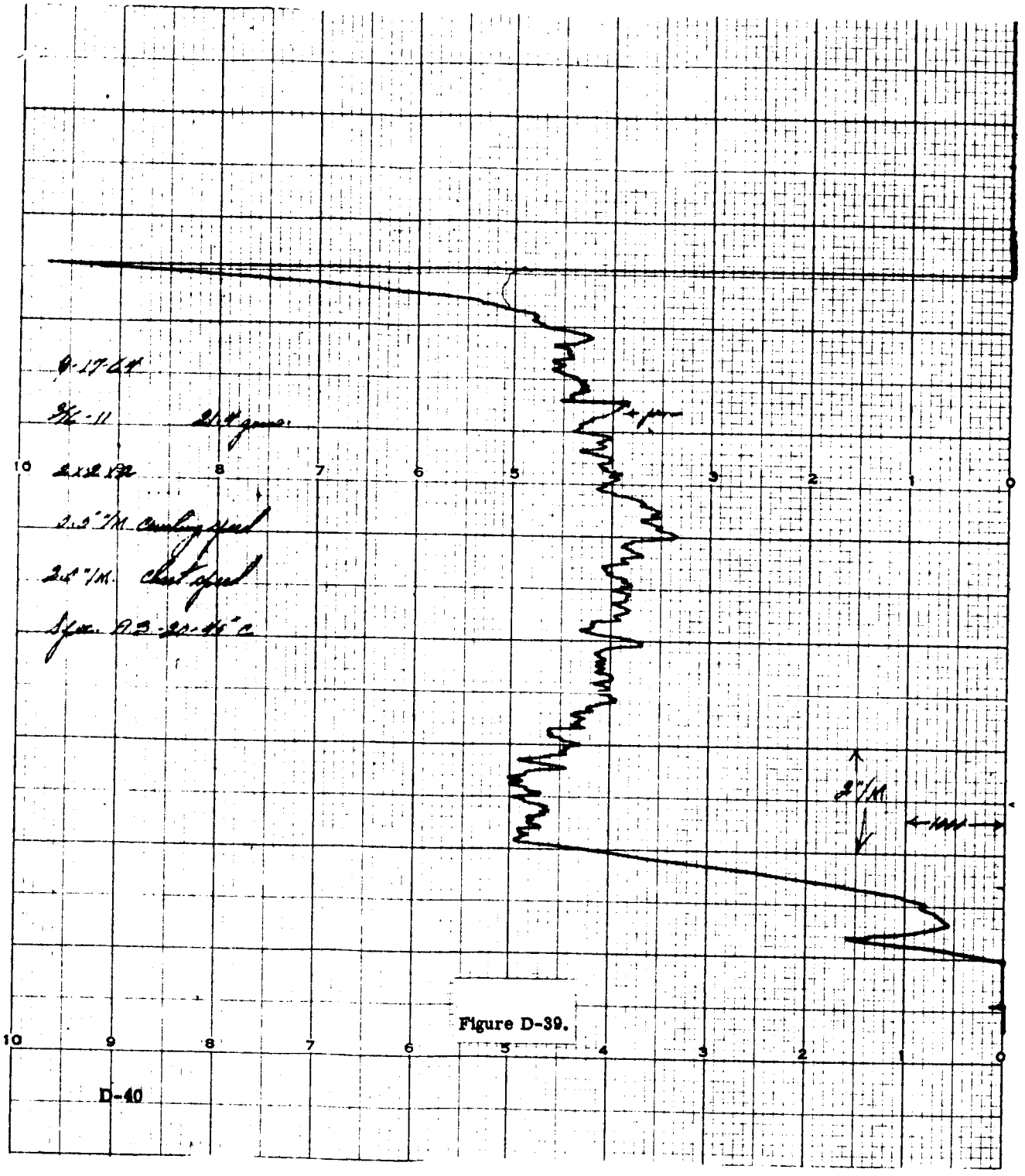

Figure D-39.

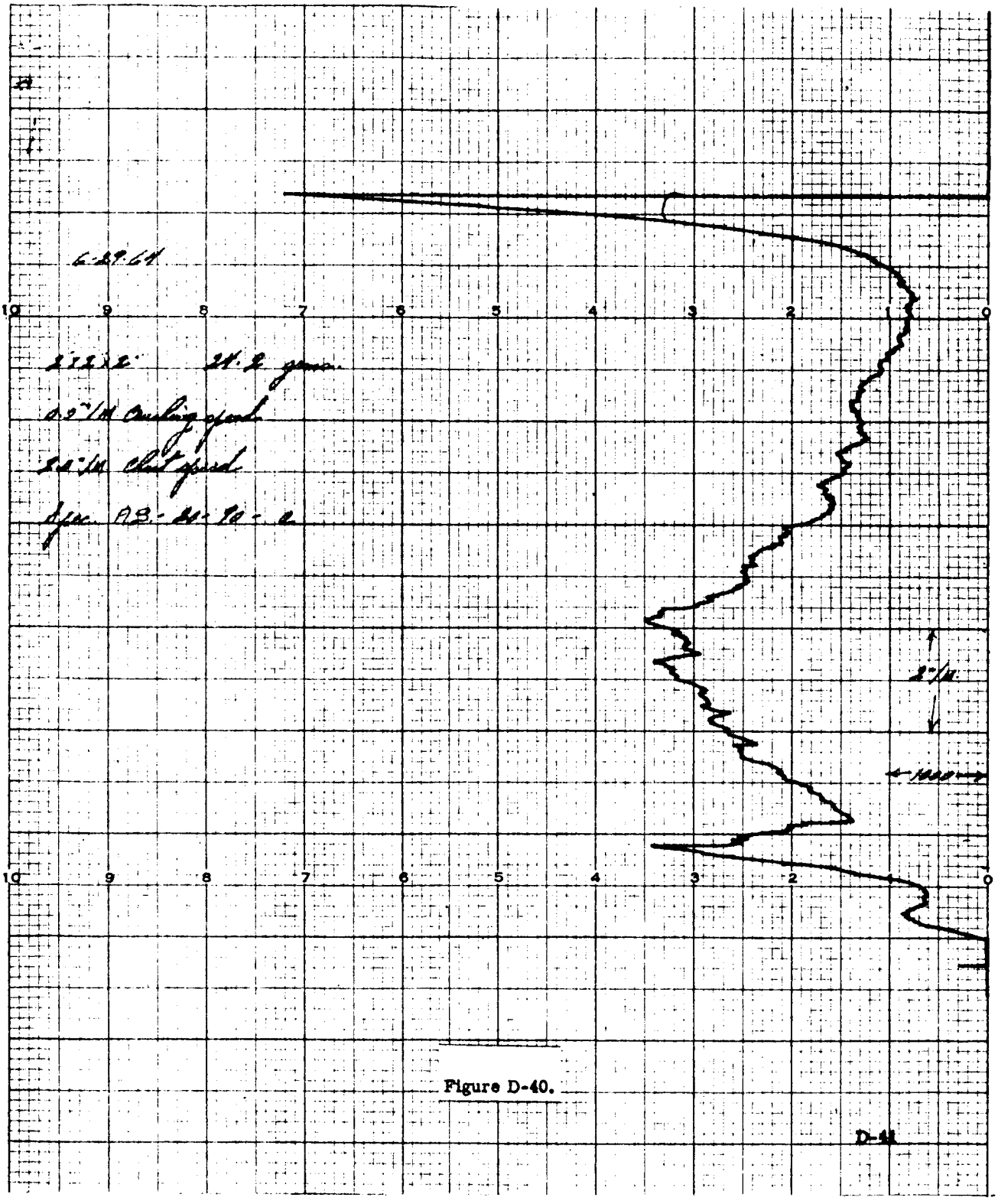

Figure D-40.

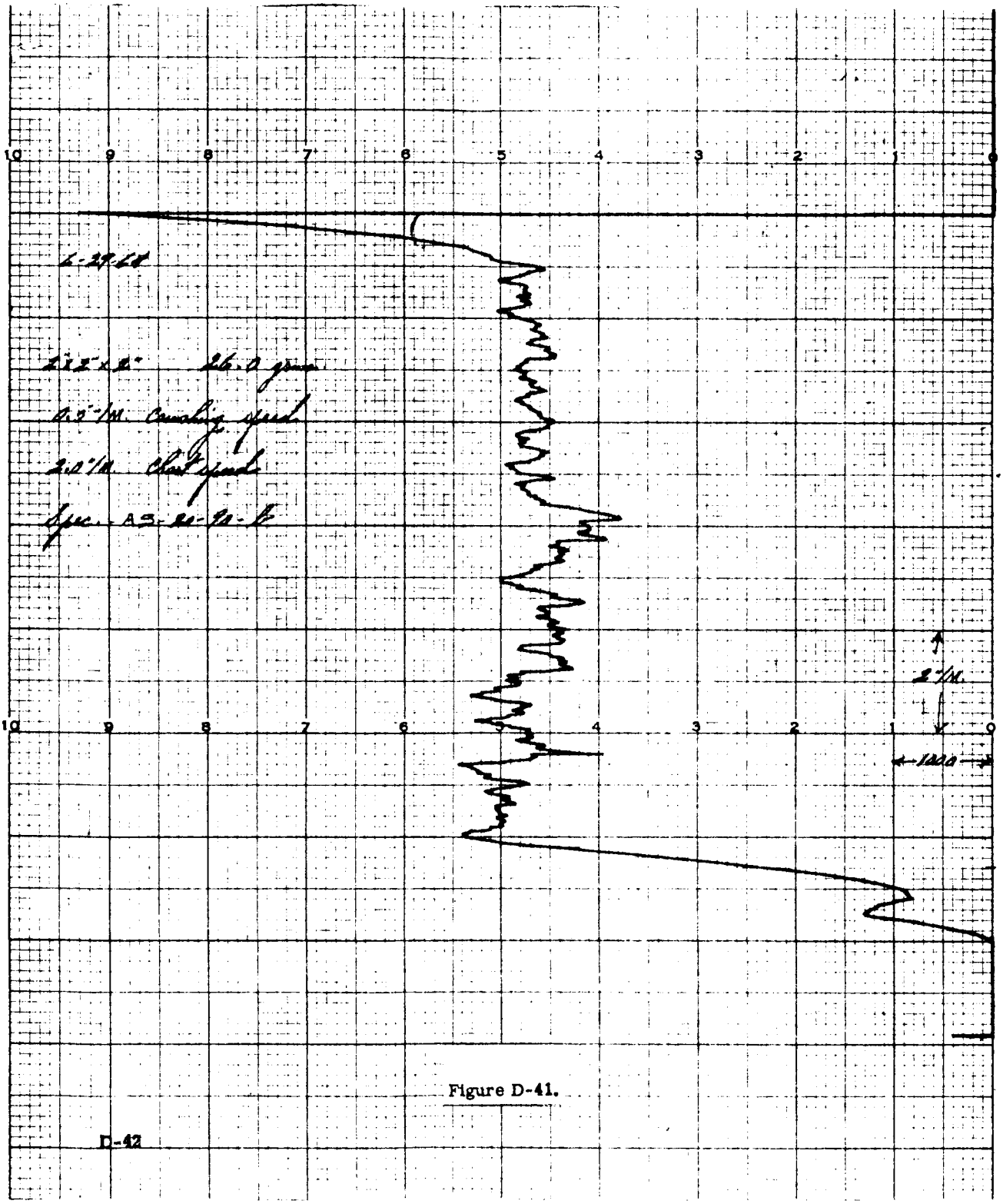
10
9
8
7
6
5
4
3
2
1
0
6-29-48
2½" x 2" 26.0 gms
0.9"/M. Counting speed
2.0"/M. Chart speed
Spec. AS-20-50-E
2"/M.
←1000→

Figure D-41.

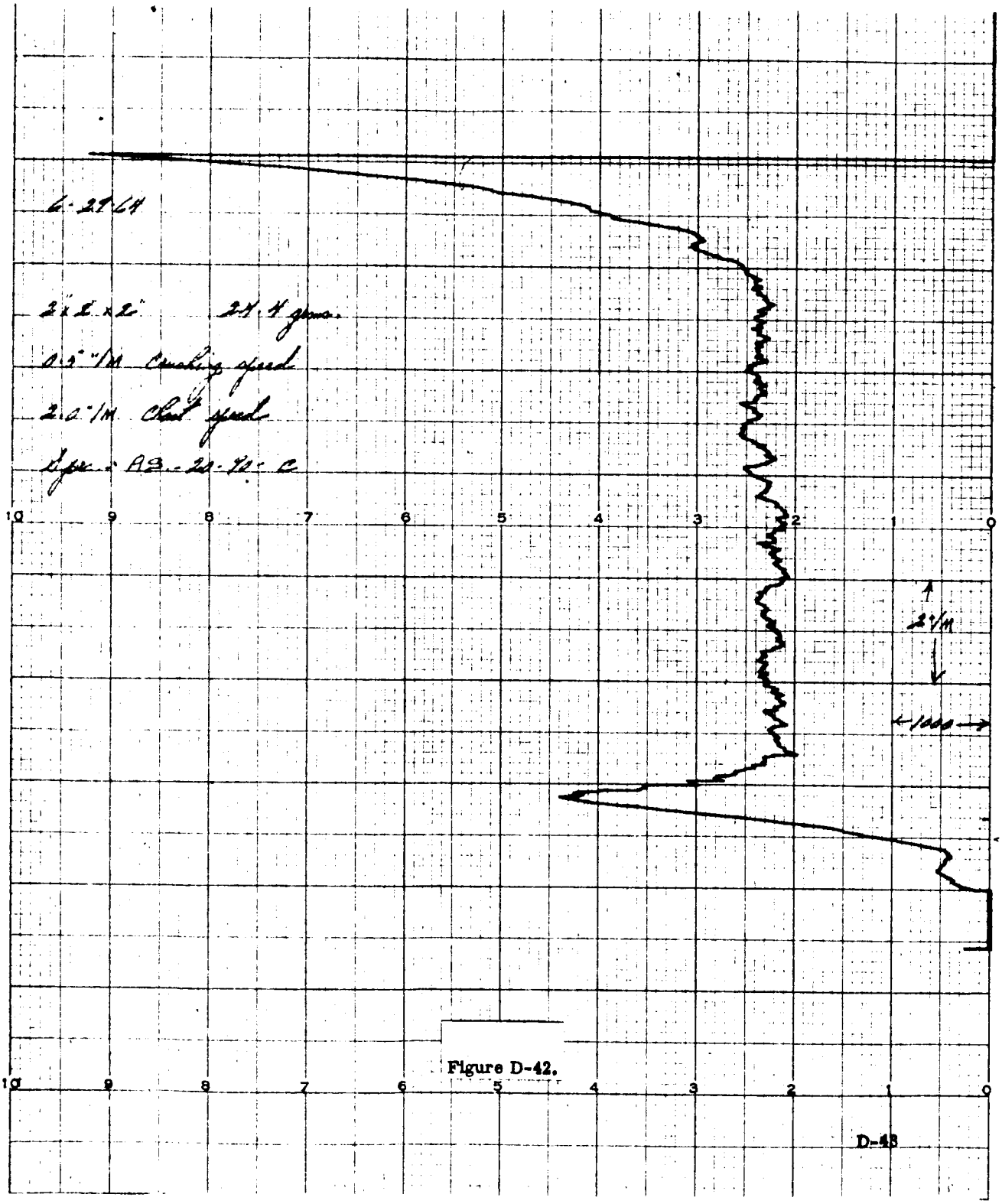
6-29-64
2" x 2" x 2" 24.4 gms.
0.5"/M Cooling speed
2.0"/M Chart speed
Type: AB-29-24-C
10 9 8 7 6 5 4 3 2 1 0
2"/M
1000
10 9 8 7 6 5 4 3 2 1 0

Figure D-42.

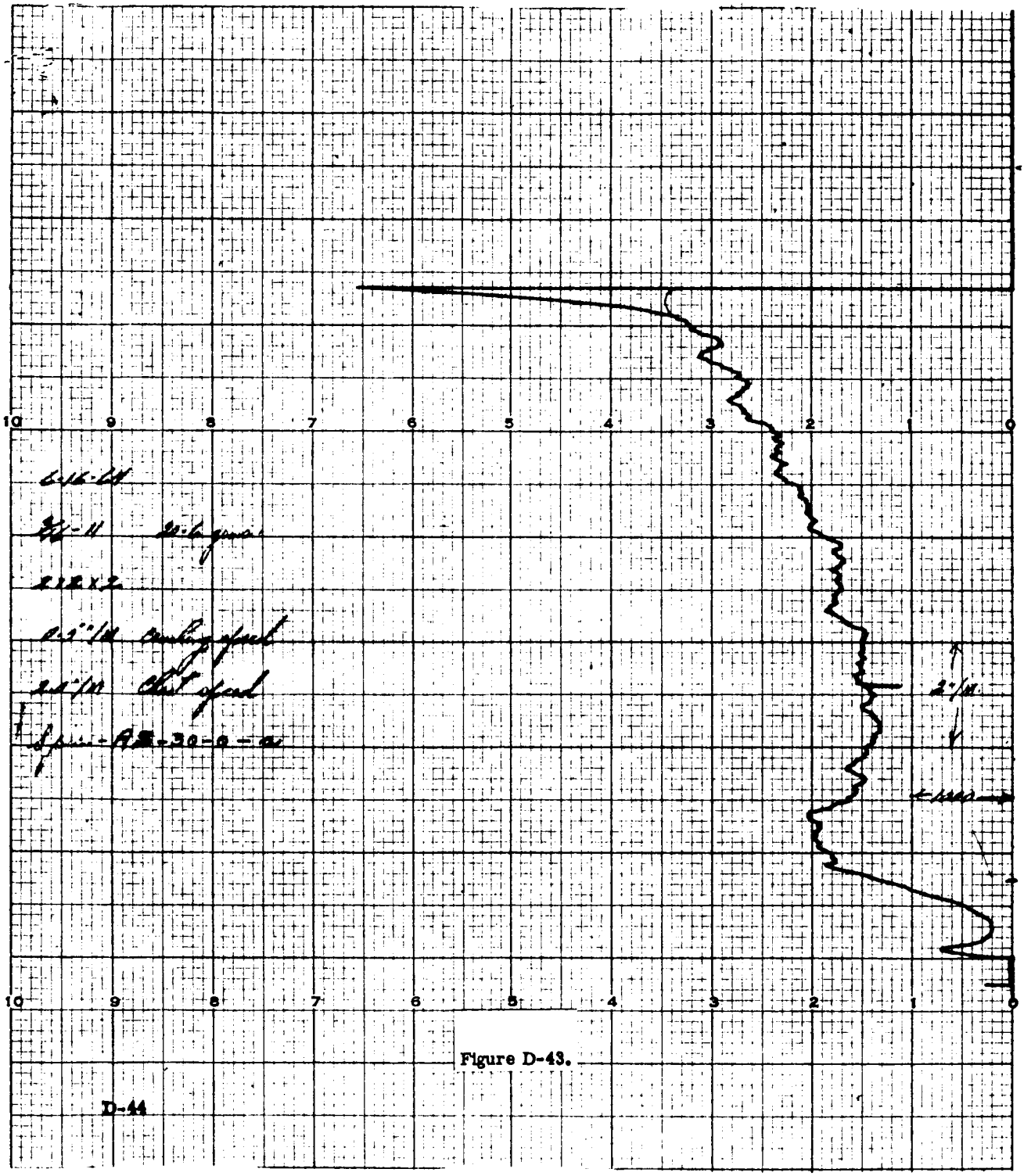

Figure D-43.

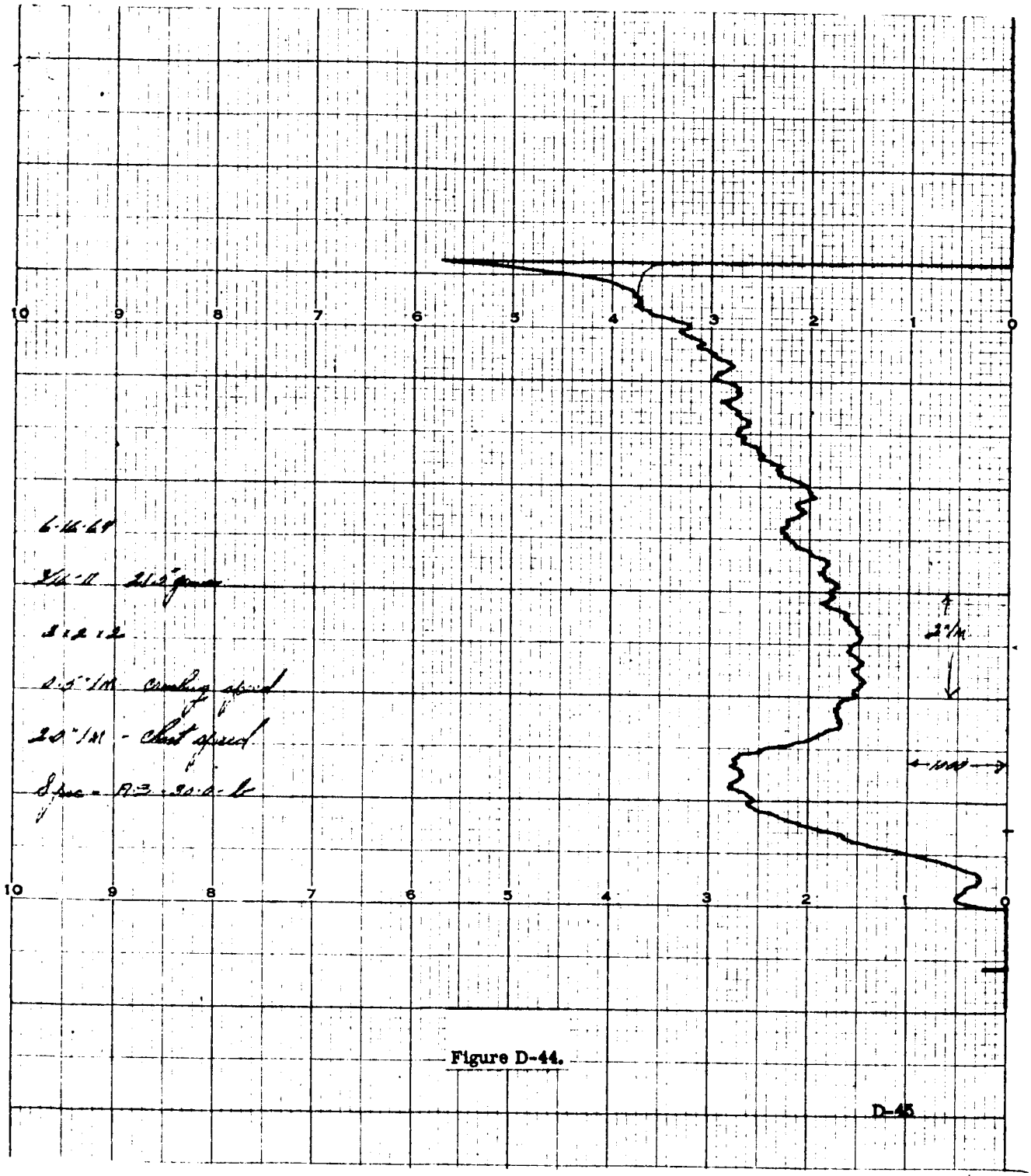
10
9
8
7
6
5
4
3
2
1
0
6-16-69
2½-11 21.2 gms
8 x 2 x 2
2.5"/M Cooling speed
20"/M - Chart speed
Spec - A-3, 20.2-b
2"/M
10
9
8
7
6
5
4
3
2
1
0

Figure D-44.

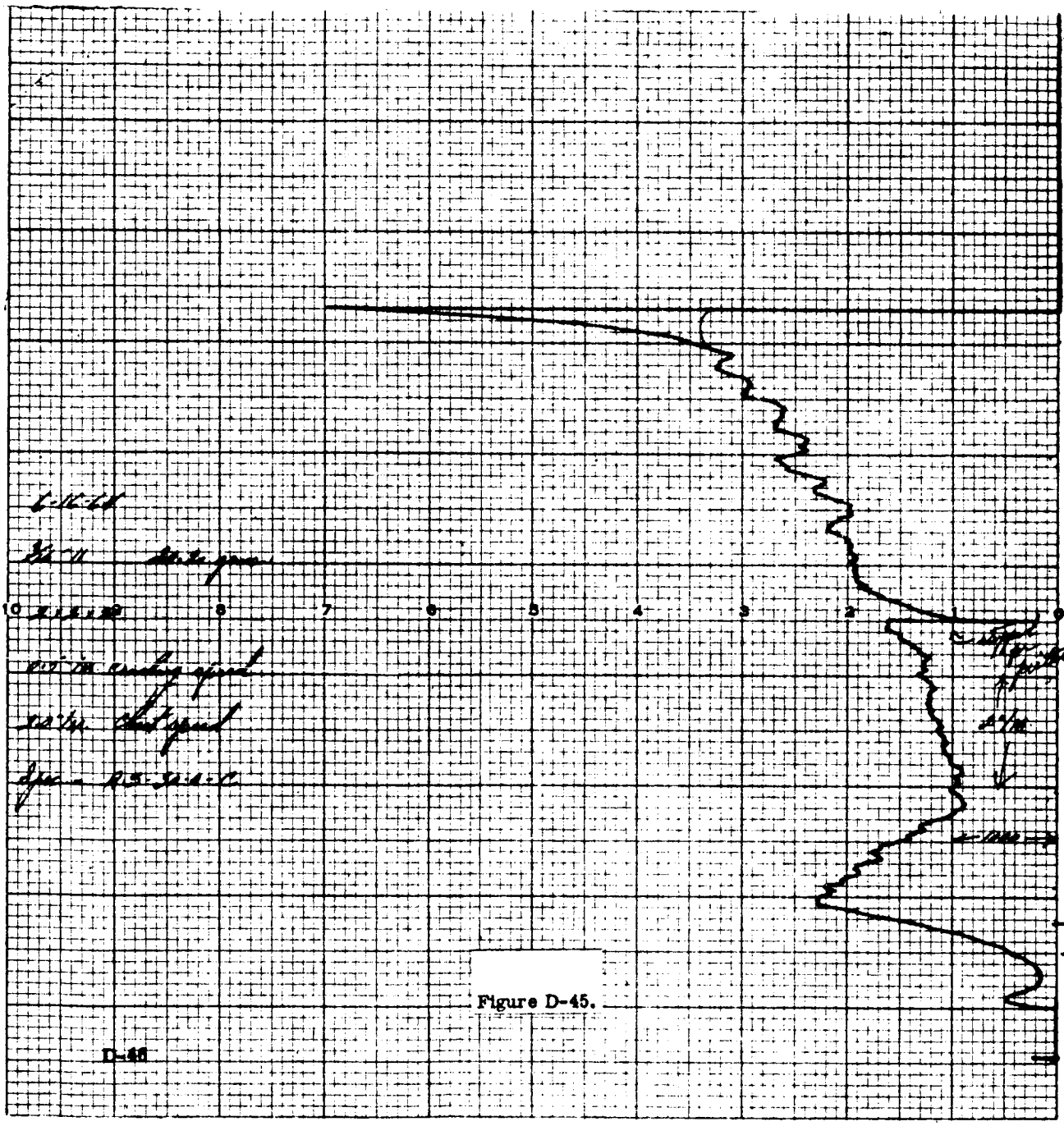

Figure D-45.

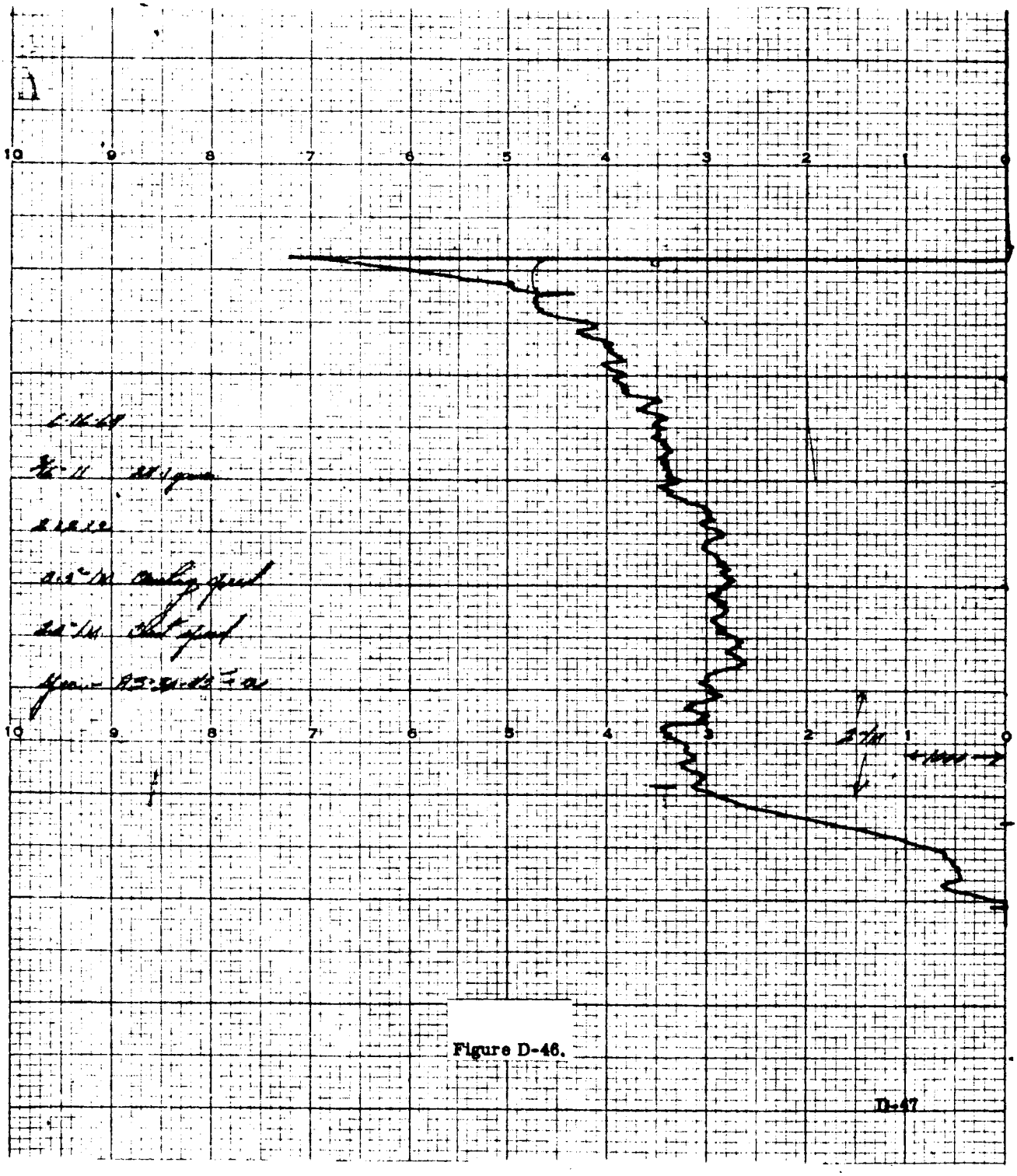

Figure D-46.

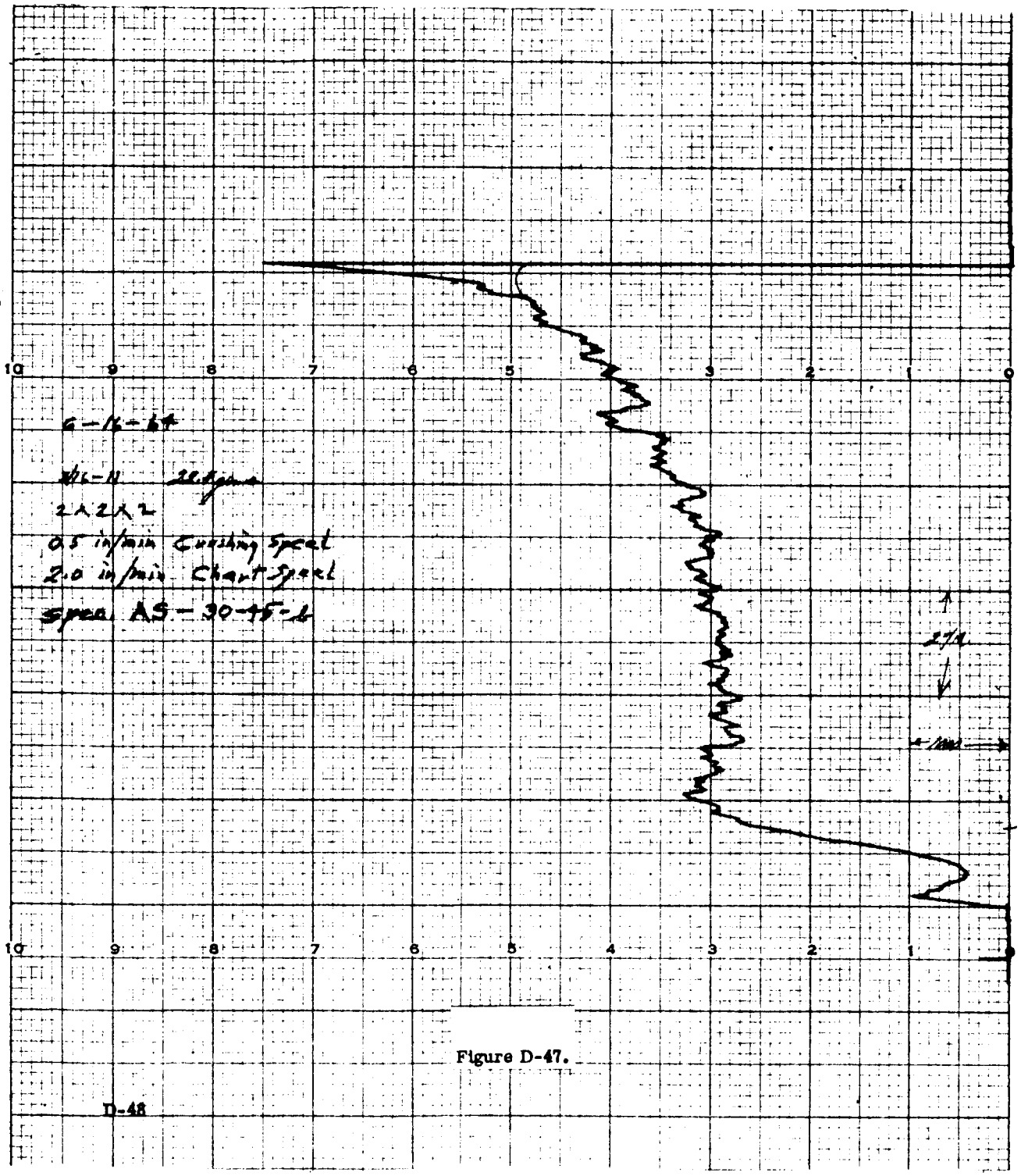
10
9
8
7
6
5
4
3
2
1
0
6-16-64
Alc-N 22.6 gm
2 x 2 x 2
0.5 in/min Cutting Speed
2.0 in/min Chart Speed
Spec AS-30-45-b
2 in.
1 min

Figure D-47.

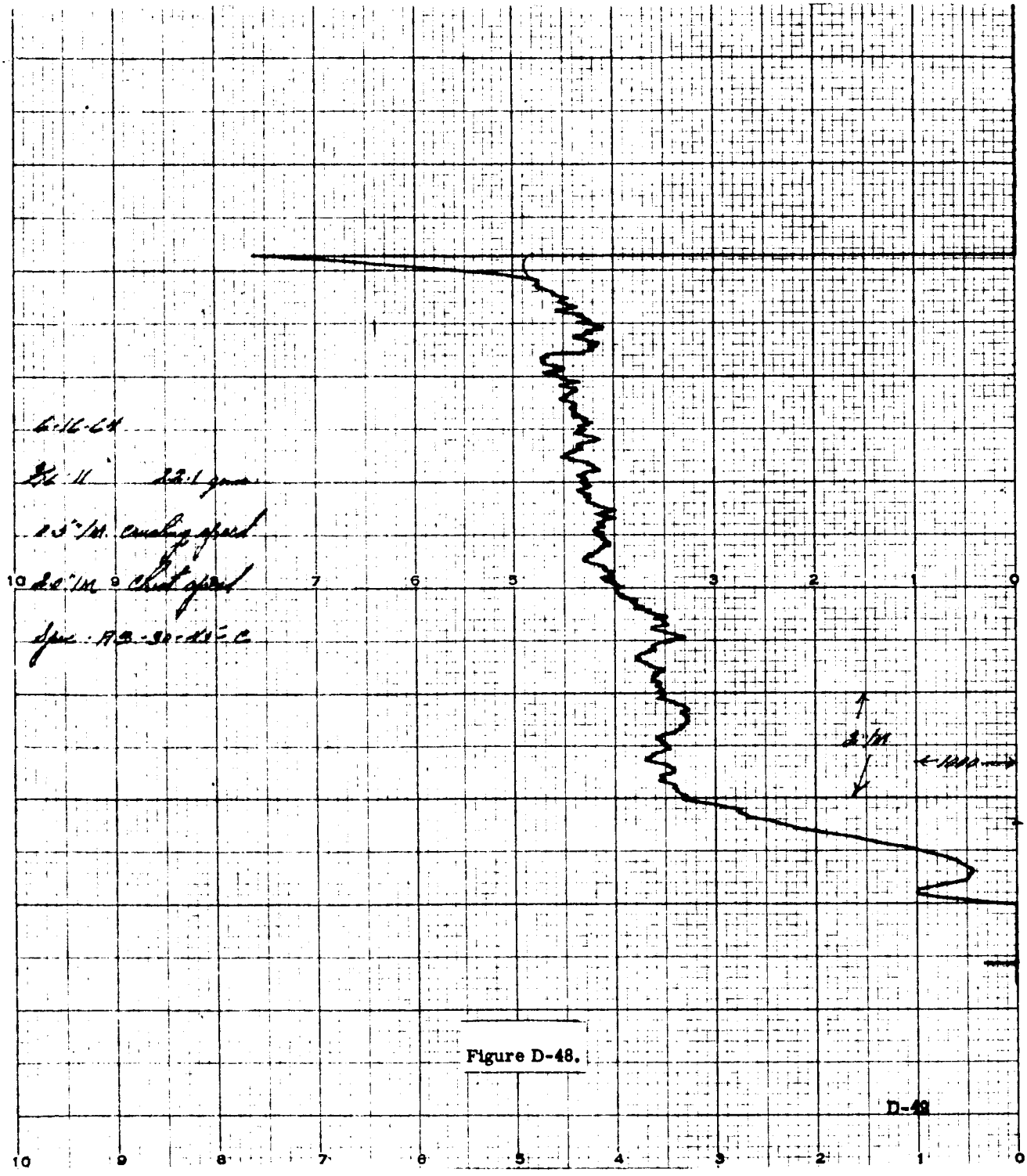

Figure D-48.

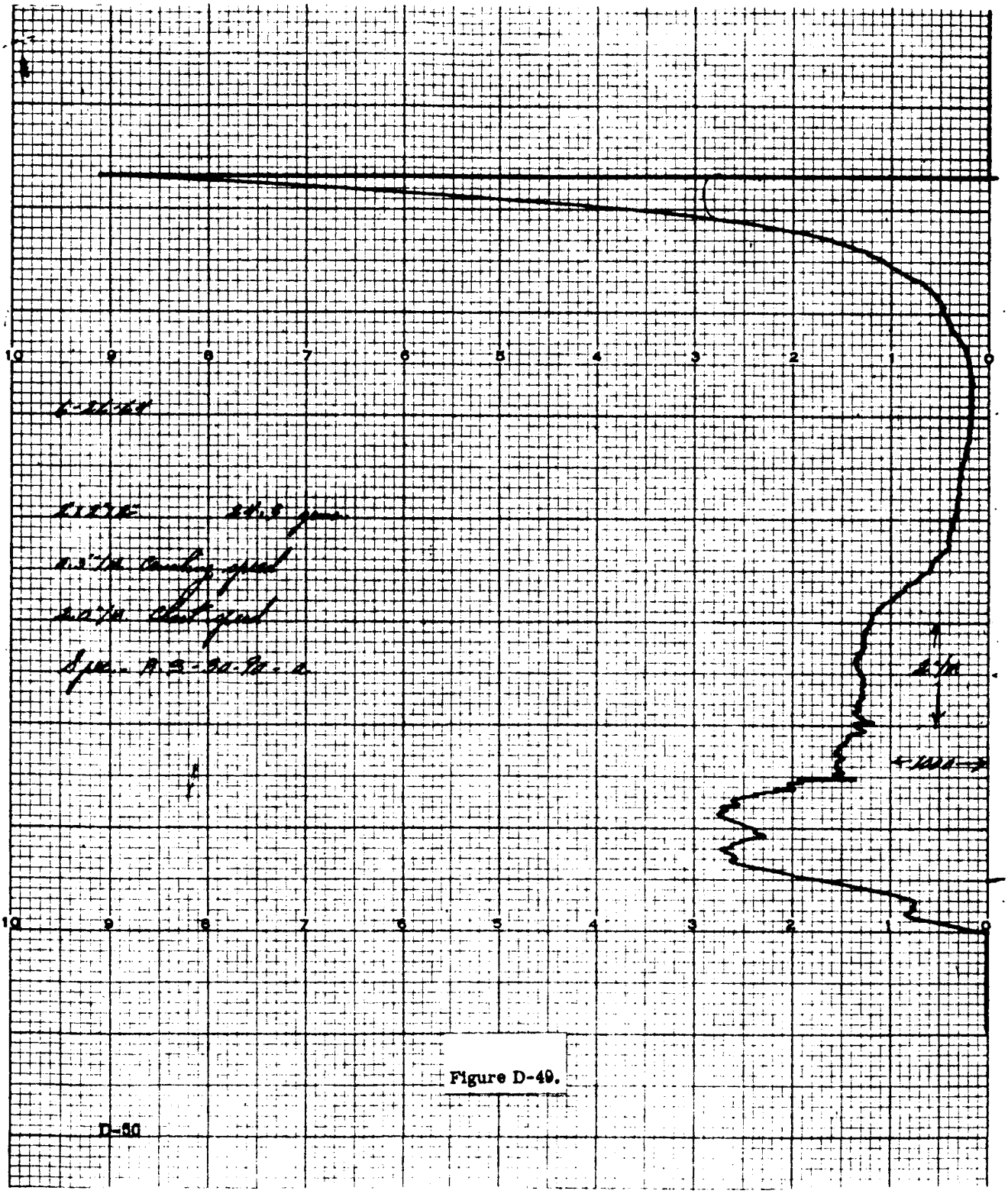

Figure D-49.

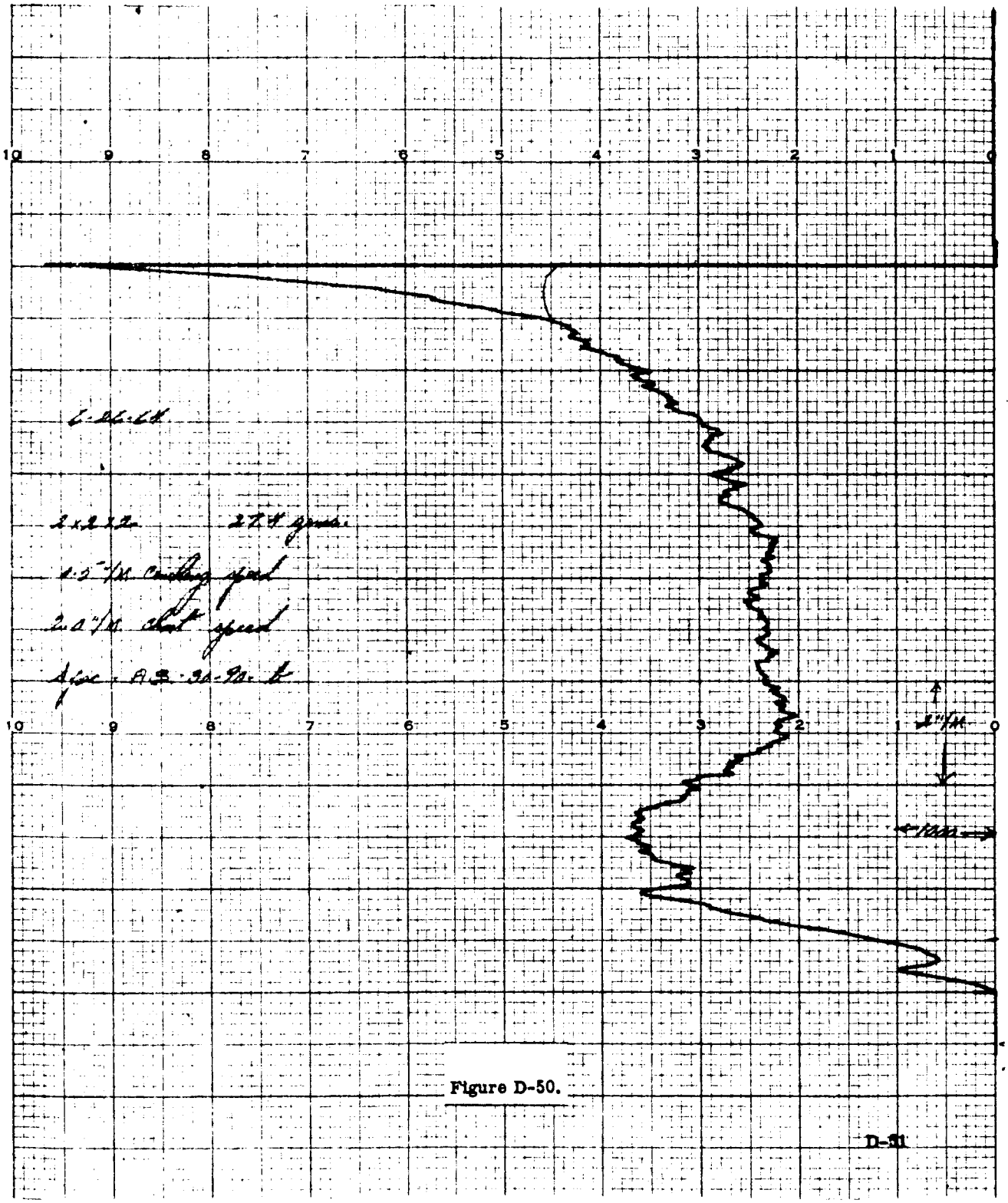

Figure D-50.

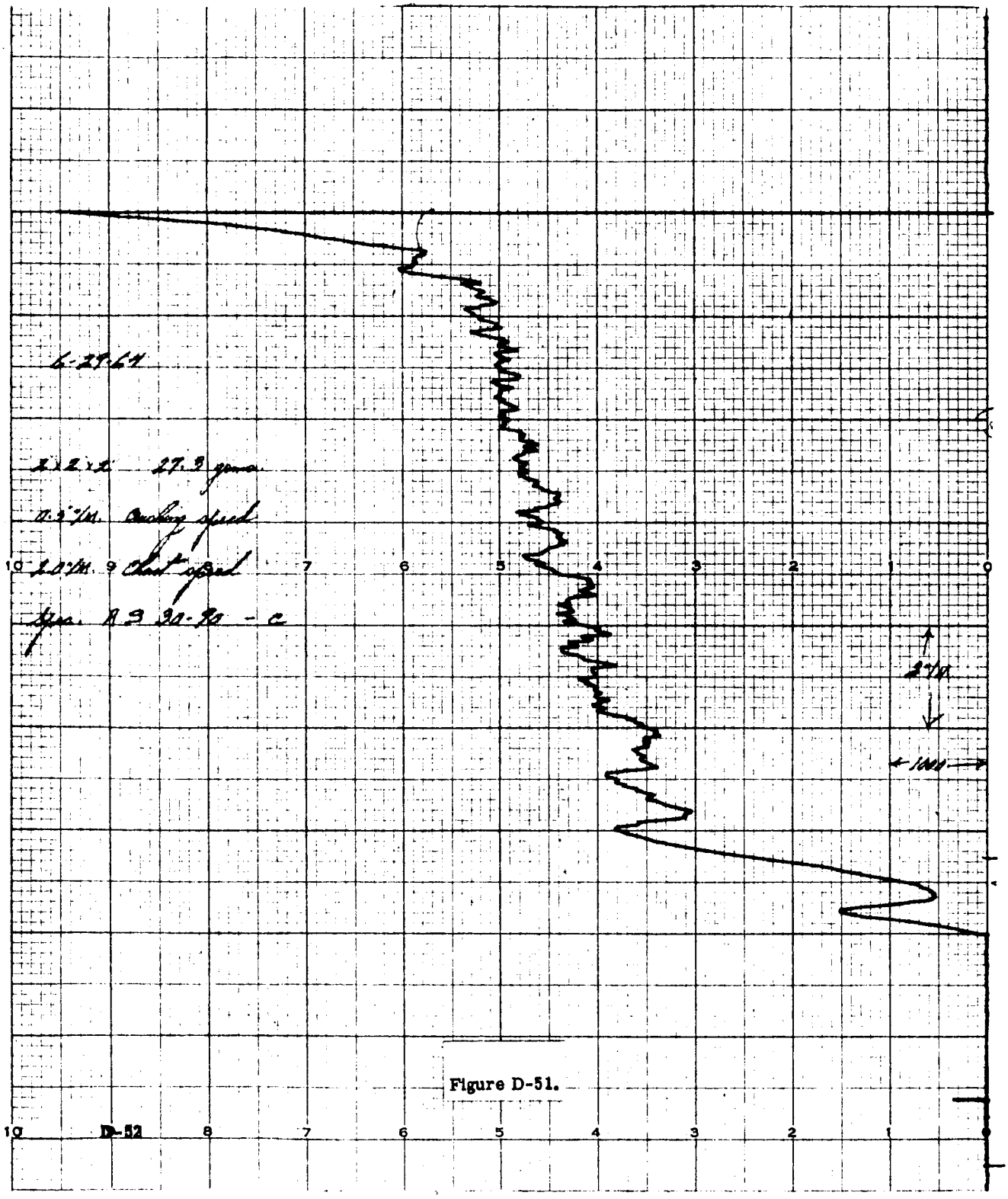
6-28-64
2 x 2 x 2 27.9 gms
11.3"/sec. Cooling speed
2.0"/sec. Chart speed
Spec. A 9 20-70 - c
10
9
8
7
6
5
4
3
2
1
0
2"
1"

Figure D-51.

APPENDIX E

CURVED SPECIMENS

APPENDIX E. CURVED SPECIMENS

Figure E-1 in this Appendix shows the successfully curved honeycomb specimens manufactured under this contract.

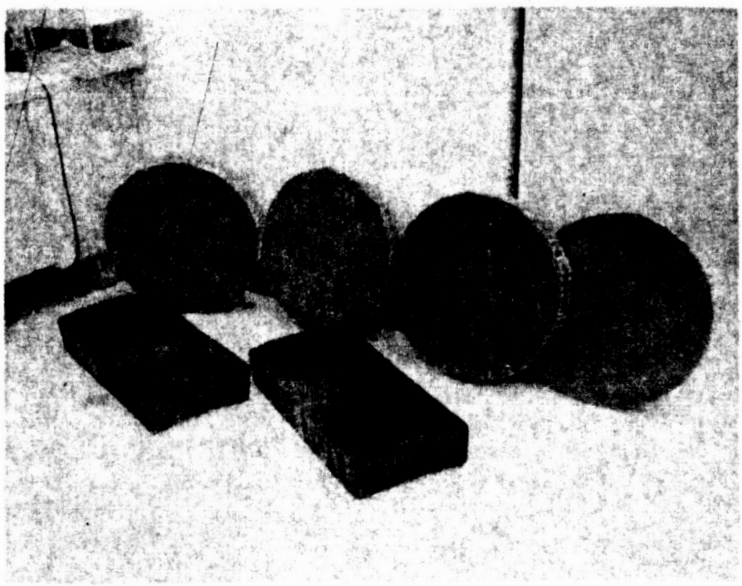

Figure E-1. Curved Specimens

64-309

DISTRIBUTION LIST

G.E. Bainton	Room U 8604	R. Rainey	CC&F1 1026A
W.R. Becraft	Room U 3032B	R.R. Reid	Room M 4022
B.H. Caldwell	Room M 7023D	A. Ringwood	Room M 2112
A.P. Coppa	Room U 8604	R.E. Roach	Room U 2612
C. Dolan	Room U 1235	B.W. Rosen	Room M 7047G
A. Garber	CC&F1 1233	W. Roths	Room U 4448
J. Green	Room U 3041	L.T. Seamans, Jr.	Room U 2420
I.J. Gruntfest	Room U 4448	J.D. Selby	Room U 8604
G.R. Hagen	Room U 4632	L.H. Shenker	Room U 3231
H.G. Lorsch (5)	Room U 2612	J.E. Tucker	Room U 3041
C.B. Mayforth, Jr.	Room U 2612	R.R. Wallace	Room M 4228
R.T. Mayer	Room M 4632	A.A. Watts	Room M 9543
W.M. Meyers (15)	Room U 1212	F.W. Wendt	Room M 4214
R.J. Mustaro (2)	Room M 2626	R. Wooten	Room U 3032
G.F. Oberrender, Jr.	Room U 3228		

R. Wansor
General Electric Defense Products Operation
McCulloch Building
6151 West Century Boulevard
Los Angeles, California

Mr. J.F. Curtis (6+1 Repro.)
Contract Administrator
Jet Propulsion Laboratories
California Institute of Technology
4800 Oak Grove Drive
Pasadena, California